Univerzita Karlova

1. lékařská fakulta

Studijní program: Biochemie a patobiochemie

Studijní obor: Biochemie a patobiochemie

UNIVERZITA KARLOVA
1. lékařská fakulta

Mgr. Jitka Neburková

Cílené biokompatibilní nanočástice pro terapii a diagnostiku rakoviny

(Targeted biocompatible nanoparticles for therapy and cancer diagnostics)

Dizertační práce

Školitel: Mgr. Petr Cígler, PhD.

Praha, 2018

Prohlášení:

Prohlašuji, že jsem závěrečnou práci zpracovala samostatně a že jsem řádně uvedla a citovala všechny použité prameny a literaturu. Současně prohlašuji, že práce nebyla využita k získání jiného nebo stejného titulu.

Souhlasím s trvalým uložením elektronické verze mé práce v databázi systému meziuniverzitního projektu Theses.cz za účelem soustavné kontroly podobnosti kvalifikačních prací.

V Praze, 11.6. 2018

Jitka Neburková

Identifikační záznam:

NEBURKOVÁ, Jitka. *Cílené biokompatibilní nanočástice pro terapii a diagnostiku rakoviny [Targeted biocompatible nanoparticles for therapy and cancer diagnostics]*. Praha, 2018. 78 s., 7 příl. Dizertační práce (Ph.D.). Univerzita Karlova v Praze, 1. lékařská fakulta. Vedoucí práce Cígler, Petr.

Poděkování:

Ráda bych poděkovala svému školiteli Petru Cíglerovi za možnost vypracovat dizertační práci v jeho laboratoři, jeho cenné rady, za mnoho různorodých projektů, které jsem měla možnost řešit, a za samostatnost, které jsem se naučila po dobu studia. Dále bych chtěla poděkovat celému kolektivu laboratoře Syntetické nanochemie, který je velmi přátelský a vždy ochotný pomoct a poradit, a ostatním spolupracovníkům, kteří mi umožnili uskutečnit řešené projekty. Největší dík patří mé rodině za cennou podporu, které se mi od nich vždy dostane.

TABLE OF CONTENTS

SUMMARY

Nanoparticles (NPs) have considerable potential in targeted medicine. NPs can merge various functions and serve as labels for imaging or as nanocarriers in therapy. Modification of NPs with targeting ligands can lead to highly specific interactions with targeted cancer cells. However, the efficacy of targeting depends on the ratio between specific and non-specific interactions of a NP with the cell. Non-specific interactions of NPs are unrelated to targeted receptors and need to be eliminated in order to decrease background noise during imaging and adverse effect of drugs on healthy tissues.

In this thesis, surface modifications of NPs were explored mainly on biocompatible carbon NPs called nanodiamonds (NDs), which have exceptional fluorescent properties such as long fluorescence lifetime, no photobleaching and photoblinking and sensitivity of their fluorescence to electric and magnetic field. Main issues addressed in this thesis are low colloidal stability of NDs in buffers and media, their non-specific interactions with proteins and cells and limited approaches for ND surface modifications. These issues were solved by coating NDs with a layer of biocompatible, hydrophilic, and electroneutral poly(ethylene glycol) or poly[*N*-(2-hydroxypropyl) methacrylamide] polymers. Optimized polymer coating provided NDs steric stabilization in concentrated buffers, eliminated non-specific interactions with cells and enabled further bioorthogonal functionalization of NDs. Modification of NDs was demonstrated using various targeting ligands. First, NDs were modified with targeting peptide cyclic RGD. These conjugates showed reasonable targeting effect thanks to the elimination of non-specific interactions. The specific interactions of NDs with cancer cells were further improved upon surface modification with transferrin and small-molecule inhibitor of glutamate carboxypeptidase II.

The developed biocompatible interface of NDs enabled further biomedical applications. First, NDs with gold layer and polymer coating were shown to efficiently target and kill cancer cells using photothermal ablation. Second, optical relaxometric nanosensors working under physiological conditions were created from NDs with polymer layer containing Gd^{3+}complexes. The chemically programmable structure of the polymer enabled optical readout of localized chemical processes occurring on an extremely small scale (10^{-22}–10^{-20} mol).

Key words: nanoparticles, nanodiamonds, surface modifications, polymer coating, anti-fouling, core-shell, cell targeting, biomedical applications

SOUHRN

Nanočástice mají mnoho předpokladů k tomu, aby byly použity v cílené medicíně. Mohou zastávat více funkcí najednou a sloužit tak jako zobrazovací značky nebo nosiče účinných látek pro terapii. Po modifikaci vhodným cílícím ligandem mohou specificky interagovat s rakovinnými buňkami. Účinnost cílení nicméně závisí na poměru mezi specifickou a nespecifickou interakcí nanočástic s buňkami. Nespecifické interakce nanočástic s buňkami nesouvisí s cíleným receptorem a musí být odstraněny, aby bylo možné snížit pozadí zobrazování, případně snížit škodlivý efekt léků na zdravé tkáně.

V této práci byly povrchové modifikace nanočástic zkoumány především na biokompatibilních uhlíkových nanočásticích nanodiamantech, které vykazují výjimečné fluorescenční vlastnosti jako je dlouhá doba života fluorescence, fluorescence bez fotodestrukce („photobleaching“) a blikání („photoblinking“) a citlivost fluorescence k elektromagnetickému poli. Hlavními nedostatky nanodiamantů, které jsou v této práci řešeny, jsou nízká koloidní stabilita částic v pufrech a médiích, jejich nespecifické interakce s proteiny a buňkami a omezené možnosti modifikací povrchu. Tyto nedostatky byly překonány pokrytím nanodiamantů vrstvou biokompatibilních, hydrofilních a elektroneutrálních polymerů poly(etylenglykolu) a poly[*N*-(2-hydroxypropyl) metakrylamidu]. Optimalizovaná polymerní vrstva poskytovala částicím stabilizaci v koncentrovaných pufrech, eliminovala nespecifické interakce s buňkami a umožnila bioortogonální modifikace cílícími ligandy. Pro cílení k rakovinným buňkám byly nanodiamanty nejprve modifikovány cyklickým peptidem RGD. Tyto částice vykazovaly výrazný cílící efekt díky eliminaci nespecifických interakcí nanočástic s buňkami. Specifická interakce nanodiamantů s rakovinnými buňkami byla dále vylepšena po modifikaci proteinem transferinem a nízkomolekulárním inhibitorem glutamát karboxypeptidázy II.

Díky vyvinutému biokompatibilnímu povrchu bylo možné nanodiamanty využít v biomedicínských aplikacích. Nejprve byly nanodiamanty s vrstvou zlata a polymeru použity pro účinné cílení a zabití rakovinných buněk pomocí fototermální ablace. Dále byly nanodiamanty s polymerní vrstvou a komplexy s Gd^{3+} ionty použity pro vytvoření optických relaxometrických nanosenzorů pracujících ve fyziologických podmínkách. Povrchová struktura nanosenzorů umožnila optické čtení lokalizovaných chemických dějů s extrémní citlivostí (10^{-22}–10^{-20} mol).

Klíčová slova: nanočástice, nanodiamanty, povrchové modifikace, polymerní vrstva, cílení buněk, biomedicínské aplikace

LIST OF ABBREVIATIONS

AIBN	azobis(isobutyronitrile)
ATRP	atom transfer radical polymerization
BSA	bovine serum albumine
CCRF-CEM	human T lymphoblast
CVD	chemical vapor deposition
DLS	dynamic light scattering
DMAEMA	2-(dimethylamino)ethyl methacrylate
DNA	deoxyribonucleic acid
DND	detonation nanodiamond
EPR	the enhanced permeation and retention
GCPII	glutamate carboxypeptidase II
GSH	glutathione
HeLa	human adenocarcinoma cell line
HER2	human epidermal growth factor receptor 2
HPHT	high pressure and high temperature
HPMA	*N*-(2-hydroxypropyl)methacrylamide
HUVEC	human umbilical vein endothelial cell line
ICP-MS	inductively-coupled plasma mass spectrometry
LNCaP	human prostate adenocarcinoma cells
ND	nanodiamond
NHS	*N*-hydroxysuccinimide
NIR	near infrared
NP	nanoparticle
(N-V)	nitrogen vacancy
ODMR	optically detected magnetic resonance

PBS	phosphate buffer saline
PEG	poly(ethyleneglycol)
PEI	polyethyleneimine
PHPMA	poly[*N*-(2-hydroxypropyl)methacrylamide]
PPEGMA	poly[PEG methyl ether methacrylate]
PG	polyglycerol
Qβ	bacteriophage virus-like particle
RAFT	reversible addition-fragmentation chain transfer
RGD	peptide with three amino acid sequence arginine-glycine-glutamic acid
RNA	ribonucleic acid
SDS-PAGE	sodium dodecyl sulfate–polyacrylamide gel electrophoresis
SPR	surface plasmon resonance
TBS	tris-buffered saline
TEM	transmission electron microscopy
TEOS	tetraethoxysilane
TGA	thermogravimetric analysis
U-87 MG	human glioblastoma cell line
U2OS	human osteosarcoma cancer cell line
MPyV	mouse polyomavirus-like particle
U-251 MG	glioblastoma cell line

1. INTRODUCTION

1.1. Nanoparticles for targeted nanomedicine

Optical imaging is a key tool in contemporary biomedicine with emerging applications, such as cancer diagnosis. Merging diagnostic imaging ability with a therapeutic function results in a "theranostic" agent. The biggest drawback of the current theranostic techniques is their lack of specificity and resulting systemic toxicity. Compared with conventional small-molecule drugs and probes, NPs (NPs) have a prolonged circulation time and stability in blood stream and can, therefore, increase tumor exposure, resulting in improved treatment effects and lower systemic toxicity. Merging various functions is a promising direction of diverse NPs (lipid and polymer based NPs, viral NPs or inorganic NPs) used in biomedicine. (Fernandez-Fernandez et al., 2011) Inorganic NPs such as gold, silica, magnetic, carbon NPs or quantum dots have special features such as plasmonic, magnetic or fluorescent properties useful for various biological applications. NPs can be used as contrast agents for magnetic resonance imaging, optical and photoacoustic imaging. However, their disadvantage is their colloidal instability in biological media and abiological origin resulting in a problematic elimination from the organism. On the other hand, organic NPs such as lipids, polymeric or protein NPs are not foreign materials, but they lack the added value of special physical properties (e.g. fluorescence, magnetism) and therefore serve only as carriers. Lipid and polymeric NPs are reaching the clinical studies most frequently, however gold, iron and silica NPs have been also tested. (Wicki et al., 2015) A few of the NPs have been already approved by the FDA (Food and Drug Administration) for clinical use. (Bobo et al., 2016)

Cellular uptake of NPs into the tumors is enhanced through inherent nature of passive targeting (the enhanced permeation and retention – also known as EPR effect) and also possibly using active targeting. (Prokop and Davidson, 2008) EPR effect is based on a fact that newly formed tumor blood vessels have large gaps among endothelial cells and NPs can get through these gaps from blood to tumor tissue. Active targeting is facilitated by targeting molecules (ligands), which recognizes and binds to targeted moiety via molecular recognition. NPs that are modified with targeting ligands can specifically recognize only targeted receptors on certain cells and they interact with other cell types in lower extent (Fig. 1). Targeting molecules can be covalently attached on the surface of the NPs in high concentration; therefore, avidity to a targeted moiety is greatly increased, circumventing a low affinity of many ligands. (Prokop and Davidson, 2008) Convenient NP carriers can carry a large amount of a drug and do not induce

immune reaction resulting in the prolonged half-life in the blood. Both the prolonged circulating time in organism and accumulation of carriers in targeted place enhance the effect of the drug in tumor tissue and enables to use a lower dose of the NP drug carriers having lower adverse effects on healthy tissues.

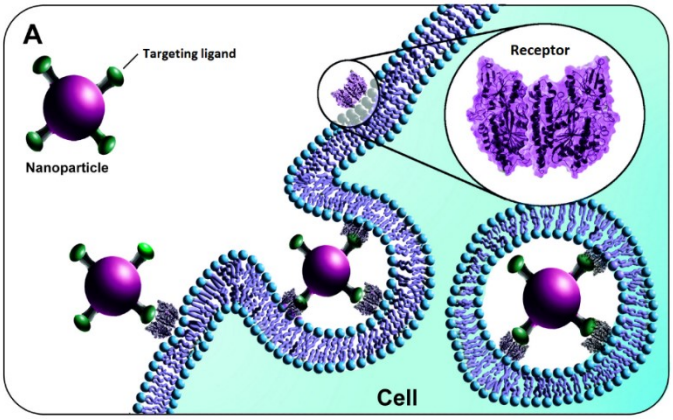

Fig.1 The overall scheme of targeting using NPs bearing polyvalent array of targeting ligands, which binds to receptor, anchored in cell membrane. In certain cases, the NP is then endocytosed. Adapted from (Neburkova et al., 2018).

1.2. Nanodiamonds

Carbon-based nanomaterials have garnered a great deal of interest over the past three decades, starting with the fullerenes, carbon nanotubes and graphene and lately more and more attention is put on carbon nanodots and nanodiamonds (NDs). (Georgakilas et al., 2015) Carbon NPs differ in hybridization of carbon atoms (sp^2 or sp^3), size and therefore in their physicochemical properties. In our laboratory, we focus mostly on the NDs.

NDs show low toxicity and are considered to be highly biocompatible carbon NPs; they are polydisperse in both size and shape (Fig. 2A). There are three main preparation techniques yielding NDs with distinct properties.

Detonation diamonds (DNDs) are prepared upon detonation of certain explosives (trinitrotoluene and hexogen) in presence of a non-oxidizing cooling medium. DNDs have small size of primary grains (2-10 nm), but tend to form clusters (100-200 nm). Thanks to their high surface to volume ratio, they can adsorb substantial amount of cargoes and are often studied as drug delivery or transfection agents. (Mochalin et al., 2012) ND particles can be created also by plasma-assisted chemical vapor deposition (CVD NDs). CVD NDs are grown as nanocrystalline films of grain size 5 nm to several micrometers and are widely used for biosensor applications. (Butler and Sumant, 2008). NDs grown in high pressure and high temperatures conditions (HPHT) form micron-size crystals which can be milled to approximately 50 nm grains. These HPHT NDs contain nitrogen impurities from preparation process, which give rise, after proper treatment, to fluorescent nitrogen-vacancy (N-V) centers.

HPHT NDs are therefore used as cellular labels an nanosensors, enabling bioimaging for extended time thanks to their exceptional optical properties. (Chang et al., 2008) In our laboratory, we work almost exclusively with fluorescent HPHT NDs.

1.2.1. Surface chemistry on NDs

After synthesis, the NDs are contaminated with a small amount of various sp^2 carbon phases. These can be removed by oxidation in air at elevated temperature (510 °C) for several hours, at which sp^3 carbon is not yet burned. (Osswald et al., 2006) After this procedure the surface of NDs is highly heterogeneous, containing carboxyl or hydroxyl groups, ketones, anhydrides, lactones and other groups present. (Krueger and Lang, 2012) The heterogeneity of the surface is further reduced using oxidative treatment in mineral acids. (Havlik et al., 2013) This process produces surface with high fraction of hydroxyls and carboxylic acids. Such pretreated NDs form stable colloidal solutions in water.

Modifications of these hydroxyl and carboxyl groups on NDs were thoroughly studied. All the approaches of surface modification require harsh reaction conditions, because the groups are sterically hindered by close proximity of the surface and the modification efficiency is generally low. Instead of full conversion, we speak about enrichment of the surface by certain moieties (hydrogen atoms, halogen atoms or hydroxyl groups). There is a difference between surface functionalization of NDs according to their origin. DNDs because of their smaller size (higher surface to volume ratio) and many sp^2 carbon atoms on the surface are more prone to the modification and more studied than HPHT NDs. (Krueger and Lang, 2012)

Biomolecules can be attached to the ND surface using both non-covalent and covalent interaction. For attachment of molecules, usually carboxyl groups are utilized, either for non-covalent electrostatic interaction or for covalent modification. The carboxylic acids can be easily converted to active esters, which readily react with amines forming amides. (Zhang et al., 2009a; Fu et al., 2012) Non-covalent attachment is experimentally easy (NDs are incubated in the solution along with biomolecules), utilizing adhesion and electrostatic interactions. However, the conformation of the attached proteins is not under control. Since the attachment is reversible, there is also the risk of molecule detachment if ND are introduced to the molecules with higher affinity to the surface. Covalent attachment is experimentally more difficult to perform, leads to lower yields, however, the point of attachment is fully under control. Maintaining a proper conformation and molecule orientation can be essential for retaining the activity of the attached biomolecules. Low coverage of the surface can lead to the lower activity of the protein, because of many reactivity sites bind to the surface non-specifically and the

protein conformation is loosen. Blocking of the free space by other non-active protein can be utilized to create more "crowded" environment. (Nguyen et al., 2007) To retain activity, spacers between surface and biomolecules are often used. Active site of the biomolecules is then no longer hindered by surface and the modification yield and reactivity is therefore higher. NDs can be also modified by synthetic polymers, which will be discussed in chapters related to the specific applications.

DNDs modified with various molecules were used for further mentioned biological applications. Immobilization of enzyme trypsin on DNDs was shown to be beneficial. Enzyme attachment results in long-lasting stability of the enzyme, which enables repeated use and easier separation from the solution. Catalytic properties of the enzyme can be also improved. (Wei et al., 2010) Recently, DNDs were identified as one of the most efficient nanomaterial for enhancing contrast agents. Relaxivity of paramagnetic ions conjugated to the surface is increased. DNDs coupled with Gd(III) chelators were used to observe tumor differentiation and growth in T_1-weighted images *in vivo* in mice. (Rammohan et al., 2016)

1.2.2. Optical properties of NDs

HPHT NDs can host (N-V) centers (Fig. 2B), which emit red fluorescence in the visible range (Fig. 2C), favorable for optical bioimaging due to low auto-fluorescence of the cell (near infrared (NIR) window of biological tissues) as well as the better permeation of the longer wavelengths through the tissue.

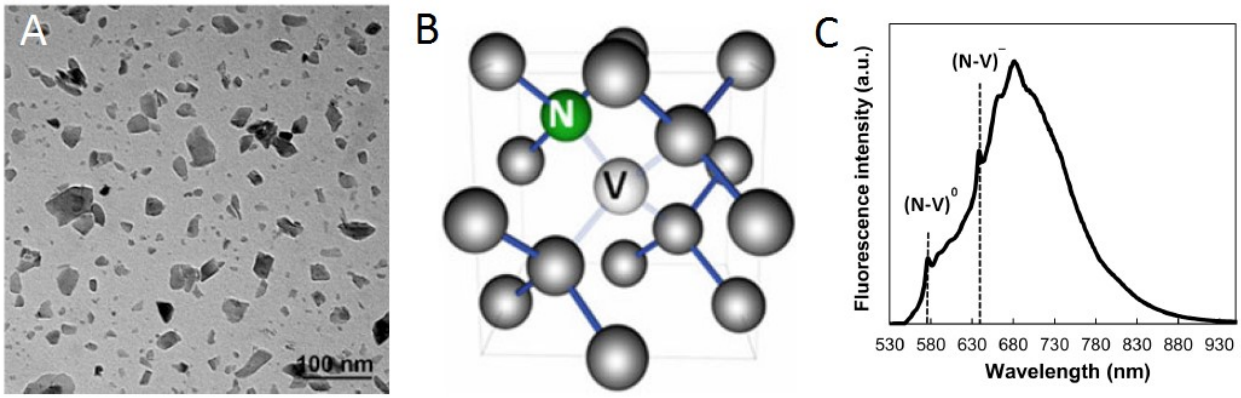

Fig. 2 (A) Transmission electron microscopy (TEM) image of pristine HPHT NDs. (B) Schematic picture of a (N-V) center. N is substitutional nitrogen, V is a carbon vacancy. (C) Fluorescent emission spectra of NDs with maximum in NIR region, $(N\text{-}V)^0$ and $(N\text{-}V)^-$ are two different electronic transition states of the (N-V) center.

Vacancies are produced by knocking out a carbon atom from the lattice. This can be achieved using irradiation with high-energy beam of particles (usually electrons, protons or

helium ions) in cyclotron or microtone. A nitrogen atom is already present instead of a carbon atom in the crystal lattice as an impurity resulting from a production process. In next step, the vacancy has to get into close proximity of the nitrogen. This can be done using annealing at elevated temperatures, when the vacancy gets adjacent to nitrogen atom forming the (N-V) center. Two different electronic transition states of the (N-V) center exist inside the material: neutral diamagnetic $(N\text{-}V)^0$ and negatively charged paramagnetic $(N\text{-}V)^-$ with different photoluminescence and spin properties. (N-V) centers have a long fluorescence lifetime (typically in few tens of nanoseconds) and are resistant to photobleaching (irreversible destruction of a fluorophore in time upon illumination) and photoblinking (reversible changing of bright and dark state). (Rehor et al., 2016) Fluorescence intensity is dependent on amount of (N-V) centers and it is thus dramatically higher for larger particles with more centers. Fluorescence intensity can be adjusted by treatment optimization. (Havlik et al., 2013) Although the procedure was lately thoroughly optimized, the low intensity of ND fluorescence is the main drawback of the particles. However, thanks to the extraordinary properties of (N-V) centers, NDs can be utilized in many biological applications which are not suited for highly fluorescent toxic quantum dots, photobleachable fluorescent dyes and proteins.

Charged states of (N-V) centers respond to certain chemical processes at ND surface such as different oxidation states of surface carbons or adsorption of charged molecules. This effect was used for preparation of optical sensors. Petrakova et al. observed gradual oxidation of hydrogenation NDs based on the shape of fluorescent spectra. (Petrakova et al., 2011) Change in shape of fluorescent spectra was observed also after adsorption of charged polymers on the surface. (Petrakova et al., 2015, 2016)

1.2.2.1. Optically detected magnetic resonance (ODMR)

The specific electronic structure of $(N\text{-}V)^-$ centers also enables use of NDs as ultrasensitive magnetic and electric field sensors. (Chipaux et al., 2018) $(N\text{-}V)^-$ center is a three-level emission system (Fig. 3A); the relaxation from exited state can occur directly to the ground state or through metastable state with longer emission time. Longer emission time leads to lower emission efficiency. Both the ground state and the excited state are split to three sublevels with electronic spin states bearing different magnetic spin levels ($m_s = 0$ and double degenerate $m_s = \pm 1$). After excitation from the level with $m_s = 0$, relaxation always occurs through a radiative decay (fluorescence can be observed). Relaxation from the exited $m_s = \pm 1$ state can occur both by radiative decay with fluorescence or by a transition to metastable state without observable fluorescence. The fluorescence of $(N\text{-}V)^-$ centers is therefore spin state selective. The energy

gap between the sublevels m = 0 and m = ± 1 (2.87 GHz) is in microwave region. Applying microwave field leads to switching between $m_s = 0$ and $m_s = \pm 1$ states (that become energetically equal) and results in a drop of the fluorescence. This modulation can be adjusted in a controlled way.

If external magnetic field is present, the spin states $m_s = \pm 1$ are no longer degenerated (effect called Zeeman splitting). From the position of the lines in the electron paramagnetic resonance spectra (Fig. 3B,C), external magnetic field can be calculated with high accuracy and sensitivity. This allows quantifying of external electric and magnetic fields via optically detected magnetic resonance (ODMR). (Balasubramanian et al., 2008; Hegyi and Yablonovitch, 2013; Rehor et al., 2016)

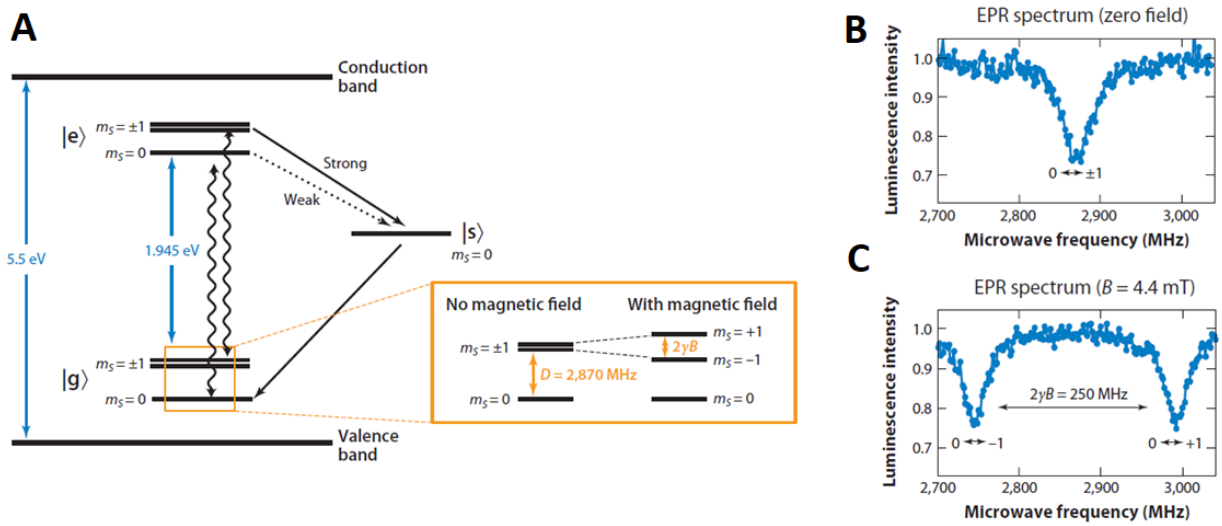

Fig. 3 (A) The electronic energy levels in $(N\text{-}V)^-$ center. Three level system with two possibilities of relaxation (directly to the ground state or through metastable state resulting in the drop of the fluorescence). The difference in spectra between situation without (B) and with (C) applied magnetic field, depicted also in yellow rectangle in A. Adapted from (Schirhagl et al., 2014).

1.2.3. Biocompatibility of NDs

Post-synthetic oxidative procedure results in significant improvement of the biocompatibility of NDs. Biocompatibility and low toxicity are key properties for using NDs in biomedical applications. According to the William's definition, "biocompatibility refers to the ability of NPs to perform its desired function without eliciting any undesirable local or systemic effects in the recipient". "NPs toxicity is related to the ability of particles to adversely affect normal physiology or interrupt the normal structure of organs or tissues." (Williams, 2008; Li et al., 2012) NPs are usually considered to be toxic because of their small size and possibility to internalize into cells and localize in critically important organelles. The toxicity depends on

number of features such as purity of the material, surface charge, shape, diameter and many other parameters. Adverse effects of NPs appear to be concentration dependent and cell-type dependent. However, NDs after post-synthetic modifications are considered to be biocompatible and with a very low toxicity, superior to other carbon and inorganic NPs. Highly ordered and oxidized sp^3 carbon atoms of HPHT NDs are likely the reason of the low toxicity compared with other carbon NPs. Many groups studied the toxicity and biocompatibility of HPHT NDs, usually using colorimetric metabolic assays. The results of the studies are very positive: none or low cytotoxicity (both short- and long-term) was observed in various types of assays. Generation of reactive oxygen species, inducing of apoptosis, differentiation or genotoxicity and adverse change in metabolic activity or proliferation were studied. (Chipaux et al., 2018)

Relatively few *in vivo* studies have been carried out on HPHT NDs. (Laan et al., 2018) A study on *Ceanorhabditis elegans* has shown no oxidative stress and no change in size or life length was observed for several days. The introduction of NDs into the worms by either feeding them with colloidal ND solution or by microinjection influenced the ND distribution. The distribution was also dependent on the surface modification of the NDs. (Mohan et al., 2010) Toxicity (including unchanged body weight or water consumption) was not observed in mice and rats over a 5-month period after intradermal administration. Even multiple injections did not cause observable toxicological effects. (Vaijayanthimala et al., 2012) Both short- and long-term biodistribution in organs are also very important parameters to study. HPHT ND after intratracheal instillation in mice were entrapped predominantly in lung and liver after 28 day without significant excretion (NDs were barely detectable in urine and feces). Although, no symptoms of abnormality were observed. (Yuan et al., 2009)

1.2.4. Cellular fate of NDs and bioimaging

HPHT NDs are a promising alternative to already existing fluorescent dyes. Although the fluorescence intensity is not as high as for quantum dots or organic dyes, emission in near-infrared region with low autofluorescence enables ND observation under confocal microscope. Better signal-to-noise ratio can be achieved thanks to the long fluorescence lifetime of NDs. Short lifetime emitters can be filtrated in time-gated images and only fluorescence of NDs observed in fluorescence lifetime imaging microscopy. (Faklaris et al., 2008; Kuo et al., 2013) NDs are utilized for long-term *in vitro* tracking of single particle because of no photobleaching and photoblinking. Three-dimensional trajectory of NPs can be tracked over long periods of time, determining for example cellular entry, localization, diffusion coefficient of the particles

inside the cells or reveal details about intracellular therapeutic activities. (Chang et al., 2008; Zhang et al., 2009a; Hui et al., 2017)

NDs enter spontaneously into the cells. The rate of the internalization and internalization pathway depends on the factors such as size, shape, charge and surface modifications. Small particles enter to the cell more freely than large aggregates; size and shape also determine the type of endocytosis involved. (Lee et al., 2013; Vaijayanthimala et al., 2009) Colloidal stability of the particles is therefore important because of the ability of particles to enter the cell and provide its function. Charge and surface modification regulate the interactions with biomolecules (proteins, lipids and polysaccharides) on the cell surface. Presence of the serum proteins and possibility (or impossibility) of adsorption on ND surface also greatly effects the interaction. (Vaijayanthimala et al., 2009) The higher uptake of positively charged NPs (due to the interaction with negatively charged cell membrane) is the reason of higher toxicity of these particles in contrast to negatively charged NPs. (Marcon et al., 2010)

Many scientists also studied the uptake mechanism. Decrease in NDs internalization after application of factors such as low temperature and sodium azide (sodium azide inhibits cytochrome oxidase and leads to energy depletion) suggests the dependence on temperature and energy and implies active transport pathway. (Faklaris et al., 2009; Vaijayanthimala et al., 2009) Inhibitors of specific endocytic pathway suggest clathrin-mediated pathway (Fig. 4A). (Faklaris et al., 2009; Vaijayanthimala et al., 2009)

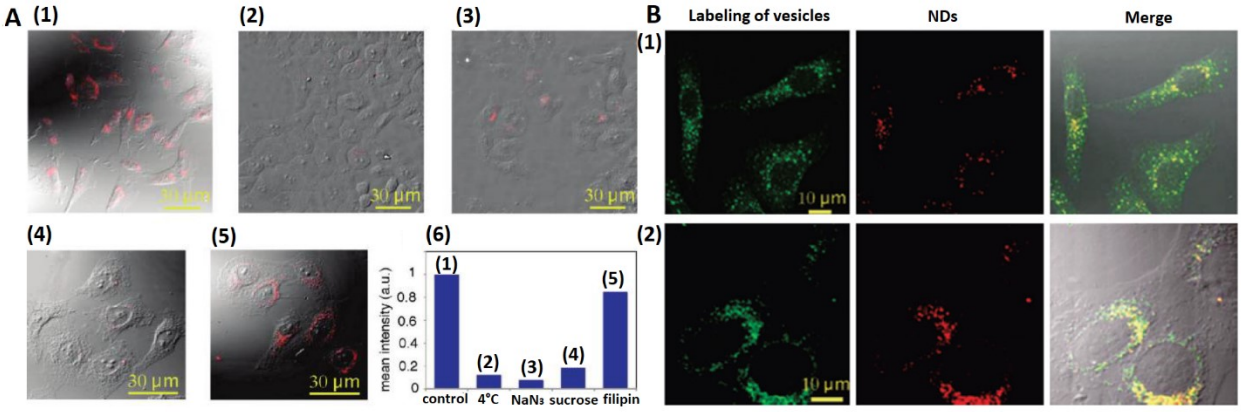

Fig. 4 Uptake of the NDs (red fluorescence) to the human adenocarcinoma HeLa cell. (A) NDs incubation with over 2 hours (1) at 37°C; (2) at 4°C; at 37°C after pretreatment with (3) NaN3 (10 mM); (4) sucrose (0.45 M); (5) filipin (5 µg/ml). (B) Co-localization experiment of NDs with (1) green-labeled endosomes; (2) green-labeled lysosomes. Co-localization appear in yellow in merged figure. Adapted from (Faklaris et al., 2009).

The endocytic pathway can change according to surface modification. Installing of molecules undergoing caveolae pathway (such as folic acid) on the surface of NDs results in

internalization by caveolin-mediated pathway. (Zhang et al., 2009a) Macropinocytosis take place in case of large aggregates of NPs. (Alhaddad et al., 2012; Liu et al., 2009) After endocytosis, cell membrane is engulfed and NDs are localized mainly in endosomes, which later fuse to lysosomes. (Alhaddad et al., 2012; Faklaris et al., 2009) Co-localization experiments with various labeled compartments were done to prove the localization (Fig. 4B).

Chu et al. observed liberation from endosomes dependent on the shape of the particles. Sharp particles were able to escape the endosome by rupturing the endosomal membrane. This phenomenon was observed more generally, not only for NDs, but also for gold and silica NPs. (Chu et al., 2014) Ability to escape from endosome and to avoid lysosome capturing is important for applications with potential in cytoplasm. In case of very small NDs (5-10 nm) the way of crossing the membrane was found different – a direct crossing. (Faklaris et al., 2009) It is also important to note, that no NDs were observed in nucleus, indicating no potential adverse effect on nucleus structure or deoxyribonucleic acid (DNA). (Alhaddad et al., 2012; Faklaris et al., 2009)

Possibility of long-term bioimaging using NDs revealed many interesting facts. Positively charged modified NDs were observed to internalize to the cell by endocytosis, to end up inside vesicles and to be transported from the cytoplasm of one cell to the cytoplasm of another cell through intracellular communication pathways. (Epperla Chandra Prakash et al., 2015) NDs were also used for direct monitoring of trafficking processes of transmembrane signaling cascade. NDs modified with transforming growth factor (TGF) were able to label endogenous TGF-β receptor and displayed its localization. (Liu Wenliang et al., 2015)

Much more challenging bioimaging *in vivo* was first shown on small 1 mm long worm *C.elegans*. Penetration and localization of NDs was observed by confocal microscope. Non-changing signal through the embryogenesis implied the possibility of long-term imaging *in vivo*. (Mohan et al., 2010) NDs were observed by fluorescent camera also in mammals (rat or mice) despite high tissue auto-fluorescence and absorption in the bulky bodies. The auto-fluorescence (emission after excitation upon short wavelength 430 nm) was subtracted from the signal of ND to increase signal-to-noise ratio. Long-term imaging and tracking in the body was shown on mice lymph nodes. (Vaijayanthimala et al., 2012) ODMR can be used with advantage as another method for background-free imaging. Irradiation of the sample with resonance frequency (in microwave field) results in the drop of the ND fluorescence, while fluorescence of rest of the sample remain unchanged. This method was used in cell culture studies

(McGuinness et al., 2011) as well as in more complex models such as in *C. elegans* and mouse. (Igarashi et al., 2012)

ODMR measurements can be further exploited to measure temperature in nanoscale, because spin resonance of $(N\text{-}V)^-$ center is temperature-dependent. (Sotoma et al., 2018) Difference in temperature was measured also inside living cells. Change in temperature was measured nearby gold NPs (distance of 200 nm), which were heated upon using a laser. (Kucsko et al., 2013)

1.2.5. Drug delivery

One of the most important application of NPs is delivery of therapeutic agents (drugs, toxins or nucleic acids). Small molecule drugs (Laan et al., 2018) or biomolecules toxins (Liu et al., 2008) were loaded (almost exclusively non-covalently) on the surface of NDs. Up to now, DNDs were mostly used for the drug delivery because of their smaller size (and larger surface to volume ratio) and higher loading efficiency. DNDs after modification tend to form clusters with drug loaded amid the grains. Small molecules such as doxorubicin (an apoptosis-inducing drug used for chemotherapy), poorly soluble 4-hydroxytamoxifen (an antagonist of the estrogen receptor in breast tissue) or epirubicin (inhibitor of DNA and ribonucleic acid (RNA) synthesis used for chemotherapy) were attached to the ND. The efficiency of the drugs attached to NDs was dramatically increased (Huang et al., 2007; Chen et al., 2009; Moore et al., 2013).

NDs with attached nucleic acids are promising material for gene therapy. (Chipaux et al., 2018) NDs proved to be useful as non-viral gene delivery system. Such system has to be able to penetrate the cell membrane, to escape from endosome and release the nucleic acid for successful gene expression or gene silencing. (Neuhaus et al., 2016) Both nucleic acids and oxidized NDs are negatively charged, therefore modification of the surface usually by positively charged polymer has to take place. All kinds of polyethyleneimines (PEI) or poly(allylamine) were attached to the surface. It was shown that DNDs with PEI has higher transfection efficiency than ND-NH_2 or free PEI. (Zhang et al., 2009b) The transfection and release of nucleic acids using ND-PEI can be observed thanks to the fluorescence of NDs on confocal microscope, either for DNA (Petrakova et al., 2016) or antisense RNA (Lukowski et al., 2018). The polymer type determines the route of entry to the cell and therefore efficiency of the transfection. The polymer coating not only enables nucleic acid attachment but also results in positively charge particles easier uptaken to the cells (due to negative charge of the cell membrane). Comparison of NDs with standard lipofectamine showed similar transfection

capability with improved cytotoxicity profile of NDs. (Alhaddad et al., 2011, 2012) It should be also noted that the polymer on the surface of NDs protects nucleic acid against enzymatic cleavage. It is also possible to build up a polymer directly from surface (more details are in following chapters). In this way, a cationic polymer from 2-(dimethylamino)ethyl methacrylate (DMAEMA) was synthetized on the surface. This structure proved to be efficient in transfection with low cytotoxicity. (Zhang et al., 2011a) Not only positively charged polymers, but also positively charged peptides (Arg_8 or Lys_8) exposed on NDs with neutral polymer were able to form complexes with plasmid DNA through electrostatic interactions. (Zhao et al., 2014a) Successful transfection of silencing RNA (siRNA) by plasma hydrogenated cationic DNDs (DNDs with positive charge but without polymer) and subsequent gene silencing was shown in Ewing sarcoma cell line. (Bertrand et al., 2015)

1.2.6. Cellular targeting of NDs

The major goal of targeted nanomedicine is to prepare NPs modified with molecules specifically interacting with receptors expressed on the cells and thus enhancing internalization to these cells. To successfully target, high specific and low non-specific interactions with cells need to be achieve by control of the surface, colloidal stability, modification suitability and efficiency. For targeting, HPHT NDs are more used than DNDs due to their fluorescence properties and possibility to observe the final destination of particles. Various kinds of molecules were used to modify the ND surface ranging from small molecules such as hormones or peptides to large proteins and antibodies.

1.2.6.1. Cellular targeting with proteins

Targeting with a large protein molecule is easier to achieve, because the large molecules hinder the ND surface. This results in lower non-specific interaction with cells than bare NDs and therefore in a more efficient targeting. Most commonly used protein for targeting is transferrin. Transferrin is a non-heme iron-binding glycoprotein, which transports two Fe^{3+} ions and controls levels of free iron in the body. Transferrin with two Fe^{3+} ions (holo-transferrin) is internalized to the cells by clathrin-mediated pathway to the early endosome, where the pH is lower and the Fe^{3+} ions are released to the cytoplasm. Complex of transferrin and transferrin-receptor is then recycled and removed from the cell by exocytosis. Transferrin is released from the complex and receptor returns to the cell membrane, where is prepared for internalization of next holo-transferrin (Fig. 5)

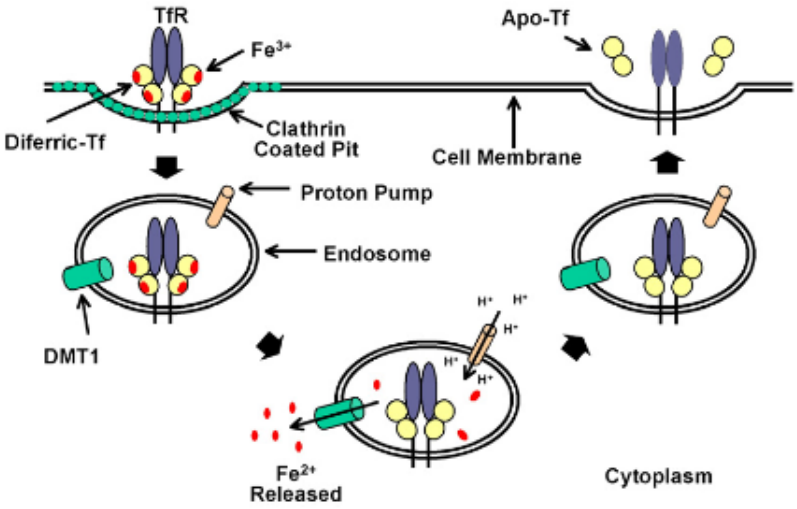

Fig. 5 Cellular uptake of iron by receptor-mediated endocytosis. Holo-transferrin (Diferric-Tf) is bound to the receptor and endocyted via clathrin-coated pits. After pH decrease, reduced Fe^{2+} are released and transported by divalent metal ion transporter 1 (DMT1) to cytoplasm. Receptor-transferrin complex returns to the membrane, where transferrin without ferric ions (Apo-Tf) is released. Adapted from (Daniels et al., 2006a).

Transferrin receptors are expressed in all cells with nuclei and therefore present on almost every cell membrane. However, the transferrin receptors are overexpressed in high extent on cancer cells with high rate of proliferation and metabolic activity. Amount of transferrin receptors correlate with tumor stage and cancer prognosis. (Li and Qian, 2002; Daniels et al., 2006b)

NDs modified with transferrin were internalized in the cells in higher manner than NDs without transferrin and were observed under confocal microscope and using flow cytometry. The role of transferrin was confirmed by preincubation of the cells with free transferrin, which blocks the receptors and decrease the internalization of NDs inside the cell. (Li and Zhou, 2010; Weng et al., 2009; Wang et al., 2014; Weng et al., 2012; Wang et al., 2015; Rehor et al., 2015) ND-transferrin particles delivered doxorubicin inside the cells (Wang et al., 2014, 2015) and displayed phototoxicity after irradiation with 532 nm laser. This is the excitation wavelength for NDs that are able to transform light into thermal heating. (Weng et al., 2012)

Growth hormone receptor is another cell membrane structure with high potential as a promising target. It can be selectively targeted either by growth hormone (Cheng et al., 2007; Li et al., 2017) or by monoclonal antibodies against epidermal growth factor receptor. (Zhang et al., 2011b) Growth hormone modified NDs were tracked using Raman mapping, thanks to the strong Raman signal of sp^3 atom in diamond at 1332 cm^{-1}. Growth hormone receptor is overexpressed in 30% of solid tumors (Zhang et al., 2011b) and the system of growth hormone

and its receptor is likely to be participated in human colorectal cancer. (Cheng et al., 2007) However, a change of cell morphology and promotion of cancer cell migration was observed for HeLa cells during targeting; further investigation of this potential risk is needed. (Li et al., 2017)

Several toxins, such as chlorotoxin-like peptide BmK-CT and α-bungarotoxin, were attached on the surface of NDs with the effect of both targeting and killing the cells. The toxins are targeting the matrix metalloproteases and α-7-nicotinic acetylcholine receptor, respectively. (Fu et al., 2012; Liu et al., 2008)

1.2.6.2. Cellular targeting with small molecules

Targeting with small molecules (e.g. vitamins and peptides) has many advantages. Small molecules are easier to handle, because their stability and conformation is not sensible as for proteins. In addition, much higher loading of the surface can be achieved and the small molecule is favorably exposed to the environment. On the other hand, small size molecules do not cover the surface properly and therefore do not assure colloidal stability and do not shield the surface from non-specific interactions with cells.

Efficient targeting is ensured by combination of two factors, high specific interaction with the targeted cells (dependent on choice of the molecule, its interaction with target, sufficient loading) and low or none non-specific interaction with healthy cells. Only accomplishment of both factors can lead to significant difference in interaction between cancer cells and normal cells. Considering that peptides do not lower the non-specific interaction with the cells, surface has to be first modified with polymers guaranteeing the protection of the surface. Polymer coating is a very important aspect thoroughly discussed in next chapters. For now, it should be noted that all NDs discussed in this chapter are coated with polymer, quality of which influence the efficiency of targeting.

Another commonly used targeting moiety is folate (vitamin B9). The receptor for folate is overexpressed on human tumor cells due to increased metabolic activity and need of DNA synthesis. NDs with attached folate were tracked using the inherent ND fluorescence in three dimensions over more than 5 minutes during endocytosis. (Zhang et al., 2009a) (Fig. 5)

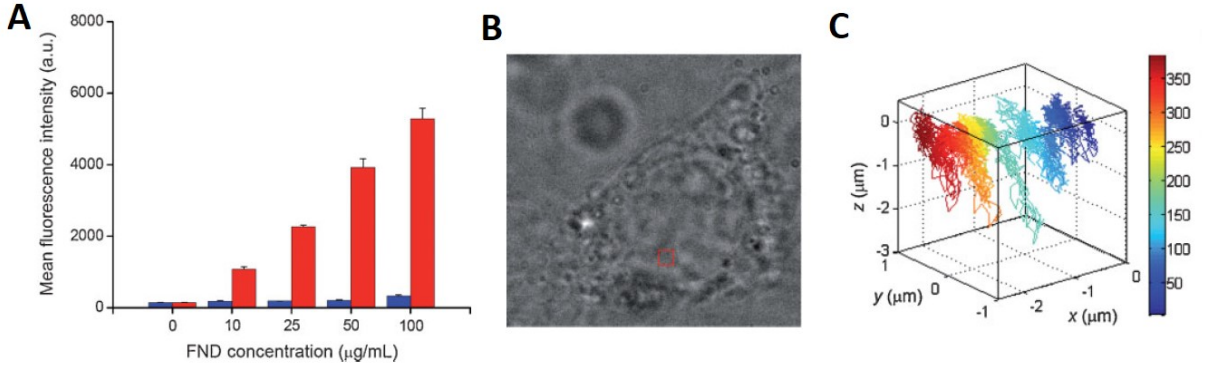

Fig. 5 (A) Dependence of internalization of polymer-coated ND (blue) and NDs modified with folate (red) on ND concentration. (B) Bright field image of the HeLa cell with marked red square, where (C) three-dimensional tracking of single ND modified with folate was observed over a time period of 370 seconds. Adapted from (Zhang et al., 2009a).

The uptake was inhibited if free folate was pre-incubated with the cells, confirming the mechanism of binding to the cells. The conversion from clathrin-mediated endocytosis (in case of only polymer-coated NDs) to caveolae-mediated pathway in case of ND-folate conjugates was suggested. Increase of the uptake in comparison to non-modified particles was approximately 12-fold. (Zhang et al., 2009a) Physically adsorbed doxorubicin to ND-folate conjugate was released in acidic pH environment (present either in tumor environment or inside of the cells in endosome or lysosome). Toxicity of the doxorubicin-ND-folate conjugate followed directly the amount of folate receptors on the surface of different cells and was directly proportional to the time incubated in the cells. (Dong et al., 2015) Mitochondrial localizing sequence (MLS) attached to the doxorubicin-ND-folate conjugate delivered conjugate not only across the membrane of cancer cells but also selectively to mitochondria (confirmed by electron microscopy imaging). Significant toxicity of conjugate was detected in comparison to free doxorubicin. (Chan et al., 2017)

Two peptides were until now utilized for ND targeting to cancer cells. First, sequence from antibody against human epidermal growth factor receptor 2 (anti-HER2), a six-amino acid peptide (KCCYSL), interacts with HER2 receptor overexpressed on the surface of breast cancer cells. The degree of overexpression correlates with the aggressiveness of the cancer. Anti-HER2-ND conjugates were internalized to overexpressing tumor cells in higher manner than in case of controls (particles without peptides, peptide pretreatment or cells with lower expression of protein). However, the difference between specific and non-specific interaction was only approximately 2-fold. The longer residence of this conjugate in the region of HER2-positive

tumor was observed. The presence of NDs was used in photoacoustic imaging *in vivo* on mice tumor model. (Zhang et al., 2015)

The second peptide often used for targeting of NDs is RGD peptide. (Slegerova et al., 2015; Zhao et al., 2014b, 2014c) RGD sequence occurs in many proteins of extracellular matrix (such as fibronectin, collagen and others) and specifically interacts with the integrin protein. Integrin receptors consist of α and β subunits and differ in their structure. $\alpha_V\beta_3$ receptor is overexpressed on cancer cells (e.g. glioblastoma) and in the tumor neovasculature. Interaction of RGD with integrin can be enhanced by cyclization of the peptide. Zhao et al. observed dose-dependent internalization to glioblastoma cells overexpressing the integrins over HeLa cells.

Drug *cis*-platin was attached to the conjugate and released at acidic pH in lysosome two times faster than in neutral culture media, confirming toxicity of the conjugate. Toxic effect of the conjugate was not higher in glioblastoma cells than of free *cis*-platin, however almost none was observed in control cells (compared with effect of free *cis*-platin) and for conjugate without RGD peptide modification. This emphasize the importance of targeted drug delivery. (Zhao et al., 2014b) Similar phenomenon was observed for DNDs with the same surface structure (doxorubicin was used instead of *cis*-platin in this study). Importance of evading the macrophage system was also highlighted and demonstrated in the study. (Zhao et al., 2014c)

1.2.7. Polymeric shells on NDs

Although NDs showed to be biocompatible material convenient for biological applications such as bioimaging, targeting or drug delivery, better control of ND surface and properties related to the surface is needed. Limitations of NDs are i) colloidal stability in biological media and buffers, ii) limited modification yields with biomolecules caused by steric hindrance of the surface, iii) adsorption of proteins to the surface causing non-specific interactions with cell surface. Addressing these limitations can broaden ND scope of biological applications and improve their effect. The often and successfully used solution to these problems is a polymer layer unchanging spectral properties of NDs, as further discussed below.

1.2.7.1. Colloidal stability of NDs

Size, composition and chemical groups on the surface determine NPs colloidal stability. Generally, larger particles are less colloidally stable than smaller ones and the stability of NPs increases with increasing surface charge. The charge of the particles is reflected by parameter called zeta potential. NPs with zeta potential higher than 30 mV and lower than -30 mV are considered to be stable thanks to the repulsive Coulomb forces stabilizing such colloidal

dispersion. Oxidized NDs have zeta potential approximately - 40 mV, which makes them stable in water. (Rehor et al., 2016) Although for biological applications, stability has to be ensured in the solutions with electrolytes. Electrolytes disturb the equilibrium between repulsive Coulomb forces and attractive van der Waals forces. Disruption of this equilibrium results in compression of the electrostatic double layer and leads to aggregation of the NPs. (Edwards and Williams, 2004) Instability in solutions of electrolytes is a common feature for all inorganic NPs. Biopolymer coating provides steric stabilization of NPs and prevents close contact of NPs and subsequent aggregation. Usually, proteins and synthetic polymers are used to coat NPs. Proteins adsorbed on NDs from the serum improve particle stability, prevent formation of aggregates and facilitate cell uptake. This simple approach helps in some of biological applications, although for majority of them protein coating is unfavorable and dense layer of synthetic polymer has to be grown on NDs.

1.2.7.2. Efficient modification of NDs with biomolecules

As already mention above in chapter 1.2.1, direct modification of the surface groups (either alcohols or carboxyl groups) is problematic. Groups are in close proximity to the surface, which hinders them from further reactions and enables only low yields under harsh conditions. Another problem concerning large biomolecules is retaining their activity and function. Proteins have usually one interaction site that can be unfavorably oriented to the ND surface and therefore not accessible to the surrounding. Flexible linkers between the surface and biomolecule can enable movement of the biomolecule and can enhance biomolecule efficiency. Layer of hydrophilic flexible polymer fulfills this requirement and enhance both biomolecule modification yield and its functionality.

Furthermore, only carboxylic acids and hydroxyl groups are present on oxidized NDs in higher extent, which limits surface modification with biomolecules to amide coupling or esterification. On the other hand, first modification of NDs with synthetic polymers results in diverse modifications with a wide variety of moieties with tunable reactivity. For example, bioorthogonal reactions ensures specificity without using protecting groups. Among others, azide-alkyne cycloaddition catalyzed by Cu(I) ions, designated as “click” reaction, enables high yield for large substrates, is experimentally simple and can be done with high efficacy in mild conditions in an aqueous environment. (Lallana et al., 2012)

1.2.7.3. Non-specific interaction of NDs with proteins and cells

NDs favorably adsorb proteins from the solution. (Hemelaar et al., 2017) For some applications, non-specific adsorption is advantageous; however, for other biological applications it causes inconveniences. Proteins create on the surface of NDs "protein corona", which completely change surface properties and influence the uptake pathway. (Lynch and Dawson, 2008) The "protein corona" consist of inner layer (the hard corona), which exchange very slowly, and outer layer (the soft corona) with freely exchanging proteins. Due to the hard corona's long lifetime, NDs interacts with surroundings via the protein surface layer as inseparable part. Moreover, if NDs are first modified with a molecule and further introduced to the serum proteins, "protein corona" shield the molecule attached to the surface and decrease its interactions with target. Cell membranes expose many protein structures that can interact with NDs. After exposition of NDs to the cells, NDs are spontaneously uptaken. "Protein corona" also helps NDs to be internalized, because ND surface exhibits familiar proteins (Fig. 6). (Hemelaar et al., 2017)

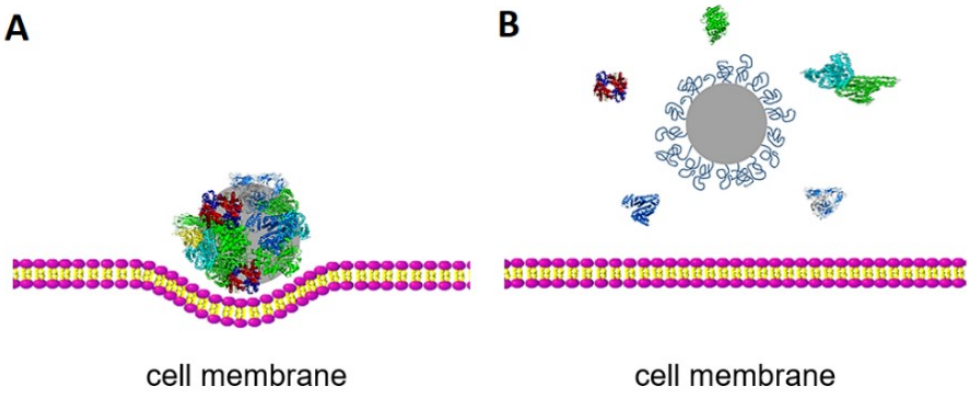

Fig. 6 (A) NDs are covered with proteins in serum-containing media, which facilitate the uptake in the cell. (B) Polymer-coated NDs do not interact with proteins and cell membranes and remain intact outside of the cell.

This is also the reason why simple protein coating is unsatisfactory solution for achieving colloidal stability of NDs. Spontaneous internalization is unacceptable for applications such as cell targeting and needs to be eliminated. NDs first has to be shielded from any interaction with cells and then modified with targeting molecule enhancing only interaction to targeted cells. Neutral hydrophilic dense polymeric shells create "stealth" coating with antifouling effect. Proper polymer coating should reduce recognition of NDs by immune system. Avoiding the immune response prolongs the circulation time, which is key requirement for *in vivo* applications. (Cigler et al., 2017; Neburkova et al., 2017)

1.2.7.4. Classification of coating polymers

Polymers for preparation of antifouling layers should meet certain criteria such as biocompatibility, hydrophilicity, neutral charge (optimally) or negative charge (alternatively). Usually, poly(ethyleneglycol) (PEG) or its derivatives are used. Terminal hydroxyl groups of the PEG can be enzymatically oxidized to aldehydes, which further reacts with biomolecule amines. This adverse effect can be bypassed by using methoxy-derivatives of PEG such as poly[PEG methyl ether methacrylate] (PPEGMA). Immune reaction to PEGylated NPs was recently reported. This is known as "PEG dilemma". Therefore, demand for other types of polymers raised. Polymers should share convenient properties of PEG, but lack the unfavorable ones. Lately, polymers based on polyglycerol (PG), polyoxazolines or methacrylate derivatives were used for NP coating. (Amoozgar and Yeo, 2012) PG is more hydrophilic than PEG and less susceptible to oxidation. Thanks to its hyperbranched structure, PG cover NPs very efficiently. Poly[*N*-(2-hydroxypropyl) methacrylamide] (PHPMA) is hydrophilic, non-immunogenic polymer with functionalizable side chains enabling further modifications.

1.2.7.5. Attachment method

Similarly to any other modification, surface of NPs can be modified with polymers using non-covalent interaction or covalent interaction (Fig. 7A). Non-covalent interactions of negatively charged NDs mediated through electrostatic interactions or hydrophobic interactions can be utilized for either positively charged polymers (useful for gene delivery, not for "stealth" coating) or for block copolymers. Polymers spontaneously adsorb on the surface, similarly to proteins, if their interaction with surface is more favorable than with solvent. (Netz and Andelman, 2003) Positively charged polymers stabilize the particles in buffers thanks to both steric and charge stabilization. However, as the whole chain have the affinity to the surface, potential problem arise if mixing NDs with the polymer in the solution. One polymer can bind to more ND particles and cause aggregation from the solution. This can be prevented by slowly adding NDs to the polymer solution, usually during sonication in a bath. (Alhaddad et al., 2012) In case of block copolymers, hydrophobic interaction of one part of the polymer occur with ND surface, the rest of the polymer (usually the hydrophilic part) is exposed to the solution.

Covalent modifications are used typically for neutral hydrophilic polymers. Preparation of the polymer first in the solution, its characterization and then attachment by the end-functionality to the surface of ND is called "grafting to" method (Fig. 7A). "Grafting to" method is experimentally easier and various end-functionalized polymers (usually PEG) are accessible. Usually carboxyl groups on the ND surface react in amide coupling with *N*-hydroxysuccinimide

(NHS-ester) on PEG. Density of the polymer chains on the surface is limited. First, the reactivity of the groups on the surface is reduced, second, the polymer chain is large molecule and the reaction between two large moieties is less efficient. Moreover, polymer chain with its end-functionality has to diffuse to the surface reactive groups through the existing polymer layer. This difficulty of reaching the surface also decreases the yield of reaction. Alternatively, polymers can grow directly on the surface of NDs from monomers in "grafting from" method (Fig. 7A). Only synthetic polymers can be attached by this method to the surface. Without steric hindrance of the polymer chains, the efficiency of coating by this method is high. Monomers are much smaller and therefore diffuse to the surface much easier and the layer is prepared in more uniform way. (Cigler et al., 2017; Neburkova et al., 2017) Common strategy living radical polymerization prevents termination of the reaction. For this method, surface needs to be first modified with initiator of the polymerization. For atom transfer radical polymerization (ATRP), halide-terminated NDs are needed. RAFT agents need to be installed on NDs for reversible addition-fragmentation chain transfer (RAFT) polymerization. RAFT polymerization does not require use of metal catalysts as ATRP and use azobis(isobutyronitrile) (AIBN) as an initiator. Conventional radical polymerization reactions were also employed to coat NDs in polymer. These polymerizations are sensitive to oxygen species, which terminate the reaction. PG is grown by non-radical ring-opening polymerization that results in hyperbranched structure.

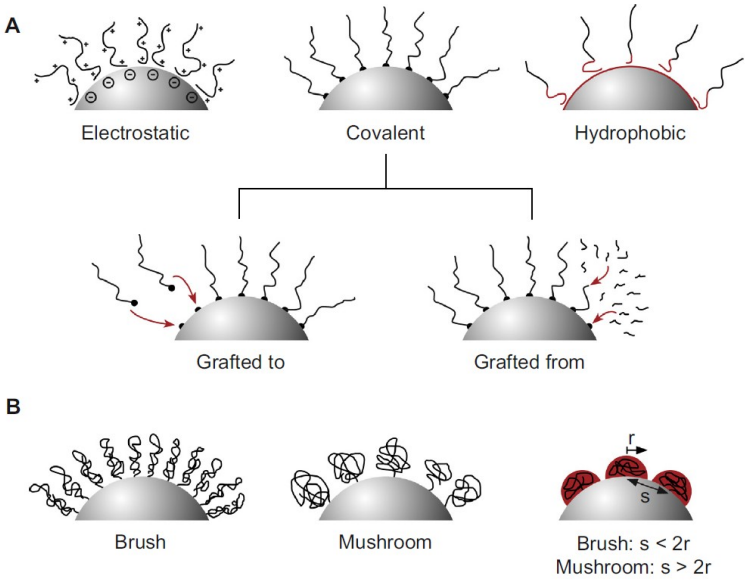

Fig. 7 (A) Various approaches of coating polymers on surface of ND: electrostatic, covalent or hydrophobic interaction. Covalent grafting can be done by either "grafting to" or "grafting from" approach. (B) Different conformation of polymer coils upon surface immobilization (more dense brush, more sparsely attached mushroom conformation). Adapted from (Neburkova et al., 2017).

Density of polymer coating is crucial parameter alongside with polymer type. Polymer coils installed sparsely on the surface in "mushroom" conformation do not provide as good "stealth" properties as dense polymer coating in "brush" conformation (Fig. 7B). "Grafting to" is considered to be a method ensuring stability in buffers, enabling further modifications, but less effective in shielding non-specific interaction. Best results in reducing non-specific interactions were shown on polymers created by "grafting from" method.

1.2.7.6. Examples of ND coating with polymers

Interesting compromise between protein and polymer coating was shown by Wu et al. (Wu et al., 2015) Simplicity of non-covalent adsorption of protein to NDs with better coating properties of neutral hydrophilic PEG was combined in coating NDs with albumin-derived copolymer. Albumin was first PEGylated, and then unfolded and functionalized by amine moieties to increase adsorption efficiency to negatively charged oxidized NDs through non-specific interaction. NDs were colloidally stable (in 1 M NaCl solution and across a broad pH range), internalized and tracked throughout the cells. Doxorubicin was linked to the conjugate by acid-cleavable linker a released inside cancer cells. (Wu et al., 2015) PEG polymers are installed on NDs covalently by "grafting to" approach. Marcon et al. coated NDs with Zonyl polymer (block copolymer based on a perfluoroalkyl chains and PEG chains). Zonyl polymer, modified with alkyne groups, reacted with azide-modified NDs. This coating enhanced particle stability in buffers such as phosphate-buffered saline (PBS) and reduced protein adsorption of bovine serum albumin (BSA) by 30%. (Marcon et al., 2011)

For targeting experiments, NDs are usually coated with polymer, particularly PEG. However, NDs modified with proteins as targeting ligands were except few cases (Rehor et al., 2015; Wang et al., 2014) not modified with polymer. Particles are stable thanks to the protein stabilization; therefore, more stabilization seems to be redundant. However, proper PEG coating enhance antifouling properties of the particles and is thus beneficial. In case of transferrin-coated NDs, PEG did not help to improve the efficiency of the targeting as was not dense enough to decrease non-specific interactions. However, no direct comparison of particles with and without PEG was performed. Either optimization of surface coating would be needed, or changing the polymerization procedure to "grafting from". Polymer is always use to coat NDs with small-molecule targets. NDs are first modified on activated carboxylic acids using amidic coupling with PEG-amine to enhance stabilization and decrease non-specific interactions and then modified with folate or HER2 peptide. (Chan et al., 2017; Dong et al., 2015; Zhang et al., 2009a, 2015) Colloidal stability of the particles was improved, however

proper coating to almost eliminate the non-specific interaction was achieved only by (Zhang et al., 2009a). Specific interaction of ND-folate particles with HeLa cells in presence of medium with serum was 12-fold higher than of non-targeted NDs. This has been one of the highest differences between specific and non-specific interaction in case of ND.

Various types of radical polymerizations were used for methacrylate derivative polymers. Hydrophilic poly(methacrylic acid) (PMAA) brushes were first attached to the DNDs by Li et al. by ATRP polymerization. First, hydrophobic poly(tert-butyl methacrylate) was introduced to the surface, subsequently hydrolyzed by acids to hydrophilic polymer, modifiable by protein. (Li et al., 2006) RAFT polymerization was applied to polymerize DNDs with PPEGMA and initiator AIBN. Together with PPEGMA polymer, monomer displaying macromolecular ligands able to form complex with cisplatin drug was co-polymerized to the layer and NDs with loaded drugs were delivered into tumor cells. (Huynh et al., 2013) The ratio of polymers was evaluated by thermogravimetric analysis (TGA), method used very often for evaluation of content of polymer in ND sample. TGA determines the weight ratio of polymer (that degrades above 200°C) and ND (oxidized around 600°C) as a loss during temperature increase. (Zhao et al., 2011)

Non-radical ring-opening polymerization of glycidol was used for preparation of dense polymeric layer on NDs. (Zhao et al., 2011) NDs were colloidally stable with antifouling properties and were modified using biorthogonal reactions (azide-alkyne cycloaddition catalyzed by Cu(I) ions). (Zhao et al., 2014b) The content of hyperbranched polyglycerol layer was determined by TGA as high (40:60, PG:ND ratio). Fluorescent NDs were further modified with RGD peptide and targeted to cancer cells. Non-specific interaction of non-targeted NDs was very low, non-distinguishable from the control of cells only (Fig. 8). This has been the best result in effort of reducing non-specific interactions. In general, the potential of particles without non-specific interaction is enormous as the low specific interaction can be greatly enhanced by optimization of targeting ligand.

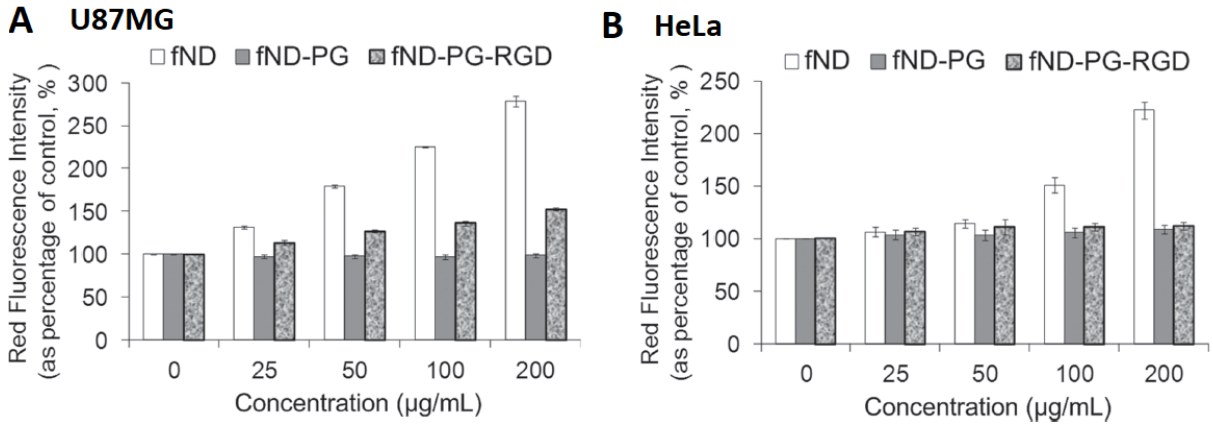

Fig. 8 Targeting of fluorescent NDs (fND), polyglycerol-coated fNDs (fND-PG), fND-PG modified with RGD (fND-PG-RGD) to two different cell lines, (A) integrin receptor overexpressing human glioblastoma U-87 MG cell line, (B) non-cancerous HeLa cells. Non-coated fND is highly spontaneously internalized, coating with polymer (fND-PG) eliminates the interaction with both cells. fND-PG-RGD particles are internalized dependent on the amount of integrin receptors on the cells. Adapted from (Zhao et al., 2014b).

2. AIMS OF THE THESIS

The objective of the thesis was to improve surface properties of NPs and show their potential in biomedical applications, such as in targeting NPs specifically inside tumor cells. The central hypothesis was to reveal if proper surface design leads to principal and significant reduction of non-specific interactions and therefore improvement of specific interactions with cancer cells. For confirmation of this hypothesis, these specific aims were proposed:

- Hypothesis: Does polymer coating enhance the colloidal stability of NDs? Experimental approach: To prepare ND particles, modify their surface with hydrophilic biocompatible polymer coating and characterize their colloidal behavior.
- Hypothesis: Does colloidal stability of NPs with polymer shell depend on polymerization method and type of the polymer?
  Experimental approach: To prepare polymer layer on NDs from various polymers by different approaches, measure colloidal stability and non-specific interactions of NDs with proteins and cells and optimize the density of polymer coating.
- Hypothesis: Does biorthogonal reactions increase surface modification yield, provide controllable way of attachment, and enhance the activity of molecules on the surface?
  Experimental approach: To examine surface biorthogonal modifications of various ligands from small molecules to proteins and find the most efficient reaction and conditions.
- Hypothesis: Is it possible to target efficiently cancer cells using NDs with attached targeting ligands?
  Experimental approach: To attach various targeting ligands on the surface of NDs and evaluate and compare targeting efficiency of individual systems.
- Hypothesis: Is targeting efficiency of the particles influenced by properties such as size, shape, composition and surface modification?
  Experimental approach: To prepare and modify diverse NPs (bioorganic monodisperse virus-like particles, polymeric nanoparticles, polymer-coated NDs) and compare their efficiency of targeting cancer cells with NDs.
- Hypothesis: Are NDs with optimized surface properties useful for bioapplications? Experimental approach: To explore applications of NDs such as photothermal ablation as therapeutic approach and preparation of ND-based nanosensors.

3. METHODS

This chapter summarizes methods used in this PhD thesis. Detailed information is described in related publications. My work (specified in chapter: My contribution to the publications) was done at Institute of Organic Chemistry and Biochemistry of the CAS, Czech Republic. Within this PhD thesis, we established collaborations with several laboratories, the most important are mentioned as follows. NDs were irradiated to become fluorescent at Nuclear Physics Institute of the CAS, Czech Republic. Synthesis of monomers for surface functionalization was provided by Institute of Macromolecular Chemistry of AS CR, Czech Republic. High-resolution transmission electron microscopy was performed at EMAT, University of Antwerp, Belgium. Thermogravimetry was measured in service laboratory at University of Chemistry and Technology, Czech Republic. Collaboration with Faculty of Science, Department of Genetics and Microbiology, Charles University, Czech Republic, concerns projects related with virus-like NPs. Gd^{3+} complexes were synthetized at Faculty of Science, Department of Inorganic Chemistry, Charles University, Czech Republic. Measurements of T_1 relaxation time were done in collaboration with 3. Physikalisches Institut, Universität Stuttgart, Germany.

Methods used in this thesis were as follows:

Synthetic methods:

Modification of NP surface by silica, preparation of gold shell, polymerization of synthetic monomers on the surface of NPs, modification of NPs with various structures (e.g. fluorescent dyes, peptides, proteins), modification of glycosylic chains of protein transferrin.

Molecular biology methods:

Transformation of *E.coli* cells with plasmid, recombinant expression of virus-like particles in *E.coli*, isolation of protein from the cell and purification.

Characterizations:

Measuring of dynamic light scattering (DLS) and zeta potential of NPs, measuring of absorption and fluorescent spectra, transmission electron microscopy (TEM), TGA, measurement of surface plasmon resonance (SPR), measurement of inhibition constants in enzymatic assay, sodium dodecyl sulfate–polyacrylamide gel electrophoresis (SDS-PAGE) of modified

transferrin, measurement of inductively-coupled plasma mass spectrometry (ICP-MS), measurement of T_1 relaxation time.

***In vitro* experiments:**

Cell culturing, incubation of NPs in the cells, measuring of metabolic biocompatible assays, flow cytometry, confocal microscopy, laser ablation.

Statistical methods:

For flow cytometry and viability experiments, statistical methods were utilized. Results were measured at least in triplicates or in monoplicates in three independent measurements. The results were evaluated by different statistic methods according to the suitability of the chosen measurements (student´s t-test, one-way ANOVA, two-way ANOVA).

4. SUMMARY OF THE RESULTS

During my PhD studies, I have co-authored ten publications in peer-reviewed journals and prepared three manuscripts waiting for either acceptance or submission. Seven of these publications are part of this thesis, chronological list of all of my publications (including book chapters) can be found at the end of the thesis.

In this thesis, surface modifications and biological applications of NDs were thoroughly studied. NDs need to be first modified with neutral hydrophilic biocompatible polymer to become colloidally stable and without non-specific interactions towards proteins and cells. Initially, we prepared NDs with PEG coating "grafted to" the surface (**Publication 1**, (Rehor et al., 2014a)). Although this coating ensures colloidal stability and enables further modifications, non-specific interactions with protein are reduced, but not eliminated. Therefore, we prepared NDs with PHPMA polymer coating using "grafting from" procedure, which creates denser polymeric layer eliminating non-specific interactions. (**Publication 2**, (Rehor et al., 2014b))

Possibility of targeting cancer cells was shown with RGD peptide attached to the surface. (**Publication 3**, (Slegerova et al., 2015)). Interaction of ND-RGD conjugate with integrin receptors overexpressed on cancer cells was 8-times higher than in case of controls. We focused further on improvement of the specific interaction and attached to NDs protein transferrin (ND-Tf). ND-Tf showed 175-times higher specific interaction than non-specific one. (**Publication 4**, (Neburkova et al., submitted)). Disadvantage of transferrin receptor is its presence on non-cancerous cells although in much lower extent. More tissue-specific system is therefore needed. Transmembrane protease glutamate carboxypeptidase (GCPII) is expressed only in few types of tissues and was used as a target for GCPII inhibitor-modified NDs (ND-inh). Interaction of ND-inh with GCPII expressing cells was 75-times higher than non-specific. (**Publication 5**, (Neburkova et al., 2018))

NDs with proper surface modifications can be used for biological applications. NDs with gold shells were used as opto-thermal convertors transforming laser light to heat. This effect was used for highly effective killing of cancer cells. (**Publication 6**, (Rehor et al., 2015)) (N-V) centers in NDs are able to sense presence of spin labels in the vicinity of ND surface. NDs with Gd^{3+} complexes attached via cleavable bond were synthetized. Measurable release of Gd^{3+} can be initiated by decrease of pH or increase of glutathione concentration, conditions present upon uptake into the cell. (**Publication 7**, (Rendler et al., 2017)

Publication 1: Fluorescent Nanodiamonds Embedded in Biocompatible Translucent Shells

Ivan Rehor, Jitka Slegerova, Jan Kucka, Vladimir Proks, Vladimira Petrakova, Marie-Pierre Adam, François Treussart, Stuart Turner, Sara Bals, Pavel Sacha, Miroslav Ledvina, Amy M. Wen, Nicole F. Steinmetz, and Petr Cigler

ND, promising material for biological applications, is not colloidally stable in biological environment. This is the major disadvantage, which needs to be addressed. Low yields of surface direct modifications and high polydispersity of particles (in both size and shape) are other problematic features.

We prepared multiple-layer structure on NDs (Fig. 9A), which improves NDs colloidal properties and behavior in solution, however it does not change the fluorescent properties of NDs.

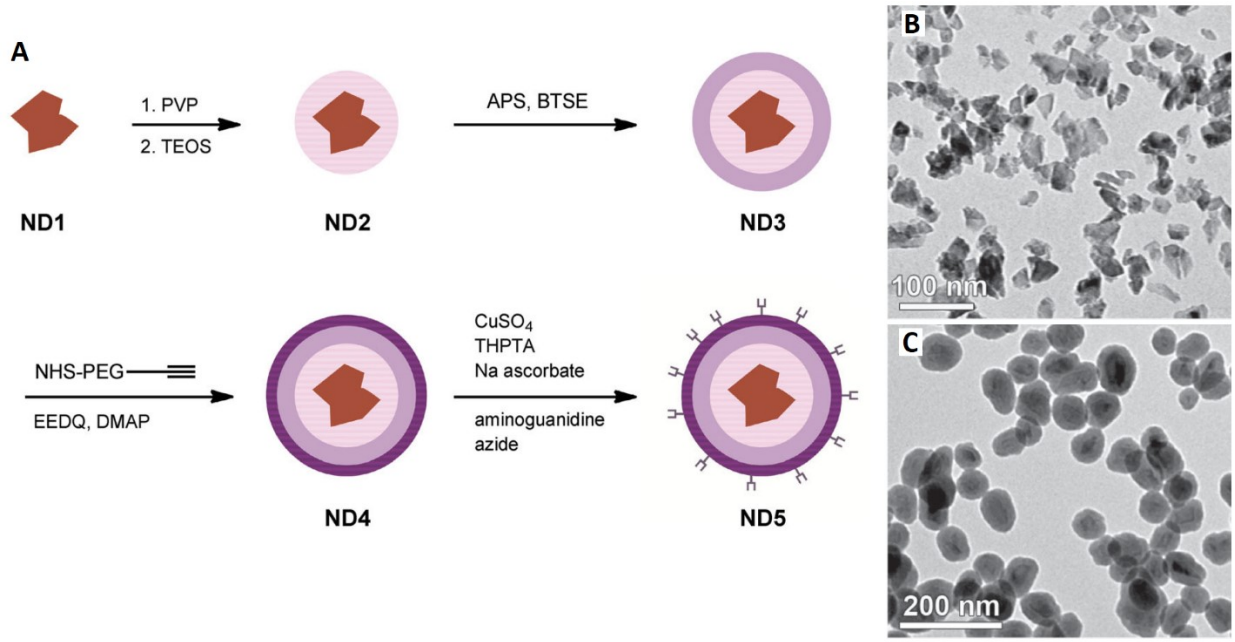

Fig 9. (A) The scheme of preparation of the multi-layer structure on NDs. ND is coated wih thick silica shell (pink), thin crosslinked aminopropyl-silica shell (violet), and PEG layer (dark violet). Condition of "click" reaction with azide-modified ligand are depicted. (B) TEM image of sharp non-coated NDs. (C) TEM image of near-spherical amino-silica coated NDs.

First, we coated NDs with cross-linked thick shell of silica. This reaction proceeds in three steps. First, NDs are mixed with polymer polyvinylpyrrolidone ensuring stability of the particles in Stöber conditions during silica shell growth (ethanol with ammonia). A silica shell layer from tetraethoxysilane (TEOS) is then grown, followed by growth of crosslinked amino-

functionalized layer ensuring the stability against hydrolysis. Silica shell modified with amino groups serves as a platform for further modifications and changes the shape of NDs from sharp NPs (Fig. 9B) to monodisperse near-spherical NPs with ND core (Fig. 9C). Flexible hydrophilic polymer (NHS-PEG-alkyne) was grafted to the surface. Alkyne moiety was further reacted in "click" reaction with either azide modified fluorogenic dye (coumarin) or radioactively labeled peptide (RGDS). Approximate load of small molecules on NDs was 8 μmol/g ND, which provides after recalculation using simple spherical model approximately 2000 molecules on each particle.

NDs were stable in PBS and even in 1 M NaCl and in wide range of pH (2-10). PEG-coated NDs, stable in PBS, were internalized in human prostate adenocarcinoma cells (LNCaP). Non-coated NDs aggregated upon introduction to PBS and as their size was increased to large aggregates, which were bound to the cell membrane without internalization (Fig. 10). Introduction of non-coated NDs to serum-containing media helps the stabilization. Adsorption of proteins from serum to the NDs protects NDs from immediate aggregation and promotes their internalization toward the cells.

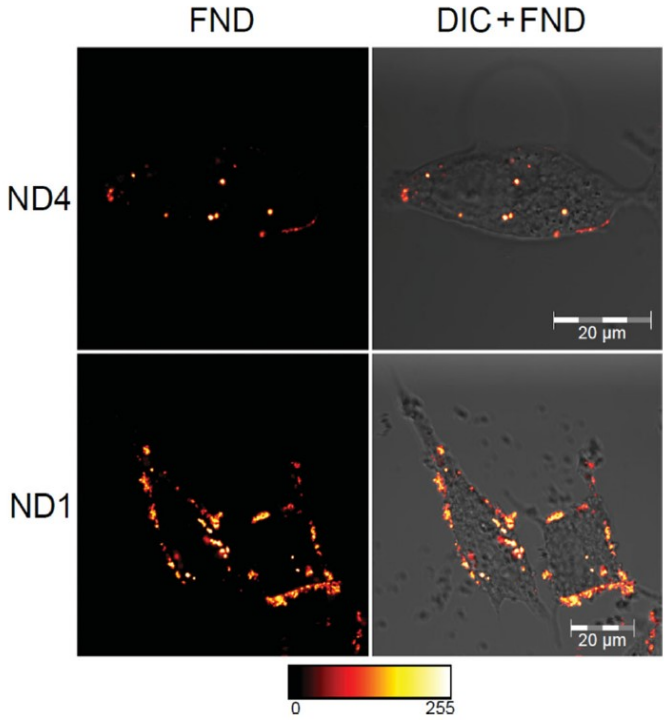

Fig. 10 Confocal microscopy images of PEGylated aminosilica-coated NDs (ND4) and non-coated NDs (ND1). Particles were pre-incubated in PBS before adding to the LNCaP cells. In the first row, image of ND fluorescence in false colors is present. The second column shows merged ND fluorescence and differential interference contrast (DIC).

Publication 2: Fluorescent Nanodiamonds with Bioorthogonally Reactive Protein-Resistant Polymeric Coatings

Ivan Rehor, Hana Mackova, Sergey K. Filippov, Jan Kucka, Vladimir Proks, Jitka Slegerova, Stuart Turner, Gustaaf Van Tendeloo, Miroslav Ledvina, Martin Hruby, and Petr Cigler

Improvement of colloidal stability of NDs is key requirement, however also non-specific interactions of NDs with proteins and cells need to be eliminated. In this paper, we present a new polymerization method on NDs not only ensuring NDs colloidal stability and enabling further surface modifications, but also decreasing non-specific interactions with proteins to minimum. The photoluminescence properties of NDs remain unchanged after polymer coating.

We coated NDs with ultrathin silica layer, which had less than 1 nm (indistinguishable on TEM, detectable by infrared spectroscopy). This layer consist of TEOS and 3-(trimethoxysilyl)propyl methacrylate mixture, grown under Stöber conditions (NDs first need to be stabilized). Methacrylate groups attached to the silica layer further reacted with monomer *N*-(2-hydroxypropyl)methacrylamide (HPMA) in radical polymerization. This radical polymerization proceeding directly on the surface ("grafting from" procedure) and initiated by AIBN leads to the growth of dense polymer layer of PHPMA (Fig. 11A). This layer is visible under high-resolution TEM and is thick few nanometers (2 to 5 nm) (Fig. 11B, C). From thermogravimetry, approximately 9% of the total mass of the prepared material was polymer.

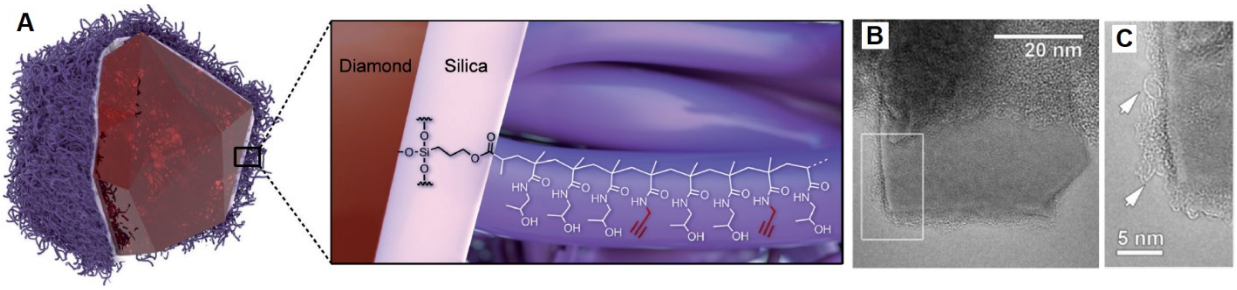

Fig. 11 (A) Scheme of polymer-coated NDs. NDs are first modified with thin silica layer, from which PHPMA with chains grow. Small portion of HPMA monomer was replaced by propargylacrylamide introducing alkyne moieties in the structure. (B) High resolution TEM image of polymer-coated NDs with few nanometers thick polymer layer. (C) area indicated in (B) in white rectangle.

A small portion of the HPMA monomer can be replaced by another monomer. In this work, either propargylacrylamide or 3-(azidopropyl)methacrylamide were mixed with the HPMA monomer and alkyne or azide moieties, respectively, were introduced to the polymer structure. Possibility of NDs modification using "click" reaction was confirmed with fluorogenic probe coumarin-azide, which becomes fluorescent only after reaction. The loading efficiency of the "click" reaction (evaluated by reaction with azide-modified AlexaFluor 488 fluorescent dye and radioactive RGDS peptide) was found to be approximately in the range of tens of micromoles per gram of NDs.

Colloidal stability of NDs was verified in typical cell biology buffers (0.1 M PBS, 2-(*N*-morpholino)ethanesulfonic acid (MES), and 4-(2-hydroxyethyl)-1-piperazineethanesulfonic acid (HEPES)). NDs were stable in a wide range of pH, with lower stability in strongly acidic conditions (pH 3). Adsorption of BSA was reduced four-fold in comparison to non-coated NDs.

Publication 3: Designing the nanobiointerface of fluorescent nanodiamonds: highly selective targeting of glioma cancer cells

Jitka Slegerova, Miroslav Hajek, Ivan Rehor, Frantisek Sedlak, Jan Stursa, Martin Hruby and Petr Cigler

Coating NDs in hydrophilic dense polymer layer and optimization of the surface is crucial condition for successful biological applications such as cancer cells targeting. In this publication, polymer layer was optimized to eliminate non-specific interactions. NDs were further modified with cyclic peptide RGD, ligand targeting integrin receptors on cancer cells.

Polymer-coated NDs (with alkyne moieties) were prepared as described in previous publication with slightly different procedure conditions. Radical polymerization was performed in more viscous DMSO instead of ethanol, volume of the reaction was 7.5-fold decreased, the polymerization temperature was decreased and time was prolonged to 3 days. The change of the conditions leads to longer polymeric chains and better surface protection. NDs' colloidal stability improved from previously described 0.15 M NaCl to even 1 M NaCl.

NDs were modified stepwise with Alexa Fluor 488-azide (because of flow cytometry measurement) and cyclic RGD-azide using "click" reaction (Fig. 12). Low molar excess of fluorescent dye results in substitution of only small fraction of alkyne moieties on the polymer and enables subsequent modification with targeting ligand.

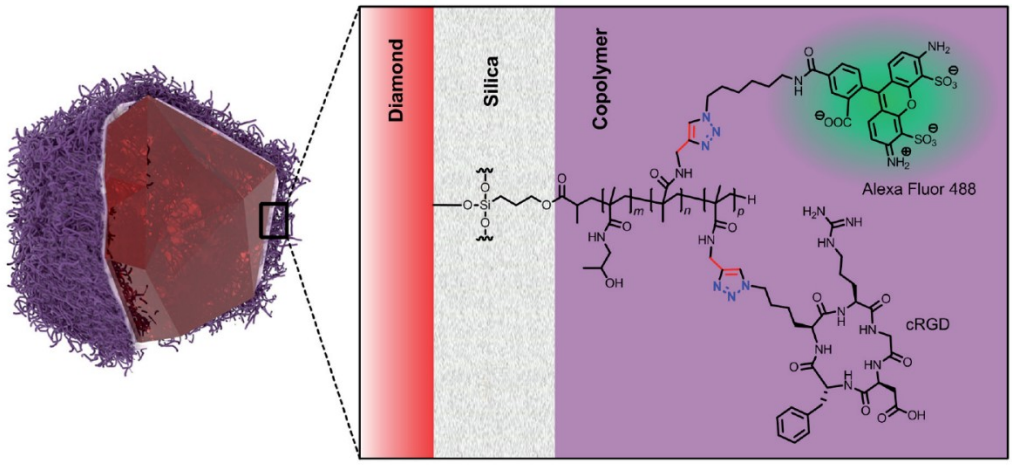

Fig. 12 Scheme of the ND surface modification. NDs are first modified with silica layer and subsequently with copolymer of PHPMA and propargylacrylamide. Polymer-coated NDs were modified with Alexa Fluor 488-azide and cyclicRGD-azide (cRGD).

We tested toxicity of the particles by cell viability assay quantifying level of adenosine triphosphate (ATP) (CellTiter-Glo®). Viability of the cells was not reduced by adding NDs

(Fig. 13A). Interaction of ND particles with cells was measured by flow cytometry (Fig. 13B) and confocal microscopy (Fig. 13C).

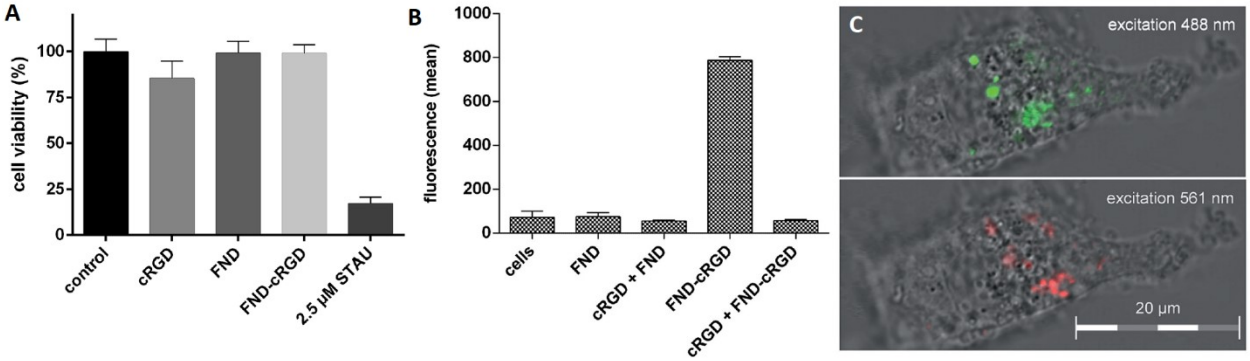

Fig. 13 (A) Cell viability of U-87 MG cells after addition of either free cyclic RGD, fluorescent ND conjugates (fluorescent ND with cyclic RGD (FND-cRGD) or without cyclic RGD (FND)) or apoptosis inducer staurosporine. (B) Fluorescence intensity measurements of fluorescent NDs with U-87 MG cells measured by flow cytometry. Only conjugate of FND-cRGD interacts significantly (ANOVA, $\alpha = 0.01$) with cancer cells. Other controls are not distinguishable among themselves on the significance level $\alpha = 0.01$. (C) Image from confocal microscope of U-87 MG cells treated with FND-cRGD conjugate observed after excitation at 488 nm (fluorescence of Alexa Fluor 488) and at 561 nm (fluorescence of NDs). Fluorescence of NDs was observed after extensive photobleaching throughout the whole spectra.

Fluorescent ND-cRGD conjugates interacted highly with U-87 MG cells, which overexpress integrin receptors on the cell membrane. Three control experiments were performed. NDs without cRGD did not bind to the cells. Pre-incubation of the cells with free cyclic RGD peptide also prevents binding of both ND-cRGD and ND to the cells. Reduction of ND-cRGD interaction after incubating cells with free cyclic RGD confirms specific interaction of ND-cRGD with integrin receptors, which are blocked upon cyclic RGD preincubation. Flow cytometry is quantitative method, however it does not distinguish between attachment of NDs on the cell membrane and internalization inside the cells. Internalization of ND-cRGD in the cells was shown by confocal microscope. NDs were shown to serve comparably to organic fluorescent dye as fluorescent labels with similar pattern. Fluorescence of NDs and Alexa Fluor 488 strongly overlaps in co-localization test. NDs are likely present in endosomes, not entering the nucleus.

Publication 4: Polyvalent display of ligand combined with antifouling bionanointerface enables extremely selective targeting of NPs to human T lymphoblast cells

Jitka Neburkova, Miroslav Hajek, Frantisek Sedlak, Stuart Turner, Jan Stursa, Petr Cigler

The difference between specific and non-specific interaction of targeted NDs with cancer and normal cells is the crucial aspect of satisfactory targeted carrier. Elimination of non-specific interaction was already shown in previous publication. The specific interaction is dependent on the selection of targeting ligand-receptor system (interaction coefficient, amount of receptors on the cells), the amount of ligand on the surface or the attachment method of the ligand.

In this work, we used transferrin as a targeting ligand. As a protein, transferrin has one recognizing epitope interacting with transferrin receptor. Therefore, method of attachment needs to be considered to enhance interaction with transferrin receptor. There are two glycosylic sites present in transferrin (each with two sialic acids) at the distant place far from the recognizing epitope. The structure of diol in sialic acid can be cleaved by meta-periodate to aldehydes. We modified aldehyde groups with 3-aminooxypropylazide using oxime ligation. This reaction is bio-orthogonal to other moieties in the protein. Transferrin-modified with azide was coupled to alkyne modified NDs (Fig. 14) Polymer-coated NDs were prepared by the same optimized procedure as in previous publication.

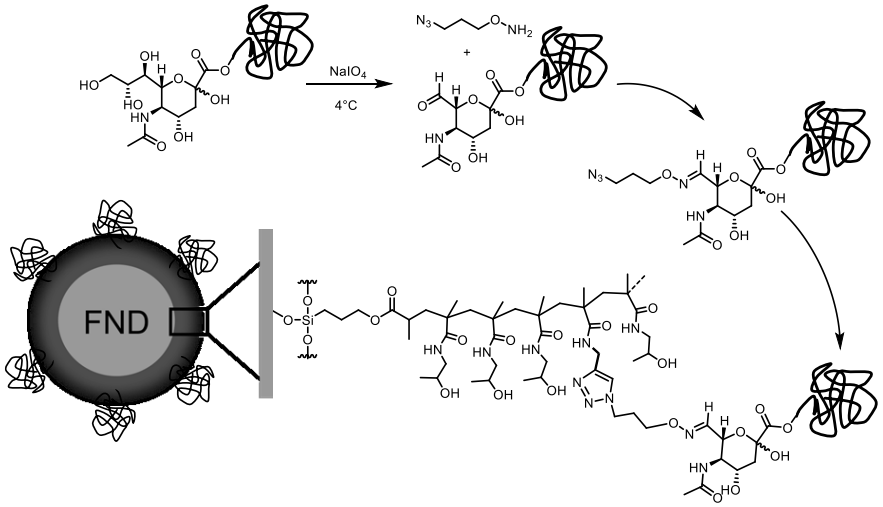

Fig.14 Preparation of fluorescent ND conjugate with protein transferrin. Transferrin is firstly oxidized by meta-periodate ($NaIO_4$) and further reacts with linkage 3-aminooxypropyl-1-azide. Transferrin-azide is conjugated using azide-alkyne cycloaddition catalyzed by Cu (I) ions to polymer-coated NDs modified with alkyne moieties.

First, we measured the toxicity of all fluorescent ND conjugates with metabolic assay on three cell types used for targeting experiments (human umbilical vein endothelial cell line (HUVEC), human osteosarcoma cancer cell line (U2OS) and human T lymphoblast (CCRF-CEM)). We observed no toxicity for any ND particle (Fig. 15A). Efficiency of targeting of NDs with transferrin (ND-Tf) was measured by flow cytometry. (Fig. 15B)

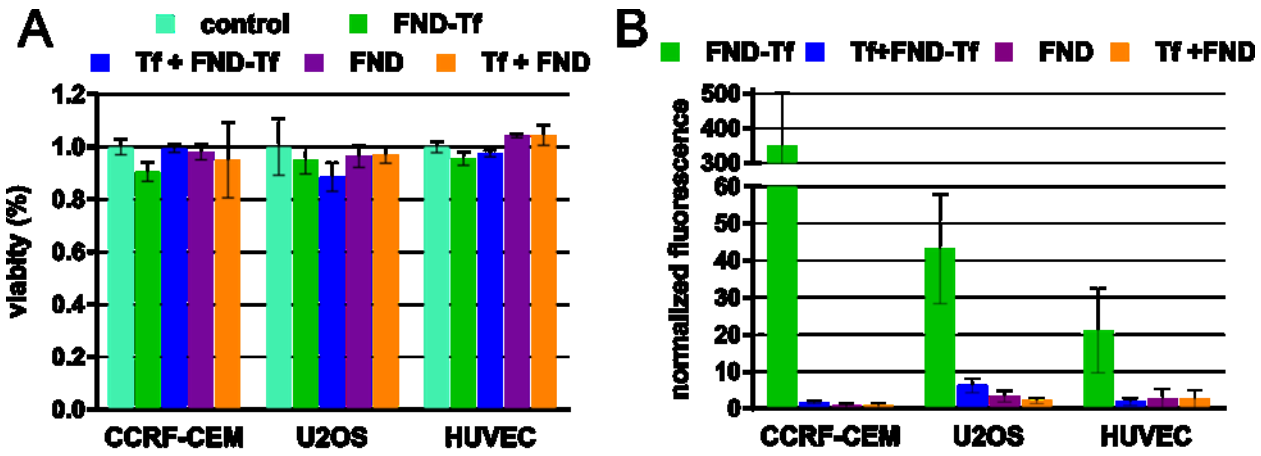

Fig. 15 (A) Viability assay (XTT) of fluorescent ND conjugates (with transferrin, FND-Tf; without transferrin, FND) with all three cell lines used in targeting experiment. No apparent toxicity was observed. (B) Fluorescence intensity measurements of three cell lines with ND conjugates measured by flow cytometry. Only FND-Tf conjugate interacts significantly with all three cell types with the interaction dependent on the amount of transferrin receptors on the surface. All negative controls for each cell lines are statistically not distinguishable among each other.

Fluorescent ND-Tf conjugate have significantly higher interaction with all tested cell lines than negative controls. Pre-incubation with free transferrin blocks the interaction of ND-Tf suggesting specific uptake of ND-Tf through transferrin receptor. To prove inter-cellular selectivity between cells with different amount of transferrin receptor, we cultivated cells in co-culture. We used simple method how to distinguish between cell types and how to evaluate their interaction with NDs. We mixed two cell types (normal and cancer cell line), added NDs for 1 hour-incubation, washed the cells, added cell-specific antibodies with different fluorescent dyes and measured the fluorescence using flow cytometer. The interaction of ND-Tf conjugate with cell lines is proportional to the amount of transferrin receptor presents on the cells (cancer cells expressed more transferrin receptors). ND-Tf are localized inside the cells as observed with confocal microscope.

Publication 5: Inhibitor−GCPII Interaction: Selective and Robust System for Targeting Cancer Cells with Structurally Diverse NPs

Jitka Neburkova, Frantisek Sedlak, Jirina Zackova Suchanova, Libor Kostka, Pavel Sacha, Vladimir Subr, Tomas Etrych, Petr Simon, Jitka Barinkova, Robin Krystufek, Hana Spanielova, Jitka Forstova, Jan Konvalinka, and Petr Cigler

Specific interaction is dependent on the selection of targeting ligand-receptor system. If the binding affinity is high (as we shown in case of transferrin-transferrin receptor system), the internalization of the particles is enhanced. There is uncertainty about the influence of the coating density of ligand on the particle surface. Receptors for cancer targeting (such as receptors for transferrin, folate or RGD) are usually overexpressed on cancer cells, but present also on non-cancerous cells. More tissue-specific receptors are needed, ideally only receptors present on cancer cells.

In this work, we chose to target more tissue-specific receptor, GCPII. GCPII is a membrane protease primarily expressed in the prostate, central nervous system, small intestine and kidney, with different functions in these tissues. Expression in other tissues is much lower. GCPII is overexpressed by prostate cancer cells and in neovasculature of most solid tumors. GCPII can be target either by large antibody or small-molecule inhibitor. We modified NPs with inhibitor, which is stable, easy-to-handle and has high affinity to the GCPII (in nanomolar range).

Apart from NDs, other NPs were used in this study. NDs, virus-like NPs and polymer NPs were adopted to cover a broad range of representatives. Polydisperse inorganic NDs with diameter approximately 54 nm (Fig. 16A) are unable to change their size. Two types of virus-like particles based on either bacteriophage Qβ or mouse polyomavirus (MPyV) are hollow, have bioorganic origin (consist of proteins) and their flexibility is also limited. They are expressed in transfected cells and self-composed to spherical NPs. Virus-like particles are all monodisperse in size and shape. Qβ NPs are more stable and smaller, with size 27 nm (Fig. 16B). MPyV have diameter approximately 45 nm (Fig. 16C) and are susceptible to disintegration, which complicates their handling, however can be utilized in packing cargoes inside. Polymeric NPs stands in the study for small, flexible, hydrophilic particles, very often used in biological applications.

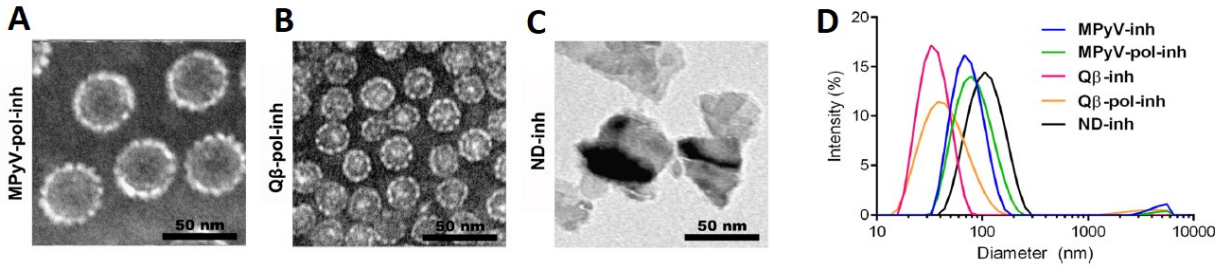

Fig. 16 TEM image of surface modified (A) MPyV particles, (B) Qβ particles, (C) NDs. (D) Intensity distribution of various NPs modified with inhibitor in water measured by DLS.

NDs were modified with already thoroughly described PHPMA coating bearing azide groups. Inhibitor-alkyne was attached using "click" reaction. Either amidic coupling or "click" reaction was used to attach inhibitors to virus-like particles. Virus-like particles are colloidally stable without polymer coating; however non-specific interactions occur, especially of MPyV. MPyV interacts with several cell receptors and cell-surface glycoproteins and are spontaneously internalized inside cells. Therefore, PHPMA coating was introduced to the surface of virus-like particles in half of the samples. All NPs were modified with fluorescent dyes. Polymeric particles, based on PHPMA polymer, were synthetized and characterized directly with inhibitor and dye attached.

First, we evaluated the interaction of NPs with GCPII *in vitro*. Interaction of NP-inhibitor with GCPII presented on the surface of gold chip was measured by SPR (Fig.17).

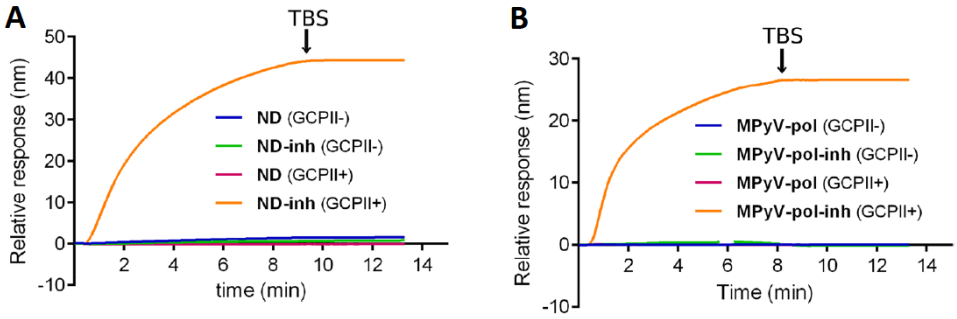

Fig. 17 SPR measurement of (A) NDs, (B) polymer-coated MPyV. NPs were injected through channel and led to interact with either surface with GCPII ($GCPII^+$) or without ($GCPII^-$). After approximately 8 minutes, buffer Tris-buffered saline (TBS) was injected and no desorption was observed.

All NP-inh conjugates interacted with GCPII surface and did not bind to the surface without GCPII, similarly NPs without inhibitor did not bind to any surface. Inhibition constant (K_i) was calculated from interaction of NP-inh with GCPII in the solution. K_i for small-molecule

inhibitor is in nanomolar range. K_i decreases to subnanomolar range after attachment of the inhibitor to the polymer and to picomolar range for other NP-inh conjugates.

Successful targeting of NPs with cells is more demanding with many other factors and components present in such system. NPs were added to the cells and fluorescent signal was detected using flow cytometry (Fig. 18). NP-inh conjugates show high interaction with GCPII-expressing cells. For NDs, polymer-coated and uncoated Qβs and polymeric particles, no non-specific interaction were observed (either of NP-inh with cells without GCPII expression or NP without inhibitor with both types of the cells). MPyV particles exhibit high non-specific interactions toward the cells (unrelated to GCPII receptor). These interactions were even higher than specific interaction of MPyV-inh. Coverage of MPyV with PHPMA polymer reduce the non-specific interaction, however, the coverage of few tens of PHPMA polymers seems to be insufficient as the non-specific interaction is not eliminated.

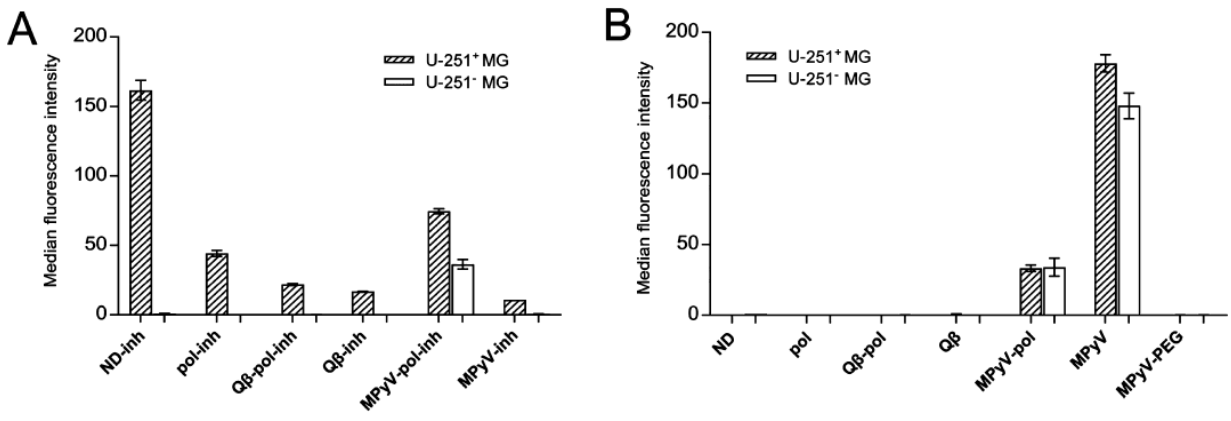

Fig. 18 Flow cytometry measurement of NPs (A) with inhibitor and (B) NPs without inhibitor on either glioblastoma cells expressing GCPII (U-251$^+$ MG) or without GCPII expression (U-251$^-$ MG). Fluorescence is normalized to autofluorescence of negative cells and adjusted to the relative fluorescence of particles (to overcome the problem of differently fluorescent NPs). Significant difference (on significance level of $\alpha = 0.001$) between NP-inhibitor particles on U-251$^+$ MG cell and all negative controls.

Confocal microscopy revealed that NP-inh particles are internalized inside the cells in peri-nuclear region. (Fig. 19A) From negative controls, MPyV with polymer and above all without polymer were also observed to interact with the cells, similarly to the results from flow cytometry. MPyV particles non-specifically interacting with cells seem to be located near cell membrane (Fig. 19B).

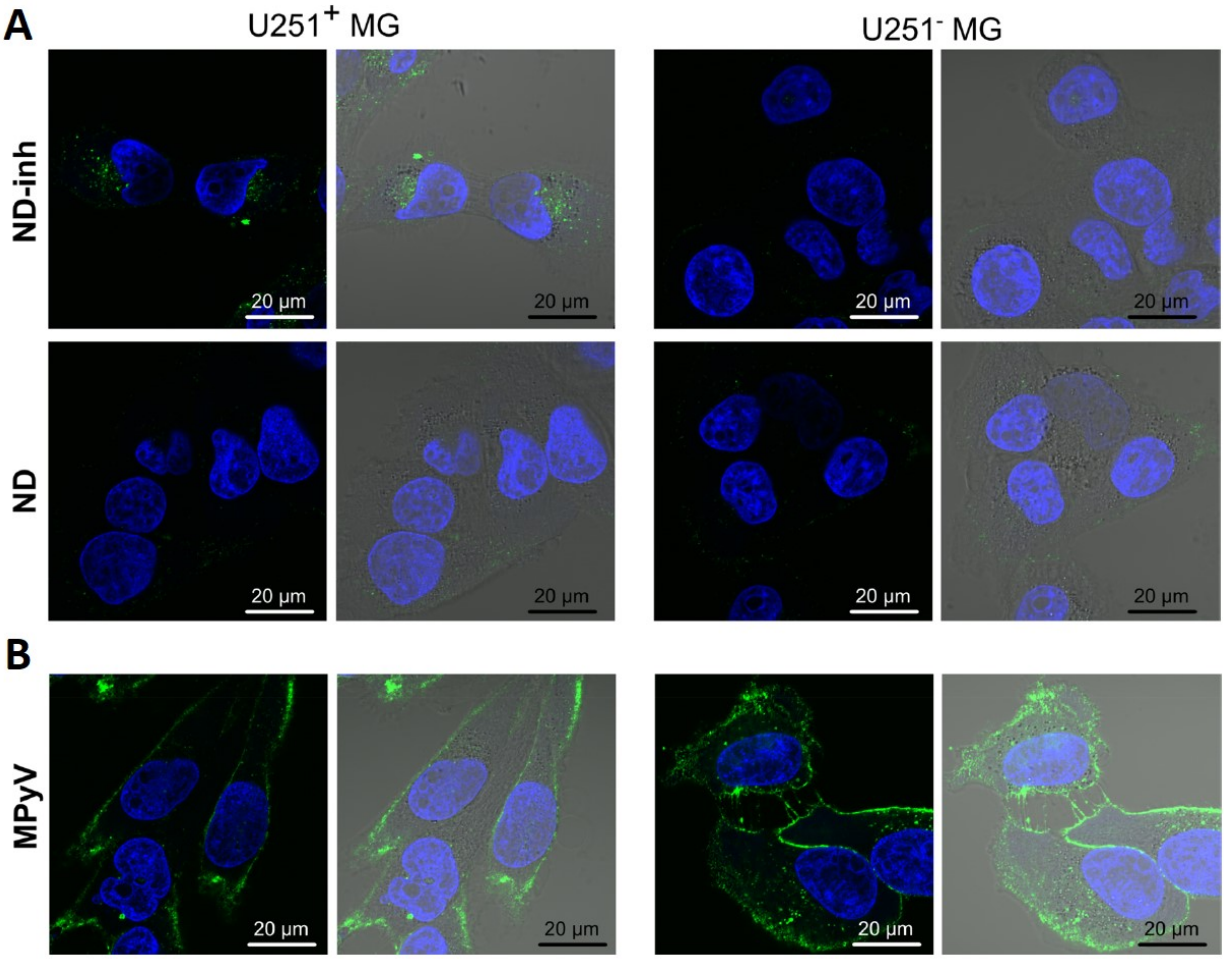

Fig. 19 Confocal microscopy of (A) ND particles (labeled with Alexa Fluor 488) interacting with either cells expressing GCPII (U-251^{+} MG) or without GCPII expression (U-251^{-} MG). (B) Non-specific interaction of non-coated non-modified MPyV particles with U-251 MG cells.

Publication 6: Plasmonic Nanodiamonds: Targeted Core–Shell Type NPs for Cancer Cell Thermoablation

Ivan Rehor, Karin L. Lee, Kevin Chen, Miroslav Hajek, Jan Havlik, Jana Lokajova, Milan Masat, Jitka Slegerova, Sourabh Shukla, Hamed Heidari, Sara Bals, Nicole F. Steinmetz, Petr Cigler

Once we master the control of NDs' surface and properties, NDs can be used for broad spectrum of biomedical applications. For therapy, special features of NPs such as photothermal ablation can be utilized. Certain NPs transform light to heat. Cells that contain NPs are illuminated, heated up and killed. Once NPs are targeted only to cancer cells, light can be applied to whole tissue using laser with harmful effect only on cells internalizing the NPs. Photothermal effect was shown also on ND particles, however gold NPs, explicitly gold nanoshells are much suitable material. Gold NPs as noble-metal NPs show quantum size effects, such as phenomenon called localized plasmon resonance. Gold nanoshells have very high extinction coefficient in a near-infrared imaging window region, where the light penetrate favorably into the tissue.

In this publication, we prepared multiple-layer structure with gold nanoshell (Fig. 20A) and utilized the resulting NPs in thermal ablation of HeLa cells. We prepared NDs (Fig. 20B) with a silica layer, making NDs more spherical (Fig. 20C) as shown previously. Small gold seeds (2-3 nm) were adsorbed on the surface of silica layer (Fig. 20D) and a compact gold layer was then grown from Au^{3+} salt and reduction agent carbon oxide in the solution (Fig. 20E). From common TEM, thickness and compactness of the shell cannot be recognized. Three-dimensional reconstitution and thickness of the shell (approximately 12.6 nm) was measured using electron tomography (HAAF-STEM). Absorption spectrum of prepared blue-colored ND@Au particles had maximum at 675 nm. Stability of prepared ND@Au in buffered solution (PBS and media with serum) was ensured by polymer coating with 5-kDa PEG. Heterobifunctional PEG was attached to the surface by lipoic acid, moiety with affinity to the gold. Alkyne groups at the second end of the PEG chains were functionalized further with secondary fluorescent label Alexa Fluor 647-azide and transferrin-azide using subsequent "click" reaction.

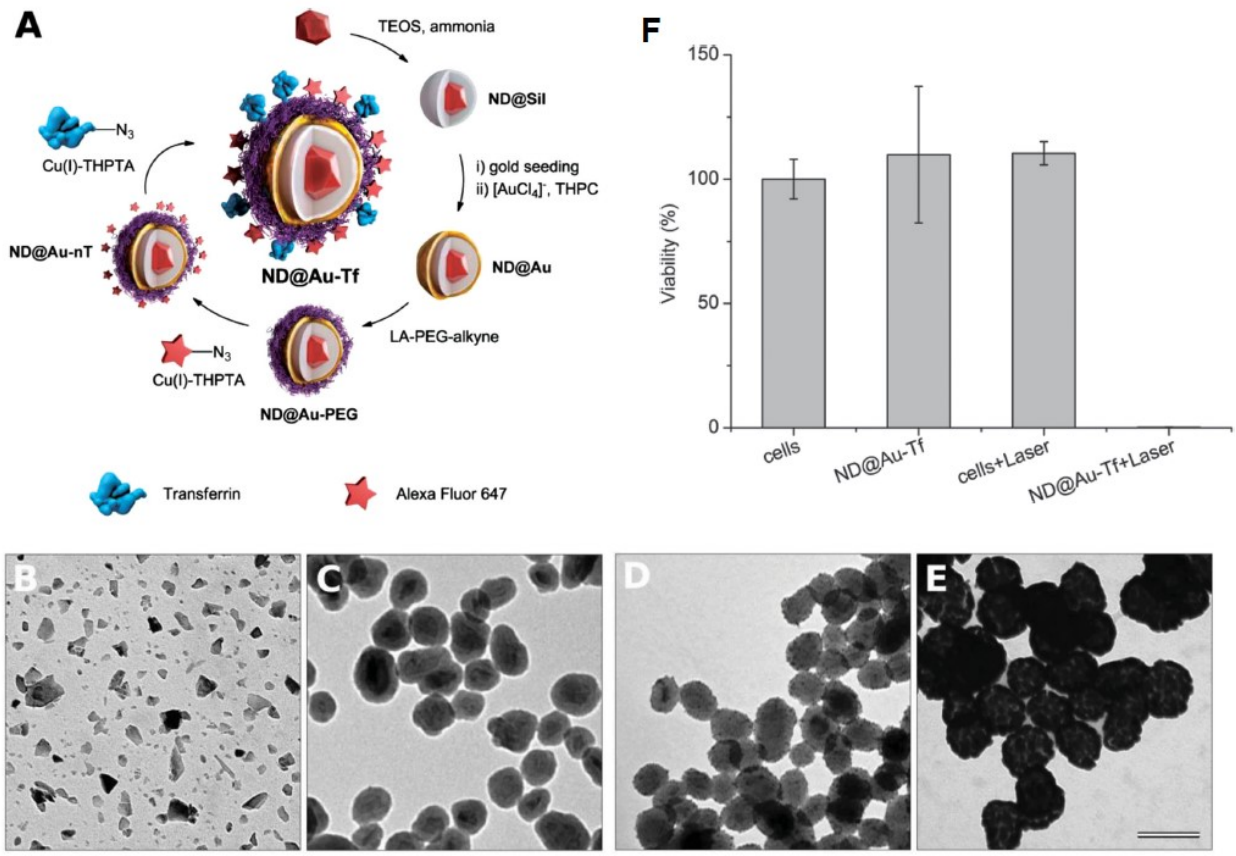

Fig. 20 (A) Scheme of ND modification with multi-layer system. First, NDs are coated with thick silica layer, gold seeds are attached and further grown to compact gold shell. Second, modification of ND@Au with PEG, Alexa Fluor 647 and transferrin followed. TEM images of (B) NDs, (C), silica-coated NDs, (D) silica-coated NDs with gold seeds, (E) silica-coated NDs with gold layer (ND@Au). (F) Cell viability of HeLa cells measured by luciferase assay with delay 24 hours after laser ablation (1 minute, 37 W/cm^2).

Transferrin interacted with transferrin receptors on targeted cells (a human breast cancer cell line SKBR3 or HeLa cells) and resulted in higher interaction of ND@Au-Tf particles than non-targeted particles with cells. ND@Au-Tf particles were internalized inside the cells in contrast to non-targeted particles, which, if interacted, co-localized with the membrane according to confocal studies. We demonstrated the possibility of killing cancer cell upon red laser irradiation. Cells without NPs did not change their viability (according to luciferase assay) upon laser irradiation, similarly to non-radiated cells with NPs. Only HeLa cells exposed to both ND@Au-Tf and laser irradiation were completely killed after one minute of irradiation (power laser 37 W/cm^2) (Fig. 20F).

Publication 7: Optical imaging of localized chemical events using programmable diamond quantum nanosensors

Torsten Rendler, Jitka Neburkova, Ondrej Zemek, Jan Kotek, Andrea Zappe, Zhiqin Chu, Petr Cigler, Joerg Wrachtrup

NDs' optical properties are sensitive to electric and magnetic field. Paramagnetic ions, such as Gd^{3+}, create a fluctuating magnetic field that can be sensed by (N-V) relaxometry. T_1 electronic relaxation time of (N-V) center is influenced by the number of spins (Gd^{3+} complexes) within effective (N-V) sensing radius, therefore their detachment from the surface can be measured (Fig. 21A).

In this publication, we attached Gd^{3+} complexes to the surface of PHPMA-coated NDs (prepared by the same procedure as previously in (Slegerova et al., 2015)). Instead of targeting ligands, Gd^{3+} complexes modified with azide were attached to alkyne-modified NDs. Gd^{3+} complexes with cleavable linkage sensitive to either acidic pH (hydrazone linker) or increased redox potential (disulfide linker) were prepared (Fig. 21B).

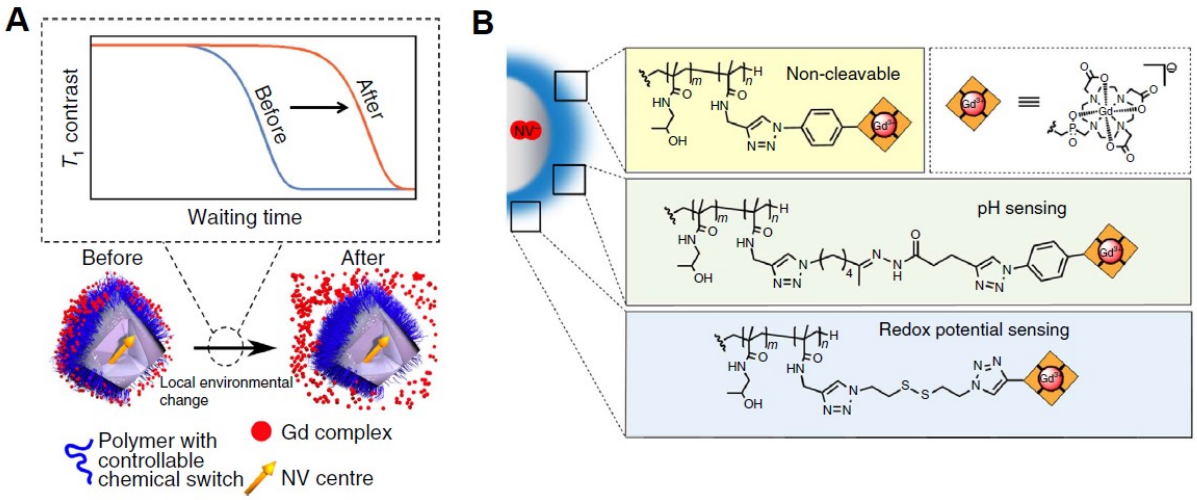

Fig. 21 (A) Cartoon showing the sensing mechanism of a ND-polymer-Gd hybrid nanosensor in response to a local environmental change. (B) Chemical structure of the polymer interface with Gd^{3+} complexes attached via a non-cleavable and two types of cleavable linkers.

The release of Gd^{3+} complexes was evaluated by ICP-MS (Fig. 22A). Detachment of Gd^{3+} complexes in both acidic pH and increased concentration of glutathione (GSH) occurs in a physiologically relevant time (within 1 hour) under physiological conditions (pH 4.5-7.4, 1-10 mM GSH, which corresponds to condition change after NDs entering the cells) (Fig. 22B).

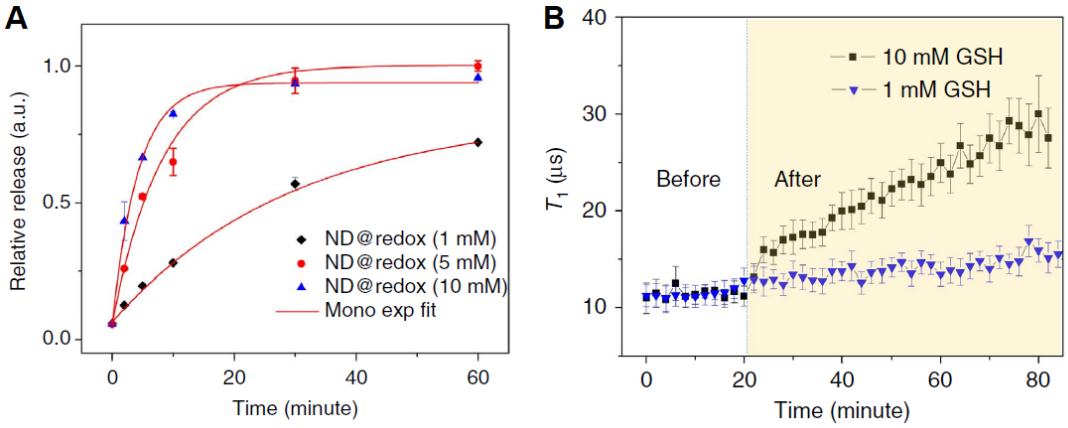

Fig. 22 (A) Release kinetics of Gd^{3+} complexes in redox-sensing particles in the presence of 1, 5 and 10mM glutathione (GSH) in buffer analyzed by ICP-MS. (B) Time-dependent ensemble measurement for T_1 of the redox-sensing particles in buffer solution before and after addition of 1mM or 10mM GSH.

Perfect stability of polymer-coated NDs in buffers enabled T_1 measurement to be done in a microfluidic channel that mimics cellular environments. Measurement of T_1 relaxation time of (N-V) centers corresponds to ICP-MS measurements. The pH sensing system operates in quite a broad pH range (pH 2.0-7.4) with accuracy ± 0.7 pH unit (Fig. 23A). We were able to distinguish under confocal microscope NPs of various T_1 relaxation time, for example NPs incubated in acidic pH and new-comers from neutral pH (Fig. 23B).

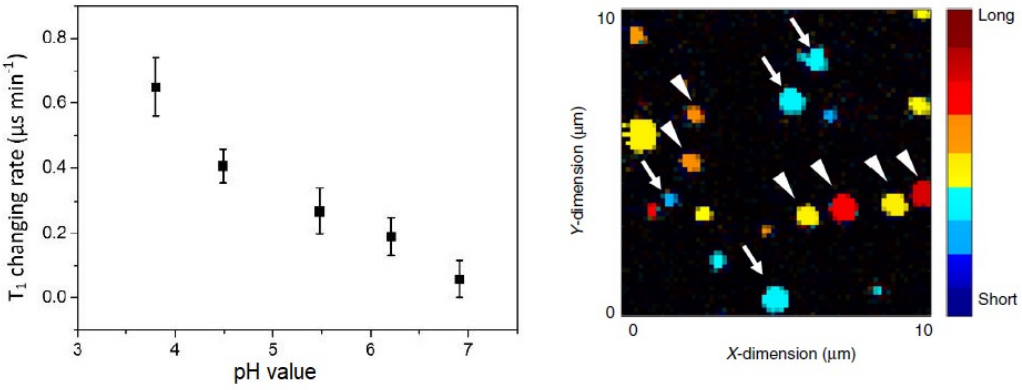

Fig. 23 (A) Dependence of the fitted T_1 changing rate of acidic-sensing NPs on pH. T_1 points were measured for 120 seconds. (B) T_1 contrast image of NPs incubated in pH 2.0 and freshly added NPs from pH 7.4 buffer. White arrows point to newly added ones. The color bar indicates the T_1 value ranging from short (blue) to long (red).

These sensors working under physiological conditions can enable further monitoring of intracellular processes that are important for various bioapplications.

5. MY CONTRIBUTION TO THESE PUBLICATIONS

The presented data were all result of team effort of all co-authors. Here I summarized my involvement in individual publications:

Publication 1: Surface modification of NDs (preparation and optimization of silica and polymer coating), imaging of NDs in cells

Publication 2: Surface modification of NDs (preparation and optimization of silica and polymer coating)

Publication 3: Surface modification of NDs (preparation of silica, polymer coating, reactions with fluorescent dye and targeting peptide), optimization of polymer coating, characterization of the particles, cell experiments (cell viability assay, flow cytometry, confocal microscopy), preparation of the manuscript

Publication 4: Chemical modification of transferrin, surface modification of NDs (preparation of silica, polymer coating, reactions with fluorescent dye and targeting protein), characterization of the particles, cell experiments (cell viability assay, flow cytometry, confocal microscopy), preparation of the manuscript

Publication 5: Surface modification of NDs (preparation of silica, polymer coating, reactions with fluorescent dye and small-molecule inhibitor), expression of Qβ virus-like particles, their isolation and modification (polymer coating, modification with fluorescent dye and small-molecule inhibitor), characterization of the particles (DLS, TEM, SPR, matrix-assisted laser desorption/ionization MALDI), cell experiments (flow cytometry, confocal microscopy), preparation of the manuscript

Publication 6: Chemical modification of transferrin glycosylic chains with azide moieties, its purification and characterization

Publication 7: Surface modification of NDs (preparation of silica, polymer coating, reactions with Gd^{3+} complexes), characterization of the NDs (DLS, zeta potential, TEM), exploration of the conditions and kinetics of the Gd^{3+} release from the surface (ICP-MS measurements)

6. DISCUSSION

NPs can be used for various biological applications in both diagnostics and therapy. Especially, targeted nanomedicine has remarkable potential in cancer related applications. Superiority of NPs emerges from their proper size, ability of acquire various functions and extreme local concentration of ligands achieved around the NPs resulting in increased affinity (phenomenon called avidity). Mastering surface properties and preparation of controllable interface are key requirements for all applications. In this PhD thesis, I focused on preparation of such surfaces with low non-specific interactions and high specific interaction toward cancer cells. The central NPs used in this thesis are biocompatible polydisperse NDs. Many researchers previously published polymer coatings on NDs, although the quality of the coating was not sufficient to protect NDs from non-specific interactions with cells. Usually, "grafting to" procedures introducing PEG on the surface were established. (Dong et al., 2015; Wang et al., 2014; Zhang et al., 2015)

We chose PEG and "grafting to" approach for our first attempt to coat NDs with polymer. (Rehor et al., 2014a) PEG was grown on amino-modified silica layer on NDs. NDs were rounded by thick silica layer and their size polydispersity was reduced. Shape of NPs influence their fate in cells. Sharp NPs (including NDs) were shown to disrupt the membrane of endosomes and to escape from the vesicle to the cytoplasm. Rounded NPs went through the endocytosis pathway and were excreted. (Chu et al., 2014) We were able to ensure ND-PEG stability in buffers and therefore fulfill fundamental condition for further applications. However, ND-PEG conjugates were internalized spontaneously inside the cells, so their non-specific interactions with cells were not eliminated. We therefore further focused on modification of NDs with "grafting from" approach, which was reported as a method introducing denser polymers on surfaces. (Zhao and Brittain, 2000) "Grafting from" method is experimentally more demanding; however has potential to provide NPs with polymer coatings in conformation of dense brushes. For "grafting from" approach, we selected PHPMA as a hydrophilic biocompatible non-immunogenic polymer. First, silica coating was installed on the surface of NDs. 3-(Trimethoxysilyl)propyl methacrylate as a part of the silica mixture reduce the thickness of the silica shell during the reaction. This molecule block the growth of the layer by capping the formed silica layer by organic substituent. This method does not lead to rounded NDs, however for many applications we need the close proximity of the polymer shell to the core of ND. Thin silica shell (approximately 1-2 nm) does not significantly enlarge the NDs

and can be utilized also for other types of NPs as a general approach to NP modification. The main motivation of 3-(Trimethoxysilyl)propyl methacrylate presence is preparation of the platform from which HPMA monomer further polymerize. Prepared PHPMA-coated NDs were colloidally stable and the protein adsorption was four-fold lower than for non-coated NDs. (Rehor et al., 2014b) Nevertheless, after further optimization, (Slegerova et al., 2015) we achieved NDs with dense polymeric coating and no measurable non-specific interaction with cells. The growth of the polymer layer in a more viscous environment and in lower temperature resulted in better coating. Stability of these optimized PHPMA-coated NDs was ensured in biologically relevant buffers and media and even more harsh conditions such as 1 M NaCl.

As a next step, we focused on targeting efficiency of NDs after attachment of targeting ligand. Usually, poor targeting efficiency is an outcome of the incomplete polymer layer resulting in non-specific interactions. Satisfactory targeting efficiency (12-fold) was previously achieved only for targeting folate-modified NDs into HeLa cells. (Zhang et al., 2009a) As we are able to eliminate the non-specific interaction of cells, potential of our NDs is high. We modified PHPMA-coated NDs with cyclic RGD peptide, ligand for targeting integrin $\alpha_v\beta_3$ overexpressed on cancer cells. (Slegerova et al., 2015) Cyclization of RGD improves binding efficiency and integrin selectivity by enhancing stability and structural rigidity of the peptide. NDs were also labeled with Alexa Fluor 488-alkyne. Introduction of fluorescent dye was important in our case, because fluorescence of NDs was not compatible with our flow cytometer setup. However, flow cytometry can be used for detection of ND fluorescence. (Zhang et al., 2009a) We observed 8-times higher interaction of ND-cRGD than interaction of negative controls with glioma cancer cells on flow cytometer. As negative controls, NDs without peptide and pre-incubation with free cyclic RGD were used. Free cyclic RGD binds to the receptor and blocks the receptor from further interactions. If the subsequent interaction of ND-cRGD is blocked, as in this case, the interaction is specific and requires the receptor. We observed no significant difference between non-treated cells and cells treated with negative controls. Therefore, we were successful in our goal of eliminating non-specific interaction. Flow cytometry is a quantitative method, but does not provide information about NDs localization. According to the results from confocal microscopy, ND-RGD were localized inside the cells. Similarly successful in decreasing non-specific interaction of NDs was group of professor Komatsu with polymer layer consisting of PG. (Zhao et al., 2014b) However, the increase of interaction of ND-PG modified with peptide cyclic-RGD in comparison to controls was only 50%.

Further, we focused on increasing specific interactions, which was in the case of our ND-RGD 8-fold. The specific interaction is affected by the system of targeting ligand-receptor (and its binding efficiency constant), conformation of more complexed ligands (proteins) and their concentration on the surface. Modifications using azide-alkyne cycloaddition catalyzed by Cu(I) ions ("click" reaction) was possible for all the prepared coated NDs as NDs have in polymer structures either azide or alkyne groups. We prefer biorthogonal reactions on the surface of NDs because of the mild conditions of the reactions, high yields and higher specificity in reactions with biomolecules. In case of small peptide, such as RGD, the chosen reaction does not play such an important role.

On the other hand, biomolecules such as proteins, contain in their structure many potential moieties for attachment using either amidic coupling or disulfide bond formation. Many amines in the molecule can be involved in the attachment using amidic coupling making it impossible to control conformation and biomolecule exposure on the surface. This control is a key for enhancing interaction of ligands on NPs with their targets. Protein transferrin has one recognizing epitope towards the transferrin receptor. This reaction site needs to be exposed to the environment and not hindered by the ND surface. Site-specific attachment of transferrin on far end from the reaction site is needed. We modified the sialic acid in glycosylic chains in the structure (four in every transferrin molecule) with clickable moiety. (Neburkova et al., submitted) First, the saccharide diol structure was cleaved by meta-periodate to an terminal aldehyde. This aldehyde then reacted in biorthogonal reaction with 3-aminooxypropylazide linker, forming an aldoxime bond. Cleavage by meta-periodate needs to be carefully optimize to prevent adverse cleavage effects in the protein structure. Bioorthogonal reaction (oxime ligation) with aminooxy linker ensures introduction of maximally four azide groups in the glycosylic structure of the protein on far end from recognizing epitope.

Transferrin-azide reacted in "click" reaction with alkyne-modified PHPMA-NDs already labeled with Alexa Fluor 488-azide. The consecutive "click" reaction is performed with low molar excess of first reactive molecule (fluorescent dye) and large excess of second molecule (protein transferrin). However, the loading of second molecule is affected by the occurrence of first "click" reaction. Loading of transferrin on NDs was evaluated by two methods as 6 and 20 per one particle with and without fluorescent dye, respectively. Although 6 molecules of transferrin per one particle is not particularly high, it was enough for efficient targeting. Flow cytometry revealed 175-times higher interaction of ND-Tf with CCRF-CEM lymphoblast cells than ND without transferrin or controls with free transferrin pre-incubation.

Controls were not distinguishable from each other and from non-treated cells. Polymer surface coating fulfilled its function and NDs did not interact non-specifically. We examined interaction of NDs with three different cell-lines: two cancer cell lines (U2OS, CCRF-CEM) and one non-cancerous cell line HUVEC. We performed the experiments in co-culture to imitate cancer environment. Cancer cell line was always mixed with endothelial cell line and incubation with NDs was done in this mixture of two lines. We proposed the method how to distinguish between co-cultured cell lines by labeling them for analysis after experiment without having any influence on cell surface structures. Before analysis, specific antibodies towards cell line labeled with different fluorescent dyes were introduced. Flow cytometry on three different fluorescent channels was measured without overlapping of the fluorescence. For all three cell lines, ND-Tf conjugate signal was significantly higher than signal of controls. However, ND-Tf selectively choose cancer cells over endothelial cells from the mixture. Difference between cell lines is dependent on amount of transferrin receptors on the cell surface. Cancer cells overexpress transferrin receptors as their iron(III) uptake is higher. Expression of transferrin receptors on non-cancerous cells results in specific internalization of certain amount of ND-Tf, which nevertheless decrease the difference between cancer and non-cancerous cells. Therefore, more tissue-specific targeting system (receptor-ligand) is needed.

GCPII is expressed only in few tissues such as prostate, central nervous system, small intestine and kidney. GCPII is overexpressed on prostate tissue-cancer cells. NDs with the PHPMA structure modified with small-molecule inhibitor were prepared as well as other NPs included in this study. (Neburkova et al., 2018) We compared the targeting efficiency of one ligand within the same experimental setup dependent on various types and characteristics of NPs, surface ligand density, surface functionalization and modification method. The interaction of NP-inh particles with GCPII was studied in solution, on the artificial surface or on the cell membrane. Inhibition efficiency of NP-inh in solution was sustained. Inhibition constants (K_i) were for NP-inh conjugates in picomolar range, three orders of magnitude lower than for free inhibitors. This decrease is probably caused by avidity effect of inhibitors on the surface of NPs. NP-inh selectively interacted with GCPII bound to the gold surface of a chip in SPR measurement. Regardless the difference in inhibitor loading, surface chemistry and type and size of the NPs, all NPs were able to interact with GCPII on gold chip in a similar manner. We observed similar effect also concerning NP-inh interaction with GCPII on cell membrane measured by flow cytometry. Only interaction of ND-inh was notably higher (75-fold higher than controls), probably because of the combination of optimized bionanointerface with high

loading of inhibitors. For NDs, polymer-coated and uncoated Qβs and polymeric particles, no non-specific interaction were observed. High non-specific interactions of MPyV (unrelated to GCPII receptor) were observed because of MPyV interactions with its primary target (certain receptors and glycosylated surfaces) on the cells. Elimination of non-specific interactions was the only requirement for the efficient targeting. "Grafting to" polymerization of PHPMA to virus-like particles did not provide reasonable yield, probably because of the limited solubility of the PHPMA polymer with hydrophobic amine-reactive groups (thiazolidine-2-thiones). Therefore, the polymer did not sufficiently lowered non-specific interaction of MPyV. Decrease of non-specific interaction and denser coating was provided by PEG-coating of MPyV. Although the polymer was attached by "grafting to" approach, the yield was sufficient for protection. For targeting with small molecules, elimination of non-specific interactions has to be provided by polymeric shell. Contrary, MPyV targeted with large protein transferrin did not need to be coated with polymer, since the size of the protein by itself was sufficient to sterically hinder the MPyV. (Zackova Suchanova et al., 2017) Qβ do not show non-specific interactions with cells even without polymer coating. However, polymer coating would be needed for Qβs for *in vivo* applications, as Qβs are immunogenic. Confocal microscopy confirmed the internalization of NP-inh particles. All NP-inh were observed inside the cells in perinuclear region. Non-specifically interacting MPyV were localized near the membrane.

We showed the preparation of bionanointerface consisting of dense polymeric layer and various targeting ligands (peptide, protein, small molecule) and successful targeting ability of such particles. NDs with surface under control can be used for therapeutic applications. NDs (usually DNDs) were shown to be used as small-drug carriers, however from our point of view, other types of NPs (such as hollow organic NPs) are more useful for this purpose. Nevertheless, nanophototherapy as a therapeutic technique is worth to explore further. NPs with gold nanoshells transform very efficiently light (from the laser) to the local heat and kill the cell, in which they are internalized. NDs coated with thick silica layer served as a good platform for gold shell layer growth. (Rehor et al., 2015) Gold shell is easier to grow on rounded particles, which thick silica layer provide. Seeded growth of gold results in a fairly compact layer, however with thickness of at least 10 nm. Absorption properties of gold shells depends on the size of the core and thickness of the shell. Prepared ND@Au had maximum of the absorption peak in near-infrared region at 675 nm, where the light penetration through tissues is easier because of the lower tissue absorbance, lower auto-fluorescence and lower NIR light scattering. HeLa cells with NDs inside were completely killed after a one-minute irradiation with a pulse

750-nm pulse laser (37 W/cm^2). These irradiation conditions did not cause any adverse effect to cells without ND@Au. We examined the possibility of killing cancer cells with ND@Au in parallel with improving the polymer bionanointerface. Therefore, the experiments were done on ND@Au coated with PEG and modified with transferrin. Although ND@Au were preferentially internalized to cancer cells, the targeting effect is rather weak, because of high non-specific interaction. Nevertheless, we confirmed the possibility of killing cell by thermal ablation and now we are currently working on preparation of gold layers with PHPMA polymer coating "grafted from" the surface.

PHPMA-coated NDs were used also as a proof-of-concept for further biological applications of NDs as sensors of physiological relevant parameters. (Rendler et al., 2017) For this project, enhanced colloidal stability and possibility of further functionalization with high yield of NDs was needed. NDs with PHPMA coating were modified with Gd^{3+} complexes. Presence of paramagnetic Gd^{3+} ion shorten T_1 relaxation time of $(N\text{-}V)^-$ center. Three complexes were attached, non-cleavable one, sensitive to lower pH, and responsive to higher concentration of reduction agents. Kinetics of the cleavage was studied using ICP-MS method, in which only Gd^{3+} released from the surface was measured. It was shown that the cleavage of Gd^{3+} occur in reasonable fast conditions. Too fast or slow cleavage would prevent the use of this system as a sensor inside of the cells. All cleavable Gd^{3+} complexes were cleaved within an hour in biologically relevant intracellular conditions (in pH 4.5 or GSH concentration 5 mM). Cleavage of pH-sensitive complex occurs also at pH 7.4, but in time scale of few tens of hours. On the other hand, at non-physiological pH 2.0, the cleavage is very rapid and finishes in few minutes. Similarly the concentration of GSH (1-10 mM) influenced the rate of the cleavage. The T_1 relaxation time and its change can be measured because of the colloidal stability in microfluidic channel. The change of T_1 relaxation time was caused only by the Gd^{3+} cleavage, no shrinking or swelling of the polymer layer was observed. No change in T_1 was observed for controls (NDs with non-cleavable Gd^{3+} complex). The kinetics of T_1 relaxation time change (relaxation rate) was in agreement with release measurement from ICP-MS and theoretical model. The T_1 relaxation time measurement is fast and the T_1 relaxation rate can be fitted with high precision from two-minute measurement. For pH sensor, value of pH can be extracted from the relaxation rate. NDs with different T_1 relaxation time can be distinguished under confocal microscope due to the fast T_1 measurement. Disadvantage of this sensor is its irreversibility; however, that is common feature for all of the NP sensor introduced so far. (Howes et al., 2014) Attempt of preparation of even better reversible sensors is of the particular interest.

7. CONCLUSIONS

In this thesis, a superior nanobiointerface on NPs was proposed, prepared and studied. NPs with optimized biocompatible surfaces were shown to have potential in biomedical applications. The particular hypotheses listed within aims of the thesis were successfully answered.

- NDs were coated with multilayer structure consisting of silica and polymeric shell. They were stable in buffer solutions.
- Different polymerization methods ("grafting to" and "grafting from") with different types of polymers (PEG or PHPMA) provided diverse ability of surface protection. Ability of polymer shell to increase colloidal stability, to decrease non-specific interactions with proteins and cells and to enable high yield surface modifications was studied. Dense polymeric shells from PHPMA "grafted from" the surface of NDs showed the best results in eliminating non-specific interactions.
- PHPMA-NDs were modified with biorthogonal "click" reactions with various ligands including fluorescent dyes and targeting ligands (peptide RGD, protein transferrin and small-molecule inhibitor of protease). The controlled way of attachment and environmental exposition was important especially for transferrin.
- Successful targeting was shown for all PHPMA-coated ND conjugates with increasing targeting effect from peptide, small-molecule inhibitor to protein.
- Differences in targeting of various types of NPs were studied on NDs, virus-like NPs and polymeric NPs modified with small-molecule GCPII inhibitor. The highest targeting effect was observed for NDs, although other types of the NPs were also successfully targeted to cancer cells overexpressing GCPII. Requirement of proper polymerization methods for preparation of dense polymeric shells was again confirmed.
- Apart from targeting, two other biological applications were studied. First, NDs were modified with plasmonic gold nanoshell and their ability to kill the cancer cells using photothermal ablation was investigated. The cells with internalized NDs were effectively killed upon a short exposition to near-infrared laser. Second, pH and redox potential was measured by selective release of Gd^{3+}-complexes from NDs. The release resulted in change of T_1 relaxation time of NDs enabling optical readout of localized chemical processes occurring on an extremely small scale (10^{-22}–10^{-20} mol) using confocal microscopy.

8. CHRONOLOGICAL LIST OF MY PUBLICATIONS

(including book chapters)

Lukas Balek, Marcela Buchtova, Michaela Kunova Bosakova, Miroslav Varecha, Silvie Foldynova-Trantirkova, Iva Gudernova, Iva Vesela, Jan Havlik, **Jitka Neburkova**, Stuart Turner, Mateusz Adam Krzyscik, Malgorzata Zakrzewska, Lars Klimaschewski, Peter Claus, Lukas Trantirek, Petr Cigler, Pavel Krejci: Nanodiamonds as "artificial proteins": Regulation of a cell signalling system using low nanomolar solutions of inorganic nanocrystals, Biomaterials, doi: 10.1016/j.biomaterials.2018.05.030, **2018.** Impact factor: 8.402

Jitka Neburkova[#], Frantisek Sedlak[#], Jirina Zackova Suchanova[#], Libor Kostka, Pavel Sacha, Vladimir Subr, Tomas Etrych, Petr Simon, Jitka Barinkova, Robin Krystufek, Hana Spanielova, Jitka Forstova, Jan Konvalinka, Petr Cigler: Inhibitor−GCPII Interaction: Selective and Robust System for Targeting Cancer Cells with Structurally Diverse NPs, Molecular Pharmaceutics, doi: 10.1021/acs.molpharmaceut.7b00889, **2018.** [#]***Equal contribution.*** Impact factor: 4.44

Torsten Rendler[#], **Jitka Neburkova**[#], Ondrej Zemek, Jan Kotek, Andrea Zappe, Zhiqin Chu, Petr Cigler, Joerg Wrachtrup: Optical imaging of localized chemical events using programmable diamond quantum nanosensors, Nature Communications *8*, 14701, **2017**. [#]***Equal contribution.*** Impact factor: 12.124

Jirina Zackova Suchanova, **Jitka Neburkova**, Hana Spanielova, Jitka Forstova, Petr Cigler: Retargeting Polyomavirus-Like Particles to Cancer Cells by Chemical Modification of Capsid Surface, Bioconjugate Chemistry, *28*, 307, **2017**. Impact factor: 4.818

Jitka Neburkova, Jan Vavra, Petr Cigler: Coating nanodiamonds with biocompatible shells for applications in biology and medicine, Current Opinion in Solid State and Materials Science, *21*, 43, **2017.** Impact factor: 6.938

Jitka Slegerova, Miroslav Hajek, Ivan Rehor, Frantisek Sedlak, Jan Stursa, Martin Hruby, Petr Cigler: Designing the nanobiointerface of fluorescent nanodiamonds: highly selective targeting of glioma cancer cells, Nanoscale, *7*, 415, **2015**. Impact factor: 7.367

Ivan Rehor, Karin L. Lee, Kevin Chen, Miroslav Hajek, Jan Havlik, Jana Lokajova, Milan Masat, **Jitka Slegerova**, Sourabh Shukla, Hamed Heidari, Sara Bals, Nicole F. Steinmetz, Petr Cigler: Plasmonic nanodiamonds: targeted core-shell type NPs for cancer cell thermoablation, Advanced Healthcare Materials, *4*, 460, **2015**. Impact factor: 5.11

Ivan Rehor, **Jitka Slegerova**, Jan Kucka, Vladimir Proks, Vladimira Petrakova, Marie-Pierre Adam, François Treussart, Stuart Turner, Sara Bals, Miroslav Ledvina, Amy M. Wen, Nicole F. Steinmetz, Petr Cigler: Fluorescent Nanodiamonds Embedded in Biocompatible Translucent Shells, Small, *10*, 1029, **2014**. Impact factor: 8.643

Ivan Rehor, Hana Mackova, Sergey K. Filippov, Jan Kucka, Vladimír Proks, **Jitka Slegerova**, Stuart Turner, Sara Bals, Miroslav Ledvina, Martin Hruby, Petr Cigler: Fluorescent

nanodiamonds with bioorthogonally reactive protein-resistant polymeric coatings, ChemPlusChem, *79*, 21, **2014**. Impact factor: 2.797

Jitka Slegerova, Petr Cígler: Nanodiamanty – fluorescenční a vizualizační sondy, Chem. Listy, *108*, 387, **2014**. Impact factor: 0.387

Book chapters:

Jitka Neburkova, Miroslav Hajek, Ivan Rehor, Jiri Schimer, Frantisek Sedlak, Jan Stursa, Martin Hruby, Petr Cigler: Targeting Glioma Cancer Cells with Fluorescent Nanodiamonds via Integrin Receptors. In: Methods in Pharmacology and Toxicology; Humana Press, *in press,* **2017**. DOI: 10.1007/7653_2017_68

Jitka Neburkova, Jan Vavra, Helena Raabova, Goutam Pramanik, Jan Havlik, Petr Cigler: Nanodiamonds embedded in shells. In: Nanodiamonds: Advanced Material Analysis, Properties and Applications. Arnault J.-C., ed; Elsevier, 339-363, **2017**.

Ivan Rehor **Jitka Slegerova**, Jan Havlik, Helena Raabova, Jakub Hyvl, Eva Muchova, Petr Cigler: Nanodiamonds: Behavior in Biological Systems and Emerging Bioapplications. In: Carbon Nanomaterials for Biomedical Applications. Dai L., Naik R., Zhang M., eds.; Springer, 319-361, **2016**.

Jitka Slegerova, Ivan Rehor, Jan Havlik, Helena Raabova, Eva Muchova, Petr Cigler: Nanodiamonds as Intracellular Probes for Imaging in Biology and Medicine. In: Intracellular Delivery, Vol. 2. Prokop A., ed.; Springer, 363-401, **2014**.

9. REFERENCES

Alhaddad, A., Adam, M.-P., Botsoa, J., Dantelle, G., Perruchas, S., Gacoin, T., Mansuy, C., Lavielle, S., Malvy, C., Treussart, F., et al. (2011). Nanodiamond as a Vector for siRNA Delivery to Ewing Sarcoma Cells. Small *7*, 3087–3095.

Alhaddad, A., Durieu, C., Dantelle, G., Le Cam, E., Malvy, C., Treussart, F., and Bertrand, J.-R. (2012). Influence of the Internalization Pathway on the Efficacy of siRNA Delivery by Cationic Fluorescent Nanodiamonds in the Ewing Sarcoma Cell Model. Plos One *7*, e52207.

Amoozgar, Z., and Yeo, Y. (2012). Recent advances in stealth coating of nanoparticle drug delivery systems. Wiley Interdiscip. Rev. Nanomed. Nanobiotechnol. *4*, 219–233.

Balasubramanian, G., Chan, I.Y., Kolesov, R., Al-Hmoud, M., Tisler, J., Shin, C., Kim, C., Wojcik, A., Hemmer, P.R., Krueger, A., et al. (2008). Nanoscale imaging magnetometry with diamond spins under ambient conditions. Nature *455*, 648–651.

Bertrand, J.-R., Pioche-Durieu, C., Ayala, J., Petit, T., Girard, H.A., Malvy, C.P., Le Cam, E., Treussart, F., and Arnault, J.-C. (2015). Plasma hydrogenated cationic detonation nanodiamonds efficiently deliver to human cells in culture functional siRNA targeting the Ewing sarcoma junction oncogene. Biomaterials *45*, 93–98.

Bobo, D., Robinson, K.J., Islam, J., Thurecht, K.J., and Corrie, S.R. (2016). Nanoparticle-Based Medicines: A Review of FDA-Approved Materials and Clinical Trials to Date. Pharm. Res. *33*, 2373–2387.

Butler, J.E., and Sumant, A.V. (2008). The CVD of Nanodiamond Materials. Chem. Vap. Depos. *14*, 145–160.

Chan, M.S., Liu, L.S., Leung, H.M., and Lo, P.K. (2017). Cancer-Cell-Specific Mitochondria-Targeted Drug Delivery by Dual-Ligand-Functionalized Nanodiamonds Circumvent Drug Resistance. ACS Appl. Mater. Interfaces *9*, 11780–11789.

Chang, Y.-R., Lee, H.-Y., Chen, K., Chang, C.-C., Tsai, D.-S., Fu, C.-C., Lim, T.-S., Tzeng, Y.-K., Fang, C.-Y., Han, C.-C., et al. (2008). Mass production and dynamic imaging of fluorescent nanodiamonds. Nat. Nanotechnol. *3*, 284–288.

Chen, M., Pierstorff, E.D., Lam, R., Li, S.-Y., Huang, H., Osawa, E., and Ho, D. (2009). Nanodiamond-Mediated Delivery of Water-Insoluble Therapeutics. ACS Nano *3*, 2016–2022.

Cheng, C.-Y., Perevedentseva, E., Tu, J.-S., Chung, P.-H., Cheng, C.-L., Liu, K.-K., Chao, J.-I., Chen, P.-H., and Chang, C.-C. (2007). Direct and in vitro observation of growth hormone receptor molecules in A549 human lung epithelial cells by nanodiamond labeling. Appl. Phys. Lett. *90*, 163903.

Chipaux, M., Laan, K.J. van der, Hemelaar, S.R., Hasani, M., Zheng, T., and Schirhagl, R. (2018). Nanodiamonds and Their Applications in Cells. Small.

Chu, Z., Zhang, S., Zhang, B., Zhang, C., Fang, C.-Y., Rehor, I., Cigler, P., Chang, H.-C., Lin, G., Liu, R., et al. (2014). Unambiguous observation of shape effects on cellular fate of nanoparticles. Sci. Rep. *4*, 4495.

Cigler, P., Neburkova, J., Vavra, J., Raabova, H., Pramanik, G., and Havlik, J. (2017). Chapter 13: Nanodiamonds embedded in shells. In Nanodiamonds, J.C. Arnault, ed. (Elsevier), p.

Daniels, T.R., Delgado, T., Helguera, G., and Penichet, M.L. (2006a). The transferrin receptor part II: Targeted delivery of therapeutic agents into cancer cells. Clin. Immunol. *121*, 159–176.

Daniels, T.R., Delgado, T., Rodriguez, J.A., Helguera, G., and Penichet, M.L. (2006b). The transferrin receptor part I: Biology and targeting with cytotoxic antibodies for the treatment of cancer. Clin. Immunol. *121*, 144–158.

Dong, Y., Cao, R., Li, Y., Wang, Z., Li, L., and Tian, L. (2015). Folate-conjugated nanodiamond for tumor-targeted drug delivery. RSC Adv. *5*, 82711–82716.

Edwards, S.A., and Williams, D.R.M. (2004). Double Layers and Interparticle Forces in Colloid Science and Biology: Analytic Results for the Effect of Ionic Dispersion Forces. Phys. Rev. Lett. *92*, 248303.

Epperla Chandra Prakash, Mohan Nitin, Chang Che-Wei, Chen Chia-Chun, and Chang Huan-Cheng (2015). Nanodiamond-Mediated Intercellular Transport of Proteins through Membrane Tunneling Nanotubes. Small *11*, 6097–6105.

Faklaris, O., Garrot, D., Joshi, V., Druon, F., Boudou, J.-P., Sauvage, T., Georges, P., Curmi, P.A., and Treussart, F. (2008). Detection of Single Photoluminescent Diamond Nanoparticles in Cells and Study of the Internalization Pathway. Small *4*, 2236–2239.

Faklaris, O., Joshi, V., Irinopoulou, T., Tauc, P., Sennour, M., Girard, H., Gesset, C., Arnault, J.-C., Thorel, A., Boudou, J.-P., et al. (2009). Photoluminescent Diamond Nanoparticles for Cell Labeling: Study of the Uptake Mechanism in Mammalian Cells. ACS Nano *3*, 3955–3962.

Fernandez-Fernandez, A., Manchanda, R., and McGoron, A.J. (2011). Theranostic applications of nanomaterials in cancer: Drug delivery, image-guided therapy and multifunctional platforms. Appl. Biochem. Biotechnol. *165*, 1628–1651.

Fu, Y., An, N., Zheng, S., Liang, A., and Li, Y. (2012). BmK CT-conjugated fluorescence nanodiamond as potential glioma-targeted imaging and drug. Diam. Relat. Mater. *21*, 73–76.

Georgakilas, V., Perman, J.A., Tucek, J., and Zboril, R. (2015). Broad Family of Carbon Nanoallotropes: Classification, Chemistry, and Applications of Fullerenes, Carbon Dots, Nanotubes, Graphene, Nanodiamonds, and Combined Superstructures. Chem. Rev. *115*, 4744–4822.

Havlik, J., Petrakova, V., Rehor, I., Petrak, V., Gulka, M., Stursa, J., Kucka, J., Ralis, J., Rendler, T., Lee, S.-Y., et al. (2013). Boosting nanodiamond fluorescence: towards development of brighter probes. Nanoscale *5*, 3208–3211.

Hegyi, A., and Yablonovitch, E. (2013). Molecular Imaging by Optically Detected Electron Spin Resonance of Nitrogen-Vacancies in Nanodiamonds. Nano Lett. *13*, 1173–1178.

Hemelaar, S.R., Nagl, A., Bigot, F., Rodríguez-García, M.M., Vries, M.P. de, Chipaux, M., and Schirhagl, R. (2017). The interaction of fluorescent nanodiamond probes with cellular media. Microchim. Acta *184*, 1001–1009.

Howes, P.D., Chandrawati, R., and Stevens, M.M. (2014). Colloidal nanoparticles as advanced biological sensors. Science *346*, 1247390.

Huang, H., Pierstorff, E., Osawa, E., and Ho, D. (2007). Active Nanodiamond Hydrogels for Chemotherapeutic Delivery. Nano Lett. *7*, 3305–3314.

Hui, Y.Y., Hsiao, W.W.-W., Haziza, S., Simonneau, M., Treussart, F., and Chang, H.-C. (2017). Single particle tracking of fluorescent nanodiamonds in cells and organisms. Curr. Opin. Solid State Mater. Sci. *21*, 35–42.

Huynh, V.T., Pearson, S., Noy, J.-M., Abboud, A., Utama, R.H., Lu, H., and Stenzel, M.H. (2013). Nanodiamonds with Surface Grafted Polymer Chains as Vehicles for Cell Imaging and Cisplatin Delivery: Enhancement of Cell Toxicity by POEGMEMA Coating. ACS Macro Lett. *2*, 246–250.

Igarashi, R., Yoshinari, Y., Yokota, H., Sugi, T., Sugihara, F., Ikeda, K., Sumiya, H., Tsuji, S., Mori, I., Tochio, H., et al. (2012). Real-Time Background-Free Selective Imaging of Fluorescent Nanodiamonds in Vivo. Nano Lett. *12*, 5726–5732.

Krueger, A., and Lang, D. (2012). Functionality is Key: Recent Progress in the Surface Modification of Nanodiamond. Adv. Funct. Mater. *22*, 890–906.

Kucsko, G., Maurer, P.C., Yao, N.Y., Kubo, M., Noh, H.J., Lo, P.K., Park, H., and Lukin, M.D. (2013). Nanometre-scale thermometry in a living cell. Nature *500*, 54–58.

Kuo, Y., Hsu, T.-Y., Wu, Y.-C., and Chang, H.-C. (2013). Fluorescent nanodiamond as a probe for the intercellular transport of proteins in vivo. Biomaterials *34*, 8352–8360.

Laan, K. van der, Hasani, M., Zheng, T., and Schirhagl, R. (2018). Nanodiamonds for In Vivo Applications. Small *14*, 1703838.

Lallana, E., Sousa-Herves, A., Fernandez-Trillo, F., Riguera, R., and Fernandez-Megia, E. (2012). Click Chemistry for Drug Delivery Nanosystems. Pharm. Res. *29*, 1–34.

Lee, J.W., Lee, S., Jang, S., Han, K.Y., Kim, Y., Hyun, J., Kim, S.K., and Lee, Y. (2013). Preparation of non-aggregated fluorescent nanodiamonds (FNDs) by non-covalent coating with a block copolymer and proteins for enhancement of intracellular uptake. Mol. Biosyst. *9*, 1004–1011.

Li, H., and Qian, Z.M. (2002). Transferrin/transferrin receptor-mediated drug delivery. Med. Res. Rev. *22*, 225–250.

Li, Y., and Zhou, X. (2010). Transferrin-coupled fluorescence nanodiamonds as targeting intracellular transporters: An investigation of the uptake mechanism. Diam. Relat. Mater. *19*, 1163–1167.

Li, D., Chen, X., Wang, H., Yu, Y., Liu, J., Wang, Y., Zhang, J., Zheng, M., and Zhi, J. (2017). Nanodiamonds as Raman probes for specifically targeted bioimaging: visualization and mechanism study of the biorecognition between nanodiamonds-EGF and EGFR. RSC Adv *7*, 12835–12841.

Li, L., Davidson, J.L., and Lukehart, C.M. (2006). Surface functionalization of nanodiamond particles via atom transfer radical polymerization. Carbon *44*, 2308–2315.

Li, X., Wang, L., Fan, Y., Feng, Q., and Cui, F. (2012). Biocompatibility and Toxicity of Nanoparticles and Nanotubes. J. Nanomater. *2012*, 1–19.

Liu, K.-K., Chen, M.-F., Chen, P.-Y., Lee, T.J.F., Cheng, C.-L., Chang, C.-C., Ho, Y.-P., and Chao, J.-I. (2008). Alpha-bungarotoxin binding to target cell in a developing visual system by carboxylated nanodiamond. Nanotechnology *19*, 205102.

Liu, K.-K., Wang, C.-C., Cheng, C.-L., and Chao, J.-I. (2009). Endocytic carboxylated nanodiamond for the labeling and tracking of cell division and differentiation in cancer and stem cells. Biomaterials *30*, 4249–4259.

Liu Wenliang, Yu Fenglei, Yang Jianbo, Xiang Bo, Xiao Peng, and Wang Li (2015). 3D Single-Molecule Imaging of Transmembrane Signaling by Targeting Nanodiamonds. Adv. Funct. Mater. *26*, 365–375.

Lukowski, S., Neuhoferova, E., Kinderman, M., Krivohlava, R., Mineva, A., Petrakova, V., and Benson, V. (2018). Fluorescent Nanodiamonds are Efficient, Easy-to-Use Cyto-Compatible Vehicles for Monitored Delivery of Non-Coding Regulatory RNAs. J. Biomed. Nanotechnol. *14*, 946–958.

Lynch, I., and Dawson, K.A. (2008). Protein-nanoparticle interactions. Nano Today *3*, 40–47.

Marcon, L., Riquet, F., Vicogne, D., Szunerits, S., Bodart, J.-F., and Boukherroub, R. (2010). Cellular and in vivo toxicity of functionalized nanodiamond in Xenopus embryos. J. Mater. Chem. *20*, 8064.

Marcon, L., Kherrouche, Z., Lyskawa, J., Fournier, D., Tulasne, D., Woisel, P., and Boukherroub, R. (2011). Preparation and characterization of Zonyl-coated nanodiamonds with antifouling properties. Chem. Commun. *47*, 5178.

McGuinness, L.P., Yan, Y., Stacey, A., Simpson, D.A., Hall, L.T., Maclaurin, D., Prawer, S., Mulvaney, P., Wrachtrup, J., Caruso, F., et al. (2011). Quantum measurement and orientation tracking of fluorescent nanodiamonds inside living cells. Nat. Nanotechnol. *6*, 358–363.

Mochalin, V.N., Shenderova, O., Ho, D., and Gogotsi, Y. (2012). The properties and applications of nanodiamonds. Nat. Nanotechnol. *7*, 11–23.

Mohan, N., Chen, C.-S., Hsieh, H.-H., Wu, Y.-C., and Chang, H.-C. (2010). In Vivo Imaging and Toxicity Assessments of Fluorescent Nanodiamonds in Caenorhabditis elegans. Nano Lett. *10*, 3692–3699.

Moore, L., Chow, E.K.-H., Osawa, E., Bishop, J.M., and Ho, D. (2013). Diamond-Lipid Hybrids Enhance Chemotherapeutic Tolerance and Mediate Tumor Regression. Adv. Mater. *25*, 3532–3541.

Neburkova, J., Vavra, J., and Cigler, P. (2017). Coating nanodiamonds with biocompatible shells for applications in biology and medicine. Curr. Opin. Solid State Mater. Sci. *21*, 43–53.

Neburkova, J., Sedlak, F., Zackova Suchanova, J., Kostka, L., Sacha, P., Subr, V., Etrych, T., Simon, P., Barinkova, J., Krystufek, R., et al. (2018). Inhibitor–GCPII Interaction: Selective and Robust System for Targeting Cancer Cells with Structurally Diverse Nanoparticles. Mol. Pharm.

Netz, R.R., and Andelman, D. (2003). Neutral and charged polymers at interfaces. Phys. Rep. *380*, 1–95.

Neuhaus, B., Tosun, B., Rotan, O., Frede, A., M. Westendorf, A., and Epple, M. (2016). Nanoparticles as transfection agents: a comprehensive study with ten different cell lines. RSC Adv. *6*, 18102–18112.

Nguyen, T.-T.-B., Chang, H.-C., and Wu, V.W.-K. (2007). Adsorption and hydrolytic activity of lysozyme on diamond nanocrystallites. Diam. Relat. Mater. *16*, 872–876.

Osswald, S., Yushin, G., Mochalin, V., Kucheyev, S.O., and Gogotsi, Y. (2006). Control of sp^2/sp^3 Carbon Ratio and Surface Chemistry of Nanodiamond Powders by Selective Oxidation in Air. J. Am. Chem. Soc. *128*, 11635–11642.

Petrakova, V., Nesladek, M., Taylor, A., Fendrych, F., Cigler, P., Ledvina, M., Vacik, J., Stursa, J., and Kucka, J. (2011). Luminescence properties of engineered nitrogen vacancy centers in a close surface proximity. Phys. Status Solidi A *208*, 2051–2056.

Petrakova, V., Rehor, I., Stursa, J., Ledvina, M., Nesladek, M., and Cigler, P. (2015). Charge-sensitive fluorescent nanosensors created from nanodiamonds. Nanoscale *7*, 12307–12311.

Petrakova, V., Benson, V., Buncek, M., Fiserova, A., Ledvina, M., Stursa, J., Cigler, P., and Nesladek, M. (2016). Imaging of transfection and intracellular release of intact, non-labeled DNA using fluorescent nanodiamonds. Nanoscale *8*, 12002–12012.

Prokop, A., and Davidson, J.M. (2008). Nanovehicular intracellular delivery systems. J. Pharm. Sci. *97*, 3518–3590.

Rammohan, N., MacRenaris, K.W., Moore, L.K., Parigi, G., Mastarone, D.J., Manus, L.M., Lilley, L.M., Preslar, A.T., Waters, E.A., Filicko, A., et al. (2016). Nanodiamond–Gadolinium(III) Aggregates for Tracking Cancer Growth In Vivo at High Field. Nano Lett. *16*, 7551–7564.

Rehor, I., Slegerova, J., Kucka, J., Proks, V., Petrakova, V., Adam, M.-P., Treussart, F., Turner, S., Bals, S., Sacha, P., et al. (2014a). Fluorescent Nanodiamonds Embedded in Biocompatible Translucent Shells. Small *10*, 1106–1115.

Rehor, I., Mackova, H., Filippov, S.K., Kucka, J., Proks, V., Slegerova, J., Turner, S., Van Tendeloo, G., Ledvina, M., Hruby, M., et al. (2014b). Fluorescent Nanodiamonds with Bioorthogonally Reactive Protein-Resistant Polymeric Coatings. ChemPlusChem *79*, 21–24.

Rehor, I., Lee, K.L., Chen, K., Hajek, M., Havlik, J., Lokajova, J., Masat, M., Slegerova, J., Shukla, S., Heidari, H., et al. (2015). Plasmonic Nanodiamonds: Targeted Core-Shell Type Nanoparticles for Cancer Cell Thermoablation. Adv. Healthc. Mater. *4*, 460–468.

Rehor, I., Slegerova, J., Havlik, J., Raabova, H., Hyvl, J., Muchova, E., and Cigler, P. (2016). Nanodiamonds: Behavior in Biological Systems and Emerging Bioapplications. In Carbon Nanomaterials for Biomedical Applications, M. Zhang, R.R. Naik, and L. Dai, eds. (Cham: Springer International Publishing), pp. 319–361.

Rendler, T., Neburkova, J., Zemek, O., Kotek, J., Zappe, A., Chu, Z., Cigler, P., and Wrachtrup, J. (2017). Optical imaging of localized chemical events using programmable diamond quantum nanosensors. Nat. Commun. *8*, 14701.

Schirhagl, R., Chang, K., Loretz, M., and Degen, C.L. (2014). Nitrogen-Vacancy Centers in Diamond: Nanoscale Sensors for Physics and Biology. Annu. Rev. Phys. Chem. *65*, 83–105.

Slegerova, J., Hajek, M., Rehor, I., Sedlak, F., Stursa, J., Hruby, M., and Cigler, P. (2015). Designing the nanobiointerface of fluorescent nanodiamonds: highly selective targeting of glioma cancer cells. Nanoscale *7*, 415–420.

Sotoma, S., Epperla, C.P., and Chang, H.-C. (2018). Diamond Nanothermometry. ChemNanoMat *4*, 15–27.

Vaijayanthimala, V., Tzeng, Y.-K., Chang, H.-C., and Li, C.-L. (2009). The biocompatibility of fluorescent nanodiamonds and their mechanism of cellular uptake. Nanotechnology *20*, 425103.

Vaijayanthimala, V., Cheng, P.-Y., Yeh, S.-H., Liu, K.-K., Hsiao, C.-H., Chao, J.-I., and Chang, H.-C. (2012). The long-term stability and biocompatibility of fluorescent nanodiamond as an in vivo contrast agent. Biomaterials *33*, 7794–7802.

Wang, D., Li, Y., Tian, Z., Cao, R., and Yang, B. (2014). Transferrin-conjugated nanodiamond as an intracellular transporter of chemotherapeutic drug and targeting therapy for cancer cells. Ther. Deliv. *5*, 511–524.

Wang, Z., Tian, Z., Dong, Y., Li, L., Tian, L., Li, Y., and Yang, B. (2015). Nanodiamond-conjugated transferrin as chemotherapeutic drug delivery. Diam. Relat. Mater. *58*, 84–93.

Wei, L., Zhang, W., Lu, H., and Yang, P. (2010). Immobilization of enzyme on detonation nanodiamond for highly efficient proteolysis. Talanta *80*, 1298–1304.

Weng, M.-F., Chiang, S.-Y., Wang, N.-S., and Niu, H. (2009). Fluorescent nanodiamonds for specifically targeted bioimaging: Application to the interaction of transferrin with transferrin receptor. Diam. Relat. Mater. *18*, 587–591.

Weng, M.-F., Chang, B.-J., Chiang, S.-Y., Wang, N.-S., and Niu, H. (2012). Cellular uptake and phototoxicity of surface-modified fluorescent nanodiamonds. Diam. Relat. Mater. *22*, 96–104.

Wicki, A., Witzigmann, D., Balasubramanian, V., and Huwyler, J. (2015). Nanomedicine in cancer therapy: Challenges, opportunities, and clinical applications. J. Controlled Release *200*, 138–157.

Williams, D.F. (2008). On the mechanisms of biocompatibility. Biomaterials *29*, 2941–2953.

Wu, Y., Ermakova, A., Liu, W., Pramanik, G., Vu, T.M., Kurz, A., McGuinness, L., Naydenov, B., Hafner, S., Reuter, R., et al. (2015). Programmable Biopolymers for Advancing Biomedical Applications of Fluorescent Nanodiamonds. Adv. Funct. Mater. *25*, 6576–6585.

Yuan, Y., Chen, Y., Liu, J.-H., Wang, H., and Liu, Y. (2009). Biodistribution and fate of nanodiamonds in vivo. Diam. Relat. Mater. *18*, 95–100.

Zackova Suchanova, J., Neburkova, J., Spanielova, H., Forstova, J., and Cigler, P. (2017). Retargeting Polyomavirus-Like Particles to Cancer Cells by Chemical Modification of Capsid Surface. Bioconjug. Chem. *28*, 307–313.

Zhang, B., Li, Y., Fang, C.-Y., Chang, C.-C., Chen, C.-S., Chen, Y.-Y., and Chang, H.-C. (2009a). Receptor-Mediated Cellular Uptake of Folate-Conjugated Fluorescent Nanodiamonds: A Combined Ensemble and Single-Particle Study. Small *5*, 2716–2721.

Zhang, P., Yang, J., Li, W., Wang, W., Liu, C., Griffith, M., and Liu, W. (2011a). Cationic polymer brush grafted-nanodiamond via atom transfer radical polymerization for enhanced gene delivery and bioimaging. J. Mater. Chem. *21*, 7755.

Zhang, T., Cui, H., Fang, C.-Y., Cheng, K., Yang, X., Chang, H.-C., and Forrest, M.L. (2015). Targeted nanodiamonds as phenotype-specific photoacoustic contrast agents for breast cancer. Nanomed. *10*, 573–587.

Zhang, X.-Q., Chen, M., Lam, R., Xu, X., Osawa, E., and Ho, D. (2009b). Polymer-Functionalized Nanodiamond Platforms as Vehicles for Gene Delivery. Acs Nano *3*, 2609–2616.

Zhang, X.-Q., Lam, R., Xu, X., Chow, E.K., Kim, H.-J., and Ho, D. (2011b). Multimodal Nanodiamond Drug Delivery Carriers for Selective Targeting, Imaging, and Enhanced Chemotherapeutic Efficacy. Adv. Mater. *23*, 4770–4775.

Zhao, B., and Brittain, W.J. (2000). Polymer brushes: surface-immobilized macromolecules. Prog. Polym. Sci. *25*, 677–710.

Zhao, L., Takimoto, T., Ito, M., Kitagawa, N., Kimura, T., and Komatsu, N. (2011). Chromatographic Separation of Highly Soluble Diamond Nanoparticles Prepared by Polyglycerol Grafting. Angew. Chem. Int. Ed. *50*, 1388–1392.

Zhao, L., Nakae, Y., Qin, H., Ito, T., Kimura, T., Kojima, H., Chan, L., and Komatsu, N. (2014a). Polyglycerol-functionalized nanodiamond as a platform for gene delivery: Derivatization, characterization, and hybridization with DNA. Beilstein J. Org. Chem. *10*, 707–713.

Zhao, L., Xu, Y.-H., Qin, H., Abe, S., Akasaka, T., Chano, T., Watari, F., Kimura, T., Komatsu, N., and Chen, X. (2014b). Platinum on Nanodiamond: A Promising Prodrug Conjugated with Stealth Polyglycerol, Targeting Peptide and Acid-Responsive Antitumor Drug. Adv. Funct. Mater. *24*, 5348–5357.

Zhao, L., Xu, Y.-H., Akasaka, T., Abe, S., Komatsu, N., Watari, F., and Chen, X. (2014c). Polyglycerol-coated nanodiamond as a macrophage-evading platform for selective drug delivery in cancer cells. Biomaterials *35*, 5393–5406.

10. APPENDICES

Ivan Rehor, Karin L. Lee, Kevin Chen, Miroslav Hajek, Jan Havlik, Jana Lokajova, Milan Masat, **Jitka Slegerova**, Sourabh Shukla, Hamed Heidari, Sara Bals, Nicole F. Steinmetz, Petr Cigler: Plasmonic nanodiamonds: targeted core-shell type NPs for cancer cell thermoablation, Advanced Healthcare Materials, *4*, 460, **2015**.

Torsten Rendler, **Jitka Neburkova**, Ondrej Zemek, Jan Kotek, Andrea Zappe, Zhiqin Chu, Petr Cigler, Joerg Wrachtrup: Optical imaging of localized chemical events using programmable diamond quantum nanosensors, Nature Communications *8*, 14701, **2017**.

Appendix A – Publication 1

Ivan Rehor, **Jitka Slegerova**, Jan Kucka, Vladimir Proks, Vladimira Petrakova, Marie-Pierre Adam, François Treussart, Stuart Turner, Sara Bals, Miroslav Ledvina, Amy M. Wen, Nicole F. Steinmetz, Petr Cigler: Fluorescent Nanodiamonds Embedded in Biocompatible Translucent Shells, Small, *10*, 1029, **2014**.

Fluorescent Nanodiamonds Embedded in Biocompatible Translucent Shells

*Ivan Rehor, Jitka Slegerova, Jan Kucka, Vladimir Proks, Vladimira Petrakova, Marie-Pierre Adam, François Treussart, Stuart Turner, Sara Bals, Pavel Sacha, Miroslav Ledvina, Amy M. Wen, Nicole F. Steinmetz, and Petr Cigler**

High pressure high temperature (HPHT) nanodiamonds (NDs) represent extremely promising materials for construction of fluorescent nanoprobes and nanosensors. However, some properties of bare NDs limit their direct use in these applications: they precipitate in biological solutions, only a limited set of bio-orthogonal conjugation techniques is available and the accessible material is greatly polydisperse in shape. In this work, we encapsulate bright 30-nm fluorescent nanodiamonds (FNDs) in 10–20-nm thick translucent (i.e., not altering FND fluorescence) silica shells, yielding monodisperse near-spherical particles of mean diameter 66 nm. High yield modification of the shells with PEG chains stabilizes the particles in ionic solutions, making them applicable in biological environments. We further modify the opposite ends of PEG chains with fluorescent dyes or vectoring peptide using click chemistry. High conversion of this bio-orthogonal coupling yielded circa 2000 dye or peptide molecules on a single FND. We demonstrate the superior properties of these particles by in vitro interaction with human prostate cancer cells: while bare nanodiamonds strongly aggregate in the buffer and adsorb onto the cell membrane, the shell encapsulated NDs do not adsorb nonspecifically and they penetrate inside the cells.

Dr. I. Rehor, J. Slegerova, Dr. P. Sacha, Dr. M. Ledvina, Dr. P. Cigler
Institute of Organic Chemistry and Biochemistry
AS CR, v.v.i. Flemingovo nam. 2, Prague 6, 166 10, Czech Republic
Fax: (+)420–220—183–578
E-mail: cigler@uochb.cas

Dr. J. Kucka, Dr. V. Proks
Institute of Macromolecular Chemistry AS CR
v.v.i. Heyrovského nám. 2, Prague 6, 162 06, Czech Republic

Dr. J. Kucka
Nuclear Physics Institute AS CR, v.v.i. Rez near Prague,
250 68, Czech Republic

Dr. V. Petrakova
Faculty of Biomedical Engineering
Czech Technical University in Prague
Sítná sq. 3105, 272 01 Kladno (Czech Republic) and Institute
of Physics AS CR, v.v.i, Prague 8, Czech Republic

M.-P. Adam, Prof. F. Treussart
Laboratoire de Photonique Quantique et Moléculaire
UMR 8537 CNRS and ENS Cachan
F-94235 Cachan (France), Laboratoire Aimé Cotton
CNRS, Université Paris Sud and ENS Cachan,
F-91405, Orsay, France

Dr. S. Turner, Prof. S. Bals
EMAT, University of Antwerp
Groenenborgerlaan 171, B-2020, Antwerp, Belgium

A. M. Wen, Prof. N. F. Steinmetz
Department of Biomedical Engineering
Case Western Reserve University
School of Medicine and Engineering
10990 Euclid Avenue, Cleveland, Ohio, USA

DOI: 10.1002/smll.201302336

small NANO MICRO

1. Introduction

Fluorescent nanodiamonds (FNDs) are a recently introduced class of biocompatible[1–6] luminescent probes.[7–10] Their exceptional optical properties for bioimaging are facilitated by the presence of nitrogen-vacancy centers, NV, which are localized defects of the diamond crystalline lattice.[11,12] The NV center is extremely photostable, showing no photobleaching or photoblinking. Upon excitation by green light (typically 532 nm wavelength laser), NV center emits in red to near infrared part of spectrum (emission maximum ~700 nm for the negatively charged NV^- center[12]) with high quantum efficiency (up to 90% in nanodiamond).[13] Its fluorescence therefore falls into the so-called tissue absorption window and is well-separated from cell or tissue autofluorescence.[14] FNDs were successfully used as fluorescent probes[15–18] and sensors[19,20] in vitro, allowing for single particle tracking inside cell.[21] They were also successfully visualized and tracked in small mammals.[2] Unique electron structure of NV center allows for selective turn-off of its emission by external electromagnetic field.[19,22,23] This property was successfully used for background-free imaging of nanodiamonds.[24,25]

Fluorescence lifetime of NV center (>10 ns) is substantionally longer than lifetime of autofluorescence (<4 ns). Therefore use of time-gated techniques like fluorescence lifetime imaging microscopy (FLIM) is also a way to suppress background signal, as shown for cells in culture[18] and recently demonstrated in vivo.[26]

In vivo long term cell tracking is an essential method in cell-based therapies such as adoptive immunotherapy and stem-cell therapy.[27,28] The biocompatibility of FNDs, their absolute optical stability and ability to observe them in vivo makes them an ideal candidate for in vivo long term tracking of stem cells, as was recently demonstrated.[29]

Although unmodified FNDs have been demonstrated as biocompatible nanoparticles,[1,3,4,17,30] a better control of nanodiamond properties is crucial for development of highly sophisticated probes enabling, for example, construction of multimodal nanoprobes or stealth[31] FNDs, which are able to target selectively cancer cells and tumors in vivo. Among the key issues of FND are still limited options for their bioorthogonal modifications by biomolecules, their colloidal behavior in buffers and biological media as well as a control of their size and shape. Overcoming these issues is essential for construction of advanced bioprobes.

We focused on optimizing properties of the brightest available FNDs that can be prepared from high-pressure high-temperature (HPHT) type nanodiamonds (NDs).[18,32–34] Although chemical modifications on the surface of detonation NDs is well described and many approaches for introduction of various functionalities were described,[35–38] the situation with HPHT NDs is more complicated due to their lower reactivity and surface/volume ratio. Direct covalent attachment of (bio)molecules to HPHT NDs surface is performed typically via amide bonds,[39] adsorption of proteins[2,40–42] or functionalization of artificially created surface graphene structures.[43] Because these conjugation reactions are rather nonspecific, the attention is currently paid onto sophisticated organic systems enabling selective, bioorthogonal bond formation.[44]

As typical colloidal dispersions, unmodified NDs in solution lose their colloidal stability at higher ionic strength and aggregate.[44,45] This behavior presents a serious disadvantage for direct biological application, as all biological liquids or cultivation media contain high concentrations of salts. Salt-caused aggregation could be overcome by chemical modification of the ND surface[46] or by attachment of hydrophilic polymers[47–50] or proteins[2,40–42] to the ND surface.

Strikingly, in contrast to many kinds of nanoparticles that can now be controllably engineered with well-defined geometric and chemical properties,[51,52] the control of HPHT ND shape is still in beginning. The available materials consist of heterogeneous nanoparticles of very irregular shape[21] bearing sharp edges and spiky vertexes (**Figure 1**A).

In a majority of publications the NDs are considered biocompatible and no toxicity was observed in cell

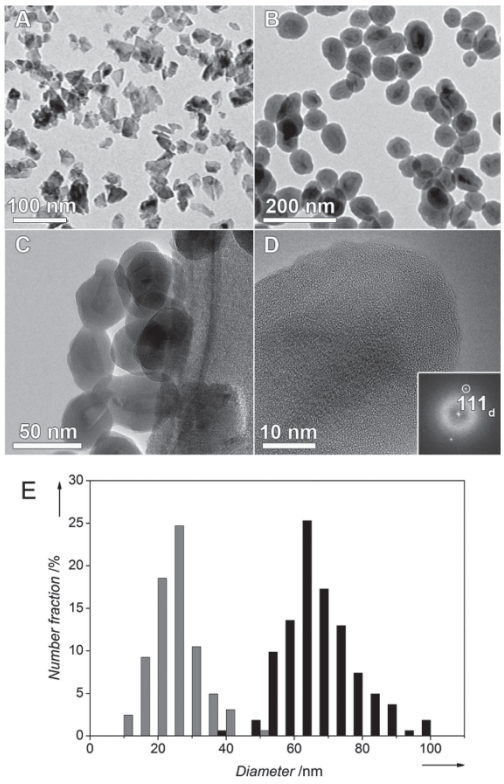

Figure 1. BF-TEM images of non-coated **ND1** (A) and aminosilica-coated **ND3** (B) particles. Several coated **ND3** particles are shown at higher magnification in (C). (D) High resolution TEM image showing the uniform silane surface coating. The crystallinity of the diamond core is evidenced by the presence of 111 diamond lattice planes, indexed in the Fourier Transform inset. (E) Histograms from image analysis of TEM micrographs of non-coated **ND1** (gray) and aminosilica-coated **ND3** (black) particles.

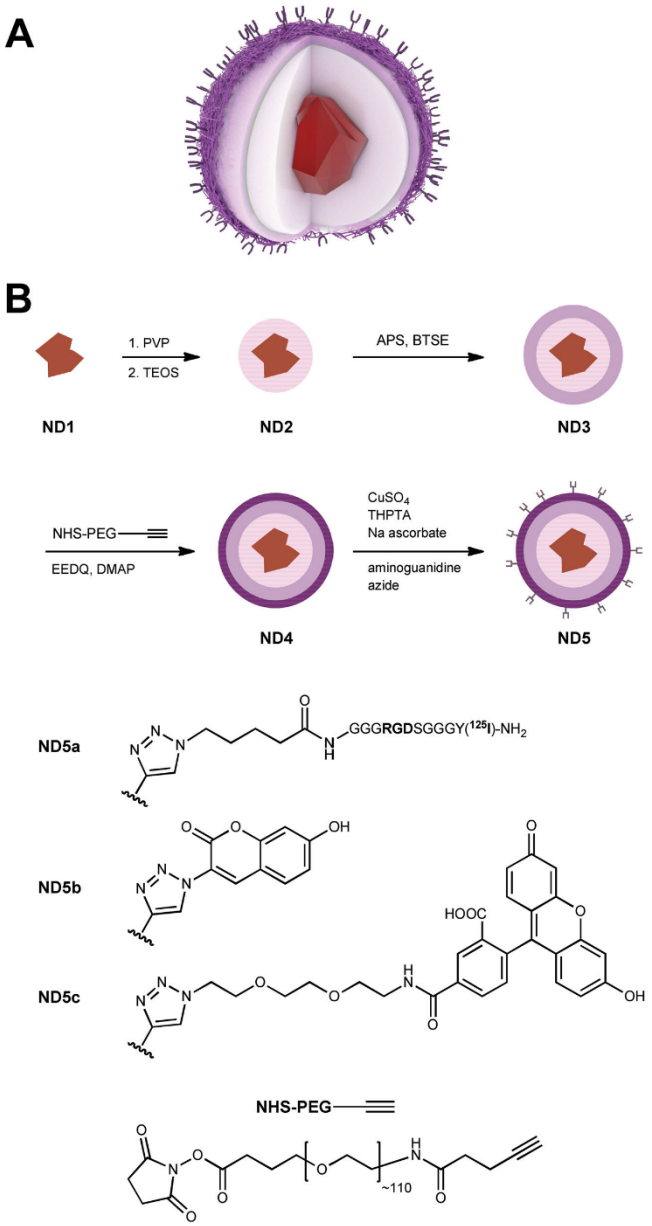

Scheme 1. The schematic structure (A) and preparation (B) of the particles. The fluorescent diamond nanocrystal is consecutively coated by silica shell (pink), thin crosslinked aminopropyl-silica shell (violet), and PEG-alkyne layer (dark violet). Azide-labeled ^{125}I-RGDS peptide (**ND5a**), coumarin (**ND5b**), and fluorescein (**ND5c**) moieties are attached. TEOS – tetraethoxysilane, BTSE – 1,2-bis(triethoxysilyl)ethane, APS – (3-aminopropyl)triethoxysilane, PVP – polyvinypyrrolidone, EEDQ – 2-ethoxy-1-ethoxycarbonyl-1,2-dihydroquinoline, DMAP – dimethylaminopyridine.

studies[1-5,17,18,53] nor in animal models experiments[2,54–56] (for a review see ref. [4]). However, several recent works document toxic effects of NDs in vitro[57,58] as well as in vivo,[59] indicating that their biocompatibility should not be overgeneralized. Generally, a nanoparticle's biological response strongly depends on its size and shape (for a review see refs. [31,60]) The shift from spherical to non-spherical shapes can significantly affect the behavior of a nanoparticle in biological environment[61] During finishing of this article three pioneering works dealing with the spiky ND shape appeared.[62–64] Among others it has been demonstrated that coating by silica shell can transform NDs to pseudo-spherical particles of improved shape homogeneity.[63,64]

Here we introduce a composite surface architecture on bright HPHT FNDs enabling selective bioorthogonal attachment of various (bio)molecules by click chemistry. The architecture comprises silica shell, which normalizes the spiky ND shape into pseudo-spherical. The silica surface allows simple modification with polyethyleneglycol (PEG) chains, responsible for colloidal stability of particles in buffers. The PEG chains can be further modified with a molecule of choice using click reaction. Obtained particles are fairly monodisperse in shape and colloidaly stable in ionic buffers. Noteworthy, the surface architecture has no adverse effects on the unique fluorescence of NV centers. Comparing to non-coated NDs, we demonstrate superior behavior of coated NDs in in vitro tissue culture; their application for prostate cancer cell labeling and imaging is shown.

2. Results and Discussion

2.1. Preparation and Structure of the Shell-Coated NDs

The architecture is designed from two covalently connected layers surrounding the ND particle: i) a solid crosslinked silica shell[65] bearing ii) a flexible polyethylene glycol (PEG) layer (**Scheme 1A**). The particle is therefore exposed to solution by a polymeric interface that protects it from electrolyte-induced precipitation. At the same time we took advantage of PEG heterofunctionality and we decorated the

NANO MICRO small

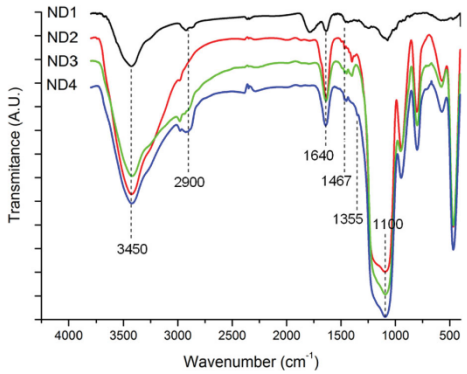

Figure 2. Normalized IR spectra of noncoated (**ND1**), silica-coated (**ND2**), aminosilica-coated (**ND3**), and PEGylated aminosilica-coated (**ND4**) fluorescent nanodiamonds. For clarity, spectra are shifted along the y-axis.

opposite ends of polymer chains by alkyne moieties enabling the use of click chemistry.[66]

The silica shell can be grown by controlled hydrolysis of tetraalkoxysilylesters or substituted trialkoxyalkylsilylesters,[67] in which the alkyl group allows further surface modification. The presence of the alkyl group, on the other hand, weakens the compactness of the shell, making it hydrolytically labile and also colloidally unstable in aqueous media.[68] To avoid hydrolytic lability, we used a crosslinking agent, bis(triethoxysilyl)ethane (BTSE), that improves the shell's resistance to hydrolysis[69] (Scheme 1B). First, the TEOS-based shell was formed (**ND2**), followed by growth of a crosslinked amino-functionalized layer from a mixture of APS and BTSE (**ND3**). Notably, this procedure enabled direct functionalization of nanodiamond by silane-based moieties without any reductive pretreatment that is an essential step in anhydrous silylation procedure introduced by Krueger and collaborators.[36] Amino-modified silica surface was used for attachment of the heterobifunctional PEG chain bearing *N*-hydroxysuccinimidyl group at one end of the chain and alkyne moiety at the other. *N*-hydroxysuccinimidyl group served for formation of an amidic anchor, whereas the alkyne moiety was used for attachment of various molecules to the particle by click chemistry in the next reaction step.

The composition of the shell was confirmed by IR spectroscopy indicating the presence of both Si-O bands and characteristic diamond bands (**Figure 2**). The characteristic peaks present in all silica-coated samples at about 1110 cm^{-1} correspond to the asymmetric stretching vibrations of the Si–O–Si from silica shells. The peaks at about 1640 cm^{-1} and 3450 cm^{-1} also indicate the formation of silica coating on the surface, corresponding to silanol groups (Si–OH) as well as to OH groups from nanodiamond and residual water. Bands at 2900, 1467, and 1355 cm^{-1} are characteristic for PEG.

The bright field transmission electron microscopy (BF-TEM) images in Figure 1 show NDs before and after encapsulation. The diamond particles themselves (**ND1**, Figure 1A) are of irregular shape (circularity ~0.67), with

Table 1. Elemental composition of FND bearing different surface architectures.

	% C	% H	% N
ND1	93.7	0.38	0.06
ND2	19.6	1.28	0.29
ND3	19.8	1.90	1.10
ND4	21.5	2.07	0.66

sharp edges and often elongated in one dimension (needle–like). Their diameter (expressed as average circular equivalent diameter – see Supporting information) is 27 ± 7 nm. After coating (Figure 1B-D), the particles become more spherical (circularity ~0.87), and their diameter rises to 66 ± 10 nm (Figure 1E). Notably, spherical shape of nanoparticles is generally considered as the proper, biocompatible geometry for bio-applications.[61,70]

The optimal size of nanoparticular biolabels is considered to be between 10 and 100 nm, depending on specific application.[31] Both original and coated particles fall into this size range. The total mass of the sample rises approximately 4-fold upon encapsulation, which corresponds to the data from elemental analysis (**Table 1**). The thickness of the shell can be varied by changing the amounts of silylesters during encapsulation. Indeed, the thinner shell leads to smaller particles, however, their shape is more distant from spherical (Figure S1 in Supporting information).

In order to confirm the presence of the various coatings on **ND4** directly, we performed spatially resolved electron energy-loss spectroscopy (EELS) measurements using the spectrum imaging technique in STEM mode[71] (**Figure 3**). The acquired EELS data were used to generate an element-specific map for silicon and element- and bond-specific maps for amorphous carbon and diamond. The diamond map in Figure 3C confirms the size and irregular shape of the diamond core. The Si map shows the ~10–20 nm thick silica shell surrounding the diamond core. Some amorphous carbon is measured at the surface of the diamond core in the amorphous carbon map, which is to be expected in most ND samples.[72] The predominant amorphous carbon signal, however, arises from the thin layer of PEG at the surface of the silica coating.

2.2. Stability Studies and Chemical Modifications

Because low colloidal stability of nanoparticles in buffers and biological liquids is a typical limitation for their applications in biodisciplines, we tested the stabilization effects of this PEG layer on the particles. The difference between **ND1** and **ND4** particles after dissolving in PBS buffer is clearly observable with the naked eye (**Figure 4**). Aggregation of colloidal aqueous solutions of **ND4** at various pH and ionic strength were further monitored using dynamic light scattering (Figure S2 in Supporting Information). The particles were colloidally stable (i.e., their hydrodynamic diameter remained unchanged within the experimental error) across a wide working pH range (2–10) and extreme ionic strength (1 M NaCl). After one week a precipitation was observable

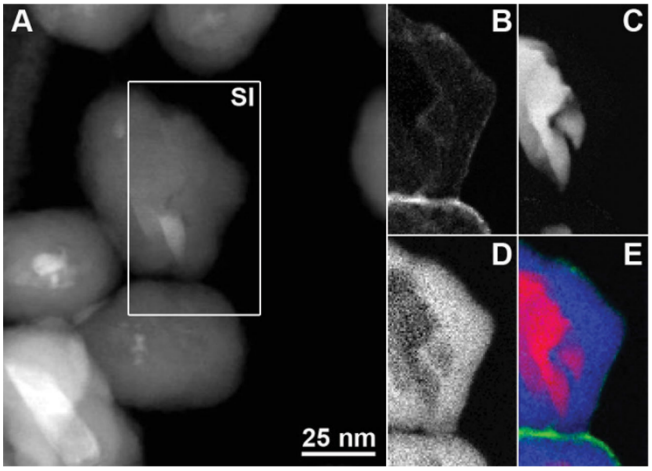

Figure 3. STEM-EELS analysis of PEGylated aminosilica-coated **ND4** nanoparticles. (A) Annular dark field STEM image with the 72*129 pixel spectrum image (SI) region indicated by the white rectangle. (B-E) STEM-EELS maps for (B) amorphous carbon, (C) diamond, (D) silicon, and (E) a color map showing diamond (red), silicon (blue), and amorphous carbon (green).

in the alkaline solution (pH = 10) only, while the other alternatives were stable at least for two weeks. Furthermore, particles exhibited long term (at least 1 month) stability in PBS and tissue culture media, which is essential for their use in bioapplications.

The function of the mid-size (5000 Da) heterobifunctional PEG in the surface architecture is not only a colloidal protection: its terminal alkyne group exposed to the solution is available for selective attachment of various (bio) molecules via click chemistry. In order to demonstrate the applicability of particles as a modular platform for construction of different probes, three selected azide-modified molecules were attached to the **ND4** particles: ^{125}I-labeled RGDS peptide[73,74] (**ND5a**), coumarin[75] (**ND5b**), and fluorescein[76] (**ND5c**) (for structures see Scheme 1B).

The RGDS peptide exhibits targeting properties towards tumor cells and here served as a model structure for our future studies. Its radiolabeling[73] enabled highly sensitive monitoring of conjugation yield by radioactivity measurements. The consecutive post-reaction washing steps (Figure S3 in Supporting information) revealed that only a small amount of peptide can be released after the excess from reaction has been washed away. The total load of peptide estimated from radioactive measurements was 8 μmol g^{-1}. To confirm that the peptide is bound selectively by click chemistry and not only adsorbed to the particle surface, a control reaction without Cu^{I} catalyst was performed. The total amount of peptide attached in control was only ~4% of the load reached by reaction in the presence of Cu^{I} catalyst. The vast majority of RGDS attached by reaction in presence of catalyst was therefore covalently bound to the PEG chains, and only a very small fraction of physisorbed peptide remained on the particles after post-reaction washings. Because presence of hydrophobic RGDS peptide on a nanoparticle can lead to its aggregation, we tested also the long-term colloidal stability of conjugate **ND5a** in PBS buffer using DLS. The colloidal behavior introduced already by PEG layer was preserved even after attachment of the peptide: the particles remained stable for at least one month.

To directly confirm the covalent grafting mechanism, the fluorogenic probe coumarin azide[75] was attached to the particles, providing **ND5b**. The dye itself is non-fluorescent, but a highly fluorescent structure is formed upon cycloaddition to an alkyne. Compared with the control sample reacted in the absence of Cu^{I}, the reaction of coumarin azide with the particles in the presence of Cu^{I} catalyst produced a characteristic bright fluorescent product (Figure S4 in Supporting information).

Figure 4. Photography of **ND1** and **ND4** dispersions (0.5 mg mL^{-1}) in PBS, 30 min after mixing. **ND1** (left) precipitates and finally gives sediment at the bottom of the tube, while **ND4** (right) remains in the form of stable colloid scattering the laser beam (red laser pointer).

2.3. Spectroscopic Characterization

Modification of FND surface chemistry has been shown to produce changes in NV centers charge state which is strongly reflected in fluorescence spectra.[77] To evaluate the possible influence of the silica shell on FND fluorescence, we measured the photoluminescence spectra for **ND1** and **ND4** (**Figure 5**). The normalization to the diamond Raman signal enabled us to compare the relative change in fluorescence caused by formation of the shell. The spectra show that the shell behaves as an inert translucent layer: its presence has no significant influence on the fluorescence and the spectrum retains its intensity and characteristic shape.

For detailed understanding of the conjugation process and quality of the resulting conjugate we aimed to measure the fraction of FNDs that are not properly modified by either silica shell or PEG-alkyne and therefore cannot be further modified by click reaction. Using total internal reflection fluorescence microscopy (TIRF) we characterized conjugate

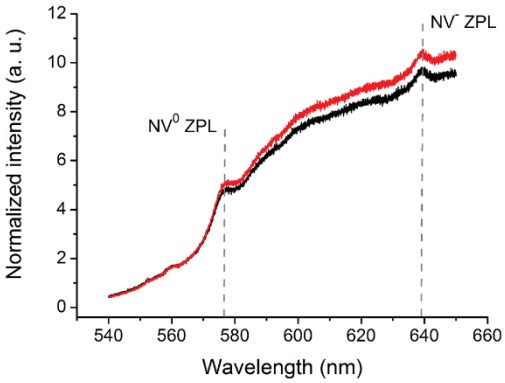

Figure 5. Normalized photoluminescence spectra of non-coated (**ND1**, black) and PEGylated silica-coated (**ND4**, red) FNDs. For comparison of relative change in fluorescence caused by formation of the shell the spectra were normalized to the diamond Raman signal. The relative difference in photoluminescence intensity is within the standard deviation of the measured data. Each spectrum shows an average of 50 normalized measurements. The standard deviation was 8.9% for **ND1** and 9.4% for **ND4**. ZPL – zero phonon line.

ND5c bearing a secondary fluorescent probe, fluorescein,[76] at the single particle level. From 5 measurements, we counted 400 red spots that colocalize with green ones, and only 20 that do not colocalize (Figure S6 in Supporting information). This result confirmed us that the vast majority (>95%) of the FNDs are properly modified and the reaction procedure, although performed in very diluted solutions (240 µM fluorescein-azide), is robust enough to provide high yield conjugation (for experimental details and further discussion see Figures S5-S7 in Supporting information). It should be noted, that the total load of fluorescein on particles was 9 µmol g^{-1} of NDs (estimated by UV-Vis spectroscopy) which is in agreement with conjugation yields of RGDS peptide (8 µmol g^{-1}, see above). Because the loads of both molecules obtained by different methods (scintigraphy and UV-Vis spectroscopy, respectively) are in excellent agreement despite the different character of the molecules, this load represents apparently an upper limit for covalent attachment of molecules to the particles. The quantities can be recalculated, using simple spherical model, giving a number of approximately 2000 molecules attached to a single nanoparticle. This quantity is sufficient not only for targeting of a probe, but also for applications more demanding on a cargo payload, like MR imaging contrast agents or drug delivery systems.

2.4. Imaging of Coated NDs in Cells

We examined the differences between **ND1** and **ND4** particles in interaction with human prostate cancer cells. The unmodified, "naked" nanoparticles have due to high free energy to the environment a much greater nonspecific affinity for the cell surface than particles modified by proteins[78] or sterically protecting polymers. Using in vitro tissue culture experiments, we examined whether the shell structure on **ND4** is able to compensate this effect compared to "naked" **ND1**. For this experiment we choose serum-free PBS buffer, a well-defined medium enabling control and analysis of binding events on cells.[79] We dispersed both **ND1** and **ND4** particles in PBS buffer and exposed cells for one hour to this solution. After washing the cells with ND-free PBS buffer we observed the cellular localization of the particles using confocal microscopy (**Figure 6**). While the **ND4** were found internalized inside prostate cancer cells (LNCaP cell line), the **ND1** were mostly adhered on the cell membrane. This difference may be explained by the observation that **ND1** are strongly aggregating and subsequently precipitating in PBS buffer (Figure 4), while the **ND4** are colloidaly stable under these conditions (see above). We hypothesized that the presence of large aggregates of **ND1** formed in the buffer promotes cell binding but prevents internalization, possibly because the larger aggregates are energetically not favored to be endocytosed.

To prevent the aggregation as well as decrease the free energy of particles we preincubated **ND1** in cell growth medium containing serum. Noncovalent adsorption of serum albumin has been already described as an option for stabilizing NDs in aqueous solutions.[21] We tested the aggregation state of **ND1** in cell media using DLS, which showed rapid formation of still ≈600 nm large aggregates. Due to serum

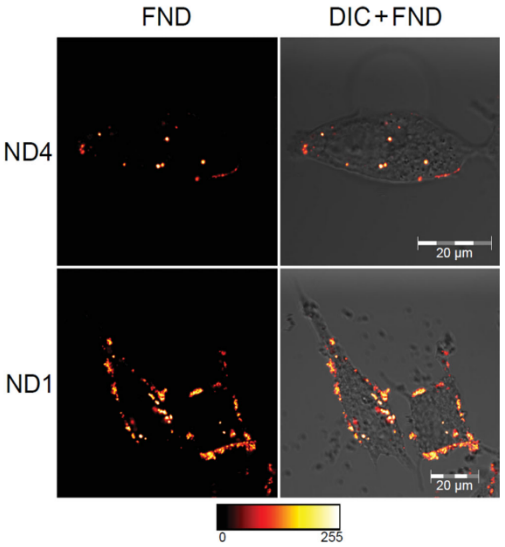

Figure 6. Confocal microscopy images of PEGylated aminosilica-coated (**ND4**) and noncoated (**ND1**) particles preincubated in PBS and internalized by LNCaP cells. The displayed images are fluorescence from NDs (FND) in false colours (left) and merged differential interference contrast (DIC) and FND fluorescence (right). FNDs were dispersed in PBS before adding to cells in medium (final concentration 200 µg ml^{-1}). Cells were washed by PBS after one hour incubation, incubated for subsequent 23 hours and observed after fixation. Fluorescence of FND was collected by Zeiss LSM 780 at 639–758 nm upon excitation at 532 nm. For full set of images see Figure S8 in the Supporting Information.

proteins stabilization the ND-serum complex did not further agglomerate or precipitate for several days (in contrast to **ND1** which precipitates in PBS in less than 30 minutes). In cell experiment, we indeed observed very similar behavior for both serum media treated **ND1** and **ND4** samples: the particles were internalized into cells without nonspecific cell membrane adhesion (Figure S8 in Supporting information). However, in case of **ND1** the cells were interacting with very different, 600 nm particles resulting from association of **ND1** nanoparticles in presence of serum proteins and ions from medium. In contrast, colloidal behavior of **ND4** was not influenced by any biologically relevant liquid used in study (see Figure S2) and particles we taken up in non-aggregated form.

From these studies, it is clear that the shell architecture, or more precisely its bionanointerface formed by hydrophillic PEG, prevents the nonspecific adsorption of particles to the cell membrane. This property is a key starting point for any study on cell recognition or targeting.

3. Conclusion

In summary, this study introduces hybrid near-spherical nanoparticles combining the advantages of fluorescence of NV color centers in NDs with a bio-orthogonally reactive translucent shell. We have demonstrated in bulk solution as well as at the single particle level that the surface architecture is not quenching or otherwise modifying the unique fluorescent properties of NV centers. The attachment of molecules or biomolecules can be performed selectively at high conversion efficiencies using click chemistry in aqueous buffers or biological media while keeping the excellent colloidal stability of the particles. Morever, the bionanointerface of particles prevents their nonspecific adhesion on cell membrane, as proven on human prostate cancer cells. Our design based on unique photophysical properties of non-photobleachable NV center in combination with silica coating can therefore serve as a versatile biocompatible platform, providing new directions for construction of various sophisticated imaging probes or targeted systems.[80]

4. Experimental Section

Chemicals and Solvents: Tetraethoxysilane (TEOS), 1,2-bis(triethoxysilyl)ethane (BTSE), (3-aminopropyl)triethoxysilane (APS), polyvinypyrrolidone MW = 10 000 g mol^{-1} (PVP), 2-ethoxy-1-ethoxycarbonyl-1,2-dihydroquinoline (EEDQ), and dimethylaminopyridine (DMAP) were purchased from Sigma-Aldrich. NHS-PEG(5000)-alkyne (Scheme 1B) was purchased from Iris Biotech. ^{125}I-labeled RGDS peptide azidopentanoyl-GGGRGDSGGGY(^{125}I)-NH_2,[73] coumarin-azide,[75] fluorescein-azide[76] (Scheme 1B), and THPTA ligand[66] were synthesized according to published procedures.

Infrared (IR) spectroscopy: IR spectra were recorded from 4000–400 cm^{-1} on a Bruker Equinox spectrometer using KBr pellets. The sample weight was 1.0 mg/pellet for all samples.

Raman Spectroscopy: Photoluminescence spectra were measured with a Renishaw InVia Raman Microscope at an excitation wavelength of 514 nm with 25 mW laser power. Spectra were recorded at room temperature and normalized to the diamond Raman peak (excitation at 488 nm). The measurements were performed on aqueous solutions (as received, 1:1, 1:2, 1:5, and 1:10 dilutions) in a Hellma fluorescence cuvette (type no. 105.252-QS). A set of 10 measurements was performed on each sample. All spectra were normalized to the diamond Raman peak.

Elemental Analysis: Elemental analysis was performed with a CHN PE 2400 Series automatic analyzer. Each sample was measured three times, and the results were averaged.

UV-Vis Spectroscopy: UV-Vis spectra were recorded with a Specord 210 (Analytik Jena) spectrometer in the 300–700 nm range at room temperature with an optical path of 1 cm.

Luminescence Spectroscopy: Luminescence measurements were performed on an Edinburgh Instruments FS900 spectrofluorimeter, equipped with a 450 W xenon arc lamp, a microsecond flash lamp, and a red-sensitive photomultiplier (300–850 nm).

Electron Microscopy: To prepare the samples, a drop of diluted colloidal solution was placed on a carbon-coated copper grid and left to dry. Bright field transmission electron microscopy (TEM) experiments presented in Figure 1A and S1 were performed using a JEOL JEM-1200EX electron microscope operated at 60 kV. All other TEM, high resolution TEM, STEM, and spatially-resolved EELS experiments were carried out on a FEI Titan 80–300 "cubed" microscope fitted with an aberration-corrector for the imaging lens and the probe forming lens and a GIF Quantum energy filter for spectroscopy, operated at 80 kV to minimize knock-on damage to the sample. STEM-EELS experiments were performed using a convergence semi-angle α of ~21 mrad and a collection semi-angle β of ~200 mrad, using a beam current of approximately 80 pA. A fine electron probe (diameter ~1.5 Å) was scanned over a region of the sample, acquiring an EELS spectrum at each point. All spectra were acquired at an energy dispersion of 0.4 eV per pixel and an energy resolution of approximately 1.2 eV. Chemical maps for the C signals (amorphous carbon and diamond) were generated by fitting the carbon K-edge to known references for diamond and amorphous carbon. The Si maps were generated by plotting the intensity under the background-subtracted Si $L_{2,3}$-edge in each pixel using a 22 eV broad energy window.

The size distributions of coated and noncoated particles in TEM microphotographs were calculated with ImageJ software, using more than 150 particles for each sample. Average particle sizes are expressed in the form of average circular equivalent diameter. It is defined as the diameter of a spherical particle that has the same area as the observed particle.

Dynamic Light Scattering (DLS): DLS was recorded with a Zetasizer Nano ZS system (Malvern Instruments) at room temperature. Sample concentrations were 0.05 mg/mL.

Radioactivity Measurements: Gamma emission of ^{125}I was measured with an ionization-chamber Bqmetr 4 applied activity indicator (Empos, Prague, Czech Republic). The concentrations of RGDS in samples were calculated from a measured activity of a sample and known activity per 1 mg of labeled RGDS.[73]

Total Internal Reflection Fluorescence (TIRF) Microscopy: The TIRF microscope is a home-made setup relying on a Zeiss Axiovert 35 mount and a x100 and 1.49 numerical aperture microscope objective (Ref. UAPON 100XOTIRF, Olympus, Japan). We used continuous-wave diode-pumped solid-state lasers sources, one at a wavelength of 488 nm and 50 mW maximum power for fluorescein excitation (Sapphire 488–50 LP, Coherent Inc., USA) and the other

NANO MICRO small

at 561 nm for excitation of NV color centers in nanodiamonds, at 100 mW maximum power (SLIM-561–100, Oxxius S.A., France). We used two different filter sets depending on the detection channel: the "green channel" dedicated to fluorescein and the "red channel" for FND fluorescence. The "green channel" filter set is composed of a dichroic beamsplitter (Ref. z488rdc Chroma, AHF Analysentechnik, Germany) and a 50 nm band-pass filter centered on 525 nm, which is close to the maximum of fluorescein fluorescence (ET525/50, AHF). The "red channel" filter set is composed of a dichroic beamsplitter with a sharp edge at 561 nm and a 97% flat transmission above this wavelength (Ref. ZT561rdc Chroma, AHF) and a 75 nm band-pass filter centered on 697 nm, which is the maximum of the NV color center fluorescence (HC 697/75, Ref. F39–697, AHF). The detection was performed with a cooled electron multiplied CCD array detector (iXon-DU885, Andor Technology, Ireland).

For colocalization statistics, five TIRF fields of view were analyzed (an example of one field is depicted in Figure S6). To obtain similar maximal counting rates of 160 kilo counts/s (kcts/s), excitation laser intensities of 32 kW cm^{-2} at a 561 nm excitation wavelength (Figure S6A) and 3 kW cm^{-2} at a 488 nm excitation wavelength (Figure S6B) were used.

Confocal Microscopy: Confocal microscope Zeiss LSM 780 was equipped with the In-Tune laser (with minimum power 1.5 mW per wavelength) tuned to 532 nm wavelength and an oil-immersion objective (Plan-Apochromat 63x/1.40 Oil DIC M27). The fluorescence images were collected in ZEN 2011 software at room temperature using InTune laser, intensity 100% at 532 nm, QUASAR PMT spectral channel #34 in range 639–758 nm with master gain set to 1200 V (or 850 V in case of **ND1** pre-incubated in PBS), offset 0, digital gain 1, pinhole at diameter 67 µm (1.35 Airy unit) and with line averaging 2. For continuous maintenance of focus Definite focus was used. Images were processed using the GIMP2 Program where images were cropped to selection and input level of black points was set to 15. Fluorescence from nanodiamonds is displayed in false colors in red-to-white LUT.

Nanodiamond Pretreatment (**ND1**): Nanodiamonds were supplied by Microdiamant Switzerland (MSY 0–0.05). The particles were oxidized by air in a Thermolyne 21100 tube furnace at 510 °C for 5 hours. The nanodiamonds were subsequently treated with a mixture of HNO_3 and H_2SO_4 (85 °C, 3 days), washed with 0.1 M NaOH and 0.1 M HCl, washed five times with water, and freeze-dried.[41] Purified nanodiamond powder (160 mg), containing approximately 100–200 ppm of natural nitrogen impurities, was pressed in an aluminum target holder and irradiated with a 15.5 MeV proton beam extracted from the isochronous cyclotron U-120M for 70 min (fluence 6×10^{16} cm^{-2}). The irradiated material was annealed at 900 °C for 1 h and subsequently oxidized for 6 h at 510 °C. The nanodiamonds were then treated with a mixture of HNO_3 and H_2SO_4 (85 °C, 3 days), washed with 0.1 M NaOH and 0.1 M HCl, washed five times with water, and freeze-dried. Prior to use, the particles were dissolved in water (2 mg/mL) and sonicated with a probe (Cole-Parmer, 750 W) for 30 minutes. The resulting transparent colloid was filtered using a 0.2 µm PVDF microfilter to provide colloidal solution of **ND1** particles.

Coating of Nanodiamond Particles with Amino-terminated Silica (**ND3**): Polyvinylpyrrolidone (96 mg, 9.6 µmol) was dissolved in water (204 mL) and sonicated for 10 minutes in an ultrasonic bath. **ND1** colloid (6 mL, 2 mg mL^{-1}) was added, and the mixture was stirred for 24 hours. The colloid was then concentrated via centrifugation in two steps. In the first step (40,000 rcf, 1 hour), the volume was reduced to approximately 12 mL. The second centrifugation step (30,000 rcf, 30 min) was performed in microvials and reduced the solvent volume to approximately 0.4 mL. Sedimented nanodiamonds were resuspended in ethanol (12 mL) in a round bottom flask and sonicated in an ultrasonic bath for 2–4 min. TEOS (112 mg, 539 µmol) was added. After 2 minutes of vigorous stirring, ammonia solution (25%, 500 µL) was added, and the reaction mixture was stirred for 14 h, affording **ND2**. BTSE (12 mg, 34 µmol) and APS (12 mg, 54 µmol) were added to the solution. After approximately 2 h, the reaction mixture became turbid, a portion of particles slowly precipitated from solution and stuck to the walls of the reaction vessel. The reaction mixture was stirred for an additional 24 hours. The product was purified by centrifugation (14,000 rcf, 5 min) with ethanol (12 mL, 4x) and MeCN (12 mL, 2x) and was dissolved in 6 mL of MeCN. The **ND3** particles were stored in the freezer (–18 °C) as a stable colloid for several weeks without changes in particle characteristics (confirmed with TEM, and DLS) or reactivity.

Grafting of PEG Chains (**ND4**): NHS-PEG-alkyne (42 mg, 8.4 µmol), EEDQ (8.4 mg, 34 µmol), and DMAP (4.1 mg, 34 µmol) were dissolved together in 6.4 mL MeCN. The resulting solution was placed into an ultrasonic bath cooled to 18 °C. Using a syringe pump, the **ND3** colloid (6 mg ND, i.e., 24 mg of particles in 3 mL solution) was slowly added to the reaction mixture in 30 min. The mixture was sonicated at 18 °C for an additional 2.5 hours and then gently shaken for 16 hours. The product was purified by centrifugation (14 000 rcf, 5 min) with MeCN (6 mL, 3x), ethanol (12 mL, 1x), and water (6 mL, 2x) and was dissolved in water or PBS (3 mL). For long term storage, the product (**ND4**) was kept in MeCN at –18 °C.

Functionalization of ND4 by ^{125}I-Labeled RGDS, coumarin azide, and fluorescein azide (**ND5a-c**): A solution of Cu-catalyst was prepared in a separate vial by mixing $CuSO_4 \cdot 5H_2O$ (20 µL of a 25 mM solution) and THPTA ligand (20 µL of a 50 mM solution).

The click reactions were performed similarly to those described in ref.[4] by mixing reactants in a 1.5 mL vial in the following order and quantities:

1. Water (87 µL)
2. Aqueous colloid of ND4 (250 µL containing 0.5 mg of ND, i.e., 2 mg of particles)
3. 125I-labeled RGDS (222 µL of a 0.46 mM aqueous solution) or fluorescein azide (5.90 µL of a 17.3 mM DMSO solution) or coumarin azide (13.5 µl of a 7.6 mM DMSO solution)
4. Aminoguanidine hydrochloride (32 µL of a 100 mM solution)
5. Cu-catalyst solution (16.5 µL) (see above)
6. Sodium ascorbate (32 µL of a 100 mM solution)

The vials were well-sealed and kept for 3 h without stirring or shaking. Nanoparticles **ND5a**, **ND5b**, and **ND5c** were isolated in almost quantitative yield by centrifugation (14 000 rcf, 5 min) and washed with water (1×, 1 mL) and PBS buffer (3×, 1 mL). The amount of molecules attached to the nanoparticles after every washing was quantified by UV-Vis spectrophotometry in the case of fluorescein azide or by radioactivity measurements in the case of ^{125}I-labeled RGDS (see Figure S3).

Cell Culture and Cellular Uptake: LNCaP cells (human prostate cancer cell line, ATCC) were grown in RPMI medium (Sigma) with

10% FBS serum (Sigma) in Petri dish with No. 1.5 glass bottom D35C4–20–1.5-N (BioPort Europe, s.r.o.) at 37 °C in a humidified 5% CO_2 atmosphere. After 24 hours (the cells were 20–30% confluent) the culture medium was replaced with the fresh medium containing NDs (**ND1** or **ND4**) at concentration 200 μg ml^{-1}. NDs were pre-incubated either half an hour in RPMI medium or one hour in isotonic PBS solution (pH = 7.4) before adding to the cells. After one hour of incubation the cells were washed twice with RPMI medium for removing excess of nanodiamonds. After additional 23 hours of incubation cells were fixed by 2% formaldehyde solution in PBS at 4 °C. After fixation cells were washed twice with PBS and subjected to confocal microscopy.

Supporting Information

Supporting Information is available from the Wiley Online Library or from the author.

Acknowledgements

The work was supported by GACR project P108/12/0640, MSMT CR grant No. LH11027. Part of this work was performed within OPPK project CZ.2.16/3.1.00/24016, OP VK project CZ.1.07/2.3.00/20.0306 (to VP), EU 7FP Program No. 262348 (European Soft Matter Infrastructure, ESMI), NIH/NIBIB T32 EB007509 (to A.M.W.), and Mt. Sinai Foundation (to N.F.S.). S.T. acknowledges support from the fund for scientific research flanders (FWO). P.S. has been supported by a grant of the Grant Agency of the Czech Republic P208/12/G016. The Titan microscope used for this work was partially funded by the Hercules foundation. We thank to Prof. M. Nesladek, Mr. J. Havlik, Dr. R. Hadravova and Mrs. C. Durieu for their very valuable help and to Dr. H. Hoffman for critical proofreading of the manuscript.

[1] K.-K. Liu, C.-L. Cheng, C.-C. Chang, J.-I. Chao, *Nanotechnology* **2007**, *18*, 325102.
[2] V. Vaijayanthimala, P.-Y. Cheng, S.-H. Yeh, K.-K. Liu, C.-H. Hsiao, J.-I. Chao, H.-C. Chang, *Biomaterials* **2012**, *33*, 7794–7802.
[3] A. M. Schrand, L. Dai, J. J. Schlager, S. M. Hussain, E. Osawa, *Diam. Relat. Mater.* **2007**, *16*, 2118–2123.
[4] Y. Zhu, *Theranostics* **2012**, 302.
[5] A. M. Schrand, H. Huang, C. Carlson, J. J. Schlager, E. Ōsawa, S. M. Hussain, L. Dai, *J. Phys. Chem. B* **2007**, *111*, 2–7.
[6] O. Faklaris, V. Joshi, T. Irinopoulou, P. Tauc, M. Sennour, H. Girard, C. Gesset, J. Arnault, A. Thorel, J.-P. Boudou, P. A. Curmi, F. Treussart, *ACS Nano* **2009**, *3*, 3955–62.
[7] Y. Y. Hui, C. L. Cheng, H. C. Chang, *J. Phys. Appl. Phys.* **2010**, *43*, 374021.
[8] I. Badea, R. Kaur, *Int. J. Nanomedicine* **2013**, 203–220.
[9] V. N. Mochalin, O. Shenderova, D. Ho, Y. Gogotsi, *Nat. Nanotechnol.* **2011**, *7*, 11–23.
[10] Y. Xing, L. Dai, *Nanomed.* **2009**, *4*, 207–218.
[11] G. Davies, S. C. Lawson, A. T. Collins, A. Mainwood, S. J. Sharp, *Phys. Rev. B* **1992**, *46*, 13157.
[12] F. Jelezko, J. Wrachtrup, *Phys. Status Solidi* **2006**, *203*, 3207–3225.
[13] A. Mohtashami, A. Femius Koenderink, *New J. Phys.* **2013**, *15*, 043017.
[14] R. Weissleder, V. Ntziachristos, *Nat. Med.* **2003**, *9*, 123–128.
[15] C. C. Fu, H. Y. Lee, K. Chen, T. S. Lim, H. Y. Wu, P. K. Lin, P. K. Wei, P. H. Tsao, H. C. Chang, W. Fann, *Proc. Natl. Acad. Sci. USA* **2007**, *104*, 727–732.
[16] Y.-K. Tzeng, O. Faklaris, B.-M. Chang, Y. Kuo, J.-H. Hsu, H.-C. Chang, *Angew. Chem. Int. Ed.* **2011**, *50*, 2262–2265.
[17] V. Vaijayanthimala, Y.-K. Tzeng, H.-C. Chang, C.-L. Li, *Nanotechnology* **2009**, *20*, 425103.
[18] O. Faklaris, D. Garrot, V. Joshi, F. Druon, J. P. Boudou, T. Sauvage, P. Georges, P. A. Curmi, F. Treussart, *Small* **2008**, *4*, 2236–2239.
[19] L. P. McGuinness, Y. Yan, A. Stacey, D. A. Simpson, L. T. Hall, D. Maclaurin, S. Prawer, P. Mulvaney, J. Wrachtrup, F. Caruso, R. E. Scholten, L. C. L. Hollenberg, *Nat. Nanotechnol.* **2011**, *6*, 358–363.
[20] A. Ermakova, G. Pramanik, J.-M. Cai, G. Algara-Siller, U. Kaiser, T. Weil, Y.-K. Tzeng, H. C. Chang, L. P. McGuinness, M. B. Plenio, B. Naydenov, F. Jelezko, *Nano Lett.* **2013**, *13*, 3305–3309.
[21] Y.-R. Chang, H.-Y. Lee, K. Chen, C.-C. Chang, D.-S. Tsai, C.-C. Fu, T.-S. Lim, Y.-K. Tzeng, C.-Y. Fang, C.-C. Han, H.-C. Chang, W. Fann, *Nat. Nanotechnol.* **2008**, *3*, 284–288.
[22] G. Balasubramanian, I. Y. Chan, R. Kolesov, M. Al-Hmoud, J. Tisler, C. Shin, C. Kim, A. Wojcik, P. R. Hemmer, A. Krueger, T. Hanke, A. Leitenstorfer, R. Bratschitsch, F. Jelezko, J. Wrachtrup, *Nature* **2008**, *455*, 648–651.
[23] J. R. Maze, P. L. Stanwix, J. S. Hodges, S. Hong, J. M. Taylor, P. Cappellaro, L. Jiang, M. V. G. Dutt, E. Togan, A. S. Zibrov, A. Yacoby, R. L. Walsworth, M. D. Lukin, *Nature* **2008**, *455*, 644–647.
[24] A. Hegyi, E. Yablonovitch, *Nano Lett.* **2013**, *13*, 1173–1178.
[25] R. Igarashi, Y. Yoshinari, H. Yokota, T. Sugi, F. Sugihara, K. Ikeda, H. Sumiya, S. Tsuji, I. Mori, H. Tochio, Y. Harada, M. Shirakawa, *Nano Lett.* **2012**, *12*, 5726–5732.
[26] Y. Kuo, T.-Y. Hsu, Y.-C. Wu, J.-H. Hsu, H.-C. Chang, *Proc. SPIE* **2013**, *8635*, 863503.
[27] M. F. Kircher, S. S. Gambhir, J. Grimm, *Nat. Rev. Clin. Oncol.* **2011**, *8*, 677–688.
[28] A. Taylor, K. M. Wilson, P. Murray, D. G. Fernig, R. Lévy, *Chem. Soc. Rev.* **2012**, *41*, 2707–2717.
[29] T.-J. Wu, Y.-K. Tzeng, W.-W. Chang, C.-A. Cheng, Y. Kuo, C.-H. Chien, H.-C. Chang, J. Yu, *Nat. Nanotechnol.* **2013**, *8*, 682–689.
[30] S.-J. Yu, M.-W. Kang, H.-C. Chang, K.-M. Chen, Y.-C. Yu, *J. Am. Chem. Soc.* **2005**, *127*, 17604–17605.
[31] A. Prokop, J. M. Davidson, *J. Pharm. Sci.* **2008**, *97*, 3518–3590.
[32] V. Vaijayanthimala, H.-C. Chang, *Nanomed.* **2009**, *4*, 47–55.
[33] B. R. Smith, D. W. Inglis, B. Sandnes, J. R. Rabeau, A. V. Zvyagin, D. Gruber, C. J. Noble, R. Vogel, E. Ōsawa, T. Plakhotnik, *Small* **2009**, *5*, 1649–1653.
[34] J. Havlik, V. Petrakova, I. Rehor, V. Petrak, M. Gulka, J. Stursa, J. Kucka, J. Ralis, T. Rendler, S.-Y. Lee, R. Reuter, J. Wrachtrup, M. Ledvina, M. Nesladek, P. Cigler, *Nanoscale* **2013**, *5*, 3208–3211.
[35] A. Krueger, D. Lang, *Adv. Funct. Mater.* **2012**, *22*, 890–906.
[36] A. Krueger, *J. Mater. Chem.* **2008**, *18*, 1485.
[37] A. M. Schrand, S. A. C. Hens, O. A. Shenderova, *Crit. Rev. Solid State Mater. Sci.* **2009**, *34*, 18.
[38] L. Moore, E. K.-H. Chow, E. Osawa, J. M. Bishop, D. Ho, *Adv. Mater.* **2013**, *25*, 3532–3541.
[39] B. Zhang, Y. Li, C.-Y. Fang, C.-C. Chang, C.-S. Chen, Y.-Y. Chen, H.-C. Chang, *Small* **2009**, *5*, 2716–2721.
[40] T. Nguyen, H. C. Chang, V. W. Wu, *Diam. Relat. Mater.* **2007**, *16*, 872–876.
[41] L.-C. L. Huang, H.-C. Chang, *Langmuir* **2004**, *20*, 5879–5884.
[42] M.-F. Weng, S.-Y. Chiang, N.-S. Wang, H. Niu, *Diam. Relat. Mater.* **2009**, *18*, 587–591.
[43] I. P. Chang, K. C. Hwang, J. A. Ho, C.-C. Lin, R. J.-R. Hwu, J.-C. Horng, *Langmuir* **2010**, *26*, 3685–3689.

[44] S. A. Dahoumane, M. N. Nguyen, A. Thorel, J.-P. Boudou, M. M. Chehimi, C. Mangeney, *Langmuir* **2009**, *25*, 9633–9638.
[45] V. K. A. Sreenivasan, E. A. Ivukina, W. Deng, T. A. Kelf, T. A. Zdobnova, S. V. Lukash, B. V. Veryugin, O. A. Stremovskiy, A. V. Zvyagin, S. M. Deyev, *J. Mater. Chem.* **2011**, *21*, 65–68.
[46] Y. Liang, T. Meinhardt, G. Jarre, M. Ozawa, P. Vrdoljak, A. Schöll, F. Reinert, A. Krueger, *J. Colloid Interface Sci.* **2011**, *354*, 23–30.
[47] I. Rehor, H. Mackova, S. K. Filippov, J. Kucka, V. Proks, J. Slegerova, S. Turner, G. Van Tendeloo, M. Ledvina, M. Hruby, P. Cigler, *ChemPlusChem* **2013**, DOI: 10.1002/cplu.201300339.
[48] L. Zhao, T. Takimoto, M. Ito, N. Kitagawa, T. Kimura, N. Komatsu, *Angew. Chem. Int. Ed.* **2011**, *50*, 1388–1392.
[49] X.-Q. Zhang, M. Chen, R. Lam, X. Xu, E. Osawa, D. Ho, *ACS Nano* **2009**, *3*, 2609–2616.
[50] L. Marcon, Z. Kherrouche, J. Lyskawa, D. Fournier, D. Tulasne, P. Woisel, R. Boukherroub, *Chem. Commun.* **2011**, *47*, 5178–5180.
[51] C. Burda, X. Chen, R. Narayanan, M. A. El-Sayed, *Chem. Rev.* **2005**, *105*, 1025–1102.
[52] A. R. Tao, S. Habas, P. Yang, *Small* **2008**, *4*, 310–325.
[53] S. Vial, C. Mansuy, S. Sagan, T. Irinopoulou, F. Burlina, J.-P. Boudou, G. Chassaing, S. Lavielle, *ChemBioChem* **2008**, *9*, 2113–2119.
[54] E. K. Chow, X.-Q. Zhang, M. Chen, R. Lam, E. Robinson, H. Huang, D. Schaffer, E. Osawa, A. Goga, D. Ho, *Sci. Transl. Med.* **2011**, *3*, 73ra21–73ra21.
[55] Y. Yuan, X. Wang, G. Jia, J.-H. Liu, T. Wang, Y. Gu, S.-T. Yang, S. Zhen, H. Wang, Y. Liu, *Diam. Relat. Mater.* **2010**, *19*, 291–299.
[56] A. P. Puzyr, A. V. Baron, K. V. Purtov, E. V. Bortnikov, N. N. Skobelev, O. A. Mogilnaya, V. S. Bondar, *Diam. Relat. Mater.* **2007**, *16*, 2124–2128.
[57] Y. Xing, W. Xiong, L. Zhu, E. Osawa, S. Hussin, L. Dai, *ACS Nano* **2011**, *5*, 2376–2384.
[58] V. Thomas, B. A. Halloran, N. Ambalavanan, S. A. Catledge, Y. K. Vohra, *Acta Biomater.* **2012**, *8*, 1939–1947.
[59] X. Zhang, J. Yin, C. Kang, J. Li, Y. Zhu, W. Li, Q. Huang, Z. Zhu, *Toxicol. Lett.* **2010**, *198*, 237–243.
[60] N. Daum, C. Tscheka, A. Neumeyer, M. Schneider, *Wiley Interdiscip. Rev. Nanomed. Nanobiotechnol.* **2012**, *4*, 52–65.
[61] E. Hutter, S. Boridy, S. Labrecque, M. Lalancette-Hébert, J. Kriz, F. M. Winnik, D. Maysinger, *ACS Nano* **2010**, *4*, 2595–2606.
[62] A. Bumb, S. K. Sarkar, N. Billington, M. W. Brechbiel, K. C. Neuman, *J. Am. Chem. Soc.* **2013**, *135*, 7815–7818.
[63] E. von Haartman, H. Jiang, A. A. Khomich, J. Zhang, S. A. Burikov, T. A. Dolenko, J. Ruokolainen, H. Gu, O. A. Shenderova, I. I. Vlasov, J. M. Rosenholm, *J. Mater. Chem. B* **2013**, *1*, 2358–2366.
[64] N. Prabhakar, T. Näreoja, E. von Haartman, D. Sen Karaman, H. Jiang, S. Koho, T. A. Dolenko, P. Hänninen, D. I. Vlasov, V. G. Ralchenko, S. Hosomi, I. Vlasov, C. Sahlgren, J. M. Rosenholm, *Nanoscale* **2013**, *5*, 3713–3722.
[65] S. T. Selvan, *Biointerphases* **2010**, *5*, FA110.
[66] V. Hong, S. I. Presolski, C. Ma, M. G. Finn, *Angew. Chem. Int. Ed.* **2009**, *48*, 9879–9883.
[67] C. Graf, D. L. J. Vossen, A. Imhof, A. van Blaaderen, *Langmuir* **2003**, *19*, 6693–6700.
[68] M. Etienne, A. Walcarius, *Talanta* **2003**, *59*, 1173–1188.
[69] Z. Zhang, A. E. Berns, S. Willbold, J. Buitenhuis, *J. Colloid Interface Sci.* **2007**, *310*, 446–455.
[70] B. D. Chithrani, W. C. W. Chan, *Nano Lett.* **2007**, *7*, 1542–1550.
[71] R. F. Egerton, *Electron Energy-Loss Spectroscopy in the Electron Microscope*, Springer, **2011**.
[72] S. Turner, O. I. Lebedev, O. Shenderova, I. I. Vlasov, J. Verbeeck, G. Van Tendeloo, *Adv. Funct. Mater.* **2009**, *19*, 2116–2124.
[73] H. Macková, V. Proks, D. Horák, J. Kučka, M. Trchová, *J. Polym. Sci. Part Polym. Chem.* **2011**, *49*, 4820–4829.
[74] V. Proks, J. Jaroš, O. Pop-Georgievski, J. Kučka, Š. Popelka, P. Dvořák, A. Hampl, F. Rypáček, *Macromol. Biosci.* **2012**, *12*, 1232–1242.
[75] K. Sivakumar, F. Xie, B. M. Cash, S. Long, H. N. Barnhill, Q. Wang, *Org Lett* **2004**, *6*, 4603–4606.
[76] M. Berchel, J.-P. Haelters, H. Couthon-Gourvès, L. Deschamps, P. Midoux, P. Lehn, P.-A. Jaffrès, *Eur. J. Org. Chem.* **2011**, *2011*, 6294–6303.
[77] V. Petrakova, A. Taylor, I. Kratochvilova, F. Fendrych, J. Vacik, Jan Kucka, J. Stursa, P. Cigler, M. Ledvina, A. Fiserova, P. Kneppo, M. Nesladek, *Adv. Funct. Mater.* **2012**, *22*, 812–819.
[78] D. Walczyk, F. B. Bombelli, M. P. Monopoli, I. Lynch, K. A. Dawson, *J. Am. Chem. Soc.* **2010**, *132*, 5761–5768.
[79] A. Salvati, A. S. Pitek, M. P. Monopoli, K. Prapainop, F. B. Bombelli, D. R. Hristov, P. M. Kelly, C. Åberg, E. Mahon, K. a Dawson, *Nat. Nanotechnol.* **2013**, *8*, 137–43.
[80] C. E. Ashley, E. C. Carnes, G. K. Phillips, D. Padilla, P. N. Durfee, P. A. Brown, T. N. Hanna, J. Liu, B. Phillips, M. B. Carter, N. J. Carroll, X. Jiang, D. R. Dunphy, C. L. Willman, D. N. Petsev, D. G. Evans, A. N. Parikh, B. Chackerian, W. Wharton, D. S. Peabody, C. J. Brinker, *Nat. Mater.* **2011**, *10*, 389–397.w

Received: July 30, 2013
Published online: February 5, 2014

NANO MICRO small

Supporting Information

for *Small*, DOI: 10.1002/smll.201302336

Fluorescent Nanodiamonds Embedded in Biocompatible Translucent Shells

*Ivan Rehor, Jitka Slegerova, Jan Kucka, Vladimir Proks, Vladimira Petrakova, Marie-Pierre Adam, François Treussart, Stuart Turner, Sara Bals, Pavel Sacha, Miroslav Ledvina, Amy M. Wen, Nicole F. Steinmetz, and Petr Cigler**

Supporting Information

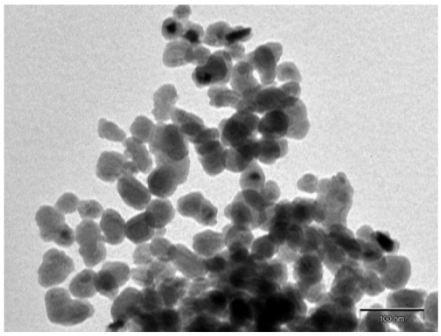

Figure S1: BF-TEM images of aminosilica-coated particles prepared with a half amount of tetraethoxy silane compared to the particles **ND3** (Figure 1B).

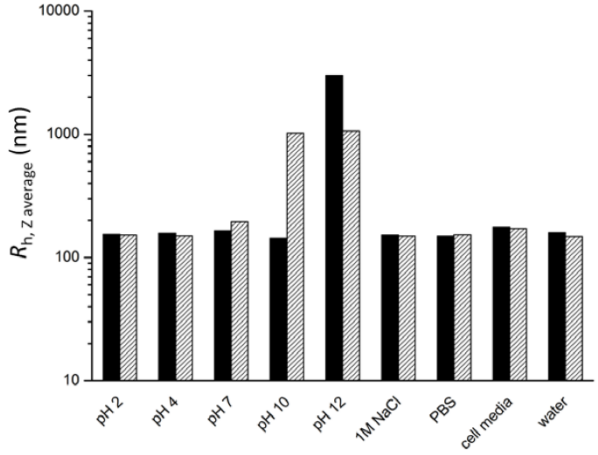

Figure S2: Aggregation states (expressed as zeta averages from DLS measurement) of colloidal aqueous solutions of **ND4** particles at pH 2, 4, 7, 10, and 12 (pH adjusted using HCl and NaOH solutions), in 1M NaCl, PBS buffer and serum-containing cell grow media (Sigma Aldrich RPMI-1640 + serum). Measurements were performed 24 hours (black bars) and 2 weeks (hatched bars) after sample preparation. The sample at pH 12 precipitated during the first two hours, and the sample at pH 10 precipitated after one week. All other samples remained colloidally stable.

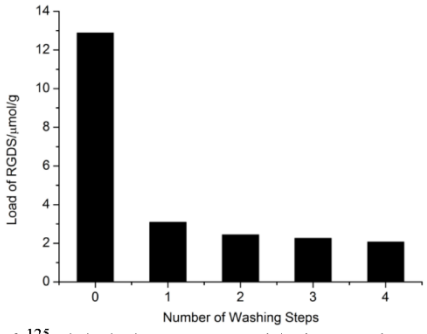

Figure S3: The content of ^{125}I-labeled RGDS peptide in reaction mixture and in the **ND5a** sample after the specified number of washings (1 mg of nanoparticles was washed with 1.2 mL of water and isolated *via* centrifugation. The activity of colloid was measured after each washing step using ionization chamber.

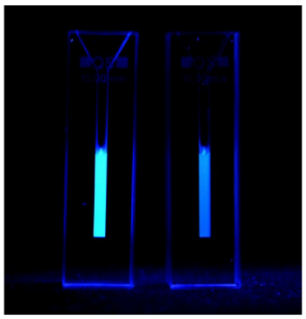

Figure S4: UV-irradiated spectroscopic cuvettes with reaction mixtures after fluorogenic click reaction of **ND4** with coumarin-azide in the presence (left) and absence (right) of Cu(I) catalyst. The fluorescence of product **ND5b** is clearly observable in the left cuvette.

Single particle measurements

Fraction of ND1 displaying NV color center fluorescence

The fraction of fluorescent NDs was determined using a setup combining an atomic force microscope (AFM, MFP- 3D-BIO, Asylum Research, USA) with an inverted confocal microscope sensitive to single NV color center photoluminescence (see ref.[1] for example). Nanodiamonds were first spin-coated on a quartz coverslip, which was then simultaneously raster-scanned by AFM and confocal microscopes. From scans of the mixtures shown in Figure S5 and three additional scans (not shown), we observed that 97 of 134 nanodiamonds, i.e., 74%, were fluorescent. Moreover, the maximal nanodiamond size measured by AFM was about 100 nm (probably an aggregate of two particles), in relatively good agreement with TEM (Figure 1).

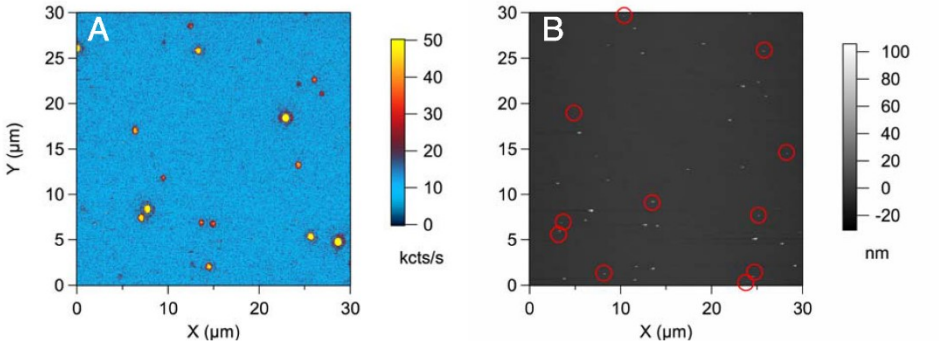

Figure S5: AFM and confocal microscopy simultaneous imaging of non-coated FNDs deposited on a quartz converglass. (A) Photoluminescence image (scale in kilocounts s^{-1} on the single-photon counting module). (B) AFM image of the same field of view. The red circles are centered on NDs that do not exhibit fluorescence. Note that the AFM scan is slightly shifted by about 1 µm towards the negative x-axis, and by about 400 nm towards the positive y-axis.

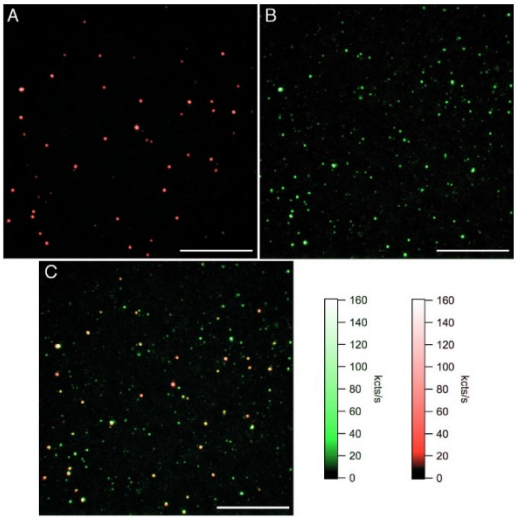

Figure S6: TIRF microscopy images of the fluorescein-labeled particles (**ND5c**), spincoated on a quartz converglass. (A) Red detection channel image showing only NV center fluorescence; (B) Green detection channel, showing fluorescein signal in the same field of view; (C) Merged image in which colocalized spots appear in yellow-white. All red spots of (A) colocalize with green spots of (B). Scale bars: 10 µm, intensity scales in kilo counts per second (kcts s^{-1}) on the detector.

Individual photoluminescence (PL) spectra of ND4

A large number of green spots that do not colocalize with red ones (total of 530), originating from NV centers, were detected in TIRF microscopy images (see Figure S6). To understand this observation, the individual particle spectra were measured using a home-made confocal microscope with an imaging spectrograph, equipped with a cooled CCD array on its detection channel. **ND4** particles were spincoated on a quartz coverslip similarly as for the analysis shown in Figure S5. The PL of the sample was raster-scanned using a continuous wave (cw) excitation laser at a wavelength of 488 nm and a combination of a dichroic beamsplitter (z488rdc Chroma, AHF Analysentechnik, Germany) and a longpass filter with a steep edge at 488 nm (RazorEdge LP02-488RS, Semrock Inc., USA). This allowed us to record the full PL spectra. The excitation laser was then positioned on an individual FND to record the spectrum. Figure S7 shows three different types of spectra obtained for different particles. A large majority of the spectra (about 90%) displays only NV° or NV^- PL characteristics (Figure S7A) with a very low signal in the green bandpass detection channel of the TIRF microscope setup. A rare green signal that could come from a color center emitting in the green like the H3 center[3] or Raman from silica (see Figure S7C) can therefore be ruled out. These observations, along with the fact that only 26% of the **ND1** particles do not display NV center fluorescence (Figure S5), indicate that the green spots in Figure S6 that do not colocalize with NV emission are mostly not related to FND. The most probable cause of the non-colocalized green signal is the presence of fluorescent impurities in the solvent that we can detect considering the single emitter sensitivity of our setup.

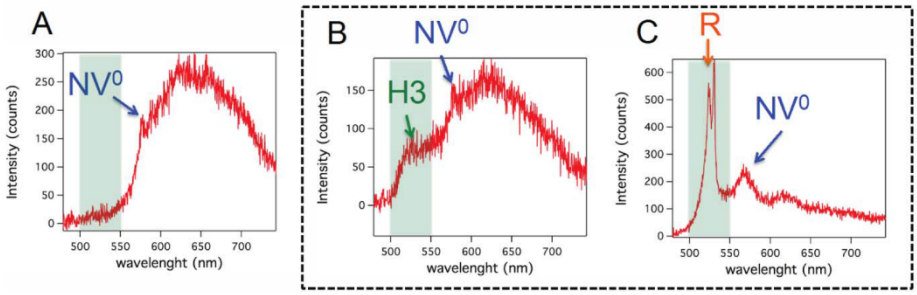

Figure S7: Photoluminescence spectra of individual PEGylated aminosilica-coated (**ND4**) FNDs, excited with a cw laser at 488 nm wavelength (1 mW power). The light green rectangles indicate the detection range of the green channel on the TIRF setup. (A) PL spectrum of an **ND4** particle displaying mostly neutral NV center emission characterized by a zero-phonon line at 575 nm (indicated by the arrow). (B) PL spectrum of another **ND4** particle, showing in addition to NV° emission, the presence of a green emitting center, the H3, corresponding to N-V-N,[2] which would give a significant signal in the TIRF green detection channel. (C) PL spectrum of yet another **ND4** particle displaying narrow peaks in the TIRF green detection channel (labeled with R). We attribute these peaks to the 1873 cm^{-1} Raman peak of amorphous silica,[3] which results in a peak at 537 nm for the 488 nm excitation wavelength used, very close to the 532 nm peak maximum observed.

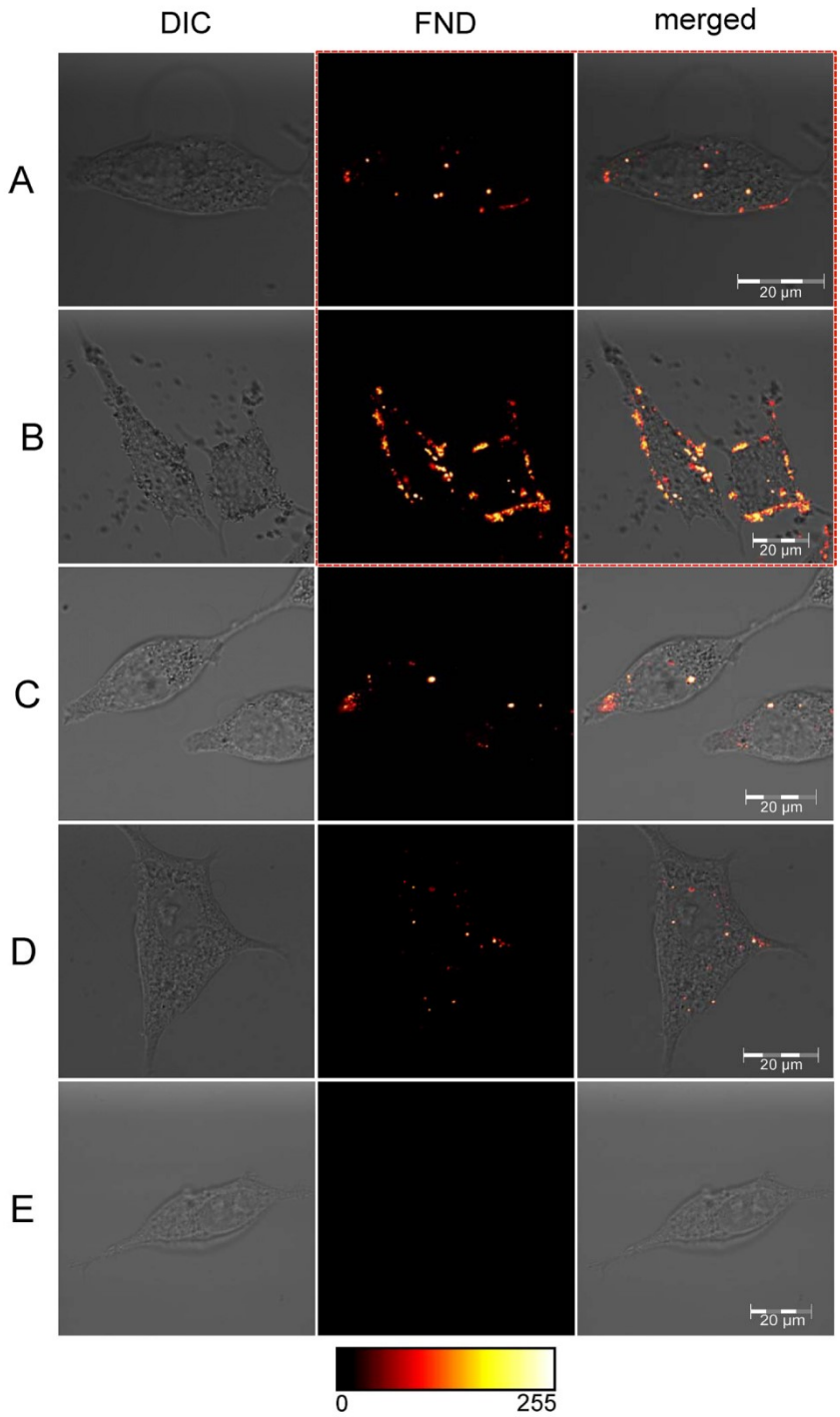
DIC
FND
merged
A
B
C
D
E
20 µm
0
255

Figure S8. Images of FNDs internalized by LNCaP cells: (A) PEGylated aminosilica-coated **ND4** and (B) non-coated **ND1**, dispersed in PBS; (C) **ND4** and (D) **ND1** pre-incubated in medium containing serum proteins; (E) cells without nanodiamonds. The displayed images are differential interference contrast (left), fluorescence from NDs (middle), and merged image (right). All the cells were washed by PBS after one hour incubation with NDs (final concentration 200 μg mL^{-1}), incubated for subsequent 23 hours and observed after fixation with solution of 2% formaldehyde. Fluorescence of FND was collected by Zeiss LSM 780 at 639–758 nm upon excitation at 532 nm. The upper right part of the image marked by a red line is identical with Figure 6.

References

1 Rondin, L.; Dantelle, G.; Slablab, A.; Grosshans, F.; Treussart, F.; Bergonzo, P.; Perruchas, S.; Gacoin, T.; Chaigneau, M.; Chang, H.-C.; Jacques, V.; Roch, J.-F. *Phys. Rev. B* **2010**, *82*, 115449.

2 Wee, T.-L.; Mau, Y.-W.; Fang, C.-Y.; Hsu, H.-L.; Han, C.-C.; Chang, H.-C. *Diam Relat Mater* **2009**, *18*, 567–573.

3 Davis, K. M.; Tomozawa, M. *J Non-Cryst Solids* **1995**, *185*, 203–220.

Appendix B – Publication 2

Ivan Rehor, Hana Mackova, Sergey K. Filippov, Jan Kucka, Vladimír Proks, **Jitka Slegerova**, Stuart Turner, Sara Bals, Miroslav Ledvina, Martin Hruby, Petr Cigler: Fluorescent nanodiamonds with bioorthogonally reactive protein-resistant polymeric coatings, ChemPlusChem, *79*, 21, **2014**.

CHEMPLUSCHEM
COMMUNICATIONS

ChemPubSoc Europe

DOI: 10.1002/cplu.201300339

Fluorescent Nanodiamonds with Bioorthogonally Reactive Protein-Resistant Polymeric Coatings

Ivan Rehor,[a] Hana Mackova,[b] Sergey K. Filippov,[b] Jan Kucka,[b, c] Vladimir Proks,[b] Jitka Slegerova,[a] Stuart Turner,[d] Gustaaf Van Tendeloo,[d] Miroslav Ledvina,[a] Martin Hruby,*[b] and Petr Cigler*[a]

The novel synthesis of a polymeric interface grown from the surface of bright fluorescent nanodiamonds is reported. The polymer enables bioorthogonal attachment of various molecules by click chemistry; the particles are resistant to nonspecific protein adsorption and show outstanding colloidal stability in buffers and biological media. The coating fully preserves the unique optical properties of the nitrogen-vacancy centers that are crucial for bioimaging and sensoric applications.

Fluorescent nanodiamonds (FNDs) are a recently introduced class of luminescent probes.[1–5] FNDs are biocompatible[5–7] nanoparticles with sizes ranging from about five to several hundred nanometers. FNDs emit bright fluorescence in the red part of the visible spectrum (maximum at ≈700 nm), which is well separated from the cell/tissue autofluorescence. Nanodiamond fluorescence originates from so-called nitrogen-vacancy (N-V) centers. Emission from N-V centers is completely resistant to photobleaching and photoblinking.[8] The absolute stability of N-V emission is unique amongst all fluorescent dyes and is especially crucial in applications that require large laser powers, such as super-resolution microscopy.[9,10] Furthermore, the electron structure of the N-V center[11,12] allows for construction of fluorescence-read sensors[13,14] or for background-free observation of FND probes in vivo.[15,16]

[a] Dr. I. Rehor, J. Slegerova, Dr. M. Ledvina, Dr. P. Cigler
Institute of Organic Chemistry and Biochemistry, v.v.i.
The Academy of Sciences of the Czech Republic
Flemingovo nam. 2, 166 10 Prague 6 (Czech Republic)
Fax: (+420) 220-183-578
E-mail: cigler@uochb.cas.cz
Homepage: www.petrcigler.cz

[b] Dr. H. Mackova, Dr. S. K. Filippov, Dr. J. Kucka, Dr. V. Proks, Dr. M. Hruby
Institute of Macromolecular Chemistry, v.v.i.
The Academy of Sciences of the Czech Republic
Heyrovskeho nam. 2, 162 06 Prague 6 (Czech Republic)
Fax: (+420) 296-809-410
E-mail: mhruby@centrum.cz

[c] Dr. J. Kucka
Nuclear Physics Institute, v.v.i.
The Academy of Sciences of the Czech Republic
250 68 Rez near Prague (Czech Republic)

[d] Dr. S. Turner, Prof. G. Van Tendeloo
EMAT, University of Antwerp
Groenenborgerlaan 171, 2020 Antwerp (Belgium)

Supporting information for this article is available on the WWW under http://dx.doi.org/10.1002/cplu.201300339.

This article is part of the "Early Career Series". To view the complete series, visit: http://chempluschem.org/earlycareer.

The use of FNDs without any surface modification as fluorescent bioprobes or biosensors is limited for three major reasons: 1) nanodiamonds (NDs) precipitate in biological solutions,[17,18] 2) proteins nonspecifically adhere to the ND surface,[19] and 3) direct surface modifications of the ND surface are limited. The urgent need to overcome these limitations is evidenced by the large number of publications devoted to improving ND particle properties through various surface modifications (for a review, see Ref. [20]).

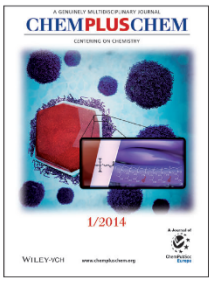

BACK COVER

Coating of NDs with polymeric shells appears to be a promising approach. After coating, ND particles exhibit an improved colloidal stability[17,19,21–23] and reduced adsorption of blood proteins.[19] Further functionalization of the polymeric shell has also been demonstrated.[17] Introduction of azide and alkyne groups onto the ND surface and their subsequent reaction using azide–alkyne cycloaddition (click reaction) was recently reported.[19,24–27]

Herein, we show simultaneous removal of the three above-described drawbacks of "naked" bright[28] FNDs by means of a novel surface architecture constructed on a FND surface. This architecture comprises an ultrathin, <1 nm silica layer (unlike recently published thick silica shells on FNDs[27,29–31]) and a polymethacrylate copolymer coating that allows further functionalization of the FNDs by click chemistry[32] (Scheme 1).

The silica shell was grown from a mixture of tetraethoxysilane and 3-(trimethoxysilyl)propyl methacrylate using a modified Stöber procedure. The presence of this coating was confirmed by infrared spectroscopy (Figure S1 in the Supporting Information). Terminal methacrylate groups of the silica coating were used to grow a dense layer of copolymers, which consisted mainly of poly[*N*-(2-hydroxypropyl)methacrylamide] (poly(HPMA)). Poly(HPMA) is a widely used hydrophilic biocompatible polymer[33] and has been used to coat various fluorescent probes.[34] We used a "grafting from" coating method, in which the polymer coating is polymerized from the surface of the FND. This approach usually offers denser and better protecting coatings than "grafting to" methods, in which the polymer is first synthesized in solution and then attached to the surface.[35,36] Polymer chains were grown using radical polymeri-

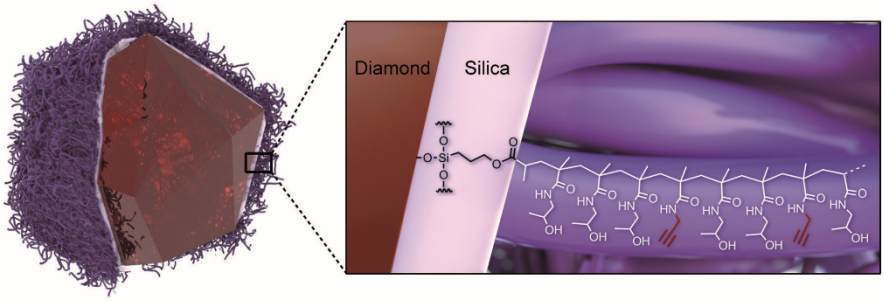

Scheme 1. Schematic structure of the polymer coating on a fluorescent nanodiamond crystal.

zation with azobis(isobutyronitrile) (AIBN) as initiator. A small fraction (5%) of HPMA monomer was replaced in the reaction mixture by propargylacrylamide (AlkMA) or 3-(azidopropyl)methacrylamide (AzMA) to introduce azide or alkyne moieties to the polymer, respectively. These groups are suitable for copper-catalyzed click reaction,[32] enabling attachment of various molecules and biomolecules to the FND surface (see below).

Figure 1 shows bright-field TEM images of FNDs modified by poly(HPMA-*co*-AlkMA). The FNDs are coated with a thin layer of polymer that evenly covers the nanodiamond surface (Figure 1a,b). The thickness of the layer varies between approximately 2 and 5 nm. The high-resolution images (Figure 1c,d) show that the surface layer is formed by chainlike structures, which are presumably the polymer strands. Thermogravimetric analysis provides additional evidence for the presence of polymers on the FND surfaces (Figure S2). Based on the difference between the silica-coated and silica–poly(HPMA-*co*-AlkMA)-coated FNDs, we concluded that the polymer comprises approximately 9% of the total mass of the prepared material.

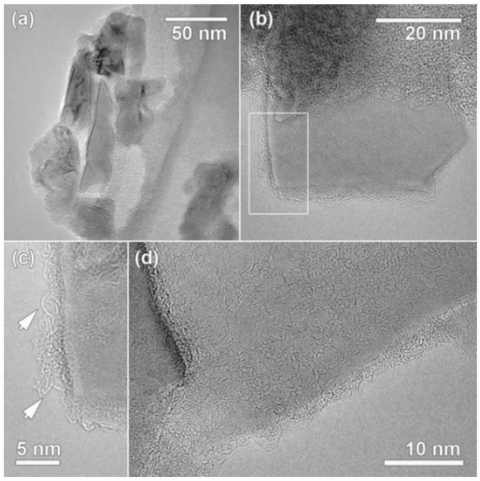

Figure 1. TEM images of FNDs coated with poly(HPMA-*co*-AlkMA). (a) Overview image showing the irregular shape and size of the coated FNDs. (b) Single-coated FND; the polymer-coated diamond surface is shown in more detail in (c) (area indicated by the white rectangle). The arrows indicate elongated or rolled-up chainlike structures, presumably the polymer chains. (d) High-resolution TEM image of a FND surface showing the surface-coating layer.

Modifications of FND surface chemistry can cause changes in the charge state of the N-V centers, which is strongly reflected in the fluorescence spectra.[37,38] To evaluate the possible influence of our modification on FND fluorescence, we measured the photoluminescence spectra of noncoated and poly(HPMA-*co*-AlkMA)-coated FNDs (Figure S3). The spectra show that the shell behaves as an inert translucent layer; its presence has no significant influence on the shape and intensity of the fluorescence spectrum.

The colloidal stability of FNDs in buffers and biological liquids is essential for their successful application as fluorescent bioprobes. Performed experiments show the long-term colloidal stability of coated FNDs in saline, in buffers typically used in cell biology (0.1 M phosphate-buffered saline (PBS), 2-(*N*-morpholino)ethanesulfonic acid (MES), and 4-(2-hydroxyethyl)-1-piperazineethanesulfonic acid (HEPES)), and in cell-growth media (Figure S4). A stability study performed in universal Britton–Robinson buffer revealed that the particles are stable under acidic to basic conditions and become unstable in strongly acidic solutions only (Figure S5). In contrast, naked FNDs aggregate (Figure 2a) and eventually precipitate in any of these solutions.

The adsorption of blood proteins, which may lead to scavenging of particles into the reticuloendothelial system, was tested with radiolabeled bovine serum albumin (BSA). Serum albumin is the most abundant serum protein (ca. 4–5% weight concentration in plasma), which makes it the best blood protein representative.[39] To evaluate the protein resistance of the particles, we mixed noncoated and poly(HPMA-*co*-AlkMA)-coated FND solutions with ^{125}I radiolabeled bovine serum albumin (^{125}I-BSA).[39] After incubation, FNDs were removed by centrifugation, and the remaining radioactivity in the supernatant (corresponding to the BSA concentration) was measured (for

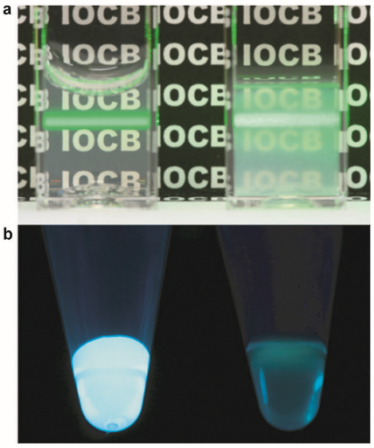

Figure 2. Properties of polymer-coated FNDs. (a) Poly(HPMA-*co*-AlkMA)-coated FNDs (left) and naked nanodiamonds (right) dispersed in PBS buffer (30 min after mixing; concentration 0.5 mg mL^{-1}). The laser beam is strongly scattered by the precipitating naked FND particles, and the polymer-coated particles form a stable colloidal solution. (b) The reaction of poly(HPMA-*co*-AlkMA)-coated FNDs (left) and control poly(HPMA)-coated FNDs (right), with the fluorogenic probe coumarin-azide (lighted by UV lamp). The bright fluorescence results from the click reaction.

details, see Supporting Information). We observed that the introduction of the polymeric film on FNDs caused a nearly fourfold reduction in the total adsorbed amount of BSA. This reduction slightly exceeds the 3.2-fold reduction described for amphiphilic polymer zonyl-coated NDs.[19]

A copper-catalyzed alkyne–azide cycloaddition reaction (click reaction)[32] was used to modify the poly(HPMA-*co*-AlkMA)-coated FNDs with various model molecules. We chose this reaction owing to its excellent bioorthogonality and mild reaction conditions (see below). First, to directly confirm the covalent grafting mechanism, the fluorogenic probe coumarin-azide[40] was attached to the poly(HPMA-*co*-AlkMA)-coated particles. The dye itself is nonfluorescent, but a highly fluorescent structure is formed upon cycloaddition to an alkyne. The reaction of coumarin-azide with the particles in the presence of a Cu^{I} catalyst produced a characteristic bright fluorescent product, whereas the control reaction performed in the absence of Cu^{I}, remained dark(Figure 2b).

Several molecules were attached to the surface of the HPMA copolymer-coated FNDs to demonstrate the versatility of the conjugation procedure and to quantify the yield of the click reaction (see the Supporting Information). As a representative fluorescent dye we used Alexa488-azide, because its high extinction coefficient allows quantification using absorption spectroscopy. To test the performance of the reaction in the inverse azide–alkyne arrangement, we coupled Alexa488-alkyne with poly(HPMA-*co*-AzMA)-coated FNDs under the same conditions. As an example of a peptide we used ^{125}I-labeled GGGRGDSGGGY-azide (RGDS-azide),[41,42] a vectoring molecule used in nanoparticle targeting of tumor cells.[43,44] The presence of the ^{125}I label enabled the highly sensitive monitoring of the conjugation yield by radioactivity measurements. All of these reactions were performed in aqueous solutions with approximately 100 μM concentrations of modifying molecules. The reaction time was 2 h. The loads of modifying molecules were found to be in the range of tens of micromoles per gram of FNDs in all cases. The results show that our surface architecture allows a stable covalent connection of various molecules to the nanoparticles.

In summary, this study describes the preparation and properties of a versatile platform for FND-based bioprobe construction. A new modification of the FND surface using an ultrathin silica shell bearing methacrylate groups as a platform for polymer growth is presented. The methacrylamide copolymeric layer grafted from the silica surface simultaneously overcomes the three current main limits to the bioapplicability of naked FNDs: buffer solubility, nonspecific protein binding, and the possibility of a convenient chemical modification. Moreover, it does not alter the fluorescent properties of the FNDs. The attachment of molecules to FNDs can be performed selectively using click chemistry in aqueous buffers or biological media, while maintaining the excellent colloidal stability of the particles. Our design, based upon the unique photophysical properties of N-V centers in FNDs, provides a versatile biocompatible platform for the construction of bioimaging probes or targeted systems. Experiments on cancer cell targeting and fluorescence imaging are currently in progress.

Acknowledgements

The study was supported by GACR (project P108/12/0640) and MSMT CR (grant no. LH11027). Part of this study was performed within OPPK (project CZ.2.16/3.1.00/24016), EU 7FP Program (no. 262348) (European Soft Matter Infrastructure, ESMI), and the framework of the European Research Council, ERC (grant no. 246791)—COUNTATOMS. The Titan microscope used for this study was partially funded by the Hercules foundation. S.T. gratefully acknowledges financial support from the Fund for Scientific Research Flanders (FWO). We are grateful to Dr. Vladimíra Petráková, Dr. Jan Štursa, Dr. Jan Ráliš, and Jan Havlík for their valuable help with the preparation and characterization of fluorescent nanodiamonds and to Dr. Hillary Hoffman for critical proofreading of the manuscript.

Keywords: click chemistry · fluorescence · nanoparticles · polymerization · solubilization

[1] C. C. Fu, H. Y. Lee, K. Chen, T. S. Lim, H. Y. Wu, P. K. Lin, P. K. Wei, P. H. Tsao, H. C. Chang, W. Fann, *Proc. Natl. Acad. Sci. USA* **2007**, *104*, 727–732.
[2] Y. Y. Hui, C. L. Cheng, H. C. Chang, *J. Phys. Appl. Phys.* **2010**, *43*, 374021.
[3] O. Faklaris, D. Garrot, V. Joshi, F. Druon, J. P. Boudou, T. Sauvage, P. Georges, P. A. Curmi, F. Treussart, *Small* **2008**, *4*, 2236–2239.
[4] F. Neugart, A. Zappe, F. Jelezko, C. Tietz, J. P. Boudou, A. Krueger, J. Wrachtrup, *Nano Lett.* **2007**, *7*, 3588–3591.
[5] V. Vaijayanthimala, P.-Y. Cheng, S.-H. Yeh, K.-K. Liu, C.-H. Hsiao, J.-I. Chao, H.-C. Chang, *Biomaterials* **2012**, *33*, 7794–7802.

[6] Y. Yuan, Y. Chen, J.-H. Liu, H. Wang, Y. Liu, *Diamond Relat. Mater.* **2009**, *18*, 95 – 100.
[7] A. M. Schrand, H. Huang, C. Carlson, J. J. Schlager, E. Ōsawa, S. M. Hussain, L. Dai, *J. Phys. Chem. B* **2007**, *111*, 2 – 7.
[8] F. Jelezko, J. Wrachtrup, *Phys. Status Solidi A* **2006**, *203*, 3207 – 3225.
[9] Y.-K. Tzeng, O. Faklaris, B.-M. Chang, Y. Kuo, J.-H. Hsu, H.-C. Chang, *Angew. Chem.* **2011**, *123*, 2310 – 2313; *Angew. Chem. Int. Ed.* **2011**, *50*, 2262 – 2265.
[10] K. Y. Han, K. I. Willig, E. Rittweger, F. Jelezko, C. Eggeling, S. W. Hell, *Nano Lett.* **2009**, *9*, 3323 – 3329.
[11] A. Gruber, A. Dräbenstedt, C. Tietz, L. Fleury, J. Wrachtrup, C. von Borczyskowski, *Science* **1997**, *276*, 2012 – 2014.
[12] F. Dolde, H. Fedder, M. W. Doherty, T. Nöbauer, F. Rempp, G. Balasubramanian, T. Wolf, F. Reinhard, L. C. L. Hollenberg, F. Jelezko, J. Wrachtrup, *Nat. Phys.* **2011**, *7*, 459 – 463.
[13] G. Balasubramanian, I. Y. Chan, R. Kolesov, M. Al-Hmoud, J. Tisler, C. Shin, C. Kim, A. Wojcik, P. R. Hemmer, A. Krueger, T. Hanke, A. Leitenstorfer, R. Bratschitsch, F. Jelezko, J. Wrachtrupet, *Nature* **2008**, *455*, 648 – 651.
[14] L. P. McGuinness, Y. Yan, A. Stacey, D. A. Simpson, L. T. Hall, D. Maclaurin, S. Prawer, P. Mulvaney, J. Wrachtrup, F. Caruso, R. E. Scholten, L. C. L. Hollenberg, *Nat. Nanotechnol.* **2011**, *6*, 358 – 363.
[15] R. Igarashi, Y. Yoshinari, H. Yokota, T. Sugi, F. Sugihara, K. Ikeda, H. Sumiya, S. Tsuji, I. Mori, H. Tochio, Y. Harada, M. Shirakawa, *Nano Lett.* **2012**, *12*, 5726 – 5732.
[16] A. Hegyi, E. Yablonovitch, *Nano Lett.* **2013**, *13*, 1173 – 1178.
[17] S. A. Dahoumane, M. N. Nguyen, A. Thorel, J.-P. Boudou, M. M. Chehimi, C. Mangeney, *Langmuir* **2009**, *25*, 9633 – 9638.
[18] V. K. A. Sreenivasan, E. A. Ivukina, W. Deng, T. A. Kelf, T. A. Zdobnova, S. V. Lukash, B. V. Veryugin, O. A. Stremovskiy, A. V. Zvyagin, S. M. Deyev, *J. Mater. Chem.* **2011**, *21*, 65 – 68.
[19] L. Marcon, Z. Kherrouche, J. Lyskawa, D. Fournier, D. Tulasne, P. Woisel, R. Boukherroub, *Chem. Commun.* **2011**, *47*, 5178 – 5180.
[20] A. Krueger, D. Lang, *Adv. Funct. Mater.* **2012**, *22*, 890 – 906.
[21] L. Zhao, T. Takimoto, M. Ito, N. Kitagawa, T. Kimura, N. Komatsu, *Angew. Chem.* **2011**, *123*, 1424 – 1428; *Angew. Chem. Int. Ed.* **2011**, *50*, 1388 – 1392.
[22] T. Takimoto, T. Chano, S. Shimizu, H. Okabe, M. Ito, M. Morita, T. Kimura, T. Inubushi, N. Komatsu, *Chem. Mater.* **2010**, *22*, 3462 – 3471.
[23] X. Zhang, S. Wang, C. Fu, L. Feng, Y. Ji, L. Tao, S. Li, Y. Wei, *Polym. Chem.* **2012**, *3*, 2716 – 2719.
[24] A. Barras, S. Szunerits, L. Marcon, N. Monfilliette-Dupont, R. Boukherroub, *Langmuir* **2010**, *26*, 13168 – 13172.
[25] T. Meinhardt, D. Lang, H. Dill, A. Krueger, *Adv. Funct. Mater.* **2011**, *21*, 494 – 500.
[26] E. E. Romanova, R. Akiel, F. H. Cho, S. Takahashi, *J. Phys. Chem. A* **2013**, DOI: 10.1021/jp403183x.
[27] I. Rehor, J. Slegerova, J. Kucka, V. Proks, V. Petrakova, M.-P. Adam, F. Treussart, S. Turner, S. Bals, P. Sacha, M. Ledvina, A. M. Wen, N. F. Steinmetz, P. Cigler, *Small* **2013**, DOI: 10.1002/smll.201302336.
[28] J. Havlik, V. Petrakova, I. Rehor, V. Petrak, M. Gulka, J. Stursa, J. Kucka, J. Ralis, T. Rendler, S.-Y. Lee, R. Reuter, J. Wrachtrup, M. Ledvina, M. Nesladek, P. Cigler, *Nanoscale* **2013**, *5*, 3208 – 3211.
[29] E. von Haartman, H. Jiang, A. A. Khomich, J. Zhang, S. A. Burikov, T. A. Dolenko, J. Ruokolainen, H. Gu, O. A. Shenderova, I. I. Vlasov, J. M. Rosenholm, *J. Mater. Chem. B* **2013**, *1*, 2358 – 2366.
[30] N. Prabhakar, T. Näreoja, E. von Haartman, D. Sen Karaman, H. Jiang, S. Koho, T. A. Dolenko, P. Hänninen, D. I. Vlasov, V. G. Ralchenko, S. Hosomi, I. I. Vlasov, C. Sahlgren, J. M. Rosenholm, *Nanoscale* **2013**, *5*, 3713 – 3722.
[31] A. Bumb, S. K. Sarkar, N. Billington, M. W. Brechbiel, K. C. Neuman, *J. Am. Chem. Soc.* **2013**, *135*, 7815 – 7818.
[32] V. Hong, S. I. Presolski, C. Ma, M. G. Finn, *Angew. Chem.* **2009**, *121*, 10063 – 10067; *Angew. Chem. Int. Ed.* **2009**, *48*, 9879 – 9883.
[33] J. Kopeček, *Adv. Drug Delivery Rev.* **2013**, *65*, 49 – 59.
[34] Y. Zhang, J. Yang, *J. Mater. Chem. B* **2013**, *1*, 132 – 148.
[35] F. Zhang, E. Lees, F. Amin, P. Rivera Gil, F. Yang, P. Mulvaney, W. J. Parak, *Small* **2011**, *7*, 3113 – 27.
[36] K. Binder, A. Milchev, *J. Polym. Sci. Part B* **2012**, *50*, 1515 – 1555.
[37] V. Petráková, A. Taylor, I. Kratochvilova, F. Fendrych, J. Vacik, J. Kucka, J. Stursa, P. Cigler, M. Ledvina, A. Fiserova, P. Kneppo, M. Nesládek, *Adv. Funct. Mater.* **2012**, *22*, 812 – 819.
[38] V. Petráková, M. Nesládek, A. Taylor, F. Fendrych, P. Cígler, M. Ledvina, J. Vacík, J. Štursa, J. Kučka, *Phys. Status Solidi A* **2011**, *208*, 2051 – 2056.
[39] H. Hlídková, D. Horák, V. Proks, Z. Kučerová, M. Pekárek, J. Kučka, *Macromol. Biosci.* **2013**, *13*, 503 – 511.
[40] K. Sivakumar, F. Xie, B. M. Cash, S. Long, H. N. Barnhill, Q. Wang, *Org Lett.* **2004**, *6*, 4603 – 4606.
[41] H. Macková, V. Proks, D. Horák, J. Kučka, M. Trchová, *J. Polym. Sci. Part A* **2011**, *49*, 4820 – 4829.
[42] V. Proks, J. Jaroš, O. Pop-Georgievski, J. Kučka, Š. Popelka, P. Dvořák, A. Hampl, F. Rypáček, *Macromol. Biosci.* **2012**, *12*, 1232 – 1242.
[43] M. Benezra, O. Penate-Medina, P. B. Zanzonico, D. Schaer, H. Ow, A. Burns, E. DeStanchina, V. Longo, E. Herz, S. Iyer, J. Wolchok, S. M. Larson, U. Wiesner, M. S. Bradbury, *J. Clin. Invest.* **2011**, *121*, 2768 – 2780.
[44] S. Ji, J. Xu, B. Zhang, W. Yao, W. Xu, W. Wu, Y. Xu, H. Wang, Q. Ni, H. Hou, X. Yu, *Cancer Biol. Ther.* **2012**, *13*, 206 – 215.

Received: October 3, 2013
Published online on December 11, 2013

CHEMPLUSCHEM

Supporting Information

Fluorescent Nanodiamonds with Bioorthogonally Reactive Protein-Resistant Polymeric Coatings

Ivan Rehor,[a] Hana Mackova,[b] Sergey K. Filippov,[b] Jan Kucka,[b, c] Vladimir Proks,[b] Jitka Slegerova,[a] Stuart Turner,[d] Gustaaf Van Tendeloo,[d] Miroslav Ledvina,[a] Martin Hruby,*[b] and Petr Cigler*[a]

cplu_201300339_sm_miscellaneous_information.pdf

Supporting Information

Materials and Methods

Chemicals and solvents

Tetraethoxysilane (TEOS), 3-(trimethoxysilyl)propyl methacrylate (TMPM), and polyvinylpyrrolidone MW = 10,000 g/mol (PVP) were purchased from Sigma-Aldrich, Alexa488-azide from Life Technologies. [^{125}I]-NaI solution was obtained from Lacomed Ltd. (Řež, Czech Republic). ^{125}I-labeled RGDS peptide was synthesized and radiolabeled on solid phase as previously described.[1] *N*-Propargyl acrylamide (AlkMA) and 3-(azidopropyl)methacrylamide (AzMA) were synthesized by acryloylation of propargylamine or azidopropylamine with acryloyl chloride.[1] HPMA,[2] coumarin-azide,[3] and THPTA ligand[4] were synthesized according to published procedures. For structures of reagents see Scheme S1.

HPMA and AIBN were purified directly before polymerization by recrystallization. HPMA was recrystallized twice from an acetone:hexane mixture (1:1 vol:vol). AIBN was recrystallized once from acetone. The temperature was held below 30 °C during all recrystallization procedures.

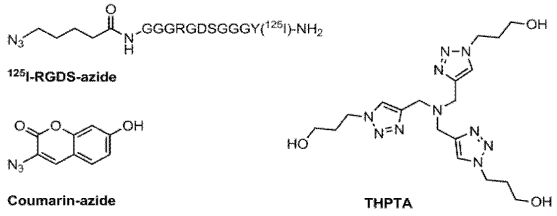

Scheme S1 Structure of reagents used for modification of nanodiamonds.

Instrumental Methods

Infrared (IR) spectroscopy

IR spectra were recorded from 4000 cm^{-1} to 400 cm^{-1} on a Bruker Equinox spectrometer using KBr pellets. The sample weight was 1.0 mg/pellet for all samples.

UV-Vis spectroscopy

UV-Vis spectra were recorded with a Specord 210 (Analytik Jena) spectrometer in the 300–700 nm range at room temperature with an optical path of 1 cm.

Luminescence spectroscopy

Luminescence measurements were performed on an Edinburgh Instruments FS900 spectrofluorimeter equipped with a 450 W xenon arc lamp, a microsecond flash lamp, and a red-sensitive photomultiplier (300–850 nm).

Thermogravimetry

Thermogravimetry was measured with a Setaram Setsys instrument. Approximately 1 mg powder sample was heated under air with a heating rate of 20 °C/min.

Electron microscopy

To prepare the samples, a drop of diluted colloidal solution was placed on a carbon-coated copper grid and left to dry. High resolution TEM experiments were carried out on a FEI Titan 80-300 "cubed" microscope fitted with an aberration-corrector for the imaging lens and operated at 80 kV to minimize knock-on damage to the sample.

Dynamic light scattering (DLS)

For stability studies in biological buffers, DLS was recorded with a Zetasizer Nano ZS system (Malvern Instruments) at 25 °C. Sample concentrations were 0.05 mg/mL.

For stability studies at various pH values, DLS was carried out on an ALV instrument equipped with a 22 mW He–Ne laser. An ALV 6000, multi-bit, multi-tau autocorrelator covering approximately 12 decades in the delay time τ was used for measurements of time autocorrelation functions. The correlation functions were analyzed with REPCALC analytical software,[5] which provides a relaxation time distribution function, $G(\tau)$. The temperature was controlled within 0.05 °C. The prepared samples were filtered into a dust-free cell. Experiments were conducted in a broad angular range (30-150°). The diffusion coefficient D was obtained from the standard relation:

$$\Gamma = \tau^{-1} = D_{tr} q^2 \qquad (1)$$

where Γ is the relaxation rate and $q = 4\pi n \sin(\theta/2)/\lambda$ is the scattering vector with λ representing the laser wavelength, n the refractive index of the solvent, and θ the scattering angle. The apparent particle hydrodynamic radius, R_h, was calculated using the Stokes-Einstein equation.

For turbid samples, R_h was additionally measured at a scattering angle (θ) of 173° on a Zetasizer Nano-ZS, Model ZEN3600 (Malvern Instruments, UK). For evaluation of data, we used the DTS (Nano) program. The universal Britton-Robinson acetate-borate-phosphate buffer with constant ionic strength (0.15 mol/L) was used for stability studies. The nanodiamond concentration was 10 mg/mL.

Radioactivity measurements

Gamma emission of ^{125}I was measured with an ionization-chamber Bqmetr 4 applied activity indicator (Empos, Prague, Czech Republic). The concentrations of RGDS in samples were calculated based on measured activity and known activity per 1 mg labeled RGDS.

ND modifications

ND pretreatment

NDs were supplied by Microdiamant Switzerland (MSY 0-0.05). The particles were oxidized by air in a Thermolyne 21100 tube furnace at 510 °C for 5 hours. The NDs were subsequently treated with a mixture of HNO_3 and H_2SO_4 (85 °C, 3 days), washed with 0.1 M NaOH and 0.1 M HCl, washed five times with water, and freeze-dried.[5] Purified ND powder (160 mg), containing approximately 100–200 ppm of natural nitrogen impurities, was pressed in an aluminum target holder and irradiated with a 15.5 MeV proton beam extracted from the isochronous cyclotron U-120M for 70 min (fluence 6 x 10^{16} cm^{-2}). The irradiated material was annealed at 900 °C for 1 h and subsequently oxidized for 6 h at 510 °C. The NDs were then treated with a mixture of HNO_3 and H_2SO_4 (85 °C, 3 days), washed with 0.1 M NaOH and 0.1 M HCl, washed five times with water, and freeze-dried. Prior to use, the particles were dissolved in water (2 mg/mL) and sonicated with a probe (Cole-Parmer, 750 W) for 30 minutes. The resulting transparent colloid was filtered using a 0.2 µm PVDF filter.

Coating of ND particles with methacrylate-terminated thin silica layer

Polyvinylpyrrolidone (96 mg, 9.6 µmol) was dissolved in water (204 mL) and sonicated for 10 minutes in an ultrasonic bath. ND colloid (6 mL, 2 mg/mL; i.e., 12 mg NDs) was added, and the mixture was stirred for 24 hours. The colloid was then concentrated via centrifugation in two steps. In the first step (40,000 rcf, 1 hour), the volume was reduced to approximately 12 mL. The second centrifugation step (30,000 rcf, 30 min) was performed in microvials and reduced the solvent volume to approximately 0.4 mL. Sedimented NDs were resuspended in ethanol (12 mL) in a round bottom flask and sonicated in an ultrasonic bath for 2-4 min. TEOS (84 mg, 404 µmol) and 3-(trimethoxysilyl) propylmethacrylate (28 mg, 113 µmol) were added. After 2 minutes of vigorous stirring, ammonia solution (25%, 500 µL) was added, and the reaction mixture was stirred for 14 h. The product was purified by centrifugation (14,000 rcf, 5 min) with ethanol (12 mL, 4x) and was dissolved in 6 mL of MeCN. The methacrylated silica-coated particles were stored in the freezer (–18 °C) as a stable colloid for several weeks without changes in particle characteristics (confirmed with TEM and DLS) or reactivity.

Coating of NDs with polymer layer

A dispersion of silica-coated NDs in ethanol (2 mg/mL, 0.5 mL; i.e., 1 mg NDs) was diluted with ethanol (9 mL). Freshly recrystallized *N*-(2-hydroxypropyl) methacrylamide (HPMA, 298 mg, 2.1 mmol), *N*-propargyl acrylamide (AlkMA, 52 mg, 0.48 mmol), and azobis(isobutyronitrile) (AIBN, 100 mg, 0.61 mmol) were added. The polymerization was carried out at 70 °C for 16 h. After polymerization, the NDs were centrifuged at 14,000 rcf. The pellet was re-dispersed in ethanol (1.3 mL) and then washed with ethanol (1.3 mL) two additional times, separated with 15 min centrifugation at 16,000, 20,000, and 25,000 g, respectively. Particles were washed three

times with water (1.3 mL each) and separated by centrifugation (30,000 g, 15 min). The NDs were re-dispersed in 1 mL water.
To obtain NDs suitable for modification with alkynes, AlkMA was substituted with the same molar amount of 3-(azidopropyl)methacrylamide (AzMA, 73 mg, 0.48 mmol).

Functionalization of coated NDs by click reaction

A solution of Cu-catalyst was prepared in a separate vial by mixing $CuSO_4 \cdot 5H_2O$ (20 µL of a 25 mM solution) and THPTA ligand (20 µL of a 50 mM solution).
The click reactions were performed similarly to those described in ref.[4] by mixing reactants in a 1.5 mL vial in the following order and quantities:

1. Aqueous colloid of poly(HPMA)-AlkMA coated NDs (250 µL containing 0.5 mg of ND)
2. ^{125}I-labeled RGDS-azide (222 µL of a 0.46 mM aqueous solution), A488 alkyne/azide (13.2 µL of 3.2 mM DMSO solution) or coumarin azide (8.4 µl of a 7.6 mM DMSO solution)
3. Aminoguanidine hydrochloride (32 µL of a 100 mM solution)
4. Cu-catalyst solution (16.5 µL) (see above)
5. Water was added to adjust the total reaction volume to 608 µL
6. Sodium ascorbate (32 µL of a 100 mM solution)

The vials were well-sealed and kept for 2 hours without stirring or shaking. Modified nanoparticles were isolated in almost quantitative yield by centrifugation (20,000 rcf, 10 min) and washed with water (2x, 1 mL) and PBS buffer (3x, 1 mL). The amount of molecules attached to the nanoparticles was quantified by UV-Vis spectrophotometry in the case of Alexa488 or by radioactivity measurements in the case of ^{125}I-labeled RGDS. The loads were found to be 20 µmol per gram of NDs in the case of Alexa488 azide and 14 µmol/g in the case of Alexa 488 alkyne, respectively. For attachment of ^{125}I-labeled RGDS-azide we used 2.5-times higher concentration than that of Alexa488-azide. The load of radiolabeled RGDS estimated by radioactivity measurements was 73 µmol/g (3.6-times higher, than in the case of Alexa488-azide). The loads of the respective molecules slightly varied in each repetition of the reaction; however, the range of yields remained always in tens of micromoles per 1 g of NDs.

Physico-chemical characterization

Stability experiments

A colloidal solution of NDs (1 mg/ml, 100 µL) was added to 10 mM buffer (900 µL). The pH of the buffer was checked before ND addition. The following buffers (pH) were used: MES (6.0), HEPES (7.4), and PBS (7.5). We also assessed particle stability in 0.15 M NaCl and in cell growth medium (RPMI-1640 + serum). The samples were stored at 4 °C, and the aggregation state was examined with DLS 2 hours, 2 days, and 2 weeks after mixing.
Universal Britton-Robinson acetate-borate-phosphate buffer with constant ionic strength (0.15 mol/L) was used for stability studies at various pH values. The pH of the buffer was set to 3.0, 5.0, 7.0, 9.0, and 11.0. The ND concentration was 10 mg/ml in all samples. The aggregation state was examined with DLS 1 hour, 1 week, and 2 weeks after mixing.

Radiolabeling of bovine serum albumin (BSA) with ^{125}I

BSA (20 mg) was dissolved in PBS (500 µL) and purified on a PD-10 desalting column (GE Healthcare, Uppsala, Sweden) using water as the eluent. BSA-containing fractions were freeze-dried. This purified BSA (3 mg) was dissolved in 300 µL PBS, pH 7.4, and [^{125}I]-NaI stock solution (20 µL, 380 MBq) was added. After addition of aqueous chloramine T (20 µL, 10 mg/mL), the mixture was incubated for 60 min at room temperature. The reaction was stopped by the addition of an ascorbic acid solution (50 µL, 10 mg/mL in PBS) and 30 min incubation at room temperature. The BSA fraction was isolated on a PD-10 column using water as eluent and was freeze-dried. Yield: 332 MBq (93%) in 3 mg protein

Albumin adsorption to nanodiamonds

An aqueous dispersion of nanodiamonds (50 µL, 1 mg/mL) was added to PBS (250 µL) containing a solution of ^{125}I-labeled BSA (5 µL, 1 mg/mL BSA in PBS, 100 MBq ^{125}I/mL) in a 1.5 mL Eppendorf vial. The entire vial was measured for radioactivity (A_{tot}) with a Bqmetr 4 ionization chamber (Empos Ltd., Prague, Czech Republic). After 30 min incubation, nanodiamonds were centrifuged, and the radioactivity of 100 µL supernatant (A_s) was measured. The mass of albumin bound to nanodiamonds m_{ads} (in µg) was calculated according to equation 2:

$$m_{ads} = 5 * [1 - (3.05 * A_s / A_{tot})] \quad (2)$$

The calculated mass of adsorbed albumin was 4.25 µg for naked nanodiamonds and 1.15 µg for poly(HPMA-AlkMA).

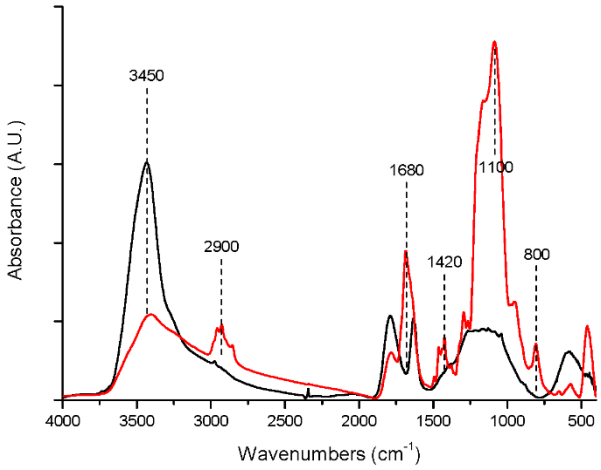

Figure S1. Normalized FTIR spectra of silica-coated NDs (red) and naked NDs (black). The characteristic peak at about 1100 cm^{-1} corresponds to the asymmetric stretching vibrations of the Si–O–Si from silica shell. The peak around 1680 cm^{-1} corresponds to the alkenyl C=C stretch vibration. Bands at 2900 cm^{-1} correspond to the alkyl stretch vibration of the trimethylene chain of silylpropylmethacrylate; the corresponding bending vibration can be found at 1420 cm^{-1}. The band at 800 cm^{-1} corresponds to the =C-H bending vibration.

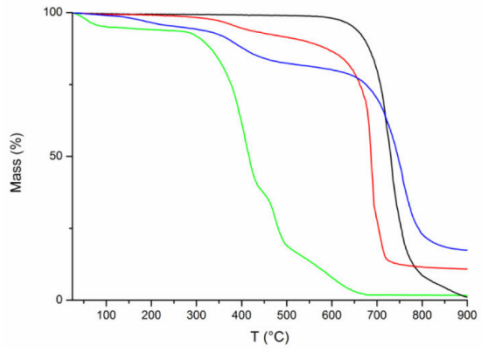

Figure S2. TGA curves of pure ND (black), pure poly(HPMA) polymer (green), ND coated with silica shell (red), and ND coated with silica shell and polymeric shell (blue).

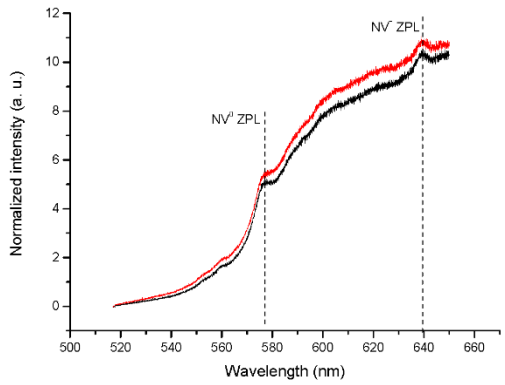

Figure S3. Normalized photoluminescence spectra of non-coated NDs (black) and poly(HPMA-AlkMA)-coated NDs. The normalization to the diamond Raman signal enabled comparison of relative change in fluorescence caused by formation of the shell. The relative difference in photoluminescence intensity is within the standard deviation of the measured data. Each spectrum shows an average of 50 normalized measurements. The standard deviation was 5.6% for ND and 6.3% for ND-poly(HPMA-AlkMA). ZPL: zero phonon line.

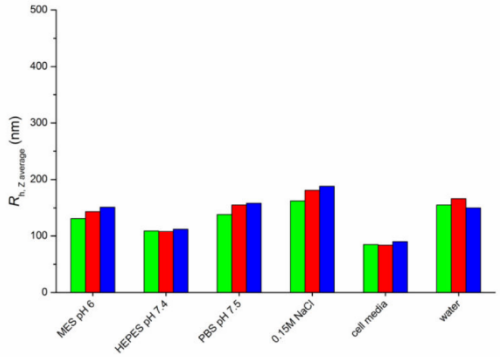

Figure S4: Stability of coated NDs in biologically relevant buffers followed by DLS two hours (green), two days (red), and two weeks (blue) after mixing.

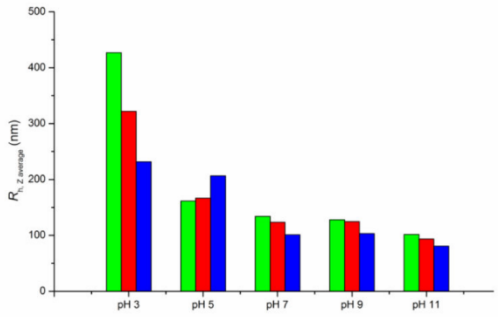

Figure S5: Stability of coated NDs in Britton-Robinson acetate-borate-phosphate buffer at various pH values followed by DLS two hours (green), two days (red), and two weeks (blue) after mixing. The increasing particle diameter at pH = 3 indicates a modest agglomeration. Nevertheless, a precipitation has not been observed in any case.

References

1. H. Macková, V. Proks, D. Horák, J. Kučka, and M. Trchová, *J. Polym. Sci. Part Polym. Chem.*, 2011, **49**, 4820–4829.
2. S. K. Filippov, P. Chytil, P. V Konarev, M. Dyakonova, C. Papadakis, A. Zhigunov, J. Plestil, P. Stepanek, T. Etrych, K. Ulbrich, and D. I. Svergun, *Biomacromolecules*, 2012, **13**, 2594–604.
3. K. Sivakumar, F. Xie, B. M. Cash, S. Long, H. N. Barnhill, and Q. Wang, *Org Lett*, 2004, **6**, 4603–4606.
4. V. Hong, S. Presolski, C. Ma, and M. G. Finn, *Angew. Chem. Int. Ed.*, 2009, **48**, 9879–9883.

Appendix C – Publication 3

Jitka Slegerova, Miroslav Hajek, Ivan Rehor, Frantisek Sedlak, Jan Stursa, Martin Hruby, Petr Cigler: Designing the nanobiointerface of fluorescent nanodiamonds: highly selective targeting of glioma cancer cells, Nanoscale, *7*, 415, **2015**.

Nanoscale

COMMUNICATION

View Article Online
View Journal | View Issue

Cite this: *Nanoscale*, 2015, **7**, 415

Received 20th May 2014,
Accepted 20th July 2014

DOI: 10.1039/c4nr02776k

www.rsc.org/nanoscale

Designing the nanobiointerface of fluorescent nanodiamonds: highly selective targeting of glioma cancer cells†

Jitka Slegerova,[a,b] Miroslav Hajek,[a] Ivan Rehor,[a] Frantisek Sedlak,[a,b] Jan Stursa,[c] Martin Hruby[d] and Petr Cigler*[a]

Core–shell nanoparticles based on fluorescent nanodiamonds coated with a biocompatible *N*-(2-hydroxypropyl)methacrylamide copolymer shell were developed for background-free near-infrared imaging of cancer cells. The particles showed excellent colloidal stability in buffers and culture media. After conjugation with a cyclic RGD peptide they selectively targeted integrin $\alpha_v\beta_3$ receptors on glioblastoma cells with high internalization efficacy.

Optical imaging using fluorescent probes is an essential tool in contemporary biomedicine with emerging applications in areas such as cancer diagnosis. Fluorescence imaging holds advantages over other imaging methods: high sensitivity, good spatial resolution and the possibility to create environment-sensitive sensors. Although various types of molecular and nanoparticle probes have been described, they typically have limited applicability due to photobleaching, photoblinking and/or intrinsic toxicity. Fluorescent nanodiamonds (FNDs), recently introduced biocompatible near-infrared fluorescent probes, do not possess any of these disadvantages, which renders them promising nanoparticles for bioimaging applications.[1–3] Point defects in the crystal lattice structure called nitrogen-vacancy (NV) centers are responsible for the fluorescence of FNDs. NV centers are non-photobleachable and non-photoblinking fluorophores with maximum emission around 700 nm (ref. 4) and a long lifetime[5] of roughly 11–19 ns. These features have led to the use of the bright HPHT FNDs (FNDs prepared from high-pressure, high-temperature NDs) in demanding optical applications such as single particle tracking inside cells,[6] long-term *in vivo* tracking of particles,[7] tracing of neuronal processes,[8,9] revealing the relationships between the particle shape and their intracellular fate[10] and fluorescence lifetime imaging microscopy *in vitro*[11] and *in vivo*.[5] The unique sensitivity of the NV center to the electric and magnetic field was also utilized for the construction of various FND-based sensors.[12–14] Here, we show selective and highly effective targeting of glioblastoma cells (U-87 MG) expressing integrin $\alpha_v\beta_3$ using polymer-modified FND particles bearing cyclic RGD peptides.

Specific ligands attached to fluorescent probes can control probe distribution in a living system by targeting certain cellular receptors or compartments. Targeting using nanoparticles has some advantages over targeting with conventional probes. Nanoparticles have a polyvalent surface, which strengthens the binding efficacy of the targeting ligands to, for example, overexpressed receptors on cancer cells. This phenomenon is called avidity.[15,16] In contrast to free ligands, nanoparticles are not filtered through glomerular capillaries due to their size, and the efficiency of targeting is therefore increased due to the prolonged blood circulation time.[17] In cancer therapy, nanoprobes accumulate nonspecifically inside solid tumors due to the abnormal leaky tumor vasculature (Enhanced Permeation Retention, EPR effect).[18] The targeting of cancer cells by HPHT FNDs has been performed *in vitro* with various ligands such as transferrin,[19] folic acid,[20] growth hormone[21] and chlorotoxin-like peptide.[22]

The RGD recognition sequence occurs in fibronectin, fibrinogen, collagen, laminin and many other proteins present in the extracellular matrix.[23–26] This sequence specifically interacts with the integrin superfamily. The integrin receptors contain non-covalently associated α and β subunits.[15,23–26] $\alpha_v\beta_3$ integrins are overexpressed on cancer cells and endothelial cells in the tumor neovasculature. Overexpressed $\alpha_v\beta_3$ integrins are found in melanoma, breast cancer, prostate cancer, pancreatic cancer, ovarian cancer, glioblastoma and neuroblastoma.[25,27] Synthetic peptides bearing the RGD sequence and antibodies against $\alpha_v\beta_3$ integrins have been successfully used in the targeted delivery of diagnostic probes and drugs to cancer cells and tumors.[15,23] The effectiveness of targeting using the RGD motif can be improved by its cyclization. Cyclic

[a]*Institute of Organic Chemistry and Biochemistry AS CR, v.v.i., Flemingovo nam. 2, 166 10, Prague 6, Czech Republic. E-mail: cigler@uochb.cas.cz*
[b]*First Faculty of Medicine, Charles University, Katerinska 32, 121 08, Prague 2, Czech Republic*
[c]*Nuclear Physics Institute AS CR, v.v.i., 250 68 Rez near Prague, Czech Republic*
[d]*Institute of Macromolecular Chemistry AS CR, v.v.i., Heyrovskeho nam. 2, 162 06, Prague 6, Czech Republic*
†Electronic supplementary information (ESI) available: Materials and methods, colloidal stability studies and cell viability studies. See DOI: 10.1039/c4nr02776k

RGD (cRGD) peptides have higher stability, structural rigidity and better binding properties and integrin selectivity compared to linear RGD.[24,28] Peptides containing the RGD sequence are also considered promising therapeutics, because of their ability to block the integrin function.[23] For example, cilengitide, a cRGD peptide that may inhibit angiogenesis, is currently being tested in phase III clinical trials for the treatment of glioblastoma.[24]

In this work, we describe selective and specific targeting of cells derived from glioblastoma (U-87 MG; an aggressive, highly vascularized brain tumor) by FNDs. Although glioblastoma cells have been previously used as a target for cRGD-modified nanoparticles such as carbon nanotubes,[29] quantum dots[30] and gold nanoparticles,[31] effective targeting of cancer cells with directly modified FNDs is not a simple task because of their strong tendency to aggregate in biological liquids (such as buffers, media and blood).[32,33] The FND aggregates adhere non-specifically to the cell surface,[34] which can, in turn, also prevent the desired tumor selectivity due to the non-specific premature entrapment into the reticuloendothelial system. The biocompatibilization of nanodiamonds can be achieved using various direct surface modifications[35] or by polymer coatings such as polyglycerol,[36–38] poly[*N*-(2-hydroxypropyl) methacrylamide],[39] poly(ethylene oxide) (PEG),[40] PEG copolymers[41,42] and Zonyl polymer.[43] However, the targeting of a brain tumor such as glioblastoma is challenging also because of limited permeability of the blood–brain barrier (BBB). In recent studies it has been shown that BBB breakdown in tumors allows nanoparticles <200 nm in diameter to bypass the BBB and enter the brain.[44] For this type of transport a minimally adhesive nanobiointerface such as a dense PEG[44] or siRNA[45] layer is the key parameter enabling the direct treatment of brain tumors without the need for targeting moieties. Another pathway for transporting the drugs into a brain tumor is convection-enhanced delivery which can be significantly enhanced by complexation of a drug with nanodiamonds.[46]

These examples show effective ways for targeting the brain tumors based on the size and surface properties of nanoparticles. We focused here rather on controlling the selectivity of targeting using active moieties attached to FNDs and on cellular delivery of these particles in the glioblastoma model. We used our recently developed core–shell nanoparticles,[39] which comprise an FND coated with an ultra-thin silica layer and a layer of biocompatible polymethacrylamide copolymer (Scheme 1). This type of copolymer has comparable biocompatible properties as PEG[47] and serves here as a "click"-reactive interface that shields the particles against aggregation and non-specific interactions in biological environments. The layer also functions as a flexible spacer between the FND and a biomolecule.

We coated the FNDs with an ultrathin (<1 nm) silica shell grown from a mixture of tetraethoxysilane and 3-(trimethoxysilyl)propyl methacrylate using a modified Stöber procedure. A methacrylated silica layer on a FND was further coated with a copolymer of *N*-(2-hydroxypropyl)methacrylamide and *N*-propargylacrylamide. The copolymer chains were grown from the nanoparticle surface ("grafting from" approach[39]) by radical polymerization with azobis(isobutyronitrile) (AIBN) as the initiator. We focused on improving the previously described coating procedure and adjusting the reaction conditions to prefer the growth of longer polymeric chains. We increased the viscosity of the reaction mixture by performing the reaction in DMSO instead of ethanol, decreased the polymerization temperature from 70 °C to 55 °C, prolonged the time from 1 to 3 days and used a 7.5-fold higher concentration of FNDs (0.85 mg ml^{-1}) and monomers [2 M *N*-(2-hydroxypropyl)-

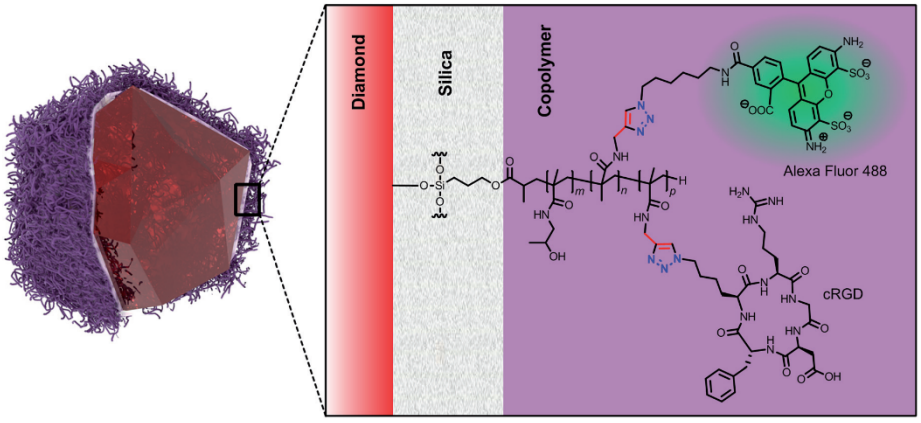

Scheme 1 Schematic structure of the fluorescent nanodiamond crystal coated with a biocompatible methacrylamide copolymer grown from an ultrathin silica shell. The copolymer bears the secondary fluorescent probe (Alexa Fluor 488) and the targeting peptide (cRGD). Both molecules were stepwise attached *via* click chemistry, providing the conjugate marked as "**FND–cRGD**" (shown here in the scheme). Reaction with only Alexa Fluor 488 provided the control particles marked in the text as "**FND**".

methacrylamide and 35 mM *N*-propargylacrylamide]. The obtained coatings further enhanced the colloidal stability of FNDs in biological environments and completely eliminated non-specific adhesion on cells. The newly prepared coated FNDs were stable even in solutions with extreme ionic strength (1 M NaCl) in contrast to our previously described polymer-coated FNDs, which were stable in NaCl solutions at concentrations up to only 0.15 M (Fig. 1S and 2S in the ESI†). In control experiments, we also did not observe any nonspecific interactions between polymer-coated FNDs and cells (see below).

To conjugate the cRGD moiety to the particles, we utilized the alkyne groups present on the copolymer chains. They are suitable for Cu(I)-catalyzed azide–alkyne cycloaddition ("click" reaction), enabling high yielding attachment of various azide-modified molecules.[48,49] The click reaction is convenient due to its high efficacy in an aqueous environment (fast kinetics under mild conditions), applicability for diverse substrates without conformational changes (from small molecules to polymers, proteins and nanoparticles) and experimental simplicity.[49–51] The click reaction is particularly attractive due to its biological inertness (bioorthogonality), in which protecting groups are avoided while specificity is ensured.[49,50]

We selected cyclic (Arg-Gly-Asp-D-Phe-Lys)-azide (Scheme 1) from a variety of cRGDs.[25] The presence of a lysine residue makes the peptide an ideal building block for further chemical conjugation reactions, such as the introduction of a bioorthogonally reactive azide group. For good targeting efficiency, the RGD peptide also needs to be exposed far from the nanoparticle surface,[52] which was here ensured by the flexibility of the polymer chains as well as by the presence of the lysine linker. The hydrodynamic diameter of the nanoparticulate bioconjugate is also kept in the range suitable for passive accumulation in solid tumor tissue due to the EPR effect or for entering the brain *via* BBB breakdown in tumors (<*ca.* 200 nm).[44] We further attached Alexa Fluor 488 to all types of particles used in the study of nanoparticles as a secondary fluorescent label because our flow cytometry setup does not allow direct observation of FND fluorescence.

We modified our polymer-coated FNDs stepwise with Alexa Fluor 488-azide and cRGD–azide using the same conjugation procedure (click chemistry). Running the reaction with a low molar excess of the first compound (Alexa Fluor 488-azide) over polymer alkyne groups resulted in substitution of only a fraction of the surface alkyne groups, providing **FNDs** (marked further in bold). This substitution resulted in approximately 300 Alexa Fluor 488 molecules per particle (*i.e.*, ~8 μmol g^{-1}) as determined spectrophotometrically. **FNDs** were then reacted with cRGD–azide, providing the **FND–cRGD** conjugate (for Experimental details, see the ESI†).

In cell experiments, we focused first on examining the potential toxicity of the particles. We tested the prepared conjugates at a concentration of 50 μg ml^{-1} on U-87 MG cells. Free cRGD (100 μg ml^{-1}) and the known apoptosis inducer staurosporine (0.3–5 μM) were used as controls (Fig. 3S and 4S in the ESI†). According to luminescent cell viability assay, **FNDs** and **FND–cRGD** did not harm cells under our experimental conditions (Fig. 1). The apparent decrease in the viability of cells incubated with free cRGD is a known consequence of cell detachment during the incubation. RGD sequences bound on a surface or macromolecule promote cell adhesion, whereas free RGD sequences in solution act as decoys, preventing adhesion.[26,53] Subsequently, we observed the interaction of particles with glioblastoma cells (U-87 MG) by flow cytometry and

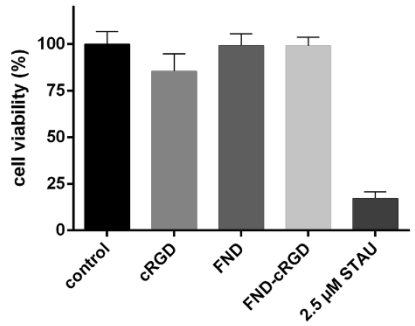

Fig. 1 Cell viability assay based on ATP quantification in cell lysates. Luminescence intensity correlates with the ATP level and thus with the quantity of metabolically active (viable) cells. Both types of polymer-coated FNDs (**FND** and **FND–cRGD** alternatives) have no impact on cell viability under the used experimental conditions. The control, FND and FND–cRGD alternatives are statistically not distinguishable among each other on the significance level α = 0.01 (ANOVA) and they are significantly different from cRGD and 2.5 μM staurosporine (α = 0.01) alternatives.

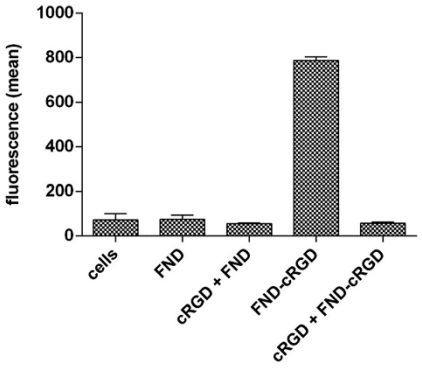

Fig. 2 Fluorescence intensity measurements of U-87 MG cells incubated with FNDs modified with cRGD (**FND–cRGD**) using flow cytometry. All types of FNDs are polymer-coated. As controls, FNDs without cRGD (**FND**) and pretreatment experiments with free cRGD peptides (cRGD + **FND** and cRGD + **FND–cRGD**) were performed. The fluorescence recorded in flow cytometry is read using Alexa Fluor 488, which is present in all types of particles. FND–cRGD specifically recognized $\alpha_v\beta_3$ integrins on U-87 MG cells. The FND + cRGD alternative is statistically significantly different from the controls (ANOVA, α = 0.01). All negative controls are statistically not distinguishable among each other on the significance level α = 0.01.

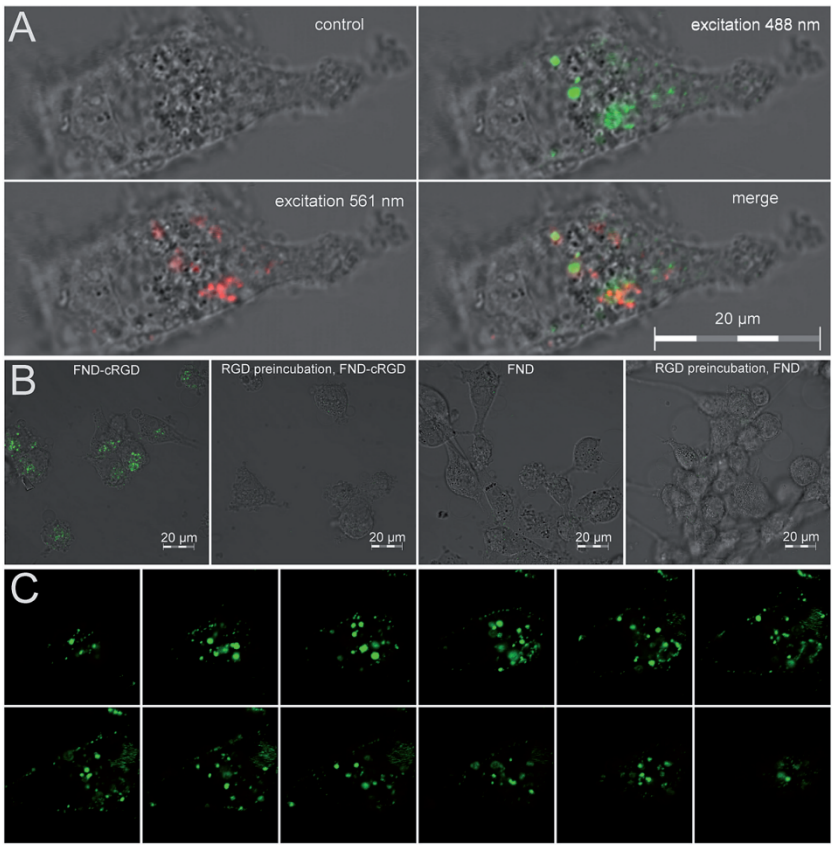

Fig. 3 Confocal fluorescence images of U-87 MG cells treated with **FND–cRGD** and **FND** nanoparticles (all particles are polymer-coated). (A) Measurement of **FND–cRGD** in cells using fluorescence of Alexa Fluor 488 and FNDs' fluorescence (excitation at 488 and 561 nm, respectively). The last picture shows merged results from both channels. The confocal images were taken at the same focal plane. The time between the measurements of Alexa Fluor 488 fluorescence and FND's intrinsic fluorescence was due to extensive photobleaching on a scale of tens of minutes. (B) Merged fluorescence and bright-field images of cells treated with **FND–cRGD** and **FND** nanoparticles with or without pretreatment with a free cRGD peptide. Only **FND–cRGD** without pretreatment was found inside the cells. The images were recorded using the Alexa Fluor 488 channel. (C) Cross-section measurement of cells treated with **FND–cRGD** shows that particles are present inside the cell. Images were recorded with a 1.5 μm step in the vertical direction and presented from left to right and top to bottom with a 28 × 28 μm field of view. The images were recorded using the Alexa Fluor 488 channel.

confocal microscopy. Either **FND** or **FND–cRGD** at a final concentration of 50 μg ml^{-1} was incubated with the cells for 1 hour.

The strong affinity of **FND–cRGD** over **FND** to U-87 MG cells was revealed by flow cytometry, which shows 12-fold higher fluorescence upon nanoparticle binding (Fig. 2; for histograms see Fig. 5S†). Differences in the surface compositions of **FND** and **FND–cRGD** (*i.e.*, the presence of a relatively hydrophobic cyclic peptide) can lead to different surface properties that are not related to integrin binding specificity. We tested therefore this possible behavior using a free cRGD peptide added in excess during pretreatment (30 min, 100 μg ml^{-1}), which saturates the RGD-binding sites (*i.e.*, $\alpha_v\beta_3$ integrins). We observed no significant differences between **FND** and **FND–cRGD** affinities when cells were pretreated with cRGD. This clearly indicates that **FND–cRGD** particles use integrins as their receptors to bind the cells and that the interaction is highly specific (Fig. 2).

We were further interested in testing the relevance of flow cytometry experiments recorded using Alexa Fluor 488 fluorescence by confocal microscopy, so we studied the colocalization of intrinsic FND and Alexa 488 fluorescence for **FND–cRGD** particles (Fig. 3A). Notably, we took advantage of the extreme photostability of FND fluorescence to record confocal images before and after photobleaching of Alexa Fluor

488 fluorescence (and cell autofluorescence). This procedure enabled background-free imaging of FND fluorescence. A similar pattern of bright spots in the merged picture (from both channel detections) showed that Alexa Fluor 488 is bound to the particles. The quantification of the colocalization data suggests that FND's fluorescence almost completely overlaps Alexa Fluor 488 fluorescence (Manderson M = 0.93) and Alexa Fluor 488 fluorescence shows also a strong overlap with FND's fluorescence (Manderson M = 0.78). These data confirmed the relevance of flow cytometry for quantification of the particle interaction with cells.

Finally, we focused on supporting the results from flow cytometry experiments using confocal microscopy and on determination whether the **FND–cRGD** particles enter the cell or remain bound to the surface. Complementary to our flow cytometry data, confocal microscopy also showed no interaction between non-targeted **FND** particles and U-87 MG cells, while the **FND–cRGD** were bound to the cells (Fig. 3B). Using confocal microscopy cross-section measurements, we found that **FND–cRGD** is localized inside the cells (Fig. 3C). This finding corresponds to the results from other studies in which internalization *via* receptor-mediated endocytosis of various RGD-targeted nanocarriers was observed.[24] Notably, a similar and effective approach as has been demonstrated here was published during revisions of this paper for targeting of the U-87 MG cells by RGD-modified polyglycerol-coated FNDs.[37]

Conclusions

We designed and prepared a novel type of FND-based nanoparticles that target glioma cells with unprecedented efficiency and specificity. The nanoparticles consist of an FND core coated with an ultra-thin silica layer and a biocompatible *N*-(2-hydroxypropyl)methacrylamide copolymer shell bearing cRGD peptides. This ligand on the nanoparticle surface is a tight-binder of integrin $\alpha_v\beta_3$ receptors, which are overexpressed on this type of cancer cells. Upon selective recognition and binding to $\alpha_v\beta_3$ receptors, the particles are internalized and localized inside the cell. Thanks to their extreme photostability, the particles can be used for background-free near-infrared imaging of cancer cells for an unlimited period of time.

Acknowledgements

The work was supported by GAČR project P108/12/0640. Irradiation of NDs was carried out at the CANAM infrastructure of the NPI AS CR Rez supported through MŠMT project no. LM2011019. The work of M. H. (IOCB AS CR) was supported by Project NPU I, LO 1302 from the Ministry of Education, Youth and Sports.

References

1 E. K.-H. Chow and D. Ho, *Sci. Transl. Med.*, 2013, **5**, 216rv4.
2 J. Slegerova, I. Rehor, J. Havlik, H. Raabova, E. Muchova and P. Cigler, in *Intracellular Delivery II*, ed. A. Prokop, Y. Iwasaki and A. Harada, Springer, Netherlands, 2014, pp. 363–401.
3 Y. Y. Hui, C. L. Cheng and H. C. Chang, *J. Phys. D: Appl. Phys.*, 2010, **43**, 374021.
4 S.-J. Yu, M.-W. Kang, H.-C. Chang, K.-M. Chen and Y.-C. Yu, *J. Am. Chem. Soc.*, 2005, **127**, 17604–17605.
5 Y. Kuo, T.-Y. Hsu, Y.-C. Wu, J.-H. Hsu and H.-C. Chang, *Proc. SPIE*, 2013, **8635**, 863503–863507.
6 Y.-R. Chang, H.-Y. Lee, K. Chen, C.-C. Chang, D.-S. Tsai, C.-C. Fu, T.-S. Lim, Y.-K. Tzeng, C.-Y. Fang, C.-C. Han, H.-C. Chang and W. Fann, *Nat. Nanotechnol.*, 2008, **3**, 284–288.
7 V. Vaijayanthimala, P.-Y. Cheng, S.-H. Yeh, K.-K. Liu, C.-H. Hsiao, J.-I. Chao and H.-C. Chang, *Biomaterials*, 2012, **33**, 7794–7802.
8 T.-C. Hsu, K.-K. Liu, H.-C. Chang, E. Hwang and J.-I. Chao, *Sci. Rep.*, 2014, **4**, 5004.
9 X. L. Le, A.-M. Lepagnol-Bestel, M.-P. Adam, A. Thomas, G. Dantelle, C.-C. Chang, N. Mohan, H.-C. Chang, F. Treussart and M. Simonneau, *Proc. SPIE*, 2012, **8232**, 823203.
10 Z. Chu, S. Zhang, B. Zhang, C. Zhang, C.-Y. Fang, I. Rehor, P. Cigler, H.-C. Chang, G. Lin, R. Liu and Q. Li, *Sci. Rep.*, 2014, **4**, 4495.
11 O. Faklaris, D. Garrot, V. Joshi, F. Druon, J. P. Boudou, T. Sauvage, P. Georges, P. A. Curmi and F. Treussart, *Small*, 2008, **4**, 2236–2239.
12 A. Ermakova, G. Pramanik, J.-M. Cai, G. Algara-Siller, U. Kaiser, T. Weil, Y.-K. Tzeng, H. C. Chang, L. P. McGuinness, M. B. Plenio, B. Naydenov and F. Jelezko, *Nano Lett.*, 2013, **13**, 3305–3309.
13 V. Petrakova, A. Taylor, I. Kratochvilova, F. Fendrych, J. Vacik, J. Kucka, J. Stursa, P. Cigler, M. Ledvina, A. Fiserova, P. Kneppo and M. Nesladek, *Adv. Funct. Mater.*, 2012, **22**, 812–819.
14 L. P. McGuinness, Y. Yan, A. Stacey, D. A. Simpson, L. T. Hall, D. Maclaurin, S. Prawer, P. Mulvaney, J. Wrachtrup, F. Caruso, R. E. Scholten and L. C. L. Hollenberg, *Nat. Nanotechnol.*, 2011, **6**, 358–363.
15 E. Ruoslahti, S. N. Bhatia and M. J. Sailor, *J. Cell Biol.*, 2010, **188**, 759–768.
16 X. Montet, M. Funovics, K. Montet-Abou, R. Weissleder and L. Josephson, *J. Med. Chem.*, 2006, **49**, 6087–6093.
17 K. Temming, R. M. Schiffelers, G. Molema and R. J. Kok, *Drug Resist. Updates*, 2005, **8**, 381–402.
18 R. K. Jain and T. Stylianopoulos, *Nat. Rev. Clin. Oncol.*, 2010, **7**, 653–664.
19 M. F. Weng, S. Y. Chiang, N. S. Wang and H. Niu, *Diamond Relat. Mater.*, 2009, **18**, 587–591.
20 B. Zhang, Y. Li, C.-Y. Fang, C.-C. Chang, C.-S. Chen, Y.-Y. Chen and H.-C. Chang, *Small*, 2009, **5**, 2716–2721.
21 C.-Y. Cheng, E. Perevedentseva, J.-S. Tu, P.-H. Chung, C.-L. Cheng, K.-K. Liu, J.-I. Chao, P.-H. Chen and C.-C. Chang, *Appl. Phys. Lett.*, 2007, **90**, 163903.

22 Y. Fu, N. An, S. Zheng, A. Liang and Y. Li, *Diamond Relat. Mater.*, 2012, **21**, 73–76.
23 J. B. Delehanty, K. Boeneman, C. E. Bradburne, K. Robertson, J. E. Bongard and I. L. Medintz, *Ther. Delivery*, 2010, **1**, 411–433.
24 F. Danhier, A. L. Breton and V. Préat, *Mol. Pharm.*, 2012, **9**, 2961–2973.
25 S. Liu, *Bioconjugate Chem.*, 2009, **20**, 2199–2213.
26 E. Ruoslahti, *Annu. Rev. Cell Dev. Biol.*, 1996, **12**, 697–715.
27 Z. Cheng, A. Al Zaki, J. Z. Hui, V. R. Muzykantov and A. Tsourkas, *Science*, 2012, **338**, 903–910.
28 S. Liu, *Mol. Pharm.*, 2006, **3**, 472–487.
29 B. R. Smith, C. Zavaleta, J. Rosenberg, R. Tong, J. Ramunas, Z. Liu, H. Dai and S. S. Gambhir, *Nano Today*, 2013, **8**, 126–137.
30 J. Gao, K. Chen, R. Xie, J. Xie, Y. Yan, Z. Cheng, X. Peng and X. Chen, *Bioconjugate Chem.*, 2010, **21**, 604–609.
31 M. Luna-Gutiérrez, G. Ferro-Flores, B. Ocampo-García, N. Jiménez-Mancilla, E. Morales-Avila, L. De León-Rodríguez and K. Isaac-Olivé, *J. Labelled Compd. Radiopharm.*, 2012, **55**, 140–148.
32 S. A. Dahoumane, M. N. Nguyen, A. Thorel, J.-P. Boudou, M. M. Chehimi and C. Mangeney, *Langmuir*, 2009, **25**, 9633–9638.
33 V. K. A. Sreenivasan, E. A. Ivukina, W. Deng, T. A. Kelf, T. A. Zdobnova, S. V. Lukash, B. V. Veryugin, O. A. Stremovskiy, A. V. Zvyagin and S. M. Deyev, *J. Mater. Chem.*, 2011, **21**, 65.
34 I. Rehor, J. Slegerova, J. Kucka, V. Proks, V. Petrakova, M.-P. Adam, F. Treussart, S. Turner, S. Bals, P. Sacha, M. Ledvina, A. M. Wen, N. F. Steinmetz and P. Cigler, *Small*, 2014, **10**, 1029.
35 A. Krueger and D. Lang, *Adv. Funct. Mater.*, 2012, **22**, 890–906.
36 L. Zhao, T. Takimoto, M. Ito, N. Kitagawa, T. Kimura and N. Komatsu, *Angew. Chem., Int. Ed.*, 2011, **50**, 1388–1392.
37 L. Zhao, Y.-H. Xu, H. Qin, S. Abe, T. Akasaka, T. Chano, F. Watari, T. Kimura, N. Komatsu and X. Chen, *Adv. Funct. Mater.*, 2014, DOI: 10.1002/adfm.201304298.
38 J.-P. Boudou, M.-O. David, V. Joshi, H. Eidi and P. A. Curmi, *Diamond Relat. Mater.*, 2013, **38**, 131–138.
39 I. Rehor, H. Mackova, S. K. Filippov, J. Kucka, V. Proks, J. Slegerova, S. Turner, G. Van Tendeloo, M. Ledvina, M. Hruby and P. Cigler, *ChemPlusChem*, 2014, **79**, 21–24.
40 T. Takimoto, T. Chano, S. Shimizu, H. Okabe, M. Ito, M. Morita, T. Kimura, T. Inubushi and N. Komatsu, *Chem. Mater.*, 2010, **22**, 3462–3471.
41 J. W. Lee, S. Lee, S. Jang, K. Y. Han, Y. Kim, J. Hyun, S. K. Kim and Y. Lee, *Mol. BioSyst.*, 2013, **9**, 1004.
42 H. B. Man, R. Lam, M. Chen, E. Osawa and D. Ho, *Phys. Status Solidi A*, 2012, **209**, 1811–1818.
43 L. Marcon, Z. Kherrouche, J. Lyskawa, D. Fournier, D. Tulasne, P. Woisel and R. Boukherroub, *Chem. Commun.*, 2011, **47**, 5178–5180.
44 E. A. Nance, G. F. Woodworth, K. A. Sailor, T.-Y. Shih, Q. Xu, G. Swaminathan, D. Xiang, C. Eberhart and J. Hanes, *Sci. Transl. Med.*, 2012, **4**, 149ra119.
45 S. A. Jensen, E. S. Day, C. H. Ko, L. A. Hurley, J. P. Luciano, F. M. Kouri, T. J. Merkel, A. J. Luthi, P. C. Patel, J. I. Cutler, W. L. Daniel, A. W. Scott, M. W. Rotz, T. J. Meade, D. A. Giljohann, C. A. Mirkin and A. H. Stegh, *Sci. Transl. Med.*, 2013, **5**, 209ra152.
46 G. Xi, E. Robinson, B. Mania-Farnell, E. F. Vanin, K.-W. Shim, T. Takao, E. V. Allender, C. S. Mayanil, M. B. Soares, D. Ho and T. Tomita, *Nanomedicine: Nanotechnology, Biology and Medicine*, 2014, **10**, 381–391.
47 J. Kopecek, *Adv. Drug Delivery Rev.*, 2013, **65**, 49–59.
48 V. Hong, S. I. Presolski, C. Ma and M. G. Finn, *Angew. Chem., Int. Ed.*, 2009, **48**, 9879–9883.
49 E. Lallana, A. Sousa-Herves, F. Fernandez-Trillo, R. Riguera and E. Fernandez-Megia, *Pharm. Res.*, 2012, **29**, 1–34.
50 G. von Maltzahn, Y. Ren, J.-H. Park, D.-H. Min, V. R. Kotamraju, J. Jayakumar, V. Fogal, M. J. Sailor, E. Ruoslahti and S. N. Bhatia, *Bioconjugate Chem.*, 2008, **19**, 1570–1578.
51 D. L. J. Thorek, D. R. Elias and A. Tsourkas, *Mol. Imaging*, 2009, **8**, 221–229.
52 U. Hersel, C. Dahmen and H. Kessler, *Biomaterials*, 2003, **24**, 4385–4415.
53 E. Ruoslahti and M. D. Pierschbacher, *Science*, 1987, **238**, 491–497.

Supplementary Information

ND pretreatment

NDs were supplied by Microdiamant Switzerland (MSY 0-0.05). The NDs were oxidized by air in a furnace (Thermolyne 21100 tube) at 510 °C for 5 h. Subsequently, the NDs were treated with a mixture of H_2SO_4 and HNO_3 (9:1) at 90 °C for 3 days and washed with water, 1 M NaOH and 1 M HCl. They were washed an additional 5 times with water and then freeze-dried. Purified ND powder (120 mg), containing approximately 100–200 ppm of natural nitrogen impurities, was irradiated in 5% aqueous colloidal solution for 210 min with a 15.7 MeV proton beam (4.9×10^{17} protons/ml) extracted from the isochronous cyclotron U-120M. The irradiated material was annealed at 900 °C for 1 h and subsequently oxidized for 4 h at 510 °C. The NDs were again treated with a mixture of H_2SO_4 and HNO_3 (9:1) at 90 °C for 3 days. The resulting material was washed with water, 1 M NaOH and 1 M HCl and an additional 5 times with water. The particles were dissolved in water (2 mg/ml) and filtered using a 0.2 μm PVDF filter, yielding ND-COOH colloid.

Coating of NDs with a methacrylate-terminated thin silica layer

Polyvinylpyrrolidone (M = 10,000, 96 mg, 9.6 μmol, purchased from Sigma-Aldrich) was dissolved in water (204 ml) and sonicated for 10 min in an ultrasonic bath. ND-COOH colloid (6 ml, 2 mg/ml) was added, and the mixture was stirred for 24 h. The colloid was then concentrated by a two-step centrifugation. In the first step (40,000 rcf, 1 hour), the volume was reduced to approximately 12 ml. The second centrifugation step (30,000 rcf, 30 min) was performed in microvials, and the solvent volume was reduced to approximately 0.2 ml. Sedimented NDs were resuspended in ethanol (12 ml) in a round bottom flask and sonicated in an ultrasonic bath for 2-4 min. Tetraethyl orthosilicate (84.06 mg, 405 μmol, purchased from Sigma-Aldrich) and 3-(trimethoxysilyl)propylmethacrylate (31.35 mg, 126 μmol, purchased from Sigma-Aldrich) were added to the round bottom flask. Ammonia (25%, 498 μl) was added after 20 s sonication in an ultrasonic bath. The reaction mixture was stirred for 14 h. The product was purified by centrifugation (14,000 - 25,000 rcf, 15 min) with ethanol (12 ml, 2 times).

Coating of NDs with a polymer layer

HPMA [700 mg, 4.82 mmol, synthesized according to published procedures[1] and freshly recrystallized twice from a mixture of acetone-hexane (1:3 v/v)] and N-propargyl acrylamide (35 mg, 0.06 mmol, synthesized by acryloylation of propargylamine with acryloyl chloride[2]) were dissolved in DMSO (2.1 ml). 2,2′-Azobis(2-methylpropionitrile) (AIBN, 200 mg, 1.22 mmol, recrystallized by thickening an ethanol solution on a rotary evaporator at a maximum temperature of 30 °C) was added to the mixture. The mixture was filtered using a 0.2 μm polytetrafluorethylene microfilter. Methacrylate-terminated ND particles (2 mg) were added. The reaction proceeded for 3 days under argon at 55 °C. The particles were centrifuged (21,000 rcf, 30 min) and purified by centrifugation with ethanol (25,000 rcf, 30 min, 1 ml, 3 times) and water (30,000 rcf, 30 min, 1 ml, 5 times).

FND colloidal stability studies

The coating method with HPMA polymer was improved compared to our recently published method[3] to yield **FNDs** with even better colloidal stability and fewer non-specific protein interactions. FNDs synthesized according to the previously published method were stable in biological solutions such as media or buffers but immediately began to aggregate in 0.5 M (and higher) NaCl concentrations, according to dynamic light scattering (DLS, Fig. 1S). The newly prepared **FNDs** are stable even after 24 h incubation in 1 M NaCl (Fig. 2S). DLS was recorded with a Zetasizer Nano ZS system (Malvern Instruments) at 25 °C. Sample concentrations were 0.1 mg/ml.

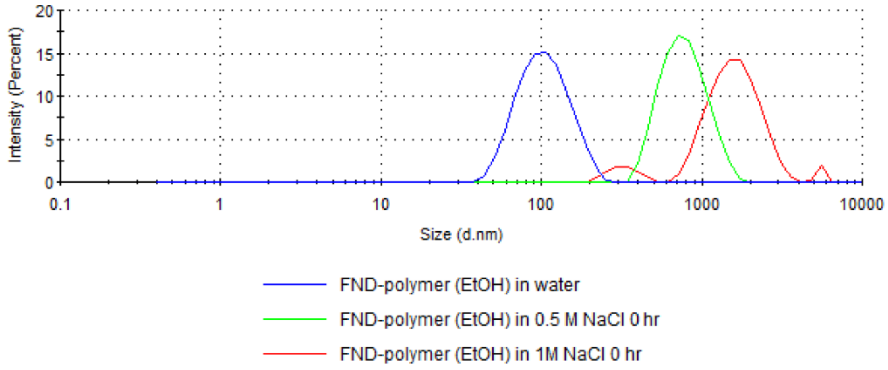

Fig. 1S Dynamic light scattering (DLS) of the size distribution of **FNDs** synthesized according to our previously published method[3] in solutions with various concentrations of NaCl. The concentration of the colloids was 0.1 mg/ml.

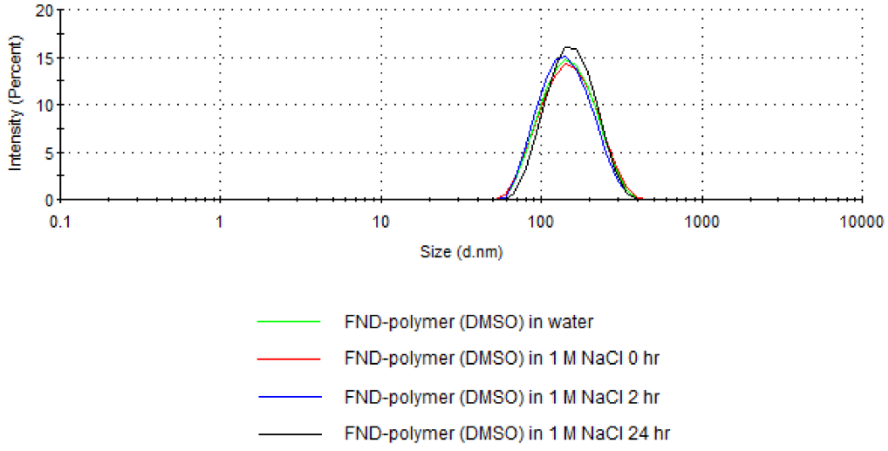

Fig. 2S Dynamic light scattering (DLS) of the size distribution of newly prepared **FNDs** in solutions containing various NaCl concentrations. The concentration of colloids was 0.1 mg/ml.

Functionalization of coated FNDs by click reaction

FNDs were modified with Alexa Fluor 488-azide (purchased from Life Technologies) and cRGD-azide (cyclo(Arg-Gly-Asp-D-Phe-Lys), purchased from Peptides International). FNDs were modified with these two ligands in consecutive reactions utilizing the same surface functionalities. Washing procedures were employed after both modification steps.

Stock solutions for copper(I)-catalyzed azide-alkyne cycloaddition reactions were prepared in water, except for the Alexa Fluor 488 stock, which was prepared in DMSO. The solutions of $CuSO_4 \cdot 5H_2O$ and tris(3-hydroxypropyltriazolylmethyl)amine (THPTA, synthesized according to published procedures[4]) were premixed (in a 1:2 concentration ratio) before they were added to the reaction mixture to yield final concentrations of 0.32 mM and 0.64 mM, respectively. The mixtures were filled to the final volume with water.

For the reaction of modified FNDs with Alexa Fluor 488-azide, the reactants were mixed in the following order and final concentrations: colloid of poly(HPMA)-alkyne modified FNDs (0.4 mg in a final reaction volume of 512 µl), Alexa Fluor 488-azide (20 µM), Cu-catalyst solution (see above), aminoguanidine hydrochloride (5 mM) and a freshly prepared solution of sodium ascorbate (5 mM). The reaction mixture was well-sealed, mixed and left for 3 h with no stirring. Modified **FNDs** were isolated by centrifugation (26,000 rcf, 10 min) and twice washed with 1 ml water. Half (0.2 mg) of the Alexa Fluor 488-modified **FNDs** was reacted in a click reaction with cRGD-azide (160 µM) under the same conditions. Polymer-coated **FNDs** modified with Alexa Fluor 488 (**FNDs**) and polymer-coated **FNDs** modified with Alexa Fluor 488 and cRGD (**FND-cRGD**) were both treated the same and were washed with water (1 ml, 7 times).

Cell culture

Human glioblastoma-astrocytoma U-87 MG cells (ATCC® HTB-14™) were cultivated in Eagle's Minimum Essential Medium (EMEM, LGC Standards Sp.z.o.o., cat. no. ATCC-30-2003) supplemented with 10% (v/v) heat-inactivated fetal bovine serum (Sigma-Aldrich), 2 mM L-glutamine (Sigma-Aldrich), 1% (v/v) non-essential amino acids (Sigma-Aldrich, cat. no. M7145) and antibiotics (100 I.U./ml penicillin, 100 µg/ml streptomycin; Sigma-Aldrich) at 37 °C in a humidified atmosphere containing 5% CO_2. Sub-confluent cells were subcultured every 3-4 days using a solution of 0.25% (w/v) trypsin and 0.53 mM EDTA (Sigma-Aldrich).

Cell viability assay

The CellTiter-Glo® Luminiscent Cell Viability Assay (Promega) was used to test U-87 MG cell viability.

U-87 MG cells were cultivated as described above. When they reached the exponential growth phase, cells were harvested and seeded into a 96-well white microtiter plate (NUNC) at 4,000 cells per well. Each well contained 90 µl cell suspension. About 24 h prior to the experiment, the growth media was replaced with 90 µl fresh media. The next day, 10 µl of 10-times concentrated modified **FND** particles were applied in pentaplicates to wells (final concentration 50 µg/ml). Free cRGD and the known apoptosis inducer staurosporine (Sigma-Aldrich) were added to the cells at concentrations of 100 µg/ml and 0.3125–5 µM, respectively. Into wells containing controls (cells without test compounds) and blanks (pure medium without cells), a volume of water equal to the volume of the compound solutions added to the experimental wells was added. After 1 h incubation with **FND** particles or compounds, the media in each well was replaced with fresh media without the tested substances and left for an additional 2 h. Then, the viability assay was performed as recommended by the manufacturer. Briefly, the loaded 96-well plate and CellTiter-Glo® substrate were equilibrated to room temperature prior to analysis (30 min). Then, the reconstituted reagent (100 µl) was added to each well, and the 96-well plate was mixed for 2 min at 370 RPM on an orbital shaker in the dark. Subsequently, the luminescent signal was allowed to stabilize for 15 min at room temperature. Luminescence was recorded using a microplate luminometer reader (Tecan GENios, Tecan, Austria). Blanks were subtracted from experimental and control measurements. The percentage of viable U-87 MG cells was counted as the ratio of luminescence from wells containing U-87 MG cells and test compounds to the luminescence signal from an untreated population control. This ratio represents the mean ± SD from 1 independent measurement performed in pentaplicate wells (or 1 independent measurement performed in triplicate wells for staurosporine). The apoptosis inducer staurosporin showed toxicity in a concentration-dependent manner (Fig 3S). The change in cell morphology after adding 2.5 µM staurosporine is shown in Fig. 4S (from inverted microscope Zeiss Axio Observer.A1).

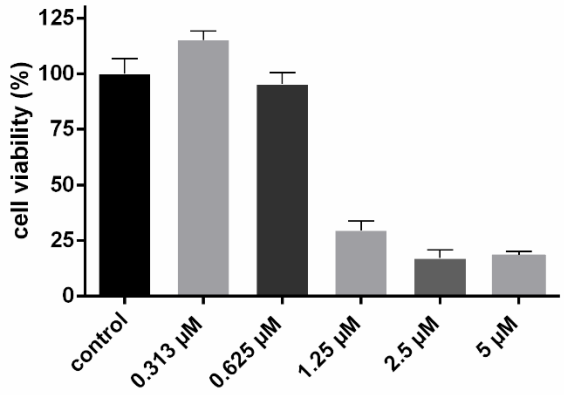

Fig. 3S Cell viability assay based on ATP quantification in cell lysates after adding the apoptosis inducer staurosporine in different concentrations. The luminescence intensity correlates with the ATP level and thus with the quantity of metabolically active (viable) cells. Experiments with 0.313 µM and 0.625 µM staurosporin are statistically not distinguishable from the control, whereas experiments with 1.25 µM, 2.5 µM an 5 µM staurosporin concentration are statistically different from control (ANOVA, $\alpha = 0.05$).

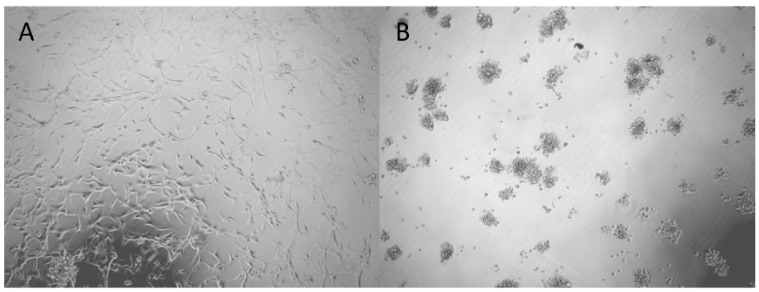

Fig. 4S Microscope observation of U-87 MG cells before (A) and after (B) adding 2.5 µM staurosporine, an inducer of apoptosis.

Flow cytometry

Five days prior to experimental treatment, U-87 MG cells were harvested in the exponential growth phase and seeded into a 24-well plate at 40,000 cells per well. Each well contained 1 ml

cell suspension. Within the cultivation period, the growth medium in the wells was replaced once with fresh medium. On the day of treatment, the cells reached approximately 60-70% confluence. In each experiment, the following 1 h treatments were performed in duplicate: control (growth medium + the corresponding amount of water), **FND** (final concentration of 50 µg/ml), **FND-cRGD** (final concentration of 50 µg/ml). Additionally, pretreatment of cells with 100 µg/ml cRGD for 30 min was performed before **FND** and **FND-cRGD** were applied to the wells (50 µg/ml). Subsequent 60 min incubation was carried out in the dark at 37 °C in a humidified atmosphere containing 5% CO_2. After treatment, cells were harvested by scraping, washed twice with 900 µl cold PBS, resuspended in 200 µl PBS, filtered through a 35-µm nylon mesh and analyzed with a BD LSRFortessa™ cell analyzer (Becton Dickinson, San Jose, CA). Ten thousand events were acquired for each analysis. Fluorescence was excited at 488 nm and detected in spectral range 515–545 nm. BD FACSDiva Software 6.0 was used to generate histograms (see Figure 5S) and analyze data. The results represent the mean ± SD from 2 independent measurements performed in duplicate and triplicate wells.

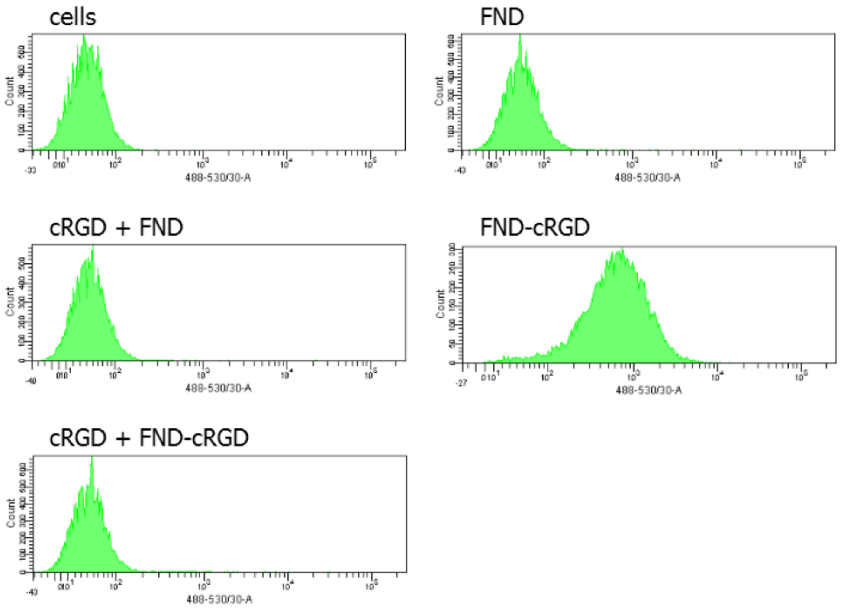

Fig. 5S Histograms obtained from flow cytometry measurements.

Confocal microscopy

Five days prior to experimental treatment, U-87 MG cells were harvested in the exponential growth phase and seeded into Petri dishes (35 mm glass bottom dish with 4 chambers, BioPort Europe, s.r.o., cat. no. D35C4-20-1.5-N) at 40,000 cells per well. Each well contained 1 ml cell suspension. Within this cultivation period, the growth medium in wells was replaced once with fresh medium. On the day of treatment, the cells reached approximately 60-70% confluence. In each experiment, the following 1 h treatments were performed: control (growth medium + the corresponding amount of water), **FND** (final concentration of 50 µg/ml), **FND-cRGD** (final concentration of 50 µg/ml). Additionally, pretreatment of cells with 100 µg/ml cRGD for 30 min was performed before **FND** and **FND-cRGD** were applied to the wells (50 µg/ml). Subsequent 60 min incubation was carried out in the dark at 37 °C in a humidified atmosphere containing 5% CO_2. After treatment, cells were washed twice with 900 µl cold PBS and fixed with a 2% formaldehyde solution in PBS for 10 min. After fixation, cells were washed twice with 900 µl PBS and stored in 1 ml PBS.

A confocal imaging of internalized **FNDs** was performed on Carl Zeiss LSM 780 confocal microscope, equipped with two solid state lasers (405 nm, 561 nm) lasers, in-tune laser (tunable laser), oil-immersion objective (Plan-Apochromat 63x/1.40 Oil DIC M27) and ultrasensitive spectral 32+2 channel detector.

Firstly, the measurement of Alexa Fluor 488 dye bound to **FNDs** was done with following setup: excitation at 488 nm by argon ion laser with 3.5 µW output power (at the sample plane), 90 µm pinhole, pixel dwell time 153 µs, pixel size 81 nm, spectral detector in the 493-630 nm range (master gain set to 850 V, digital gain 1). Bright-field images were taken by using transmitted light (PMT detector at 375 V, digital gain 1) concomitantly. An extensive bleaching for reducing unwanted background was performed after that; 30 cycles with 153 µs pixel dwell time using combined power of lasers at excitation wavelengths of 405 nm (~ 1.18 mW), 488 nm (~ 0.62 mW), 514 nm (~ 0.26 mW), 532 nm (~ 0.4 mW) and 561 nm (~ 1.69 mW).

Finally, intrinsical fluorescence of **FNDs** was examined. **FNDs** were excited using the solid state 561 nm laser (~1,69 mW), scanned with pixel size 81 nm, pixel dwell time 153 µs with 4× line averaging, 90 µm pinhole and emitted light was collected by spectral detector setup in the 569-691 nm range, in photon counting lambda mode (14 channels, digital gain 1). The measured

emission spectrum of **FNDs** in cells has maximum at 663 nm, therefore signal between wavelengths 659 - 667 nm was used for visualization of **FNDs** in cells and signal in range 624-691 nm was used for subsequent quantitative colocalization image analysis.

The fluorescence images were collected with ZEN 2011 software and processed in the GNU Image Manipulation Program or in the ImageJ software[5] with JACoP colocalization plug-in. Because of different intensity in the Alexa Fluor 488 fluorescence channel and FND channel, intensity of Alexa Fluor 488 channel was multiplied by factor 0.6 before merging the figures. Quantitative colocalization analysis was performed by JaCoP plugin. Briefly after background subtraction, threshold levels were automatically computed by Coste's method and correlation coefficients were computed.[6]

Statistical analysis

The ANOVA analysis was done using Data Analysis tool in Microsoft Excel 2010.

References

1. S. K. Filippov, P. Chytil, P. V. Konarev, M. Dyakonova, C. Papadakis, A. Zhigunov, J. Plestil, P. Stepanek, T. Etrych, K. Ulbrich, and D. I. Svergun, *Biomacromolecules*, 2012, **13**, 2594–2604.
2. H. Macková, V. Proks, D. Horák, J. Kučka, and M. Trchová, *J. Polym. Sci. Part Polym. Chem.*, 2011, **49**, 4820–4829.
3. I. Rehor, H. Mackova, S. K. Filippov, J. Kucka, V. Proks, J. Slegerova, S. Turner, G. Van Tendeloo, M. Ledvina, M. Hruby, and P. Cigler, *ChemPlusChem*, 2014, **79**, 21–24.
4. V. Hong, S. I. Presolski, C. Ma, and M. G. Finn, *Angew. Chem. Int. Ed.*, 2009, **48**, 9879–9883.
5. Rasband, W.S., ImageJ, U. S. National Institutes of Health, Bethesda, Maryland, USA, http://imagej.nih.gov/ij/, 1997–2014.
6. S. Bolte & F. P. Cordelieres, A guided tour into subcellular colocalization analysis in light microscopy, *J. Microscopy*, 2006, **224**, 213–232.

Appendix D – Publication 4

Jitka Neburkova, Miroslav Hajek, Frantisek Sedlak, Stuart Turner, Jan Stursa, Petr Cigler: Polyvalent display of ligand combined with antifouling bionanointerface enables extremely selective targeting of NPs to human T lymphoblast cells, submitted

Polyvalent display of ligand combined with antifouling bionanointerface enables extremely selective targeting of nanoparticles to human T lymphoblast cells

Jitka Neburkova[a,b], Miroslav Hajek[a], Frantisek Sedlak[a,b], Svetlana Korneychuk[c], Stuart Turner[c], Jan Stursa[d], Petr Cigler[a]

[a]Institute of Organic Chemistry and Biochemistry AS CR, v.v.i., Flemingovo nam. 2, 166 10, Prague 6, Czech Republic. E-mail: cigler@uochb.cas.cz
[b]First Faculty of Medicine, Charles University, Katerinska 32, 121 08, Prague 2, Czech Republic
[c] EMAT, University of Antwerp, Groenenborgerlaan 171 , B-2020 , Antwerp , Belgium
[d]Nuclear Physics Institute AS CR, v.v.i., 250 68 Rez near Prague, Czech Republic

ABSTRACT

Nanoparticles are covered in biological environment by protein corona, which completely change nanoparticle surface characteristic and behavior. After creating dense polymeric shells on the surface, particles gain intact surface completely suppressing non-specific interactions with proteins and cells and stability in solutions with electrolytes. Such particles with antifouling surface can be further modified with targeting moieties specifically interacting with cancer cells. Conjugate of fluorescent nanodiamonds (FNDs) coated by "grafting from" approach with polymer poly[N-(2-hydroxypropyl)methacrylamide], further modified using bio-orthogonal reactions with protein transferrin specifically and enormously strongly interact with human T-lymphoblast CCRF-CEM cell line (approximately 350-fold stronger interaction than negative controls). Interaction of these FND particles with cells is specific and occurs only by transferrin receptor as was shown in a co-culture of cancerous and non-cancerous cells. We propose the method how to distinguish between co-cultured cell lines by labeling them for analysis after experiment without having any influence on cell surface structures.

Precise control of particle stability and nanobiointerface is crucial for most bioapplications. Nanoparticle stability is ensured either by charge or steric repulsion. Inorganic nanoparticles are usually charged and therefore stable in water. Nanoparticle characteristic properties are completely altered after adsorption of protein corona in biological environment.[1] Therefore, nanoparticles need to be coat by electroneutral polymers with antifouling properties to obtain intact surface and stabilization by steric hindrance. Various hydrophilic polymers were used for this purpose such as poly(ethylene oxide), poly(2-alkyl-2-oxazolines), poly(amino acids), polysaccharides, polyglycerol or poly[N-(2-hydroxypropyl)methacrylamide] (PHPMA). PHPMA is a linear, biodegradable, non-immunogenic polymer with functionalizable side chains, introduced by Jindrich Kopecek in the mid-1970s.[2] In this work, we describe design and preparation of non-toxic PHPMA nanobiointerface, universally applicable for bioconjugation on inorganic nanoparticles, which i) possess highly suppressed ability to non-specifically bind on biostructures (proteins or cells) ii) enables biomolecules' conjugation and support their specific interaction with target.

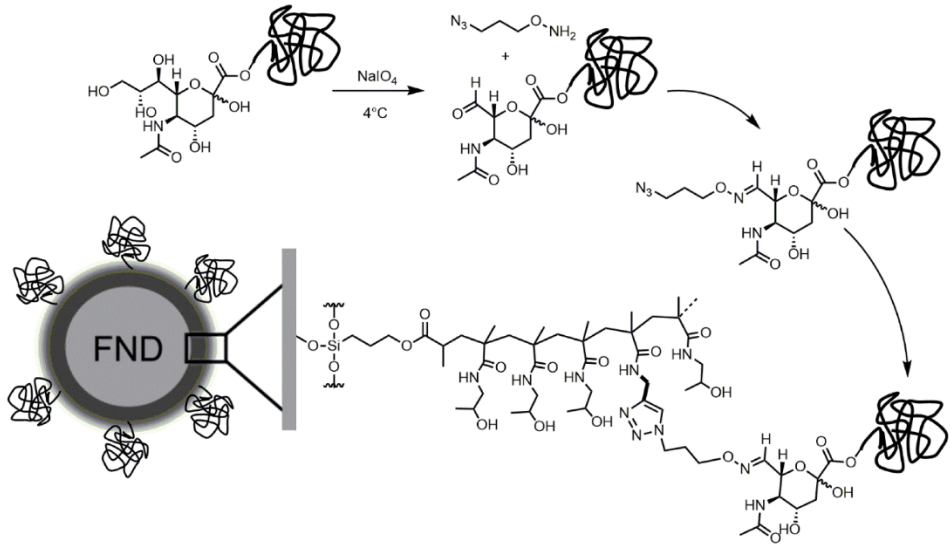

Figure 1: Preparation of FND conjugate with protein transferrin. Transferrin is firstly oxidized by meta-periodate ($NaIO_4$) and further reacted with linkage 3-aminooxypropyl-1-azide and conjugated using azide-alkyne cycloaddition catalyzed by Cu (I) ions to PHPMA-coated FNDs modified with alkyne moieties.

In past few years we have been systematically focusing on stabilization and biocompatibilization of fluorescent nanodiamonds (FNDs)[3] which can be used as extremely sensitive magnetic and electric optical nanosensors. Briefly, the optical FNDs contain point lattice defects, nitrogen-vacancy (NV) centers, which are responsible for FNDs extraordinary optical properties such as non-bleachable fluorescence, emission in near-infrared region (Figure 1S) and long fluorescence lifetime (roughly 11–19 ns).[4] FNDs can be used regarding to their properties in applications such as single particle tracking inside cells, long-term in vivo tracking of particles, fluorescence lifetime imaging microscopy in vitro and in vivo or magnetometry.[5] The unique sensitivity of the N-V center to the electric and magnetic field was also utilized for the construction of various FND-based sensors.[6] FNDs are suitable model for various inorganic nanoparticles considering their crystallinity, sharpness and polydispersity in both shape and size. The behavior of FNDs in biological environment is strongly dependent on their shape.[7] FNDs strongly adsorb biomolecules and with protein corona can be utilized in various applications.[8] Nevertheless, these FNDs without antifouling coating are difficult to selectively bind to target cells. Targeting of non-coated FNDs by various biomolecules such as chlorotoxin-like peptide[9] or transferrin[10] was shown, however, FNDs adsorb to all biostructures and their specific interaction is only slightly increased compared to non-targeted FNDs. The interaction of nanoparticles with cells needs to be mediated only by targeting molecule on the surface of nanoparticles. Layer of hydrophilic polymer on FNDs suppress the nonspecific interaction and ensure FNDs stability by preventing aggregation in biological environment. Polymer needs to create sufficiently dense brush to shield FND surface completely. The density of the surface coating greatly depends on the method of attachment. Polymers can be attached to nanoparticle surface by "grafting to" approach, when they are synthesized separately from the particles and then attached to the surface. In the "grafting from" method, the polymerization takes place directly on the surface.[11]

"Grafting to" method is considered as less effective and not completely shielded FNDs have negative zeta potential of the underlying core[12–14] and interact non-specifically with cells.[12–15] Polymer shells from polyglycerol and PHPMA prepared by "grafting from" approach yield particles with greatly reduced non-specific interactions with cells, enabling more specific interaction of targeted FNDs with cancer cells.[16,17]

For this study, we chose PHPMA-coated FNDs and as a target transferrin receptor, which is overexpressed on rapidly dividing cancer cells in different rate depending on cell type. Conjugates of transferrin with various ligands (from nucleic acids or drugs, to polymers and nanoparticles) are used for targeting and treatment of cancer cells,[18,19] reaching also phase I clinical trials.[20] Targeting with nanoparticles has some advantages over targeting with conventional probes. Nanoparticles have a polyvalent surface, which strengthens the binding efficacy of the ligands to targeted places. This phenomenon is called avidity and leads to orders of magnitude stronger binding than for the corresponding monovalent interaction and can results in enhanced discrimination between cells expressing different levels of a target receptor.[21] *In vivo*, nanoparticles are not filtered through glomerular capillaries and stays in blood circulation for a prolonged time and accumulate thanks to a leaky vasculature nonspecifically inside solid tumors (Enhanced Permeation and Retention, EPR effect).[22] FNDs modified with transferrin have been prepared previously in several publications,[10,13,15,23] nevertheless, non-specific interaction of FNDs (both non-coated and polymer-coated) with cells was high and specific interaction was maximally 4-times higher. Besides suppressing non-specific interactions, other parameters such as quantity of targeting ligands on surface, employment of a linker and the way of biomolecule attachment (to preserve its properties) can be optimize to receive optimally modified FNDs for targeting.[24] To control biomolecule coverage and exposure on surface, as little reacting groups as possible should be present in the structure. Transferrin includes 59 amino groups, theoretically reactive in amide bond formation, which were used before for FND modification.[10,13,23] There are only four sialic acids in glycosylated transferrin located at the end of two branched carbohydrate structures, which can be transformed to aldehyde and subsequently azide.[15] Modifications of these sialic acids using biorthogonal reactions bring much easier control of attachment compared to 59 amino groups.

Apart from effort to obtain FNDs with extraordinary high selectivity to transferrin receptors, we further focus on method of targeting evaluation. To imitate the environment of cancerous and non-cancerous cells together and to prove inter-cellular selectivity, we performed targeting experiments in co-culture with cells bearing different amount of transferrin receptor. Co-cultures are lately more explored, filling the gap between experiment with one cell line and *in vivo*.[25] There are different approaches how to cultivate co-cultures from labeling one cell line with fluorescent dye and adding other cell line to sophisticate 3D cultures.[26] We propose very simple protocol how to distinguish between cell lines using fluorescent labeled antibodies, importantly, cells are labeled after experiment without having any influence on cell surface structures and targeting.

To prepare intact anti-fouling surface on FNDs, we coated FNDs with a copolymer of HPMA and N-propargylacrylamide. The copolymer chains were grown by radical "grafting from" approach.[27] FNDs coated by PHPMA brushes, which typically increase hydrodynamic diameter of nanoparticles, are stable in media or buffers at least up to 1 M NaCl (Figure 2S). PHPMA creates on FNDs sufficiently dense polymer layer and therefore FNDs do not interact with cells and other biomolecules non-specifically.[17] Transferrin glycosylation chains with 1,2-diol were cleaved and subsequent oxime ligation of transferrin-aldehyde with short linkage 3-aminooxypropyl-1-azide

provide transferrin with approximately 2.7 azide groups suitable for azide-alkyne cycloaddition catalyzed by Cu(I) ions ("click" reaction) with alkynes on FNDs.[15] We modified FNDs using "click" reaction with approximately 6 molecules of transferrin-azide. Polymer shell and transferrin on the surface of nanodiamonds was observed by HR-TEM. Presence of transferrin was confirmed by EELS measurement of sulphur content originating from cysteins and methionins present in the protein (Figure 2).

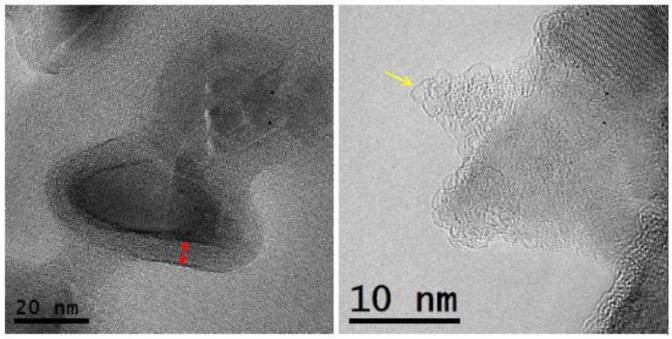

Figure 2: HRTEM image of (A) PHPMA-coated FNDs with arrow pointing out the thickness of the polymer layer and (B) transferrin (marked with yellow arrow) conjugated to FND surface. The presence of transferrin was confirmed by EELS measurement of sulphur content (see Figure S1 in Supporting information).

For cell culture experiments, three different cell lines with different rate of transferrin receptor were selected: non-cancerous human umbilical vein endothelial cell line (HUVEC), human osteosarcoma cancer cell line (U2OS) and human T lymphoblast (CCRF-CEM) cells as a cancer cell line with very high amount of transferrin receptors.[28] All FND particles are not toxic according to the XTT Cell Viability Assay under the targeting experimental conditions to all 3 different cell types used (Figure 3A).

FNDs interaction with cells was observed by flow cytometer. FNDs were incubated with cells in a co-culture. Either, U2OS and HUVEC cells or CCRF-CEM and HUVEC cells were co-cultured together to imitate the environment of cancerous and non-cancerous cells together. FND or FND-Tf particles were introduced to the cells for 1 h incubation with or without pretreatment of cells with free transferrin. After the treatment of cells with particles (to avoid any change of cell structures and receptors), antibodies recognizing specifically one cell line modified with different fluorescent labels were introduced to the cells, enabling matching of interacting FNDs with corresponding cells (Figure 3B). The remarkably stronger affinity of FND–Tf over FND and low interaction of particles with cells pre-incubated with transferrin was observed on all cell lines. Interaction of FND-Tf particles is, therefore, specific and occurs only by transferrin receptor. FND–Tf particles are localized inside the cells according to cross-section measurements of FND fluorescence (Figure 3 C-J). Enormously strong interaction (approximately 350-fold to all negative controls) was observed in case of CCRF-CEM cell line. FND-Tf particles specifically interact with cancerous CCRF-CEM cells in presence of non-cancerous HUVEC cells. Difference between two cancerous cell lines (CCRF-CEM and U2OS) in the binding of FND-Tf depends most likely on the amount of transferrin receptors on their surface, properties of the cells and is highlighted by the avidity effect of FND-Tf.

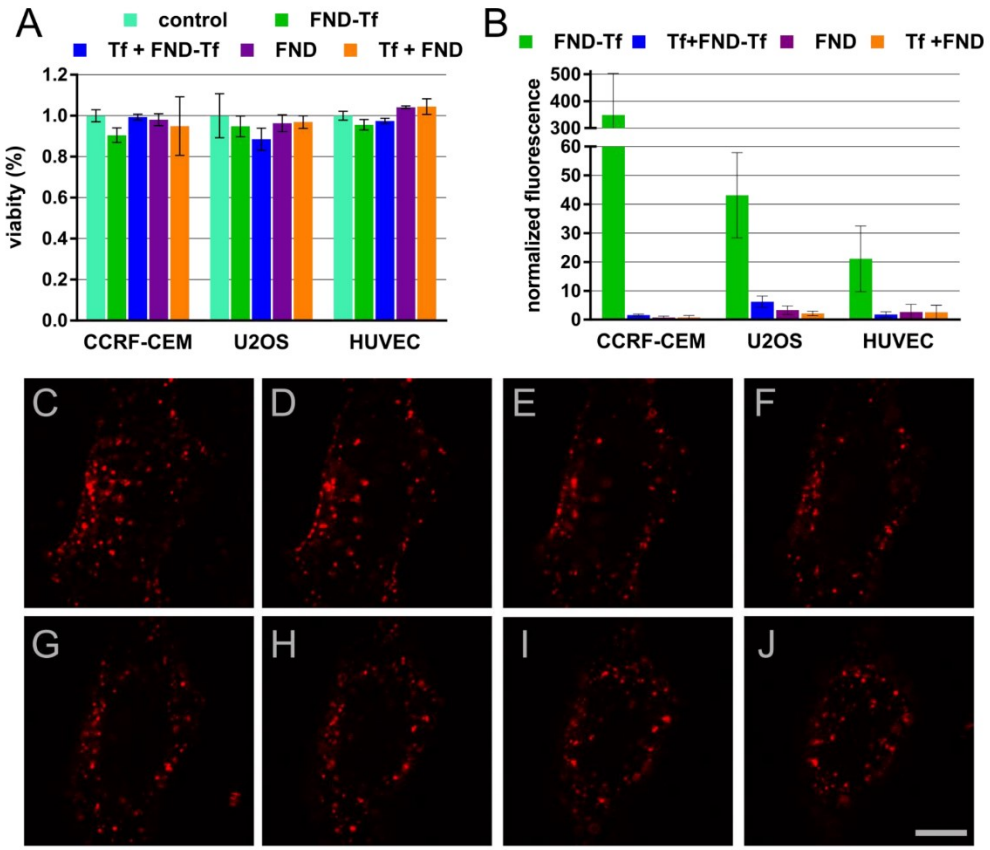

Figure 3: Interaction of FND particles with cells. (A) XTT viability assay concerning all combinations of particles used further in targeting experiment with three cell lines. All combinations have no impact on cell viability under the used experimental conditions. Alternatives are statistically not distinguishable among each other on the significance level $\alpha = 0.01$ (two-way ANOVA, GraphPad Prism). (B) Fluorescence intensity measurements of various cell lines incubated with FNDs modified with transferrin using flow cytometry. FND–Tf specifically recognized transferrin receptors. The FND-Tf alternative is statistically significantly different from the controls for all cell lines. All negative controls for each cell lines are statistically not distinguishable among each other. FND-Tf in CCRF-CEM line is statistically significantly different from FND-Tf in other cell lines (two-way ANOVA, $\alpha = 0.01$, GraphPad Prism) (C-J) Cross-section measurement of cells treated with FND–Tf shows that particles are present inside the cell. The images were recorded using FND fluorescence from N-V centers. Images were recorded with a 0.9 μm step in the vertical direction and presented from left to right and top to bottom with a 45 × 45 μm field of view.

Extremely high interaction of FND-Tf to T-lymphoblast cells is supposedly a combination of many factors. Transferrin, conjugated to FNDs using biorthogonal reactions in a sufficient amount, maintains its structure and is conveniently expose to the surroundings enabling proper interaction with transferrin receptors over-expressed on cancer cells. Exceptionally dense layer of polymer PHPMA

"grafted from" the surface of FNDs suppress all non-specific interaction of particles to proteins and cells as is shown in a co-culture of non-cancerous and cancerous cell lines, distinguished for analysis by labeling after targeting experiment without having any influence on cell surface structures.

Experimental:

FNDs with polymer PHPMA[17] and transferrin-azide[15] were prepared according to published procedures (for details see Supplementary information). PHPMA-coated FNDs (1.2 mg in a final reaction volume of 1440 µl) were reacted in azide-alkyne cycloaddition with copper (I) ions with transferrin-azide (90 µM), pre-mixed 0.32 mM $CuSO_4 \cdot 5H_2O$ and 1.6 mM tris(3-hydroxypropyltriazolylmethyl)amine (THPTA) ligand, aminoguanidine hydrochloride (5 mM) and a freshly prepared solution of sodium ascorbate (5 mM). The reaction mixture was well-sealed, left for 3 h with no stirring and washed by centrifugation. For flow cytometry measurements, we attached secondary fluorescent label Alexa fluor 488-azide to all types of FNDs according to the same protocol in two consecutive reactions (because our flow cytometry setup does not allow direct observation of FND fluorescence). Quantification of transferrin bound to the FND surface was done independently by two methods, amino acid analysis and fluorometric quantification using Qubit® protein assay and determined as approximately 6 transferrin molecules on one labeled FND particle (20 transferrin molecules on one unlabeled FND particle).

Flow cytometry measurements: One day prior to the experimental treatment, U2OS and HUVEC cells were seeded into a 6-well plate at 150,000 and 200,000 cells per well, respectively. Simultaneously, only HUVEC cells were seeded into a 6-well plate at 200,000 cells per well. Prior to the experiment, Dulbecco's Modified Eagle Medium (DMEM) without serum was added to cells and CCRF-CEM cells (1.5 million) were added to HUVEC cells. FND and FND-Tf (final concentration 50 µg/ml) were added to co-cultures for 1 h. Pretreatment of cells with 100 µg/ml free transferrin for 30 min was performed in controls before FND and FND-Tf were applied to the wells. After treatment, cells were harvested, washed with PBS and resuspended in 100 µl flow cytometry staining buffer . To the cell suspension, 2.5 µl of antibodies, specifically recognizing respective cell surface receptors, were added. CD 144 receptors on HUVEC cells were specifically labeled by antibody anti-CD 144 with VE-Cadherin fluorescent dye, CD 45 on the surface of CCRF-CEM cells with antibody anti-CD 45 conjugated with Per CP/Cy 5.5 dye. Cells were left to incubate with antibodies for 45 minutes at 4°C with gently shaking, washed with staining buffer, resuspended and analyzed with a BD LSRFortessa™ cell analyzer.

[1] M. Rahman, S. Laurent, N. Tawil, L. Yahia, M. Mahmoudi, in *Protein-Nanoparticle Interact.*, Springer Berlin Heidelberg, **2013**, pp. 21–44.
[2] Z. Amoozgar, Y. Yeo, *Wiley Interdiscip. Rev. Nanomed. Nanobiotechnol.* **2012**, *4*, 219.
[3] J. Neburkova, J. Vavra, P. Cigler, *Curr. Opin. Solid State Mater. Sci.* **2017**, *21*, 43.
[4] J. Slegerova, I. Rehor, J. Havlik, H. Raabova, E. Muchova, P. Cigler, in *Intracell. Deliv. II* (Eds: A. Prokop, Y. Iwasaki, A. Harada), Springer Netherlands, Dordrecht, **2014**, pp. 363–401.
[5] V. Vaijayanthimala, D. K. Lee, S. V. Kim, A. Yen, N. Tsai, D. Ho, H.-C. Chang, O. Shenderova, *Expert Opin. Drug Deliv.* **2015**, *12*, 735.
[6] A. Ermakova, G. Pramanik, J.-M. Cai, G. Algara-Siller, U. Kaiser, T. Weil, Y.-K. Tzeng, H. C. Chang, L. P. McGuinness, M. B. Plenio, B. Naydenov, F. Jelezko, *Nano Lett.* **2013**, *13*, 3305.
[7] Z. Chu, S. Zhang, B. Zhang, C. Zhang, C.-Y. Fang, I. Rehor, P. Cigler, H.-C. Chang, G. Lin, R. Liu, Q. Li, *Sci. Rep.* **2014**, *4*, 4495.
[8] I. Badea, R. Kaur, *Int. J. Nanomedicine* **2013**, *8*, 203.
[9] Y. Fu, N. An, S. Zheng, A. Liang, Y. Li, *Diam. Relat. Mater.* **2012**, *21*, 73.
[10] Z. Wang, Z. Tian, Y. Dong, L. Li, L. Tian, Y. Li, B. Yang, *Diam. Relat. Mater.* **2015**, *58*, 84.
[11] B. Zhao, W. J. Brittain, *Prog. Polym. Sci.* **2000**, *25*, 677.
[12] T. Zhang, H. Cui, C.-Y. Fang, K. Cheng, X. Yang, H.-C. Chang, M. L. Forrest, *Nanomed.* **2015**, *10*, 573.
[13] D. Wang, Y. Li, Z. Tian, R. Cao, B. Yang, *Ther. Deliv.* **2014**, *5*, 511.
[14] Y. Dong, R. Cao, Y. Li, Z. Wang, L. Li, L. Tian, *RSC Adv.* **2015**, *5*, 82711.
[15] I. Rehor, K. L. Lee, K. Chen, M. Hajek, J. Havlik, J. Lokajova, M. Masat, J. Slegerova, S. Shukla, H. Heidari, S. Bals, N. F. Steinmetz, P. Cigler, *Adv. Healthc. Mater.* **2015**, *4*, 460.
[16] L. Zhao, Y.-H. Xu, H. Qin, S. Abe, T. Akasaka, T. Chano, F. Watari, T. Kimura, N. Komatsu, X. Chen, *Adv. Funct. Mater.* **2014**, *24*, 5348.
[17] J. Slegerova, M. Hajek, I. Rehor, F. Sedlak, J. Stursa, M. Hruby, P. Cigler, *Nanoscale* **2015**, *7*, 415.

[18] T. R. Daniels, E. Bernabeu, J. A. Rodríguez, S. Patel, M. Kozman, D. A. Chiappetta, E. Holler, J. Y. Ljubimova, G. Helguera, M. L. Penichet, *Biochim. Biophys. Acta BBA - Gen. Subj.* **2012**, *1820*, 291.
[19] E. A. Sykes, J. Chen, G. Zheng, W. C. W. Chan, *ACS Nano* **2014**, *8*, 5696.
[20] M. E. Davis, J. E. Zuckerman, C. H. J. Choi, D. Seligson, A. Tolcher, C. A. Alabi, Y. Yen, J. D. Heidel, A. Ribas, *Nature* **2010**, *464*, 1067.
[21] C. T. Varner, T. Rosen, J. T. Martin, R. S. Kane, *Biomacromolecules* **2015**, *16*, 43.
[22] A. Prokop, J. M. Davidson, *J. Pharm. Sci.* **2008**, *97*, 3518.
[23] M.-F. Weng, B.-J. Chang, S.-Y. Chiang, N.-S. Wang, H. Niu, *Diam. Relat. Mater.* **2012**, *22*, 96.
[24] D. R. Elias, A. Poloukhtine, V. Popik, A. Tsourkas, *Nanomedicine Nanotechnol. Biol. Med.* **2013**, *9*, 194.
[25] E. C. Costa, V. M. Gaspar, J. G. Marques, P. Coutinho, I. J. Correia, *PLoS ONE* **2013**, *8*, e70072.
[26] E. C. Costa, V. M. Gaspar, P. Coutinho, I. J. Correia, *Biotechnol. Bioeng.* **2014**, *111*, 1672.
[27] I. Rehor, H. Mackova, S. K. Filippov, J. Kucka, V. Proks, J. Slegerova, S. Turner, G. Van Tendeloo, M. Ledvina, M. Hruby, P. Cigler, *ChemPlusChem* **2014**, *79*, 21.
[28] M. Szwed, A. Matusiak, A. Laroche-Clary, J. Robert, I. Marszalek, Z. Jozwiak, *Toxicol. In Vitro* **2014**, *28*, 187.

Supporting information

Polyvalent display of ligand combined with antifouling bionanointerface enables extremely selective targeting of nanoparticles to human T lymphoblast cells

Jitka Neburkova[a,b], Miroslav Hajek[a], Frantisek Sedlak[a,b], Svetlana Korneychuk[c], Stuart Turner[c], Jan Stursa[d], Petr Cigler[a]

[a]Institute of Organic Chemistry and Biochemistry AS CR, v.v.i., Flemingovo nam. 2, 166 10, Prague 6, Czech Republic. E-mail: cigler@uochb.cas.cz
[b]First Faculty of Medicine, Charles University, Katerinska 32, 121 08, Prague 2, Czech Republic
[c] EMAT, University of Antwerp, Groenenborgerlaan 171 , B-2020 , Antwerp , Belgium
[d]Nuclear Physics Institute AS CR, v.v.i., 250 68 Rez near Prague, Czech Republic

Materials and methods

FND pretreatment

Nanodiamonds (NDs) were supplied by Microdiamant Switzerland (MSY 0-0.05). NDs were oxidized by air in a furnace (Thermolyne 21100 tube) at 510 °C for 5 h. Subsequently, the NDs were treated with a mixture of H_2SO_4 and HNO_3 (9:1) at 90 °C for 3 days and washed with water, 1 M NaOH and 1 M HCl. They were washed an additional 5 times with water and then freeze-dried. Purified ND powder (120 mg), containing approximately 100–200 ppm of natural nitrogen impurities, was irradiated in an aqueous colloidal solution for 4.5 hours with a 15.9 MeV proton beam (6.61×10^{17} particles/ml) extracted from the isochronous cyclotron U 120M. The irradiated material was annealed at 900 °C for 1 h and subsequently oxidized for 4 h at 510 °C. The resulting fluorescent nanodiamonds (FNDs) (Figure 1S) were again treated with a mixture of H_2SO_4 and HNO_3 (9:1) at 90 °C for 3 days, washed with water, 1 M NaOH and 1 M HCl and an additional 5 times with water. The particles were dissolved in water (2 mg/mL) and filtered using a 0.4 μm GMF filter, yielding FND-COOH colloid.

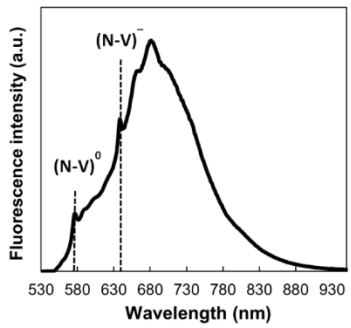

Figure 1S: Fluorescence spectra of FND with two transition states $(N\text{-}V)^0$ and $(N\text{-}V)^-$ and maximum in near-infrared part of spectra at approximately 700 nm.

Coating of FNDs with a methacryloated thin silica layer

Polyvinylpyrrolidone (MW = 10,000, 91 mg, 9.1 µmol, purchased from Sigma Aldrich) was dissolved in water (80 ml) and sonicated for 10 min in an ultrasonic bath. FND-COOH colloid (16 ml, 2 mg/ml) was added, and the mixture was stirred for 24 h. The colloid was then concentrated by a centrifugation (40,000 rcf, 1 hour), the solvent volume was reduced to approximately 2 ml. Sedimented FNDs were resuspended in ethanol (32 ml) in a round bottom flask. Tetraethyl orthosilicate (240 µl, 1076 µmol, purchased from Sigma Aldrich) and 3-(trimethoxysilyl)propylmethacrylate (80 µl, 83.6 mg, 336 µmol, purchased from Sigma Aldrich) were added to the round bottom flask. Ammonia (25%, 1333 µl) was added after 20 s sonication in an ultrasonic bath. The reaction mixture was stirred for 14 h. The product was purified by centrifugation (15,000 - 20,000 rcf, 15 min) with methanol (12 ml, 2 times).

Coating of NDs with a polymer layer

HPMA (700 mg, 4.82 mmol, synthesized according to published procedures[1] and freshly recrystallized twice from a mixture of acetone-hexanes (boiling point approximately 70 °C, 1:3 v/v)) and N-propargyl acrylamide (35 mg, 0.06 mmol, synthesized by acryloylation of propargylamine with acryloyl chloride[2]) were dissolved in DMSO (2 ml). 2,2′-Azobis(2-methylpropionitrile) (AIBN, 200 mg, 1.22 mmol, recrystallized by thickening an ethanol solution on a rotary evaporator at a maximum temperature of 30 °C) was added to the mixture. The mixture was filtered using a 0.4 µm glass microfiber microfilter. Methacrylate-terminated FND

particles (32 mg) dispersed in 0.2 mg of DMSO were added (transferred to DMSO using rotary evaporator). The reaction proceeded for 3 days under argon at 55 °C. The reaction mixture was twice diluted with ethanol before centrifugation. The particles were centrifuged (20,000 rcf, 40 min) and purified by centrifugation with ethanol (20,000 rcf, 30 min, 1 ml, 3 times), water (30,000 rcf, 30 min, 1 ml, 5 times) and store in methanol.

FND colloidal stability studies

FNDs modified with HPMA coating are stable in biological solutions such as media or buffers according to dynamic light scattering (DLS) in contrast to non-modified FNDs without polymer coating, which are unstable in PBS buffer. The polymer coated FNDs are stable even after 24 h incubation in 1 M NaCl (Figure 2S). DLS was recorded with a Zetasizer Nano ZS system (Malvern Instruments) at 25 °C. Sample concentrations were 0.1 mg/ml.

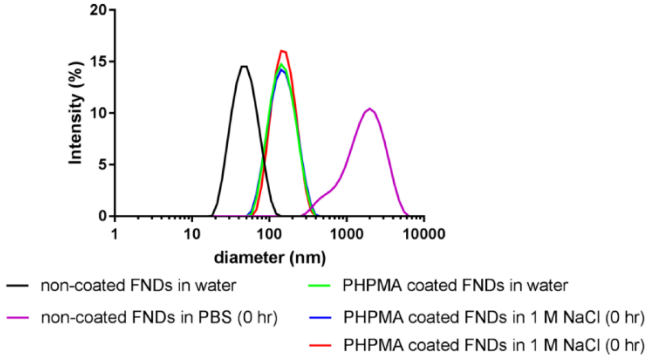

Figure 2S: Dynamic light scattering (DLS) of the size distribution by intensity of non-coated FNDs in water and PBS and FNDs coated with HPMA polymer in water and 1 M NaCl solution. The concentration of the colloids was 0.1 mg/ml. The graph was generated in GraphPad Prism 7.

Preparation of transferrin-azide (Tf-N_3)

Transferrin-azide was prepared according to previously published procedure (Figure 1).[3,4] Human holo-transferrin (Tf, 30 mg, 390 nmol) was dissolved in acetate buffer (0.1 M, pH 5.5) in concentration 2 mg/ml. $NaIO_4$ solution was slowly added to cooled Tf solution (the final

concentration 1 mM). Mixture was incubated on ice in the dark for 30 minutes and washed by HEPES buffer (0.1 M, pH 7.2) using ultrafiltration cell. Tf-aldehyde was incubated with 3-aminooxypropyl-1-azide[5] (16.2 mg, 140 μmol) in HEPES buffer with dimethyl sulfoxide (DMSO, 20%, total volume 17 ml) for 5 h at room temperature (RT) at gentle mixing. The removal of 3-aminooxypropyl-1-azide excess was performed by the in HEPES buffer (0.1 M, pH 8). Solution was freeze-dryed to obtain Tf-N_3.

Quantification of azide group in Tf-N_3 using Alexa fluor 488

Tf-N_3 was reacted with Alexa fluor 488-alkyne (A_{488}-alkyne) or Alexa fluor 488-azide (A_{488}-azide, as a negative control) (purchased by Life Technologies) using azide-alkyne cycloaddition catalyzed by copper(I) ions (CuACC). Stock solutions for CuACC reactions were prepared in water, except for the Alexa fluor 488 stocks, which were prepared in DMSO. Reagents were mixed together in following order and final concentrations: 33 μM Tf-N_3, 0.165 mM A_{488}-alkyne/azide, pre-mixed 0.66 mM $CuSO_4 \cdot 5H_2O$ and 3.3 mM tris(3-hydroxypropyltriazolylmethyl)amine ligand (THPTA, synthesized according to published procedures[6]), 5 mM aminoguanidine and freshly prepared solution of 5 mM sodium ascorbate. The reaction mixture was well-sealed, mixed and left for 3 h with no stirring. The removal of Alexa fluor 488 excess was performed by the ultrafiltration in PBS buffer. Absorption spectra of resulting solutions were measured (Figure 3S) and the amount of Alexa fluor 488 bound to Tf-N_3 was estimated according to Alexa fluor 488 calibration curve. There is none non-specific adsorption of A_{488}-azide to Tf-N_3 as it seems from the negative control. Approximately 2.7 molecules of A_{488}-alkyne are bound to 1 molecule of Tf-N_3 (calculated as a mean from 4 different Tf-N_3 preparations and measurements), which is in accordance with the theoretical maximum of 4 azide groups present in one transferrin molecule.

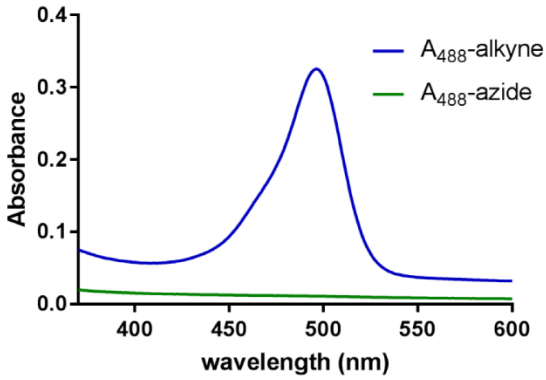

Figure 3S: Absorption spectra of A_{488}-alkyne and A_{488}-azide conjugated to Tf-N_3 molecule using CuACC reaction. While no non-specific adsorption of A_{488}-azide to Tf-N_3 occurs in the negative control, all A_{488}-alkyne binds specifically only to azide groups on Tf and therefore azide groups can be calculated. The graph was generated in GraphPad Prism 7.

Functionalization of coated FNDs by azide-alkyne cycloaddition catalyzed by copper (I) ions for flow cytometry measurements

FNDs were modified with A_{488}-azide and Tf-N_3 (prepared according the protocol decribed above). FNDs were modified with these two ligands in consecutive reactions utilizing the same surface functionalities. Washing procedures were employed after both modification steps.

Stock solutions for CuACC reactions were prepared in water, except for the A_{488}-azide stock, which was prepared in DMSO. The solutions of $CuSO_4 \cdot 5H_2O$ and THPTA were premixed (in a 1:2 concentration ratio for reaction with Alexa fluor 488 and in a 1:5 concentration ratio for reaction with Tf-N_3) before they were added to the reaction mixture.

For the reaction of modified FNDs with A_{488}-azide, the reactants were mixed in the following order and final concentrations: colloid of PHPMA-modified FNDs (2.5 mg in a final reaction volume of 3200 µl), A_{488}-azide (20 µM), pre-mixed 0.32 mM $CuSO_4 \cdot 5H_2O$ and 0.64 mM THPTA ligand, aminoguanidine hydrochloride (5 mM) and a freshly prepared solution of sodium ascorbate (5 mM). The reaction mixture was well-sealed, mixed and left for 3 h with no stirring.

Modified FNDs were isolated by centrifugation (20,000 rcf, 15 min) and three times washed with 1 ml water (20,000 rcf, 15 min). 1.2 mg of the Alexa Fluor 488-modified FNDs was reacted using CuACC reaction with Tf-N_3 (90 μM) in a final reaction volume of 1536 μl with pre-mixed 0.32 mM $CuSO_4 \cdot 5H_2O$ and 1.6 mM THPTA ligand, aminoguanidine hydrochloride (5 mM) and a freshly prepared solution of sodium ascorbate (5 mM). The reaction mixture was well-sealed, mixed and left for 3 h with no stirring. Polymer-coated FND modified with Alexa Fluor 488 and polymer-coated FND modified with Alexa Fluor 488 and Tf-N_3 were both treated the same way and were washed with water (1 ml, 15,000 rcf, 15 min, 7 times).

For cell viability assays and confocal microscopy, FNDs without Alexa fluor 488 were prepared in the reaction with Tf-N_3 under the same conditions as written above (see Experimental).

Electron microscopy

High resolution TEM, STEM, and spatially-resolved EELS experiments were carried out on a FEI Titan 80-300 "cubed" microscope fitted with an aberration-corrector for the imaging lens and the probe forming lens and a GIF Quantum energy filter for spectroscopy, operated at 80 kV to minimize knock-on damage to the sample. The ND particles were immobilized on the lacy carbon copper grids. Grids were placed on the filtration paper and ca. 50 μL of ND aqueous solution (c = 0.1 mg/ml) was placed onto the grid. HRTEM imaging was carried out with an excited electron monochromator, to extend the information transfer of the microscope. STEM-EELS experiments were performed using a convergence semi-angle α of ~21 mrad and a collection semi-angle β of ~75 mrad, using a beam current of approximately 80 pA. A fine electron probe (diameter ~1.5 Å) was scanned over a region of the sample, acquiring an EELS spectrum at each point. All spectra were acquired at an energy dispersion of 0.25 eV per pixel and an energy resolution of approximately 1.2 eV.

Detailed EELS spectra with high signal to noise ratio were acquired from spherical structures at the surface of a ND. A reference EELS spectra were also taken from the ND "bulk" and from a pure protein transferrin. The EELS spectra and the image of the structure on the surface of the ND are displayed in Figure 4S. The spectrum from Region 2 (the spherical structure) shows the presence of a faint sulphur signal (S-$L_{2,3}$ at 160 eV) confirming that the spherical structures are the transferrin.

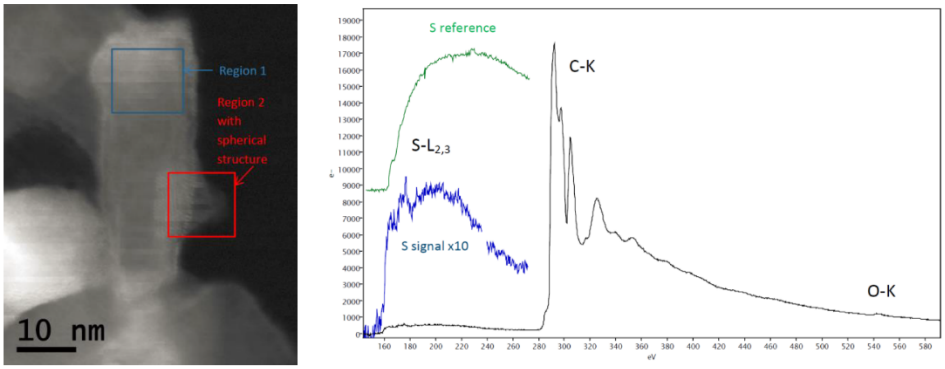

Figure 4S. (A) ADF-STEM image of the diamond particle with the spherical structure on the side (Region 2). **(B)** The spectrum taken from the spherical structure shows the presence of a sulphur signal at 160 eV. Quantification of the S/C ratio yields 1 % S (to carbon). "S reference" is related to the spectrum of transferrin.

Cell culture

The human osteosarcoma cell line U2OS, lymphoblastoid leukemia cell line CCRF-CEM, and human umbilical vein endothelial cell line HUVEC were grown at 37 °C in a humidified atmosphere containing 5% CO_2, in media supplemented with 4 mM L-glutamine (Gibco) and 10% FBS. The cultivation medium used for CCRF-CEM was Roswell Park Memorial Institute medium (RPMI-1640; Sigma-Aldrich), for U2OS it was Dulbecco's modified Eagle's medium (DMEM, Sigma-Aldrich D5796), and for HUVEC it was Endothelial Basal Medium-2 with supplements (EBM-2 SingleQuots™ Kit; Lonza). The cells were subcultured 2 to 3 times per week. To detach adherent cells (U2OS and HUVEC) from the well, we used a solution of 0.25% trypsin and 0.03% EDTA in PBS.

Cell viability assay

The influence of FND and FND-Tf on viability of CCRF-CEM, U2OS and HUVEC cells was tested using the XTT Cell Viability Assay (ATCC, cat. no. ATCC-30-1011K). The cells were cultivated as described above. When they reached the exponential growth phase, U2OS and HUVEC cells were harvested and seeded into a 96-well white microtiter plate (NUNC) at 10,000 cells per well. Prior to the experiment, the growth medium was replaced with 95 µl Dulbecco's Modified Eagle Medium (DMEM, Sigma-Aldrich D5796) without serum. CCRF-CEM were

prior to the experiment collected by centrifugation at 300 x g for 5 minutes, resuspended in DMEM medium without serum and seeded into a 96-well white microtiter plate (NUNC) at 1.5 million cells per well. 2.5 µl of free Tf (final concentration 100 µg/ml) were added to the wells with pre-incubation experiment and control. After 30 minutes, 2.5 µl of modified FND particles were applied to certain wells (final concentration 50 µg/ml). All experiments were done in tetraplicates. Into wells containing controls (cells without test compounds), a volume of water equal to the volume of the compound solutions added to the experimental wells was added. After 5.5 h incubation with FND particles or compounds, the viability assay was performed as recommended by the manufacturer. Briefly, 50 µl of activated XTT solution (5 ml of tetrazolium dye XTT solution with 100 µl of PMS (N-methyl dibenzopyrazine methyl sulfate)) was added to each well and the plate was left for an additional 2 h. The plate was then mixed for 2 min at 370 RPM on an orbital shaker. Absorbance was recorded using a microplate reader (Tecan GENios, Tecan, Austria). The percentage of viable cells was counted as the ratio of absorbance from wells containing test compounds to the absorbance signal from an untreated population control. This ratio represents the mean ± SD from 1 independent measurement performed in tetraplicate wells.

Flow cytometry

Targeting experiments using flow cytometer were done in the co-culture of two cell lines. Either U2OS and HUVEC cells or CCRF-CEM and HUVEC cells were co-cultured together.

One day prior to experimental treatment, U2OS and HUVEC cells were harvested in the exponential growth phase and seeded into a 6-well plate at 150,000 and 200,000 cells per well, subsequently. Each well contained 3 ml of cell suspension in Endothelial Basal Medium-2 with supplements Endothelial Basal Medium-2 with supplements. Simultaneously, only HUVEC cells were seeded into a 6-well plate at 200,000 cells per well in 3 ml of cell suspension in Endothelial Basal Medium-2 with supplements. On the day of treatment, the growth medium in U2OS and HUVEC co-culture was replaced with 760 µl of Dulbecco's Modified Eagle Medium (DMEM, Sigma-Aldrich D5796) without serum. CCRF-CEM were prior to the experiment collected by centrifugation at 300 x g for 5 minutes, resuspended in DMEM medium without serum and seeded into a 6-well plate with pre-seeded HUVEC cells (after removing the media from HUVEC cells) at 1.5 million cells in 760 µl per well. In each experiment, the following 1 h treatments were performed: control (growth medium + the corresponding amount of water), FND, FND-Tf

(final concentration of 50 µg/ml, labeled by Alexa fluor 488). Additionally, pretreatment of cells with 100 µg/ml free transferrin for 30 min was performed before FND and FND-Tf were applied to the wells. Cells without any added compound and with or without antibodies were used as a control. Incubations were carried out in the dark at 37 °C in a humidified atmosphere containing 5% CO_2. After treatment, cells were harvested using trypsin solution (for 1 minute in 37°C, then trypsin inhibitor was added, washed with 900 µl cold PBS and resuspended in 100 µl flow cytometry staining buffer (R&D systems FC001). To the cell suspension, 2.5 µl of antibodies, specifically recognizing cell surface receptors, were added. CD 144 receptors on HUVEC cells were specifically labeled by antibody anti-CD 144 labeled with VE-Cadherin fluorescent dye (Molecular Probes Cat. No. A18353), CD 45 on the surface of CCRF-CEM cells with antibody anti-CD 45 conjugated with Per CP/Cy 5.5 dye (Abcam Cat. No. Ab157309). Cells were left to incubate with antibodies for 45 minutes at 4°C with gently shaking. Cells were washed twice with staining buffer, resuspended in 400 µl, filtered through a 35-µm nylon mesh and analyzed with a BD LSRFortessa™ cell analyzer (Becton Dickinson, San Jose, CA). Ten thousand events were acquired for each analysis. BD FACSDiva Software 6.0 was used to generate histograms and analyze data. The results represent the mean ± SD from 4 independent measurements performed in uniplicates and

Amount of transferrin receptors was estimated from the interaction of Tf-A_{488} (50 µg/ml) with cell lines as a relative ratio of Tf-A_{488} fluorescence to a control (cells without fluorescent transferrin). Measurement was performed in triplicates.There are approximately twice more receptors on CCRF-CEM than on U2OS and 5-times more receptors on CCRF-CEM than on HUVEC cell line.

Confocal microscopy

One day prior to experimental treatment, U2OS cells were harvested in the exponential growth phase and seeded into Petri dishes (35 mm glass bottom dish with 4 chambers, BioPort Europe, s.r.o., cat. no. D35C4-20-1.5-N) at 40,000 cells per well. The well contained 1 ml cell suspension. FND-Tf (final concentration of 50 µg/ml) were added to cells, incubations was carried out in the dark at 37 °C in a humidified atmosphere containing 5% CO_2. After treatment, cells were washed

twice with 900 µl cold PBS and fixed with a 2% formaldehyde solution in PBS for 10 min. After fixation, cells were washed twice with 900 µl PBS and resuspended in 1 ml PBS.

A confocal imaging of internalized FNDs was performed on Carl Zeiss LSM 780 confocal microscope, equipped with two solid state lasers (405 nm, 561 nm) lasers, in-tune laser (tunable laser with minimum power of 1.5 mW per wavelength), oil-immersion objective (Plan-Apochromat 63x/1.40 Oil DIC M27) and ultrasensitive spectral 32+2 channel detector. Fluorescence of FNDs was excited using the solid state 561 nm laser (~1,69 mW), scanned with pixel size 93 nm , pixel dwell time 177 µs, 61 µm pinhole and emitted light was collected by spectral detector setup in the 569-691 nm range, in photon counting lambda mode (14 channels, digital gain 1). The measured emission spectrum of FNDs in cells has maximum at 661 nm, therefore signal between wavelengths 659 - 667 nm was used for visualization of FNDs in cells. The fluorescence images were collected with ZEN 2011 software.

References

1 S. K. Filippov, P. Chytil, P. V. Konarev, M. Dyakonova, C. Papadakis, A. Zhigunov, J. Plestil, P. Stepanek, T. Etrych, K. Ulbrich and D. I. Svergun, *Biomacromolecules*, 2012, **13**, 2594–2604.

2 J. Neburkova, M. Hajek, I. Rehor, J. Schimer, F. Sedlak, J. Stursa, M. Hruby and P. Cigler, in *SpringerLink*, Humana Press, 2017, p. DOI: 10.1007/7653_2017_68.

3 D. Banerjee, A. P. Liu, N. R. Voss, S. L. Schmid and M. G. Finn, *ChemBioChem*, 2010, **11**, 1273–1279.

4 I. Rehor, K. L. Lee, K. Chen, M. Hajek, J. Havlik, J. Lokajova, M. Masat, J. Slegerova, S. Shukla, H. Heidari, S. Bals, N. F. Steinmetz and P. Cigler, *Adv. Healthc. Mater.*, 2015, **4**, 460–468.

5 N. J. Hrib, J. G. Jurcak, F. P. Huger, C. L. Errico and R. W. Dunn, *J. Med. Chem.*, 1991, **34**, 1068–1072.

6 V. Hong, S. I. Presolski, C. Ma and M. G. Finn, *Angew. Chem. Int. Ed.*, 2009, **48**, 9879–9883.

Appendix E – Publication 5

Jitka Neburkova, Frantisek Sedlak, Jirina Zackova Suchanova, Libor Kostka, Pavel Sacha, Vladimir Subr, Tomas Etrych, Petr Simon, Jitka Barinkova, Robin Krystufek, Hana Spanielova, Jitka Forstova, Jan Konvalinka, Petr Cigler: Inhibitor−GCPII Interaction: Selective and Robust System for Targeting Cancer Cells with Structurally Diverse NPs, Molecular Pharmaceutics, doi: 10.1021/acs.molpharmaceut.7b00889, **2018.**

molecular pharmaceutics

Article

Cite This: Mol. Pharmaceutics XXXX, XXX, XXX−XXX

Inhibitor−GCPII Interaction: Selective and Robust System for Targeting Cancer Cells with Structurally Diverse Nanoparticles

Jitka Neburkova,[†,‡,§] Frantisek Sedlak,[†,‡,§,∥] Jirina Zackova Suchanova,[§,∥] Libor Kostka,[⊥] Pavel Sacha,[†] Vladimir Subr,[⊥] Tomas Etrych,[⊥] Petr Simon,[†] Jitka Barinkova,[†] Robin Krystufek,[†] Hana Spanielova,[†,∥] Jitka Forstova,[∥] Jan Konvalinka,[†,#] and Petr Cigler*[,†]

[†]Institute of Organic Chemistry and Biochemistry of the CAS, Flemingovo namesti 2, 166 10 Prague, Czech Republic
[‡]First Faculty of Medicine, Charles University, Katerinska 32, 121 08 Prague, Czech Republic
[∥]Department of Genetics and Microbiology, Faculty of Science, Charles University, Vinicna 5, 128 44 Prague 2, Czech Republic
[⊥]Institute of Macromolecular Chemistry of the CAS, Heyrovskeho namesti 2, 162 06, Prague 6, Czech Republic
[#]Department of Biochemistry, Faculty of Science, Charles University, Hlavova 2030, 128 43 Prague 2, Czech Republic

Supporting Information

ABSTRACT: Glutamate carboxypeptidase II (GCPII) is a membrane protease overexpressed by prostate cancer cells and detected in the neovasculature of most solid tumors. Targeting GCPII with inhibitor-bearing nanoparticles can enable recognition, imaging, and delivery of treatments to cancer cells. Compared to methods based on antibodies and other large biomolecules, inhibitor-mediated targeting benefits from the low molecular weight of the inhibitor molecules, which are typically stable, easy-to-handle, and able to bind the enzyme with very high affinity. Although GCPII is established as a molecular target, comparing previously reported results is difficult due to the different methodological approaches used. In this work, we investigate the robustness and limitations of GCPII targeting with a diverse range of inhibitor-bearing nanoparticles (various structures, sizes, bionanointerfaces, conjugation chemistry, and surface densities of attached inhibitors). Polymer-coated nanodiamonds, virus-like particles based on bacteriophage Qβ and mouse polyomavirus, and polymeric poly(HPMA) nanoparticles with inhibitors attached by different means were synthesized and characterized. We evaluated their ability to bind GCPII and interact with cancer cells using surface plasmon resonance, inhibition assay, flow cytometry, and confocal microscopy. Regardless of the diversity of the investigated nanosystems, they all strongly interact with GCPII (most with low picomolar K_i values) and effectively target GCPII-expressing cells. The robustness of this approach was limited only by the quality of the nanoparticle bionanointerface, which must be properly designed by adding a sufficient density of hydrophilic protective polymers. We conclude that the targeting of cancer cells overexpressing GCPII is a viable approach transferable to a broad diversity of nanosystems.

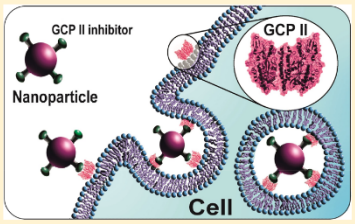

KEYWORDS: *GCPII, PSMA, inhibitor, click chemistry, targeting, cell, nanodiamond, virus-like particle, multivalent binding, polymer, nonspecific interaction*

INTRODUCTION

Targeted delivery of pharmaceuticals into tumor tissues offers promise for precise cancer diagnosis and treatment. Nanoparticle (NP)-based carriers offer several advantages over conventional therapy with cytotoxic drugs. The polyvalency of ligands strengthens binding efficacy, the size of NPs leads to prolonged blood circulation time and enables passive targeting (so-called enhanced permeation effect), and the hollow interior of NPs enables delivery of cargo.[1]

For specific cellular targeting, glutamate carboxypeptidase II (GCPII), also known as prostate-specific membrane antigen (PSMA), is a particularly interesting receptor due to its higher expression in prostate cancer tissue and cancer-associated neovasculature.[2,3] Its abundance correlates with the aggressiveness of the prostate cancer (GCPII is expressed in 80% of cells in malignant lesions[4]) and poor prognosis of the patient. In contrast to surface receptors that are present on all cell types, such as transferrin receptor, GCPII is more tissue-specific. It is primarily expressed in the prostate, central nervous system, small intestine, and kidney; expression in other tissues is much lower.[5] GCPII is a homodimeric transmembrane glycoprotein and metalloprotease with two main natural substrates, the most important of which is *N*-acetyl-L-aspartyl-L-glutamate (NAAG). In the CNS, GCPII cleaves NAAG into the neurotransmitters

Special Issue: Click Chemistry for Medicine and Biology

Received: October 10, 2017
Revised: January 22, 2018
Accepted: February 1, 2018
Published: February 1, 2018

DOI: 10.1021/acs.molpharmaceut.7b00889
Mol. Pharmaceutics XXXX, XXX, XXX−XXX

N-acetyl- L-aspartate and glutamate. In the intestine, where it is also known as folate hydrolase I, GCPII participates in the cleavage of γ-linked glutamates from pteroyl-poly(γ-glutamate), freeing the vitamin folic acid.[6] Although the substrate and physiological function of GCPII in prostate remain unknown, its overexpression in prostate cancer is well-established, and the enzyme has been exploited as a highly specific target for cancer diagnostics and therapies.

Cancer cells overexpressing GCPII have been successfully targeted with NPs bearing antibodies,[7,8] nucleic acid aptamers,[9,10] and specific inhibitors.[11−14] Despite the convenient properties of small molecules, including stability, nonimmunogenicity, and ease of large-scale synthesis, using inhibitors as targeting ligands is not common. NPs bearing inhibitors have been developed for a very small number of targets, including carbonic anhydrase IX[15] and GCPII.[11−14,16−25] This may be due to the fact that enzymes localized on the plasma membrane usually are not cancer- or tissue-specific, and to the lack of known potent inhibitors for these enzymes. Nevertheless, GCPII inhibitors previously have been used with soft polymeric NPs, including in clinical trials,[19] and with inorganic NPs.[16,22,23] Because of the very different methodological approaches and NP structures used in various studies, it is difficult to compare results.

Here, we focus on exploring the structural and chemical diversity of NP systems that can be delivered to their cellular targets using interactions between small inhibitor molecules attached to the NP and GCPII on the surface of the target cell. To do so, we use representatives of different types of NPs: polymer-coated nanodiamonds, virus-like particles based on bacteriophage Qβ and mouse polyomavirus, and polymeric nanoparticles with an inhibitor attached as a targeting ligand. Although targeted nanosystems based on all these NPs have been developed previously, targeting with small molecules is typically a more challenging approach that requires surface optimization. The range of selected particles enables us to investigate nanosystems of different size, flexibility, bionanointerface, and conjugation chemistry. We evaluate targeting efficiency under the same conditions on the same cellular model to identify the potential limitations of these GCPII-inhibitor-targeting systems.

Nanodiamonds (NDs) are relatively polydisperse (in size and shape), nontoxic carbon NPs with unique optical properties, including near-infrared unbleachable fluorescence [derived from nitrogen vacancy (NV) centers] sensitive to magnetic and electric fields.[26] Similar to other inorganic NPs, they aggregate in electrolytes (buffers and media), driven by strong van der Waals forces.[27] NDs can be colloidally stabilized by steric hindrance, either by proteins or by polymers. Although proteins can both stabilize the particles and direct them to the intended target, electroneutral polymers also can reduce nonspecific interactions with proteins and cells, which is crucial for preparation of outstanding NPs for targeting. In a biological environment, interactions of proteins with NPs form a so-called "protein corona" on the NP surface,[28,29] which can be prevented by creating a dense polymeric shell on the NP. Intact, biocompatible, and nonimmunogenic polymers can shield the surface and minimize off-target binding.[30]

NDs without a polymer shell have been targeted to cells using the protein transferrin[31−33] or small protein toxins.[34] While use of a polymer interface can be beneficial for NPs bearing proteins, it is necessary for NPs bearing small molecules, because small molecules do not have a shielding effect on the NPs. Polymer-coated NDs bearing folic acid,[35,36] RGD peptide,[37,38] and anti-HER2 peptide[39] have been targeted to cancer cells with very high efficacy.

Virus-like particles (VLPs) are safe and noninfectious virus derived NPs, usually formed in biological systems into well-defined uniform structures by a self-assembly process from multiple copies of the same capsid protein(s). VLPs are available in various sizes and shapes and display different cell binding properties. VLPs derived from plant viruses and bacteriophages usually do not efficiently bind mammalian cells, whereas VLPs derived from mammalian viruses can bind to the mammalian cell surface, engaging the carbohydrate moieties of glycocalyx.

Mouse polyomavirus (MPyV) is an example of a small (45 nm diameter) dsDNA nonenveloped mouse virus. Historically, VLPs composed of MPyV capsid protein were the first VLPs to be used for gene transfer.[40,41] Because there is no preexisting humoral immunity to MPyV in the human population, MPyV VLPs are suitable for potential clinical use. The MPyV capsid is composed of 72 subunits. Each subunit consists of 5 molecules of the major capsid protein, VP1, which form pentamers. Under experimental conditions, guided *in vitro* disassembly and reassembly can be used for passive cargo loading into the interior of VLPs, as shown for human polyomavirus JC.[42] MPyV uses GD1a, GT1b,[43] and GT1a[44] gangliosides as primary receptors that mediate transport of the virus along an infectious pathway. Moreover, $\alpha_4\beta_1$ integrin has been identified as a secondary receptor.[45] Although viral binding to gangliosides is required for high levels of virus accumulation on the cell surface, the presence of cell-surface glycoproteins also allows for virus attachment and internalization. MPyV VLPs therefore interact with a wide variety of mammalian cells via sialic acid presented on cell surface glycoproteins and glycolipids and enter cells readily. As with NDs, surface modification of VLPs with polymers may be required for selective targeting to the specific receptor and prevention of nonspecific interactions. Recently, we demonstrated that large molecules (the protein transferrin) displayed on the MPyV surface can both retarget the VLP to cancer cells and prevent the interaction with its primary receptors.[46] Targeting with small molecules has not yet been demonstrated for MPyV VLPs.

Bacteriophage Qβ is an example of a small (28 nm diameter) icosahedral virus, VLPs of which have been actively investigated for several nanotechnology applications. Qβ VLPs are highly monodisperse and very stable, and they consist of 180 protein subunits cross-linked by disulfide linkages. Qβ VLPs can package small enzymes to protect and stabilize them.[47] Unlike other types of NPs, Qβ VLPs do not interact with mammalian cells to a great degree, and therefore they do not need to be coated with polymers to decrease nonspecific interactions and efficiently target cells. Qβ VLPs have been modified with transferrin,[48] epidermal growth factor,[49] glycan,[50] and cyclic RGD[51] to target cells, as shown by M. G. Finn and collaborators. Although a polymer coating is not needed *in vitro*, for *in vivo* applications the VLP surface should be covered with polymers to improve pharmacokinetic properties and reduce immunogenicity. Qβ particles have been modified with poly(2-oxazoline)s[52] and oligo(ethylene glycol)-methacrylate[53] to enhance thermal stability and evade immune responses.

Polymeric NPs are among the most widely used NPs for bioapplications, thanks to their variability in composition, which can be adjusted according to the needs of the application.

DOI: 10.1021/acs.molpharmaceut.7b00889
Mol. Pharmaceutics XXXX, XXX, XXX−XXX

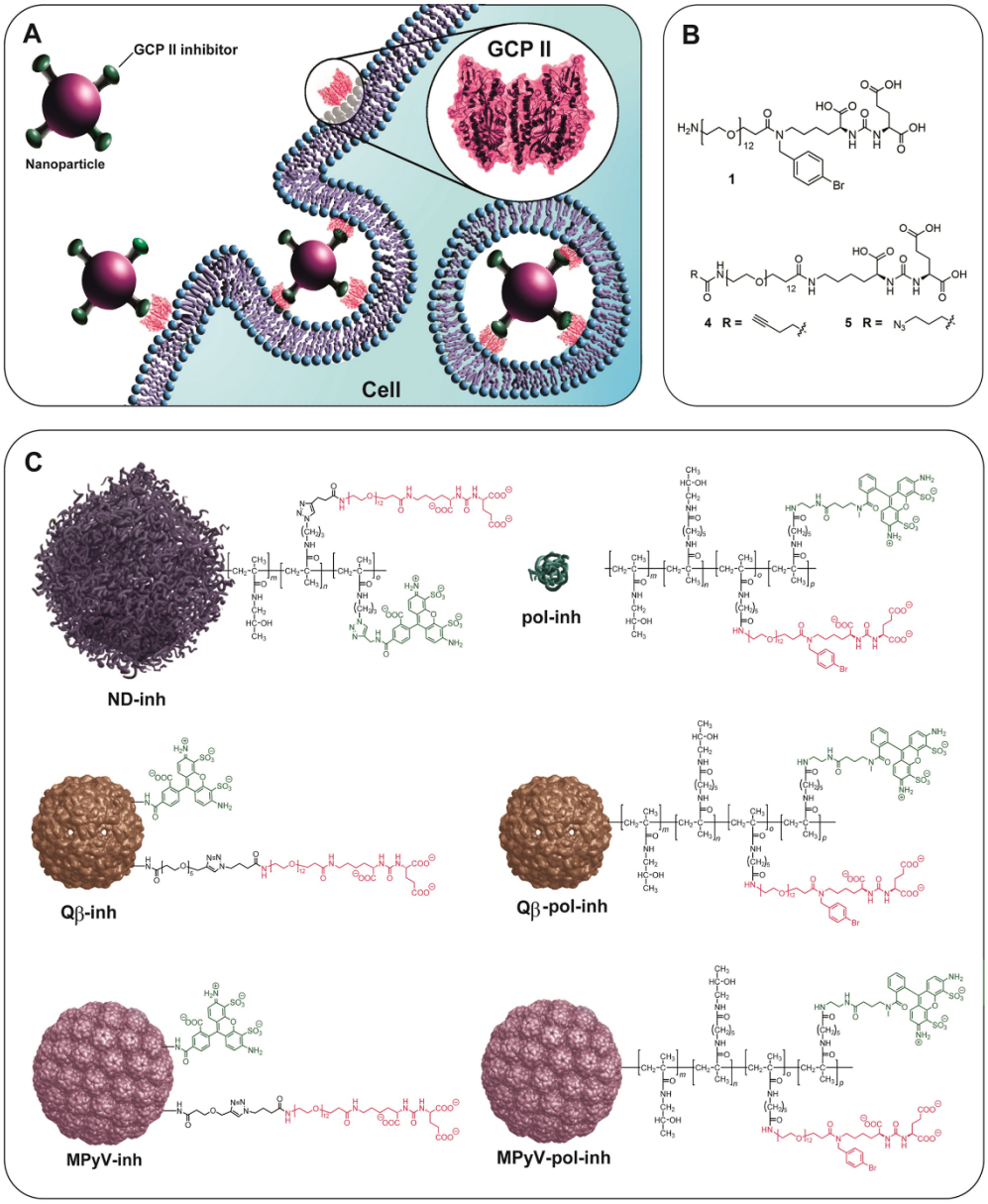

Figure 1. (A) The overall scheme of GCPII targeting using NPs bearing GCPII inhibitors. A NP bearing polyvalent array of GCPII inhibitors binds to GCPII, which is anchored in cell membrane. The nanoparticle is then endocytosed. (B) The structures of the inhibitors **1**, **4**, and **5** used for NP modifications. (C) Schematic illustration of the used NPs and molecular structure of their bionanointerface. Only particles modified with GCPII inhibitors are shown: nanodiamonds (**ND-inh**), small nanoparticles based only on the coating polymer (**pol-inh**), bacteriophage Qβ VLPs (**Qβ-inh, Qβ-pol-inh**), and mouse polyomavirus VLPs (**MPyV-inh**, **MPyV-pol-inh**). The corresponding control particles (**ND**, **pol**, **Qβ**, **Qβ-pol**, **MPyV**, and **MPyV-pol**) have always the same structure, but do not contain the GCPII inhibitors (not shown for clarity). For VLPs, the attachment of inhibitor via coating polymer is indicated by the presence of "**pol**" in the abbreviation, while the absence of "**pol**" indicates a direct attachment to surface lysines. See also Table 1 for further details.

DOI: 10.1021/acs.molpharmaceut.7b00889
Mol. Pharmaceutics XXXX, XXX, XXX−XXX

They are not prone to nonspecific interactions with cells, and therefore they are not immediately internalized. On the other hand, polymeric NPs are typically not monodisperse. Polymeric NPs are the only particles assessed in this study that have previously been used with a specific inhibitor to target GCPII. Among the most studied have been block copolymers containing a hydrophobic part, usually poly(lactid) acid, bearing the hydrophobic molecule and a hydrophilic PEG chain exposed to the environment.[12,17,19,20] For nucleic acid delivery, copolymers contained combination of polyethylenimine and PEG.[13,18] Biodegradable, nonimmunogenic, water-soluble, and biocompatible *N*-(2-hydroxypropyl)-methacrylamide (HPMA) copolymer with inhibitor targeting GCPII also has shown potential in bioapplications.[24]

The most widely used conjugation chemistry for modification of NPs with a targeting ligand is amidic coupling, which is the easiest option for molecules that naturally contain carboxyl or amine groups (such as VLPs). For amidic coupling, moieties with activated carboxyl groups with fair stability and selective reactivity to amines are needed. Here, we used the thiazolidine-2-thione group (TT) to fulfill these requirements.[54] An alternative option is use of highly effective bioorthogonal reactions, which do not have significant reactivity toward naturally occurring functional groups. The Huisgen azide–alkyne cycloaddition catalyzed by Cu(I) ions (click reaction) is popular due to its high bioconjugation efficacy without the need for protecting groups, simplicity, and variety of available substrates.[55,56] In this work, we used both amidic coupling and click reaction.

METHODS

Synthesis of GCPII inhibitors and HPMA polymers is described in the Supporting Information.

Preparation of Mouse Polyomavirus VLPs (MPyV, MPyV-inh, MPyV-PEG). MPyV particles consisting of VP1 capsid protein were produced using baculovirus expression system in *Spodoptera frugiperda* (Sf9) cells.[57] Purification of particles in cesium chloride density gradient was followed by concentration through a sucrose cushion as previously described.[57,58]

Labeling of MPyV VLPs with Alexa Fluor 488. Unmodified MPyV VLPs were dialyzed against 0.1 M HEPES, pH 7.9, and the protein concentration was adjusted to 2 mg/mL (20 mg VP1 protein in total). This solution was treated with NHS-Alexa Fluor 488 (ThermoFisher Scientific, final concentration 34 nM, 0.2 equiv per surface lysine; each MPyV VLP contains 720 surface-exposed lysines) at room temperature overnight with gentle shaking (250 rpm, TS-100C, Thermo-Shaker, Biosan). Excess dye was removed by dialysis against 0.1 M HEPES, pH 7.9 (4 °C, overnight with two buffer changes). Two-thirds of the prepared MPyV VLP mixture were used for subsequent preparation of **MPyV-inh** particles. The rest was purified and concentrated by centrifugation through two successive 20% sucrose cushions (35,000 rpm, SW41 Beckman rotor, 3 h) and dissolved in storage buffer (10 mM Tris-HCl, pH 7.4, 150 mM NaCl, 0.01 mM $CaCl_2$), providing the conjugate of MPyV VLPs (4 mg) used as a negative control (**MPyV**).

*Preparation of **MPyV-inh** by Click Reaction.* Alexa Fluor 488-labeled **MPyV** VLPs were first modified with the heterobifunctional linker propargyl-*N*-hydroxysuccinimidyl (NHS) ester (Sigma-Aldrich). To a solution of **MPyV** in 0.1 M HEPES, pH 7.9 (2 mg/mL; total amount 14 mg) was added 4.87 mg of the linker (35-fold molar excess per surface lysine) dissolved in 770 μL of DMSO (10% final concentration of DMSO). The reaction mixture was incubated at room temperature overnight with gentle shaking (250 rpm, TS-100C, Thermo-Shaker, Biosan). Excess reagents were removed by dialysis against 0.1 M HEPES, pH 7.4 (4 °C, overnight, first two buffer changes contained 10% DMSO), providing MPyV VLP–alkyne conjugate.

MPyV VLP–alkyne (5 mg in a final reaction volume of 6 mL), GCPII inhibitor **5** (see Figure 1 and Supporting Information; 213.5 nmol) in 0.1 M HEPES buffer, pH 7.4, containing 10 mM copper sulfate, 100 mM aminoguanidine, 50 mM tris(3-hydroxypropyltriazolylmethyl)amine (THPTA, synthesized according to a previously published procedure[59]), and freshly prepared 100 mM sodium ascorbate were used for click reaction. Copper sulfate and THPTA were mixed in a separate tube in a 1:5 concentration ratio prior to addition to the reaction mixture. The reaction mixture was well-sealed, mixed, and allowed to stand undisturbed at room temperature for 3 h. Excess inhibitor was removed from the resulting **MPyV-inh** conjugates by dialysis (cellulose ester membrane, 300 kDa, Biotech) against 0.1 M HEPES, pH 7.4 (4 °C, overnight), and storage buffer (4 °C, overnight). Finally, the **MPyV-inh** particles were purified and concentrated by centrifugation through two successive 20% sucrose cushions and dissolved in storage buffer.

*Preparation of **MPyV-PEG** Particles.* **MPyV** were dialyzed against 0.1 M HEPES, pH 8.0, with 0.01 mM $CaCl_2$ (4 °C, overnight). Then, the solution of particles (0.95 mg/mL, total amount 0.38 mg) was treated with 0.47 mg of acid-PEG_{13}-NHS ester (Broadpharm, BP-22330, 35-fold excess per surface lysine) at room temperature for 5 h on a rotating mixer. Excess reagents were removed by dialysis against TBS (20 mM Tris-HCl, 150 mM NaCl, pH 7.4) with 0.01 mM $CaCl_2$ (4 °C, overnight).

Characterization of the Particles. The quality of each preparation was examined by electron microscopy and SDS–PAGE. The amounts of VP1 were determined by Qubit protein assay kit (ThermoFisher Scientific). For matrix-assisted laser desorption/ionization mass spectrometry (MALDI) measurements, 15 μL of the sample (25 μg, 1.54 pmol) was mixed with 7.5 μL of 100 mM dithiothreitol (DTT) and 7.5 μL of 10 M urea for 10 min to disassemble the particles. According to MALDI measurements, we found 540 inhibitor molecules per **MPyV-inh** particle.

Preparation of Bacteriophage Qβ Particles (Qβ, Qβ-inh). Qβ particles were prepared according to a previously published procedure.[47] *Escherichia coli* BL21 (DE3) (Invitrogen) cells harboring the plasmid pET28-B (containing capsid protein) were grown in SOC supplemented with kanamycin. Starter cultures were grown overnight at 37 °C, and were used to inoculate larger cultures. Induction was performed with 1 mM IPTG at an OD_{600} of 1.0 in SOB overnight at 25 °C. Cells were harvested by centrifugation in a Beckman Coulter Avanti J-20 XP (rotor JA 17) at 5,400 rcf. The cell lysate was prepared by resuspending the cell pellet with phosphate buffer (0.1 M, pH 7.0) and sonicating at 50 W for 20 min with 5 s bursts and 5 s pause intervals. Cell debris was pelleted by centrifugation (Beckman Coulter Avanti J-20 XP) in a JA 17 rotor for 10 min (27,000 rcf), and 2 M ammonium sulfate was added to the supernatant to precipitate the Qβ VLPs. Pelleted VLPs were resuspended in phosphate buffer. Lipids and membrane proteins were then extracted from particles with 1:1 *n*-

DOI: 10.1021/acs.molpharmaceut.7b00889
Mol. Pharmaceutics XXXX, XXX, XXX−XXX

butanol:chloroform; Qβ VLPs remained in the aqueous layer. Crude Qβ VLPs were further purified by sucrose gradient ultracentrifugation (10−40% w:v). Particles were pelleted out from the sucrose solution by ultracentrifugation in a 70.1 Ti rotor (Beckman) at 70,000 rpm for 2 h.

Labeling of Qβ with Alexa Fluor 488. The unmodified Qβ VLPs (3 mg) were diluted in 0.1 M HEPES, pH 8 (5 mg/mL). This solution was treated with Alexa Fluor 488 5-SDP Ester (ThermoFisher Scientific, final concentration 280 μM, 0.2 equiv per surface lysine; each Qβ VLP contains 720 surface-exposed lysines) at room temperature overnight with gentle shaking (250 rpm, TS-100C, Thermo-Shaker, Biosan). Excess dye was removed by centrifugal filtration (Millipore, Amicon ultra 2 mL, cut off 100 kDa, 6 times) into 0.1 M HEPES, pH 8, providing the conjugate Qβ VLP used as a negative control (**Qβ**). Two-thirds of the prepared Qβ VLP mixture was used for subsequent preparation of Qβ-inh particles (**Qβ-inh**).

*Preparation of **Qβ-inh** by Click Reaction.* First, **Qβ** VLPs were modified with a heterobifunctional linker containing propargyl and NHS ester moieties (alkyne-PEG_5-NHS, Sigma-Aldrich). To a solution of **Qβ** VLPs in 0.1 M HEPES, pH 8 (5 mg/mL; total amount 2 mg), was added 3.94 mg of the linker (17-fold excess per surface lysine) dissolved in 40 μL of DMSO (10% final concentration of DMSO). The reaction mixture was incubated at room temperature overnight with light shaking. Excess reagents were removed by centrifugal filtration (Millipore, Amicon ultra 2 mL, cut off 100 kDa, 8 times) against 0.1 M HEPES, pH 7.4 (first two buffer changes contained 10% DMSO), providing Qβ VLP−alkyne conjugate.

Qβ VLP−alkyne (1.6 mg in a final reaction volume of 160 μL), GCPII inhibitor **5** (see Figure 1 and Supporting Information; 205 nmol) in 0.1 M HEPES buffer, pH 7.4, containing 5.12 mM copper sulfate, 25.6 mM tris(3-hydroxypropyltriazolylmethyl)amine (THPTA), 40 mM aminoguanidine, and freshly prepared 40 mM sodium ascorbate were used for click reaction. Copper sulfate and THPTA were mixed in a separate tube in a 1:5 concentration ratio prior to addition to the reaction mixture. The reaction mixture was well-sealed, mixed, and allowed to stand undisturbed at room temperature for 3 h. The resulting Qβ-inh VLP conjugates were purified from excess reagents by centrifugal filtration (Millipore, Amicon ultra 2 mL, cut off 100 kDa, 8 times) into 0.1 M HEPES, pH 7.4, providing **Qβ-inh** conjugate.

Characterization of the Particles. The quality of each preparation was examined by electron microscopy and SDS−PAGE. The amounts of Qβ VLPs were determined by Qubit protein assay kit (ThermoFisher Scientific). For MALDI measurements, 5 μL of the sample (50 μg, 19.5 pmol) was mixed with 2.5 μL of 100 mM DTT and 2.5 μL of 10 M urea for 10 min to disassemble the particles. According to MALDI measurements, we found 180 inhibitors per **Qβ-inh** particle.

Preparation of Poly(HPMA)-Coated VLPs (MPyV-pol, MPyV-pol-inh, Qβ-pol, and Qβ-pol-inh). Unmodified MPyV VLPs were dialyzed and diluted to a low molarity buffer (0.67 mg/mL, 4 mM HEPES, pH 8, 20 mM NaCl, 4 μM $CaCl_2$). Unmodified Qβ VLPs (1 mg/mL) were dispersed in 25 mM HEPES buffer, pH 8. Three milliliters of MPyV particles (2 mg) was added slowly to a stirred solution of either polymer with inhibitor (pol-inh) or polymer without inhibitor (pol), both with TT reactive groups (3.76 mg/160 μL Milli-Q water, approximately 1 molar equiv to surface lysines on particles). Two milliliters of Qβ particles (2 mg) was added slowly to the stirred solution of pol-inh or pol with TT reactive groups (8.69 mg/mL Milli-Q water, approximately 0.4 equiv of surface lysines on particles). Reaction proceeded for 24 h (room temperature, mixing), and afterward remaining TT reactive groups were quenched by buffered ethanolamine (10 molar equiv to TT reactive groups). The conversion of TT reactive groups was controlled by decrease of their characteristic absorption band at 306 nm. After 12 h, no TT reactive groups were present.

VLP particles were purified by ultracentrifugation in sucrose density gradient (10−40% w:v, SW 28 Beckman rotor, 2 h 30,000 rpm for **MPyV-pol** and **MPyV-pol-inh** and 3 h 40,000 rpm for **Qβ-pol** and **Qβ-pol-inh**). Particles were pelleted out from the sucrose solution by ultracentrifugation at 35,000 rpm (SW 41Ti Beckman rotor) for 3 h.

Preparation of ND and ND-inh. NDs were pretreated and coated with a methacrylate-terminated thin silica layer, according to a previously published procedure.[60] Polymer coating was performed with slight modifications. HPMA (152 mg, 1046 μmol, purchased from Polysciences and freshly purified by FLASH chromatography) and 3-(azidopropyl)-methacrylamide (8 mg, 47.6 μmol, synthesized by methacryloylation of 3-azidopropan-1-amine with methacryloyl chloride[61]) were dissolved in DMSO (480 μL). 2,2′-Azobis(2-methylpropionitrile) (AIBN, 50 mg, 0.305 mmol, recrystallized by thickening an ethanol solution on a rotary evaporator at a maximum temperature of 30 °C) was added to the mixture. The mixture was filtered using a 0.4 μm glass microfiber microfilter. Methacrylate-terminated ND particles (8 mg, 80 μL in DMSO) were added. The reaction proceeded for 3 days under argon at 55 °C. The particles were diluted three times with methanol, centrifuged (21,000 rcf, 30 min), and purified by centrifugation with methanol (25,000 rcf, 30 min, 1 mL, 3 times). Polymer-coated NDs were further modified using azide−alkyne cycloaddition catalyzed by Cu(I) ions with Alexa Fluor 488-alkyne (purchased from Life Technologies) and GCPII inhibitor **4** (see Figure 1 and Supporting Information). NDs were modified with these two ligands in consecutive reactions utilizing the same surface functionalities. Washing procedures were employed after both modification steps. Stock solutions for copper(I)-catalyzed azide−alkyne cycloaddition reactions were prepared in water, except for the Alexa Fluor 488-alkyne, which was prepared in DMSO. The solutions of copper sulfate and THPTA were premixed (in a 1:2 concentration ratio) before they were added to the reaction mixture to yield final concentrations of 0.32 mM and 0.64 mM, respectively. The mixture was filled to the final volume with 50 mM HEPES buffer, pH 7.4. For the reaction of modified NDs with Alexa Fluor 488-alkyne, the reactants were mixed in the following order and final concentrations: colloid of poly-(HPMA)-azide modified NDs (1.2 mg in a final reaction volume of 1536 μL), Alexa Fluor 488-alkyne (10 μM), Cu-catalyst solution (see above), and a freshly prepared solution of sodium ascorbate (5 mM). The reaction mixture was well-sealed, mixed, and left for 3 h with no stirring. Modified NDs were isolated by centrifugation (20,000 rcf, 20 min) and twice washed with 1 mL of water. Half (0.6 mg) of the Alexa Fluor 488 modified NDs was reacted in a click reaction with GCPII inhibitor (320 μM) under the same conditions (in a final volume of 768 μL). Polymer-coated NDs modified with Alexa Fluor 488 (**ND**) and polymer-coated NDs modified with Alexa Fluor 488 and GCPII inhibitor (**ND-inh**) were both treated the same and were washed with water (1 mL, 7 times).

DOI: 10.1021/acs.molpharmaceut.7b00889
Mol. Pharmaceutics XXXX, XXX, XXX−XXX

Surface Plasmon Resonance (SPR) Measurements. All SPR measurements were performed on a four-channel SPR sensor platform (PLASMON IV) developed at the Institute of Photonics and Electronics (IPE) of the Academy of Sciences of the Czech Republic, Prague. Gold SPR chips were loaded into a pure ethanol mixture of alkanethiols containing carboxylic terminal groups [HS-$(CH_2)_{11}$-PEG_4-OH and HS-$(CH_2)_{11}$-PEG_6-O-CH_2-COOH, molar ratio 7:3, Prochimia] with a final concentration of 0.2 mM and incubated for 1 h at 37 °C. The chips were then rinsed with ethanol and deionized water, dried with flow of nitrogen, and mounted to the prism on the SPR sensor. All experiments were performed at 25 °C. The carboxyl groups present on the gold thin sensor were activated by a solution of NHS, 1-ethyl-3-[3-(dimethylamino)propyl]-carbodiimide (EDC) at final concentrations of 12.5 mM and 62.5 mM, respectively, in deionized water for 5 min at a flow rate of 20 μL/min. Excess reagents were removed at a flow rate of 30 μL/min. Next, 10 μg/mL neutravidin in 10 mM sodium acetate buffer, pH 5.0, was loaded for 6 min. Then, a high ionic strength solution (PBS with 0.5 M NaCl) was used to wash out noncovalently bound proteins, followed by 1 M ethanolamine for deactivation of residual activated carboxylic groups. Afterward, the extracellular domain of GCPII modified with biotin (Avi-GCPII, prepared according to Tykvart et al.[62]) was loaded for 10 min. Various NPs (at final concentrations of 5 nM) in TBS were injected (association phase) for several minutes, and then TBS alone was injected (dissociation phase).

Inhibition Assay. The inhibitory effects of all particles and polymers were measured as previously described with minor modifications.[63] Briefly, in each well of a 96-well plate, 250 pg of recombinant GCPII was preincubated for 5 min at 37 °C in 90 μL of reaction buffer (25 mM BisTris propane, 150 mM NaCl, 0.001% (w/w) octaethylene glycol monododecyl ester (Affymetrix), pH 7.4) with a dilution series of inhibitor (particles or polymers). The reaction was started by adding 10 μL of the substrate, 4 μM pteroyldiglutamate. The reaction was stopped after 20 min incubation at 37 °C by adding 10 μL of 25 μM 2-(phoshonomethyl)pentanedioic acid (2-PMPA) and subsequently analyzed with an Agilent 1200 series HPLC using isocratic separation in 2.7% AcCN, 19.5 mM phosphate, pH 6.0, on an Acquity UPLC HSS T3 C18 1.8 μm column (2.1 × 100 mm, Waters) with detection at 281 nm. Obtained data were fitted by logistic equation using GraphPad (GraphPad Software, Inc.), and K_i values were calculated from the log IC_{50} the using Cheng–Prusoff equation.

Flow Cytometry. Cells (U-251$^+$ MG and U-251$^-$ MG; for preparation see Supporting Information) were detached from the dish by trypsinization, resuspended in DMEM (Sigma-Aldrich D5796) supplemented with 4 mM L-glutamine (Gibco) and 10% FBS (Gibco), and counted. An appropriate amount of cells was centrifuged (300 rcf, 5 min, 4 °C) and dissolved in serum free medium without phosphate (SFM-P, DMEM, Sigma-Aldrich D3656). Subsequently, the cells were transferred into a 96-well plate (6×10^4 cells per well) and incubated with NPs (final concentration of 4 nM) for 1 h at 37 °C, 5% CO_2. This incubation was performed in triplicate and with negative controls (SFM-P only). After the treatment, cells were centrifuged (300 rcf, 5 min, 4 °C), resuspended in 200 μL of TBS, and measured with a BD LSRFortessa flow cytometry analyzer (Becton, Dickinson and Company). The data were further analyzed with BD FACSDiva Software, version 6.0. Statistical analysis was performed in R program version 3.3.1. (2016-06-21).

Confocal Microscopy. U-251$^+$ MG and U-251$^-$ MG cells (for preparation see Supporting Information) were grown in 4-chamber Glass Bottom Microwell Dishes (Cellvis, D35C4-20-1.5-N) at approximately 30% confluence, incubated for 1 h at 37 °C, 5% CO_2 with NPs, polymers (12.5 nM, diluted in SFM-P, DMEM, Sigma-Aldrich D5796), or medium only (SFM-P). Subsequently, cells were washed with TBS, fixed with 3.7% formaldehyde for 10 min, washed again in TBS, and counterstained with 500 ng/mL Hoechst 34580 solution (Thermo Scientific). Fluorescence and transmitted light (TL) images were acquired on a Zeiss LSM 780 confocal microscope with ZEN 2011 software. The images were further processed in Fiji software (contrast enhancement of Hoechst channel and TL images).[64]

RESULTS AND DISCUSSION

Design and Preparation of Nanoparticles. To investigate the versatility of cell targeting using GCPII inhibitors, we prepared six different types of particles with various surface modifications, as shown schematically in Figure 1 (for clarity, we present the final investigated particles in **bold**, for example **Qβ-inh**). We attached to the surface of these NPs fluorescent labels (Alexa Fluor 488 or Atto 488; marked green in Figure 1) and GCPII inhibitors (marked red). As a targeting moiety, we used optimized urea-based inhibitors[65,63] **1**, **4**, and **5** that are highly polar and negatively charged, contributing to Coulombic stabilization of the particles in solution. The inhibitors were equipped by linkers terminated with either groups for click chemistry (azide, alkyne) or amino groups for conjugation to activated carboxylic acids. To remove cytotoxic Cu^{2+} ions, which can remain in the sample after click reaction, we used extensive washing procedures diluting the original concentrations of reagents by a factor of minimally 10^7 (see Methods). This decreased the copper concentration far below from cytotoxic limit, which is further suppressed by the use of THPTA ligand.[66] Furthermore, in our previous works utilizing click chemistry on similar nanoparticles,[37,46] we have observed no copper toxicity. Based on these assumptions, we have not involved cytotoxicity tests in this study.

The span of NP structural archetypes studied here includes those currently used in nanomedical applications ranging from imaging and theranostic applications to drug delivery. Polymer-coated NDs are hybrids with solid inorganic cores that retain their original shape and size during all interactions. However, their polymer shell enables flexible adjustment of targeting groups for polyvalent binding. VLPs are usually classified as soft matter nanomaterial; however, they are relatively rigid and do not undergo significant size or shape changes. Nevertheless, attachment of targeting groups to VLPs via flexible linkers can allow for a similarly flexible interaction as in polymer shells on NDs. Finally, our polymeric NPs represent the smallest and most flexible systems used in this study, and are highly susceptible to size and shape changes upon binding to a target.

VLPs from both MPyV and Qβ are formed from proteins containing lysine residues with modifiable amino groups. Both types of VLPs contain approximately 720 surface lysines per particle,[50,67] which we used to modify the particles with dyes and inhibitors either by short linkages or by polymer coating. The first approach involved labeling with Alexa Fluor 488 active ester (providing negative controls and **MPyV** or **Qβ** conjugates) to allow fluorescence visualization. Then, we modified VLPs at the remaining lysines with an excess of a short linker bearing a propargyl group and attached GCPII

DOI: 10.1021/acs.molpharmaceut.7b00889
Mol. Pharmaceutics XXXX, XXX, XXX−XXX

inhibitor−azide conjugates via click chemistry, obtaining **MPyV-inh** and **Qβ-inh** conjugates. Because MPyV VLPs can interact with sialic acid residues, which are ubiquitously distributed and broaden MPyV cell and tissue tropism,[68] we also prepared MPyV VLPs that should avoid these interactions (**MPyV-PEG**). These VLPs were prepared by covering **MPyV** with NHS PEG_{13}-carboxyl.

The second approach for MPyV and Qβ VLP modification involved coating the VLP surface with HPMA copolymer premodified with Atto 488 dye and then with GCPII inhibitors. In addition to dye and inhibitors, the copolymers also contained hydrolytically stable TT reactive groups, which can react with lysine amino groups on the VLP surface, forming amide bonds. The reaction of VLPs with polymer proceeded overnight at pH 8. We then quenched all unreacted TT groups with ethanolamine. This step is very important because unreacted TT groups can cross-link the particles in the pellet after ultracentrifugation. We incubated the VLPs with either copolymer with inhibitor (pol-inh) or copolymer without inhibitor (pol). After purification, we obtained four different types of particles: **MPyV-pol-inh**, **MPyV-pol**, **Qβ-pol-inh**, and **Qβ-pol** (see Figure 1). The same polymer used for modification of particles was reacted in parallel with 1-aminopropan-2-ol and served as two last types of NPs (**pol-inh** and **pol**).

Coating with hydrophilic polymers greatly improves the colloidal stability of NDs in buffers and media used for bioapplications.[30] Here, we modified NDs with a thin silica layer bearing methacrylate moieties, from which polymer chains of *N*-(2-hydroxypropyl)methacrylamide and 3-(azidopropyl)-methacrylamide were grown by radical polymerization. The polymer surface enables efficient modifications, because the azide groups are randomly distributed on flexible chains without substantial steric hindrance from the surface. Using click chemistry, we equipped the NDs with GCPII inhibitor-alkyne. Although NV fluorescent centers in NDs possess excellent optical features for cell imaging,[37,69,70] for the ease of comparison with other particles in this study, we used NDs without NV centers but with attached Alexa Fluor-alkyne dye, providing **ND-inh**.

Characterization of nanoparticles. We characterized the size, morphology, and colloidal stability of all prepared NPs by transmission electron microscopy (TEM) and dynamic light scattering (DLS) (see Supporting Information for methods). TEM confirmed the presence of intact, highly monodispersed VLPs and fairly monodispersed ND particles (Figure 2A, Figure S1). Analysis of the particle size distribution (Figure 2B) revealed diameters of 44.7 ± 1.6 nm for **MPyV-pol-inh**, 27.2 ± 1.6 nm for **Qβ-pol-inh**, and 53.5 ± 12.0 nm for **ND-inh**. Using DLS, we ascertained that the particles do not aggregate (Figure 2C, Figure S2F) at 37 °C. Their hydrodynamic diameters are larger than the diameters obtained from TEM, indicating the presence of hydrated polymer shells in an aqueous environment. DLS data indicated that attachment of the inhibitor through either direct conjugation or a polymer coating does not change colloidal stability of NPs.

Data obtained from SDS−PAGE analysis confirmed that unmodified VLPs can be disassembled into VP1 monomers or dimers (Figure S3). The fluorescent polymers on Qβ VLPs dissociated completely from the coat proteins during sample processing, whereas polymers on MPyV VLPs remained cross-linked with the major capsid protein VP1, forming high molecular weight complexes (Figure S3A,B). In the case of

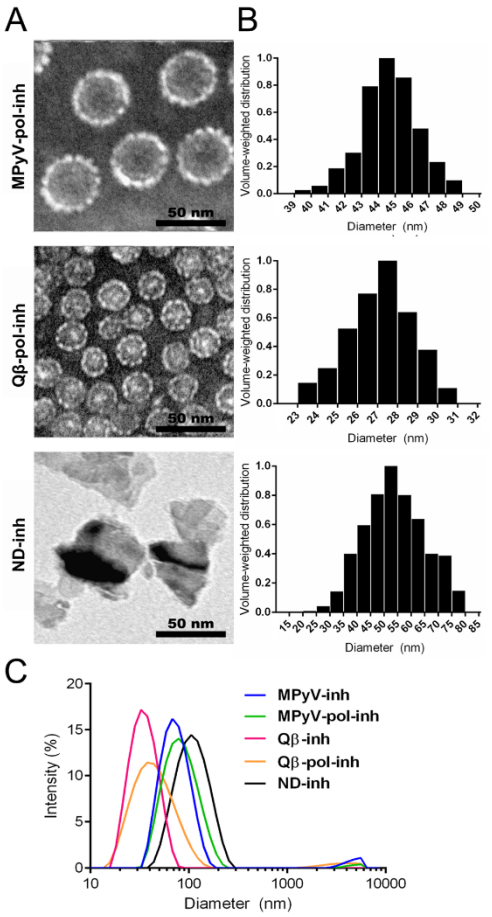

Figure 2. Characterization of NPs. (A) Representative TEM images, negative staining with 2% solution of phosphotungstic acid for **MPyV-pol-inh** and **Qβ-pol-inh**, scale bar = 50 nm. (B) Volume-weighted size distribution of the NPs according to TEM images analysis performed with ImageJ software. (C) Hydrodynamic diameters of NPs with conjugated inhibitors from DLS measurements at 37 °C (concentration 0.25 mg/mL in water).

directly modified VLPs (without polymers), the cross-linking phenomenon was seen in both types of VLPs, but was less pronounced in Qβ VLPs, likely resulting from different structural arrangements of particles. The absence of highly cross-linked complexes in these VLPs suggests that the particles potentially could more easily disassemble in cells to deliver cargo. NDs cannot be stained like proteins (Figure S3A); however, they were clearly detected at the start based on their fluorescent signal (Figure S3B). NDs did not migrate in the gel.

Increased thermal stability of VLPs can be indicative of modification on the particle surface,[52] especially in the case of MPyV, which is structurally less stable than Qβ. We monitored temperature-induced changes in MPyV particle stability by DLS (Figure S2). Nonmodified **MPyV** changed size slightly at

DOI: 10.1021/acs.molpharmaceut.7b00889
Mol. Pharmaceutics XXXX, XXX, XXX−XXX

temperatures over 60 °C (Figure S2A), and our results corresponded well with the observed temperature midpoint of denaturation (T_M = 56 °C) for MPyV particles produced in yeast.[71] Modification with HPMA copolymer resulted in higher thermal stability (up to 80 °C) (Figure S2D,E). Particles with directly conjugated inhibitor (**MPyV-inh**) (Figure S2B) or PEG (negative control, **MPyV-PEG**) (Figure S2C) did not disassemble even after incubation at 90 °C. We assume that the increased stability of the particles is mediated by the high coverage of the MPyV surface with PEG residues, which are present in both samples (the inhibitor linker is composed of PEG). The lower stability of poly(HPMA)-coated MPyV could be caused by incomplete coverage of copolymer on the surface.

Finally, we characterized the efficiency of labeling and inhibitor loading. Due to the nonhomogeneity of dye labeling between the different types of particles, we used the relative fluorescence of particles to normalize the flow cytometry data (Table 1). From quantification of dye on poly(HPMA)-coated VLPs, we estimate that there were approximately 2 HPMA copolymers on each **Qβ-pol-inh** particle and 8 molecules on **Qβ-pol**. Surface coverage of MPyV particles (which have a larger surface area) was higher, with 30 and 35 molecules of HPMA copolymer per **MPyV-pol-inh** and **MPyV-pol** particle, respectively. In general, the number of attached HPMA copolymers was lower than we expected. We hypothesize that this may be due to the high content of TT reactive groups connected to the copolymer backbone with hydrophobic alkyl linkers. Due to the flexibility of the polymer chain, folding and formation of local hydrophobic domains can occur, leading to steric hindrance and lower reactivity of TT moieties.

Table 1. Characterization of Nanoparticle Surface Modifications, Amount of the Fluorophores on the Particles, and Relative Fluorescence Intensities of NPs[a]

particle	polymer	fluorophore	fluorophores/particle	relative fluorescence
ND	HPMA	Alexa Fluor 488	110	7.7
ND-inh	HPMA	Alexa Fluor 488	67	5.3
Qβ		Alexa Fluor 488	72	9.2
Qβ-inh		Alexa Fluor 488	44	3.9
MPyV		Alexa Fluor 488	19	4.4
MPyV-inh		Alexa Fluor 488	63	7.4
MPyV-PEG	PEG	Alexa Fluor 488	30	6.9
Qβ-pol	HPMA	Atto 488	28	12.6
Qβ-pol-inh	HPMA	Atto 488	7	4.7
MPyV-pol	HPMA	Atto 488	114	30.6
MPyV-pol-inh	HPMA	Atto 488	88	23.3
pol	HPMA	Atto 488	3	1.0
pol-inh	HPMA	Atto 488	3	1.4

[a]The fluorescence intensities of the respective NPs were measured at the same molar NP concentration. The obtained values were always normalized to the fluorescence intensity of the NP with the lowest fluorescence intensity, **pol**.

We also used the dye quantification data to determine the number of inhibitor molecules on polymer-coated VLPs (Table 2). Based on known stoichiometry of the dye and inhibitor in the polymer, we obtained 12 and 180 inhibitors for **Qβ-pol-inh** and **MPyV-pol-inh**, respectively. We determined the number of inhibitors on **Qβ-inh** and **MPyV-inh** by MALDI measurement after disassembling Qβ and MPyV VLPs particles to protein subunits by treatment with dithiothreitol and urea. Although the mass spectra of the modified proteins were fairly complex (Figure S4), we were able to quantify the inhibitor loads, obtaining roughly ∼180 inhibitor molecules on **Qβ-inh** and ∼540 on **MPyV-inh** (corresponding to 25 and 75% of modified surface lysines, respectively). There were approximately 1,080 PEG molecules on **MPyV-PEG** (determined by the same approach). MALDI measurement also confirmed that inhibitor and PEG molecules were attached to the protein covalently.

Quantification of inhibitors on ND particles was a more challenging task because they cannot be disassembled to smaller units and measured by MALDI. However, based on an analogous reaction performed under identical conditions with fluorescent dye, we can assume a load of ∼250 inhibitors per ND particle.

Interaction of NPs with GCPII *in Vitro*. To analyze interactions between NPs and GCPII molecules, we performed SPR studies and inhibition assays. SPR measurements enabled us to ascertain the capacity of NPs to bind and recognize GCPII. We immobilized GCPII on SPR chips through a neutravidin−biotin interaction (GCPII+). This connection ensures that the GCPII orientation on the gold sensor is similar to the GCPII position on the plasma membrane. As a negative control, we attached neutravidin alone (GCPII−). SPR detects changes in the refractive index in the immediate vicinity of the surface layer of a sensor chip induced by particle binding to the surface, and because the particles have different refractive indices, we cannot directly compare and quantify their binding to GCPII. However, SPR measurements of all NPs bearing inhibitor verified their selectivity and strong affinity to GCPII+ chips (Figure 3). We also observed a weak interaction between **MPyV** particles and GCPII− chips. This likely reflects off-target binding between VP1 protein and neutravidin, as we observed the same interaction with streptavidin (data not shown). The very low dissociation rate (k_{off}) of the NPs from GCPII indicates an extremely strong interaction between GCPII and the inhibitor attached to the NPs. We surmise that this strength is mediated by cooperative formation of multiple bonds between ligand and layer (i.e., avidity).

Next, we investigated the ability of NPs to inhibit the processing of substrate by GCPII (Table 2). Using an HPLC inhibition assay, which monitors the cleavage of the pteroyldiglutamate substrate to folate and glutamate, we measured K_i values for all NPs decorated with inhibitor as well as for free inhibitors. The small molecule inhibitors showed K_i in low nanomolar range (2−14 nM). Their attachment to nanoparticles resulted in significant increase of inhibition efficacy, reaching subnanomolar (copolymer NP) or low picomolar (other NPs) K_i values. This behavior is most likely associated with high concentration of inhibitors at the NP surface, as documented by multivalent enhancement factors[72] in range units to tens of thousands (Table 2).

In comparison with larger and more bulky targeting ligands (for example cRGD peptide[73] and transferrin,[74,75] associating with their receptors with nanomolar and low nanomolar K_d, respectively), small molecule GCPII inhibitors can be installed on nanoparticle surface conveniently at higher loadings which can result in stronger avidity effects. Correspondingly, GCPII inhibitors reach efficacy similar to small molecule folate.[76]

DOI: 10.1021/acs.molpharmaceut.7b00889
Mol. Pharmaceutics XXXX, XXX, XXX−XXX

Table 2. Inhibition Constants for NPs and Starting Inhibitors (for Structures, see Figure 1) Measured from HPLC Inhibition Assay, Expressed as K_i and IC_{50} with Standard Deviations[a]

	inhibitor type	inhibitors/particle	inhibition: $K_i \pm 1$ SD [pM]	MEF	inhibition: $IC_{50} \pm 1$ SD [pM]
			Nanoparticles		
ND-inh	**4**	250	3.70 ± 0.67	3780	42.1 ± 4.9
pol-inh	**1**	6	323 ± 50	6.63	3660 ± 290
Qβ-pol-inh	**1**	12	3.92 ± 0.83	546	44.6 ± 6.6
Qβ-inh	**5**	180	30.3 ± 4.5	373	344 ± 26
MPyV-pol-inh	**1**	180	2.87 ± 0.60	746	31.9 ± 4.5
MPyV-inh	**5**	540	0.60 ± 0.11	18 800	6.82 ± 1.2
			Inhibitors		
1			2140 ± 290		29 600 ± 4 100
4			14 000 ± 1 700		193 000 ± 26 600
5			11 300 ± 1 200		157 000 ± 19 700

[a]For NPs, the number of inhibitors per particle, inhibitor type, and multivalent enhancement factors (MEF)[72] are shown. MEF = K_i(starting inhibitor)/K_i(nanoparticle).

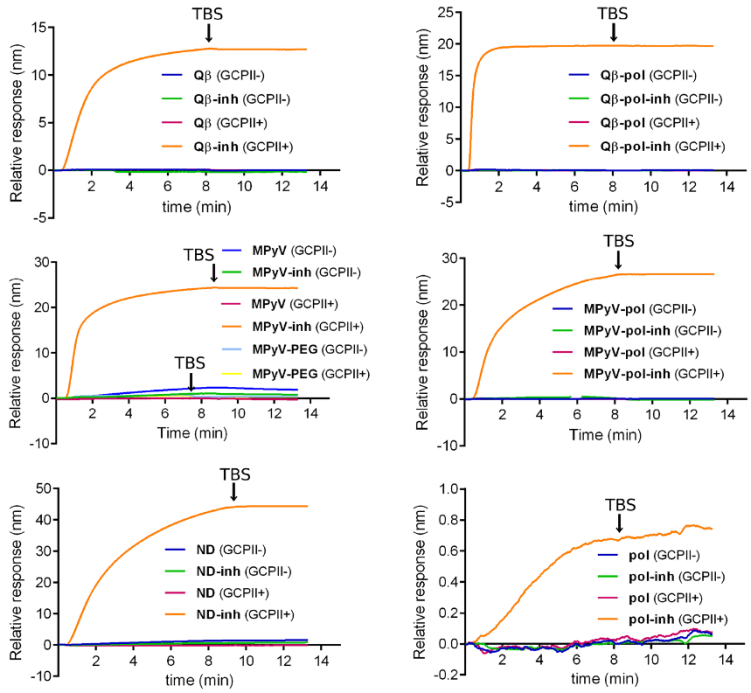

Figure 3. Interaction of NPs with GCPII. Testing of the binding capacity of all NPs to GCPII immobilized on the chip by SPR measurements. GCPII was immobilized on SPR chips through a neutravidin−biotin interaction (GCPII+). As a negative control, we attached neutravidin alone (GCPII−). NPs were injected at final 5 nM concentrations in TBS (association phase) for several minutes, and then TBS alone was injected (dissociation phase).

Cellular Uptake of NPs. Once we had verified interaction between GCPII and our modified NPs with inhibitor, we next focused on monitoring the binding ability and cellular uptake of NPs. We used the human glioblastoma cell line U-251 MG. Depending on the presence of doxycycline in the media (Tet-OffAdvanced System), these cells can overexpress GCPII on their surfaces.[63,77] This enabled us to conduct a comparative study in a very consistent way using only one type of cells. According to the level of GCPII expression, we marked the cells U-251$^+$ MG (with expression) or U-251$^-$ MG (without expression). GCPII is constantly internalized, but the turnover is greatly accelerated after binding of antibody[78,79] or HPMA copolymer with bound inhibitor.[24] The mechanism of action of polymer-induced internalization has not been studied thoroughly; however, it has been shown that antibody-induced endocytosis is clathrin-dependent and mediated by an MXXXL cytoplasmic tail motif.[79]

DOI: 10.1021/acs.molpharmaceut.7b00889
Mol. Pharmaceutics XXXX, XXX, XXX−XXX

We incubated all particles with cells, washed them with buffer, and analyzed the cells using flow cytometry (Figure 4, Figure S5). Because phosphate is a weak competitive inhibitor of GCPII,[80,81] we used phosphate-free buffers and media to avoid potential detachment of particles from the cell surface. Regardless of the size and loading of inhibitor, all particles with inhibitor formed strong interactions with U-251$^+$ MG cells, and relative fluorescence intensities were up to 160 times higher than those observed for U-251$^-$ MG cells (Figure 4A). With the exception of **MPyV-pol-inh**, the nonspecific binding of nanoparticles with inhibitor in the absence of GCPII was negligible. This is consistent with the data obtained from measurement of particles without inhibitor (Figure 4B). Consistent with previously published results, NDs,[37] polymer,[24] and Qβ particles[49] without a targeting ligand (GCPII inhibitor) did not interact with mammalian cells. In contrast, MPyV VLPs had comparably strong interactions with both U-251$^+$ MG and U-251$^-$ MG cells. We assumed that coating MPyV VLPs with polymer in **MPyV-pol** and **MPyV-pol-inh** or PEG_{13} linker (**MPyV-PEG**) would prevent the VP1-specific interaction with cells. Surprisingly, modification with PEG_{13} suppressed the VP1-specific binding of particles to both U-251$^+$ MG and U-251$^-$ MG cells to negligible levels, whereas **MPyV-pol** and **MPyV-pol-inh** VLPs maintained their capacity to interact with both cell variants. The higher load of PEG_{13} molecules (approximately 1,000 molecules) than poly(HPMA) molecules (approximately 30 molecules) per particle and better surface coverage indicate that an optimal load of shielding polymer is necessary to reduce the unwanted interactions of MPyV VLPs with glioblastoma cells. This is especially pronounced in our experimental system, because the U-251 MG cell line, as a representative of brain tissue derived cultures known to abundantly express complex gangliosides,[82] contains high levels of GD1a and GT1b gangliosides,[83] which are major MPyV receptors.[43,44] Interestingly, our results showed that the PEG linker itself or with the attached inhibitor molecule was capable of completely reducing VP1-mediated binding to sialic acid or selectively retargeting particles to GCPII, respectively.

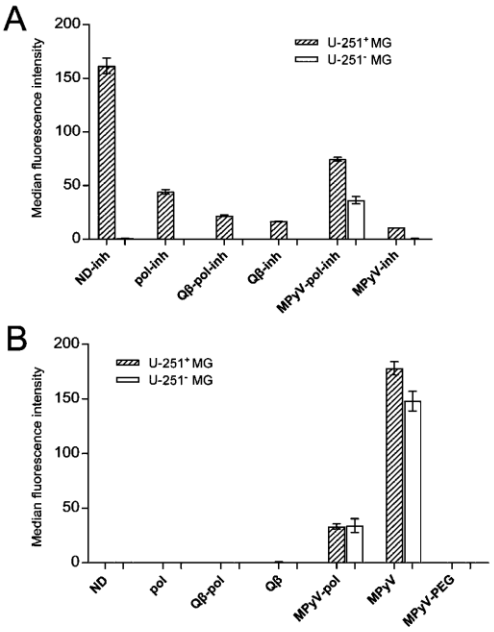

Figure 4. Flow cytometry study of NP association with U-251 MG cells with (U-251$^+$ MG) or without (U-251$^-$ MG) GCPII expression. The graphs show the interaction of NPs with (A) or without (B) inhibitor. Data represent the median of fluorescence intensity (MFI), normalized to autofluorescence of negative cells and adjusted to the relative fluorescence of particles. The standard deviations were calculated from triplicates. There were statistically significant differences between the variants containing inhibitor on U-251$^+$ MG cells and all three negative controls (NP with inhibitor on U-251$^-$ MG cells and NP without inhibitors on either U-251$^+$ MG or U-251$^-$ MG). Obtained p-values were at least $p < 0.001$, one-way ANOVA followed by Tukey's post hoc test.

We further analyzed the interaction of NPs with cells using confocal microscopy. We clearly observed a high internalization rate of NPs containing inhibitor in U-251$^+$ MG cells, and no internalization in control experiments (Figure 5A, Figure S6). MPyV VLPs were the only exception; binding of nontargeted non-PEGylated NPs was observed, similar to the flow cytometry results. We observed **MPyV**, **MPyV-pol**, and **MPyV-pol-inh** particles in close association with the plasma membrane (Figure 5B).

CONCLUSIONS

In summary, we investigated the robustness of GCPII targeting by a variety of NPs using one cell type model. The glioblastoma cell line U-251 MG provided us the unique possibility to switch on surface expression of GCPII using an external stimulus, instead of using different cell lines (with and without GCPII expression). We therefore were able to compare the targeting in a very consistent and straightforward way. Independent of the NP structure, size, polydispersity, used conjugation chemistry, and loading of targeting inhibitor molecules, we observed that all targeted NPs bound GCPII installed on an SPR chip, inhibited GCPII in solution, and interacted with GCPII on the cell membrane. Inhibition of GCPII was highly effective, reaching low picomolar K_i values for all particles except polymer NPs, which had subnanomolar K_i. We observed an increase in interaction efficacy of the original small molecule inhibitors upon installation on NP surface for 1 to 4 orders of magnitude. This effect is most likely caused by high local concentration of inhibitors which can lead in strong multivalent binding with the target surfaces. However, vast range of the observed enhancement documents specific needs of each nanosystem for recognition and binding.

In general, the specificity of target binding is limited not only by the strength of interaction but also by any other side interactions (either nonspecific or due to an unwanted side specificity). In the case of MPyV VLPs, the interface of which shows a broad tropism and can strongly interact with various receptors, we clearly observed the importance of the surface modification for targeting selectivity. A high load of short PEG chains grafted to surface lysines provided sufficient protection and enabled complete retargeting of MPyV VLPs to GCPII, while a low density of poly(HPMA) did not sufficiently mitigate the side binding. On the other hand, poly(HPMA) grafted from NDs at high density led to excellent and highly selective targeting.

DOI: 10.1021/acs.molpharmaceut.7b00889
Mol. Pharmaceutics XXXX, XXX, XXX−XXX

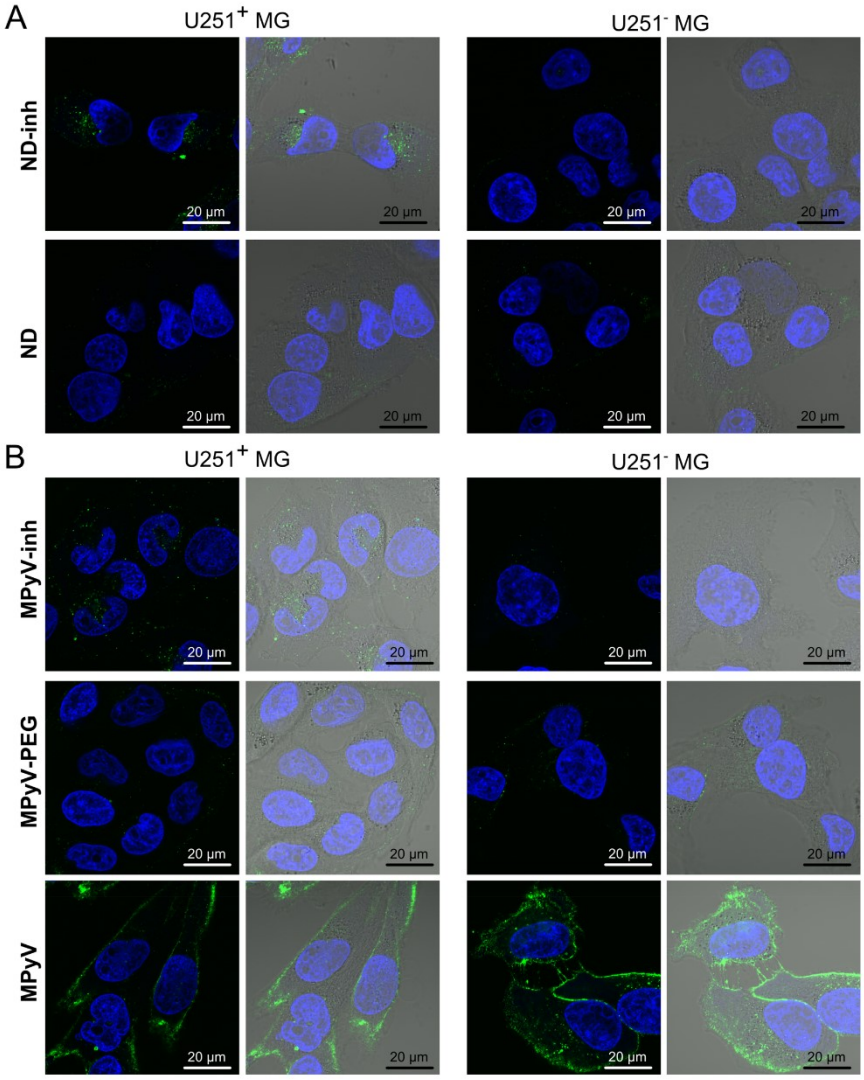

Figure 5. Confocal images of NP uptake by U-251 MG cells with (U-251$^+$ MG) or without (U-251$^-$ MG) GCPII expression incubated with NPs for 1 h. (A) Binding of ND NPs to U-251 MG cells. (B) Binding of MPyV NPs to U-251 MG cells. Confocal sections of representative cells with corresponding signal in green (NPs conjugated with Alexa Fluor 488 or Atto 488) and blue (nuclei with Hoechst staining) channels are shown. Merged images are composed of both channels and bright field image.

Our results indicate that use of small molecule inhibitors with low nanomolar range K_i displayed in polyvalent arrangements on NPs can be highly effective and selective for targeting to cells overexpressing GCPII. The robustness of the approach is limited mostly by the quality of the NP bionanointerface, which can be improved by adding a sufficient density of hydrophilic protective polymers. Based on the comprehensive data set we obtained here and on previously reported work, we believe that targeting of cancer cells overexpressing GCPII is a viable approach transferable to a broad diversity of nanosystems.

■ ASSOCIATED CONTENT

Supporting Information

The Supporting Information is available free of charge on the ACS Publications website at DOI: 10.1021/acs.molpharmaceut.7b00889.

Details of synthesis and characterization (PDF)

DOI: 10.1021/acs.molpharmaceut.7b00889
Mol. Pharmaceutics XXXX, XXX, XXX−XXX

AUTHOR INFORMATION

Corresponding Author

*E-mail: cigler@uochb.cas.cz. Fax: (+)420-220-183-578. Tel: (+)420-220-183-429.

ORCID

Tomas Etrych: 0000-0001-5908-5182

Petr Cigler: 0000-0003-0283-647X

Author Contributions

§J.N., F.S., and J.Z.S. contributed equally.

Notes

The authors declare no competing financial interest.

ACKNOWLEDGMENTS

The authors thank Dr. Jiri Schimer for fruitful discussions and Jana Starkova for her kind help with cell culturing. This work was supported by the Grant Agency of Charles University Project No. 727816 (J.N., P.C.), Grant Agency of the Czech Republic Projects No. 16-16336S (J.N., P.C.) and 16-02938S (L.K., V.S., T.E., F.S., P.S., R.K., J.K.), League Against Cancer Prague (J.Z.S., H.S., J.F.), Project SVV-260426 (J.Z.S), Ministry of Education of the Czech Republic NPU (OP PK) InterBioMed Project LO 1302 (F.S., P.S., R.K., J.K.), and OPPK Project CZ.2.16/3.1.00/24016 (F.S., P.S., R.K., J.K.).

ABREVIATIONS USED

NP, nanoparticle; GCPII, glutamate carboxypeptidase II; PSMA, prostate-specific membrane antigen; NAAG, *N*-acetyl-L-aspartyl-L-glutamate; HPMA, *N*-(2-hydroxypropyl)-methacrylamide; ND, nanodiamond; NV, nitrogen vacancy; VLP, virus-like particle; MPyV, mouse polyomavirus; TT, thiazolidine-2-thione; Sf9, *Spodoptera frugiperda*; NHS, *N*-hydroxysuccinimide; THPTA, tris(3-hydroxypropyltriazolylmethyl)amine; DTT, dithiothreitol; SPR, surface plasmon resonance; TEM, transmission electron microscopy; DLS, dynamic light scattering; MALDI, matrix-assisted laser desorption/ionization mass spectrometry

REFERENCES

(1) Fernandez-Fernandez, A.; Manchanda, R.; McGoron, A. J. Theranostic Applications of Nanomaterials in Cancer: Drug Delivery, Image-Guided Therapy and Multifunctional Platforms. *Appl. Biochem. Biotechnol.* **2011**, *165* (7−8), 1628−1651.

(2) Liu, H.; Moy, P.; Kim, S.; Xia, Y.; Rajasekaran, A.; Navarro, V.; Knudsen, B.; Bander, N. H. Monoclonal Antibodies to the Extracellular Domain of Prostate-Specific Membrane Antigen Also React with Tumor Vascular Endothelium. *Cancer Res.* **1997**, *57* (17), 3629−3634.

(3) Silver, D. A.; Pellicer, I.; Fair, W. R.; Heston, W. D.; Cordon-Cardo, C. Prostate-Specific Membrane Antigen Expression in Normal and Malignant Human Tissues. *Clin. Cancer Res.* **1997**, *3* (1), 81−85.

(4) Bostwick, D. G.; Iczkowski, K. A.; Amin, M. B.; Discigil, G.; Osborne, B. Malignant Lymphoma Involving the Prostate: Report of 62 Cases. *Cancer* **1998**, *83* (4), 732−738.

(5) Maurer, T.; Eiber, M.; Schwaiger, M.; Gschwend, J. E. Current Use of PSMA-PET in Prostate Cancer Management. *Nat. Rev. Urol.* **2016**, *13* (4), 226−235.

(6) Hlouchová, K.; Bařinka, C.; Konvalinka, J. Glutamate Carboxypeptidase II as a Therapeutic Target. In *Proteinases as Drug Targets*; RSC: 2011; pp 62−95.

(7) Mukherjee, A.; Darlington, T.; Baldwin, R.; Holz, C.; Olson, S.; Kulkarni, P.; DeWeese, T. L.; Getzenberg, R. H.; Ivkov, R.; Lupold, S. E. Development and Screening of a Series of Antibody-Conjugated and Silica-Coated Iron Oxide Nanoparticles for Targeting the Prostate-Specific Membrane Antigen. *ChemMedChem* **2014**, *9* (7), 1356−1360.

(8) Nagesh, P. K. B.; Johnson, N. R.; Boya, V. K. N.; Chowdhury, P.; Othman, S. F.; Khalilzad-Sharghi, V.; Hafeez, B. B.; Ganju, A.; Khan, S.; Behrman, S. W.; Zafar, N.; Chauhan, S. C.; Jaggi, M.; Yallapu, M. M. PSMA Targeted Docetaxel-Loaded Superparamagnetic Iron Oxide Nanoparticles for Prostate Cancer. *Colloids Surf., B* **2016**, *144*, 8−20.

(9) Kim, D.; Jeong, Y. Y.; Jon, S. A Drug-Loaded Aptamer−Gold Nanoparticle Bioconjugate for Combined CT Imaging and Therapy of Prostate Cancer. *ACS Nano* **2010**, *4* (7), 3689−3696.

(10) Kolishetti, N.; Dhar, S.; Valencia, P. M.; Lin, L. Q.; Karnik, R.; Lippard, S. J.; Langer, R.; Farokhzad, O. C. Engineering of Self-Assembled Nanoparticle Platform for Precisely Controlled Combination Drug Therapy. *Proc. Natl. Acad. Sci. U. S. A.* **2010**, *107* (42), 17939−17944.

(11) Xu, X.; Wu, J.; Liu, Y.; Saw, P. E.; Tao, W.; Yu, M.; Zope, H.; Si, M.; Victorious, A.; Rasmussen, J.; Ayyash, D.; Farokhzad, O. C.; Shi, J. Multifunctional Envelope-Type siRNA Delivery Nanoparticle Platform for Prostate Cancer Therapy. *ACS Nano* **2017**, *11* (3), 2618−2627.

(12) Sanna, V.; Pintus, G.; Roggio, A. M.; Punzoni, S.; Posadino, A. M.; Arca, A.; Marceddu, S.; Bandiera, P.; Uzzau, S.; Sechi, M. Targeted Biocompatible Nanoparticles for the Delivery of (−)-Epigallocatechin 3-Gallate to Prostate Cancer Cells. *J. Med. Chem.* **2011**, *54* (5), 1321.

(13) Chen, Z.; Penet, M.-F.; Krishnamachary, B.; Banerjee, S. R.; Pomper, M. G.; Bhujwalla, Z. M. PSMA-Specific Theranostic Nanoplex for Combination of TRAIL Gene and 5-FC Prodrug Therapy of Prostate Cancer. *Biomaterials* **2016**, *80*, 57−67.

(14) Banerjee, S. R.; Foss, C. A.; Horhota, A.; Pullambhatla, M.; McDonnell, K.; Zale, S.; Pomper, M. G. 111In- and IRDye800CW-Labeled PLA−PEG Nanoparticle for Imaging Prostate-Specific Membrane Antigen-Expressing Tissues. *Biomacromolecules* **2017**, *18* (1), 201−209.

(15) Janoniene, A.; Liu, Z.; Baranauskiene, L.; Mäkilä, E.; Ma, M.; Salonen, J.; Hirvonen, J.; Zhang, H.; Petrikaite, V.; Santos, H. A. A Versatile Carbonic Anhydrase IX Targeting Ligand-Functionalized Porous Silicon Nanoplatform for Dual Hypoxia Cancer Therapy and Imaging. *ACS Appl. Mater. Interfaces* **2017**, *9* (16), 13976−13987.

(16) Azad, B. B.; Banerjee, S. R.; Pullambhatla, M.; Lacerda, S.; Foss, C. A.; Wang, Y.; Ivkov, R.; Pomper, M. G. Evaluation of a PSMA-Targeted BNF Nanoparticle Construct. *Nanoscale* **2015**, *7* (10), 4432−4442.

(17) Chandran, S. S.; Banerjee, S. R.; Mease, R. C.; Pomper, M. G.; Denmeade, S. R. Characterization of a Targeted Nanoparticle Functionalized with a Urea-Based Inhibitor of Prostate-Specific Membrane Antigen (PSMA). *Cancer Biol. Ther.* **2008**, *7* (6), 974−982.

(18) Chen, Z.; Penet, M.-F.; Nimmagadda, S.; Li, C.; Banerjee, S. R.; Winnard, P. T.; Artemov, D.; Glunde, K.; Pomper, M. G.; Bhujwalla, Z. M. PSMA-Targeted Theranostic Nanoplex for Prostate Cancer Therapy. *ACS Nano* **2012**, *6* (9), 7752−7762.

(19) Hoff, D. D. V.; Mita, M. M.; Ramanathan, R. K.; Weiss, G. J.; Mita, A. C.; LoRusso, P. M.; Burris, H. A.; Hart, L. L.; Low, S. C.; Parsons, D. M.; Zale, S. E.; Summa, J. M.; Youssoufian, H.; Sachdev, J. C. Phase I Study of PSMA-Targeted Docetaxel-Containing Nanoparticle BIND-014 in Patients with Advanced Solid Tumors. *Clin. Cancer Res.* **2016**, *22* (13), 3157−3163.

(20) Hrkach, J.; Hoff, D. V.; Ali, M. M.; Andrianova, E.; Auer, J.; Campbell, T.; Witt, D. D.; Figa, M.; Figueiredo, M.; Horhota, A.; Low, S.; McDonnell, K.; Peeke, E.; Retnarajan, B.; Sabnis, A.; Schnipper, E.; Song, J. J.; Song, Y. H.; Summa, J.; Tompsett, D.; Troiano, G.; Hoven, T. V. G.; Wright, J.; LoRusso, P.; Kantoff, P. W.; Bander, N. H.; Sweeney, C.; Farokhzad, O. C.; Langer, R.; Zale, S. Preclinical Development and Clinical Translation of a PSMA-Targeted Docetaxel Nanoparticle with a Differentiated Pharmacological Profile. *Sci. Transl. Med.* **2012**, *4* (128), 128ra39.

(21) Huang, B.; Otis, J.; Joice, M.; Kotlyar, A.; Thomas, T. P. PSMA-Targeted Stably Linked "Dendrimer-Glutamate Urea-Methotrexate" as a Prostate Cancer Therapeutic. *Biomacromolecules* **2014**, *15* (3), 915−923.

DOI: 10.1021/acs.molpharmaceut.7b00889
Mol. Pharmaceutics XXXX, XXX, XXX−XXX

(22) Kasten, B. B.; Liu, T.; Nedrow-Byers, J. R.; Benny, P. D.; Berkman, C. E. Targeting Prostate Cancer Cells with PSMA Inhibitor-Guided Gold Nanoparticles. *Bioorg. Med. Chem. Lett.* **2013**, *23* (2), 565−568.
(23) Moon, S.-H.; Yang, B. Y.; Kim, Y. J.; Hong, M. K.; Lee, Y.-S.; Lee, D. S.; Chung, J.-K.; Jeong, J. M. Development of a Complementary PET/MR Dual-Modal Imaging Probe for Targeting Prostate-Specific Membrane Antigen (PSMA). *Nanomedicine* **2016**, *12* (4), 871−879.
(24) Šácha, P.; Knedlík, T.; Schimer, J.; Tykvart, J.; Parolek, J.; Navrátil, V.; Dvořáková, P.; Sedlák, F.; Ulbrich, K.; Strohalm, J.; Majer, P.; Šubr, V.; Konvalinka, J. iBodies: Modular Synthetic Antibody Mimetics Based on Hydrophilic Polymers Decorated with Functional Moieties. *Angew. Chem., Int. Ed.* **2016**, *55* (7), 2356−2360.
(25) Zhu, C.; Bandekar, A.; Sempkowski, M.; Banerjee, S. R.; Pomper, M. G.; Bruchertseifer, F.; Morgenstern, A.; Sofou, S. Nanoconjugation of PSMA-Targeting Ligands Enhances Perinuclear Localization and Improves Efficacy of Delivered Alpha-Particle Emitters against Tumor Endothelial Analogues. *Mol. Cancer Ther.* **2016**, *15* (1), 106−113.
(26) Rehor, I.; Slegerova, J.; Havlik, J.; Raabova, H.; Hyvl, J.; Muchova, E.; Cigler, P. Nanodiamonds: Behavior in Biological Systems and Emerging Bioapplications. In *Carbon Nanomaterials for Biomedical Applications*; Biomaterials Science and Engineering; Springer: Switzerland, 2016; pp 319−361.
(27) Slegerova, J.; Rehor, I.; Havlik, J.; Raabova, H.; Muchova, E.; Cigler, P. Nanodiamonds as Intracellular Probes for Imaging in Biology and Medicine. In *Intracellular Delivery II*; Prokop, A., Iwasaki, Y., Harada, A., Eds.; Springer Netherlands: Dordrecht, 2014; Vol. *7*, pp 363−401.
(28) Monopoli, M. P.; Åberg, C.; Salvati, A.; Dawson, K. A. Biomolecular Coronas Provide the Biological Identity of Nanosized Materials. *Nat. Nanotechnol.* **2012**, *7* (12), 779−786.
(29) Saptarshi, S. R.; Duschl, A.; Lopata, A. L. Interaction of Nanoparticles with Proteins: Relation to Bio-Reactivity of the Nanoparticle. *J. Nanobiotechnol.* **2013**, *11*, 26.
(30) Neburkova, J.; Vavra, J.; Cigler, P. Coating Nanodiamonds with Biocompatible Shells for Applications in Biology and Medicine. *Curr. Opin. Solid State Mater. Sci.* **2017**, *21*, 43−53.
(31) Weng, M.-F.; Chiang, S.-Y.; Wang, N.-S.; Niu, H. Fluorescent Nanodiamonds for Specifically Targeted Bioimaging: Application to the Interaction of Transferrin with Transferrin Receptor. *Diamond Relat. Mater.* **2009**, *18* (2−3), 587−591.
(32) Wang, Z.; Tian, Z.; Dong, Y.; Li, L.; Tian, L.; Li, Y.; Yang, B. Nanodiamond-Conjugated Transferrin as Chemotherapeutic Drug Delivery. *Diamond Relat. Mater.* **2015**, *58*, 84−93.
(33) Li, Y.; Zhou, X. Transferrin-Coupled Fluorescence Nanodiamonds as Targeting Intracellular Transporters: An Investigation of the Uptake Mechanism. *Diamond Relat. Mater.* **2010**, *19* (10), 1163−1167.
(34) Fu, Y.; An, N.; Zheng, S.; Liang, A.; Li, Y. BmK CT-Conjugated Fluorescence Nanodiamond as Potential Glioma-Targeted Imaging and Drug. *Diamond Relat. Mater.* **2012**, *21*, 73−76.
(35) Chan, M. S.; Liu, L. S.; Leung, H. M.; Lo, P. K. Cancer-Cell-Specific Mitochondria-Targeted Drug Delivery by Dual-Ligand-Functionalized Nanodiamonds Circumvent Drug Resistance. *ACS Appl. Mater. Interfaces* **2017**, *9* (13), 11780−11789.
(36) Zhang, B.; Li, Y.; Fang, C.-Y.; Chang, C.-C.; Chen, C.-S.; Chen, Y.-Y.; Chang, H.-C. Receptor-Mediated Cellular Uptake of Folate-Conjugated Fluorescent Nanodiamonds: A Combined Ensemble and Single-Particle Study. *Small* **2009**, *5* (23), 2716−2721.
(37) Slegerova, J.; Hajek, M.; Rehor, I.; Sedlak, F.; Stursa, J.; Hruby, M.; Cigler, P. Designing the Nanobiointerface of Fluorescent Nanodiamonds: Highly Selective Targeting of Glioma Cancer Cells. *Nanoscale* **2015**, *7* (2), 415−420.
(38) Zhao, L.; Xu, Y.-H.; Qin, H.; Abe, S.; Akasaka, T.; Chano, T.; Watari, F.; Kimura, T.; Komatsu, N.; Chen, X. Platinum on Nanodiamond: A Promising Prodrug Conjugated with Stealth Polyglycerol, Targeting Peptide and Acid-Responsive Antitumor Drug. *Adv. Funct. Mater.* **2014**, *24* (34), 5348−5357.
(39) Zhang, T.; Cui, H.; Fang, C.-Y.; Cheng, K.; Yang, X.; Chang, H.-C.; Forrest, M. L. Targeted Nanodiamonds as Phenotype-Specific Photoacoustic Contrast Agents for Breast Cancer. *Nanomedicine* **2015**, *10* (4), 573−587.
(40) Slilaty, S. N.; Aposhian, H. V. Gene Transfer by Polyoma-like Particles Assembled in a Cell-Free System. *Science* **1983**, *220* (4598), 725−727.
(41) Forstová, J.; Krauzewicz, N.; Sandig, V.; Elliott, J.; Palková, Z.; Strauss, M.; Griffin, B. E. Polyoma Virus Pseudocapsids as Efficient Carriers of Heterologous DNA into Mammalian Cells. *Hum. Gene Ther.* **1995**, *6* (3), 297−306.
(42) Ou, W. C.; Wang, M.; Fung, C. Y.; Tsai, R. T.; Chao, P. C.; Hseu, T. H.; Chang, D. The Major Capsid Protein, VP1, of Human JC Virus Expressed in Escherichia Coli Is Able to Self-Assemble into a Capsid-like Particle and Deliver Exogenous DNA into Human Kidney Cells. *J. Gen. Virol.* **1999**, *80* (1), 39−46.
(43) Tsai, B.; Gilbert, J. M.; Stehle, T.; Lencer, W.; Benjamin, T. L.; Rapoport, T. A. Gangliosides Are Receptors for Murine Polyoma Virus and SV40. *EMBO J.* **2003**, *22* (17), 4346−4355.
(44) You, J.; O'Hara, S. D.; Velupillai, P.; Castle, S.; Levery, S.; Garcea, R. L.; Benjamin, T. Ganglioside and Non-Ganglioside Mediated Host Responses to the Mouse Polyomavirus. *PLoS Pathog.* **2015**, *11* (10), e1005175.
(45) Caruso, M. Role of Sialic Acid-Containing Molecules and the 4 1 Integrin Receptor in the Early Steps of Polyomavirus Infection. *J. Gen. Virol.* **2003**, *84* (11), 2927−2936.
(46) Zackova Suchanova, J.; Neburkova, J.; Spanielova, H.; Forstova, J.; Cigler, P. Retargeting Polyomavirus-Like Particles to Cancer Cells by Chemical Modification of Capsid Surface. *Bioconjugate Chem.* **2017**, *28* (2), 307−313.
(47) Fiedler, J. D.; Brown, S. D.; Lau, J. L.; Finn, M. G. RNA-Directed Packaging of Enzymes within Virus-like Particles. *Angew. Chem., Int. Ed.* **2010**, *49* (50), 9648−9651.
(48) Banerjee, D.; Liu, A. P.; Voss, N. R.; Schmid, S. L.; Finn, M. G. Multivalent Display and Receptor-Mediated Endocytosis of Transferrin on Virus-Like Particles. *ChemBioChem* **2010**, *11* (9), 1273−1279.
(49) Pokorski, J. K.; Hovlid, M. L.; Finn, M. G. Cell Targeting with Hybrid Qβ Virus-Like Particles Displaying Epidermal Growth Factor. *ChemBioChem* **2011**, *12* (16), 2441−2447.
(50) Rhee, J.-K.; Baksh, M.; Nycholat, C.; Paulson, J. C.; Kitagishi, H.; Finn, M. G. Glycan-Targeted Virus-like Nanoparticles for Photodynamic Therapy. *Biomacromolecules* **2012**, *13* (8), 2333−2338.
(51) Hovlid, M. L.; Lau, J. L.; Breitenkamp, K.; Higginson, C. J.; Laufer, B.; Manchester, M.; Finn, M. G. Encapsidated Atom-Transfer Radical Polymerization in Qβ Virus-like Nanoparticles. *ACS Nano* **2014**, *8* (8), 8003−8014.
(52) Manzenrieder, F.; Luxenhofer, R.; Retzlaff, M.; Jordan, R.; Finn, M. G. Stabilization of Virus-like Particles with Poly(2-Oxazoline)s. *Angew. Chem., Int. Ed.* **2011**, *50* (11), 2601−2605.
(53) Pokorski, J. K.; Breitenkamp, K.; Liepold, L. O.; Qazi, S.; Finn, M. G. Functional Virus-Based Polymer−Protein Nanoparticles by Atom Transfer Radical Polymerization. *J. Am. Chem. Soc.* **2011**, *133* (24), 9242−9245.
(54) Šubr, V.; Ulbrich, K. Synthesis and Properties of New N-(2-Hydroxypropyl)methacrylamide Copolymers Containing Thiazolidine-2-Thione Reactive Groups. *React. Funct. Polym.* **2006**, *66* (12), 1525−1538.
(55) Lallana, E.; Sousa-Herves, A.; Fernandez-Trillo, F.; Riguera, R.; Fernandez-Megia, E. Click Chemistry for Drug Delivery Nanosystems. *Pharm. Res.* **2012**, *29* (1), 1−34.
(56) Wang, Q.; Chan, T. R.; Hilgraf, R.; Fokin, V. V.; Sharpless, K. B.; Finn, M. G. Bioconjugation by Copper(I)-Catalyzed Azide-Alkyne [3 + 2] Cycloaddition. *J. Am. Chem. Soc.* **2003**, *125* (11), 3192−3193.
(57) Forstova, J.; Krauzewicz, N.; Wallace, S.; Street, A. J.; Dilworth, S. M.; Beard, S.; Griffin, B. E. Cooperation of Structural Proteins

DOI: 10.1021/acs.molpharmaceut.7b00889
Mol. Pharmaceutics XXXX, XXX, XXX−XXX

during Late Events in the Life Cycle of Polyomavirus. *J. Virol.* **1993**, *67* (3), 1405−1413.
(58) Türler, H.; Beard, P. Simian Virus 40 and Polyoma Virus: Growth, Titration, Transformation and Purification of Viral Components. In *Virology: a practical approach*; IRL Press: Oxford, 1985; pp 169−192.
(59) Hong, V.; Presolski, S. I.; Ma, C.; Finn, M. G. Analysis and Optimization of Copper-Catalyzed Azide-Alkyne Cycloaddition for Bioconjugation. *Angew. Chem., Int. Ed.* **2009**, *48* (52), 9879−9883.
(60) Rendler, T.; Neburkova, J.; Zemek, O.; Kotek, J.; Zappe, A.; Chu, Z.; Cigler, P.; Wrachtrup, J. Optical Imaging of Localized Chemical Events Using Programmable Diamond Quantum Nanosensors. *Nat. Commun.* **2017**, *8*, 14701.
(61) Neburkova, J.; Hajek, M.; Rehor, I.; Schimer, J.; Sedlak, F.; Stursa, J.; Hruby, M.; Cigler, P. Targeting Glioma Cancer Cells with Fluorescent Nanodiamonds via Integrin Receptors. In *Methods in Pharmacology and Toxicology*; Humana Press: 2017; DOI: 10.1007/7653_2017_68.
(62) Tykvart, J.; Šácha, P.; Bařinka, C.; Knedlík, T.; Starková, J.; Lubkowski, J.; Konvalinka, J. Efficient and Versatile One-Step Affinity Purification of in Vivo Biotinylated Proteins: Expression, Characterization and Structure Analysis of Recombinant Human Glutamate Carboxypeptidase II. *Protein Expression Purif.* **2012**, *82* (1), 106−115.
(63) Tykvart, J.; Schimer, J.; Bařinková, J.; Pachl, P.; Poštová-Slavětínská, L.; Majer, P.; Konvalinka, J.; Šácha, P. Rational Design of Urea-Based Glutamate Carboxypeptidase II (GCPII) Inhibitors as Versatile Tools for Specific Drug Targeting and Delivery. *Bioorg. Med. Chem.* **2014**, *22* (15), 4099−4108.
(64) Schindelin, J.; Arganda-Carreras, I.; Frise, E.; Kaynig, V.; Longair, M.; Pietzsch, T.; Preibisch, S.; Rueden, C.; Saalfeld, S.; Schmid, B.; Tinevez, J.-Y.; White, D. J.; Hartenstein, V.; Eliceiri, K.; Tomancak, P.; Cardona, A. Fiji: An Open-Source Platform for Biological-Image Analysis. *Nat. Methods* **2012**, *9* (7), 676−682.
(65) Kozikowski, A. P.; Nan, F.; Conti, P.; Zhang, J.; Ramadan, E.; Bzdega, T.; Wroblewska, B.; Neale, J. H.; Pshenichkin, S.; Wroblewski, J. T. Design of Remarkably Simple, yet Potent Urea-Based Inhibitors of Glutamate Carboxypeptidase II (NAALADase). *J. Med. Chem.* **2001**, *44* (3), 298−301.
(66) Hong, V.; Steinmetz, N. F.; Manchester, M.; Finn, M. G. Labeling Live Cells by Copper-Catalyzed Alkyne−Azide Click Chemistry. *Bioconjugate Chem.* **2010**, *21* (10), 1912−1916.
(67) Stehle, T.; Harrison, S. C. Crystal Structures of Murine Polyomavirus in Complex with Straight-Chain and Branched-Chain Sialyloligosaccharide Receptor Fragments. *Structure* **1996**, *4* (2), 183−194.
(68) Krauzewicz, N.; Cox, C.; Soeda, E.; Clark, B.; Rayner, S.; Griffin, B. E. Sustained Ex Vivo and in Vivo Transfer of a Reporter Gene Using Polyoma Virus Pseudocapsids. *Gene Ther.* **2000**, *7* (13), 1094−1102.
(69) Hui, Y. Y.; Hsiao, W. W.-W.; Haziza, S.; Simonneau, M.; Treussart, F.; Chang, H.-C. Single Particle Tracking of Fluorescent Nanodiamonds in Cells and Organisms. *Curr. Opin. Solid State Mater. Sci.* **2017**, *21* (1), 35−42.
(70) Wu, T.-J.; Tzeng, Y.-K.; Chang, W.-W.; Cheng, C.-A.; Kuo, Y.; Chien, C.-H.; Chang, H.-C.; Yu, J. Tracking the Engraftment and Regenerative Capabilities of Transplanted Lung Stem Cells Using Fluorescent Nanodiamonds. *Nat. Nanotechnol.* **2013**, *8* (9), 682−689.
(71) Simon, C.; Klose, T.; Herbst, S.; Han, B. G.; Sinz, A.; Glaeser, R. M.; Stubbs, M. T.; Lilie, H. Disulfide Linkage and Structure of Highly Stable Yeast-Derived Virus-like Particles of Murine Polyomavirus. *J. Biol. Chem.* **2014**, *289* (15), 10411−10418.
(72) Li, M.-H.; Zong, H.; Leroueil, P. R.; Choi, S. K.; Baker, J. R. Ligand Characteristics Important to Avidity Interactions of Multivalent Nanoparticles. *Bioconjugate Chem.* **2017**, *28* (6), 1649−1657.
(73) Lucie, S.; Elisabeth, G.; Stéphanie, F.; Guy, S.; Amandine, H.; Corinne, A.-R.; Didier, B.; Catherine, S.; Alexeï, G.; Pascal, D.; Jean-Luc, C. Clustering and Internalization of Integrin $\alpha v\beta 3$ With a Tetrameric RGD-Synthetic Peptide. *Mol. Ther.* **2009**, *17* (5), 837−843.
(74) Fuchs, H.; Geßner, R. Iodination Significantly Influences the Binding of Human Transferrin to the Transferrin Receptor. *Biochim. Biophys. Acta, Gen. Subj.* **2002**, *1570* (1), 19−26.
(75) Schüler, J.; Frank, J.; Trier, U.; Schäfer-Korting, M.; Saenger, W. Interaction Kinetics of Tetramethylrhodamine Transferrin with Human Transferrin Receptor Studied by Fluorescence Correlation Spectroscopy. *Biochemistry* **1999**, *38* (26), 8402−8408.
(76) Wibowo, A. S.; Singh, M.; Reeder, K. M.; Carter, J. J.; Kovach, A. R.; Meng, W.; Ratnam, M.; Zhang, F.; Dann, C. E. Structures of Human Folate Receptors Reveal Biological Trafficking States and Diversity in Folate and Antifolate Recognition. *Proc. Natl. Acad. Sci. U. S. A.* **2013**, *110* (38), 15180−15188.
(77) Gossen, M.; Bujard, H. Tight Control of Gene Expression in Mammalian Cells by Tetracycline-Responsive Promoters. *Proc. Natl. Acad. Sci. U. S. A.* **1992**, *89* (12), 5547−5551.
(78) Liu, H.; Rajasekaran, A. K.; Moy, P.; Xia, Y.; Kim, S.; Navarro, V.; Rahmati, R.; Bander, N. H. Constitutive and Antibody-Induced Internalization of Prostate-Specific Membrane Antigen. *Cancer Res.* **1998**, *58* (18), 4055−4060.
(79) Rajasekaran, S. A.; Anilkumar, G.; Oshima, E.; Bowie, J. U.; Liu, H.; Heston, W.; Bander, N. H.; Rajasekaran, A. K. A Novel Cytoplasmic Tail MXXXL Motif Mediates the Internalization of Prostate-Specific Membrane Antigen. *Mol. Biol. Cell* **2003**, *14* (12), 4835−4845.
(80) Robinson, M. B.; Blakely, R. D.; Couto, R.; Coyle, J. T. Hydrolysis of the Brain Dipeptide N-Acetyl-L-Aspartyl-L-Glutamate. Identification and Characterization of a Novel N-Acetylated Alpha-Linked Acidic Dipeptidase Activity from Rat Brain. *J. Biol. Chem.* **1987**, *262* (30), 14498−14506.
(81) Barinka, C.; Rinnová, M.; Šácha, P.; Rojas, C.; Majer, P.; Slusher, B. S.; Konvalinka, J. Substrate Specificity, Inhibition and Enzymological Analysis of Recombinant Human Glutamate Carboxypeptidase II. *J. Neurochem.* **2002**, *80* (3), 477−487.
(82) Schnaar, R. L.; Gerardy-Schahn, R.; Hildebrandt, H. Sialic Acids in the Brain: Gangliosides and Polysialic Acid in Nervous System Development, Stability, Disease, and Regeneration. *Physiol. Rev.* **2014**, *94* (2), 461−518.
(83) Yates, A. J.; Markowitz, D. L.; Stephens, R. E.; Pearl, D. K.; Whisler, R. L. Growth Inhibition of Cultured Human Glioma Cells by Beta-Interferon Is Not Dependent on Changes in Ganglioside Composition. *J. Neuropathol. Exp. Neurol.* **1988**, *47* (2), 119−127.

DOI: 10.1021/acs.molpharmaceut.7b00889
Mol. Pharmaceutics XXXX, XXX, XXX−XXX

Supporting Information

Inhibitor-GCPII interaction: selective and robust system for targeting cancer cells with structurally diverse nanoparticles

Jitka Neburkova[1,2 #], Frantisek Sedlak[1,2,3 #], Jirina Zackova Suchanova[3 #], Libor Kostka[4], Pavel Sacha[1], Vladimir Subr[4], Tomas Etrych[4], Petr Simon[1], Jitka Barinkova[1], Robin Krystufek[1], Hana Spanielova[1,3], Jitka Forstova[3], Jan Konvalinka[1,5], Petr Cigler[1]*

[1] Institute of Organic Chemistry and Biochemistry of the CAS, Flemingovo namesti 2, 166 10 Prague, Czech Republic
[2] First Faculty of Medicine, Charles University, Katerinska 32, 121 08 Prague, Czech Republic
[3] Department of Genetics and Microbiology, Faculty of Science, Charles University, Vinicna 5, 128 44 Prague 2, Czech Republic
[4] Institute of Macromolecular Chemistry of the CAS, Heyrovskeho namesti 2, 162 06, Prague 6, Czech Republic
[5]Department of Biochemistry, Faculty of Science, Charles University, Hlavova 2030, 128 43 Prague 2, Czech Republic
* cigler@uochb.cas.cz, Fax: (+)420–220–183–578, Telephone: (+)420–220–183–429
[#] These authors contributed equally.

Synthesis of GCPII inhibitors

All chemicals were purchased from Sigma-Aldrich unless otherwise stated. All final compounds were purified using a preparative scale Jasco PU-986 HPLC (flow rate 10 ml/min), equipped with a YMC C18 Prep Column, 5 μm, 250 x 20 mm. Purity was tested on an analytical Jasco PU-1580 HPLC (flow rate 1 ml/min), invariable gradient 2-100% in 30 min unless otherwise stated, equipped with a Watrex C18 Analytical Column, 5 μm, 250 x 5 mm. Final compounds were of at least 99% purity. Structures were confirmed by HRMS at LTQ Orbitrap XL (Thermo Fisher Scientific).

Compound **1** (1-amino-40-(4-bromobenzyl)-39,47-dioxo-3,6,9,12,15,18,21,24,27,30,33,36-dodecaoxa-40,46,48-triazahenpentacontane-45,49,51-tricarboxylic acid TFA salt) was synthesized according to the procedure described by Sacha et al,[1] but replacing Boc-NH-PEG_5-COOH with Boc-NH-PEG_{12}-COOH (PurePEG, LLC). The overall yield was 10%. HRMS (ESI-pos.) $C_{46}H_{80}BrN_4O_{20}$ $[M+H]^+$ calc. 1087.4549; found 1087.4525.
Compound **2** was prepared as previously described.[2] Compounds **4** and **5** (GCPII inhibitors with alkyne or azide) were synthesized as shown in Scheme S1.

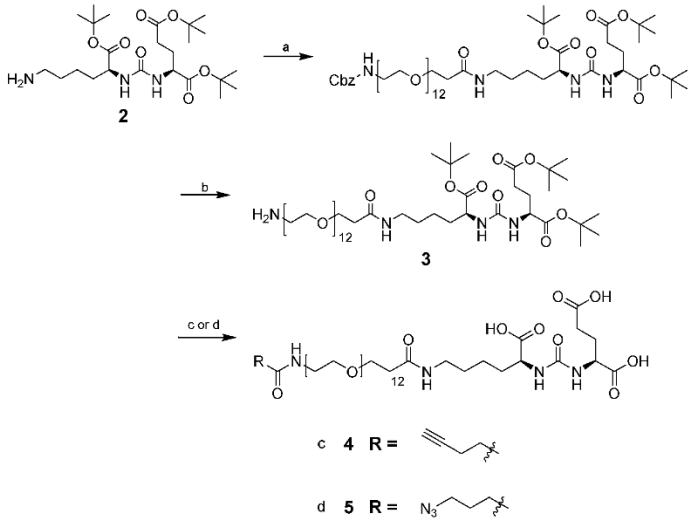

Scheme S1: Synthesis of **3**, **4**, and **5**. a) Z-NH-PEG_{12}-COOH , TBTU, DIEA, DMF; b) H_2, $Pd(OH)_2$, MeOH; c) 1) 4-pentynoic acid, TBTU, DIEA, DMF 2) TFA; d) azidobutyrate-NHS, DIEA, DMF 2) TFA.

Compound **3** (1-amino-39,47-dioxo-3,6,9,12,15,18,21,24,27,30,33,36-dodecaoxa-40,46,48-triazahen-pentacontane-45,49,51-tricarboxylic acid tri-*t*-butyl ester). A 511 mg (0.68 mmol, 1.1 eq) portion of Z-NH-PEG_{12}-COOH (IRIS Biotech) was dissolved in 1.5 mL DMF, and 297 mg TBTU (0.775 mmol, 1.25 eq) and 150 µl DIEA (0.87 mmol, 1.4 eq) were added in one portion. The reaction mixture was left stirring for 30 min, and 307 mg (0.62 mmol, 1.0 eq) **2** and 118 µl DIEA (0.68 mmol, 1.1 eq) dissolved in 1.5 ml DMF, were added to the reaction mixture in one portion. The reaction was left overnight, and the mixture was rotary evaporated to dryness. The crude product was dissolved in MeOH and a catalytic amount of $Pd(OH)_2$ was added (roughly 15 mg). The reaction flask was purged with hydrogen, and the deprotection was allowed to continue for 2 h with slightly elevated hydrogen pressure (1.05 Atm). Reaction was monitored by analytical HPLC (gradient 30-80% ACN in 30 min, Z-protected compound t_R = 19.5 min; deprotected product t_R = 12.5 min). The product was used in the next step without further purification.

Compound **4** (5,13,20-trioxo-16-oxa-4,6,12,19-tetraazatetracos-23-yne-1,3,7-tricarboxylic acid). A 17 mg (0.174 mmol, 1.2 eq) portion of 4-pentynoic acid was dissolved in 1 ml DMF along with 79 mg TBTU (0.209 mmol, 1.4 eq) and 90 µl DIEA (0.522 mmol, 3.6 eq). After 20 min, the mixture was added to 158 mg (0.145 mmol, 1.0 eq) of **3** dissolved in 1.5 ml DMF. The reaction was left overnight and the mixture was rotary evaporated to dryness. Crude product was purified using preparative scale HPLC (gradient 30-80% ACN in 60 min, t_R = 22.0 min) and the pure intermediate was rid of all solvents by dry freezing. The final deprotection was performed by adding 1 ml TFA and the reaction mixture was alternately sonicated and stirred for 15 min. TFA was removed by flow of nitrogen, and the product was purified using preparative scale HPLC (gradient 15-50% ACN in 60 min, t_R = 27.0 min) to obtain 23 mg of product (isolated yield = 47%). Analytical HPLC (gradient 2-100% ACN in 30 min, t_R = 16.1 min). HRMS (ESI-neg.) $C_{44}H_{78}N_4O_{21}$ $[M-2H]^{-2}$ calc. 498.25065; found 498.25012.

Compound **5** (56-azido-5,13,53-trioxo-16,19,22,25,28,31,34,37,40,43,46,49-dodecaoxa-4,6,12,52-tetraazahexapentacontane-1,3,7-tricarboxylic acid). A 53 mg (0.053 mmol, 1 eq) portion of **3** was

dissolved in 1 ml DMF, and 15 mg (0.064 mmol, 1.2 eq) of azidobutyrate-NHS (BroadPharm) along with 18 µl DIEA (0.106 mmol, 2.0 eq) were added. The reaction was left overnight, and the mixture was rotary evaporated to dryness. To the crude protected product 1 ml TFA was added and the reaction mixture was alternately sonicated and stirred for 15 min. TFA was removed by flow of nitrogen, and the product was purified using preparative scale HPLC (gradient 15-50% ACN in 60 min, t_R = 33.0 min) to obtain 24 mg of pure product (isolated yield = 44%). Analytical HPLC (gradient 2-100% ACN in 30 min, t_R = 15.4 min). HRMS (ESI-neg.) $C_{43}H_{79}N_7O_{21}$ $[M-2H]^{2-}$ calc. 513.75917; found 513.75952.

Synthesis of HPMA polymers

Atto488-amine (Atto488) was obtained from ATTO-TEC GmbH. The azoinitiator 2,2'-azobis(4-methoxy-2,4-dimethylvaleronitrile) (V-70) was obtained from Wako Pure Chemical Industries Ltd. *Tert*-butanol, dimethyl sulfoxide, and ethyl acetate were purchased from Sigma-Aldrich. All other chemicals and solvents were of analytical grade.

Synthesis of monomer chain transfer agent and copolymer precursor
N-(2-hydroxypropyl)methacrylamide (HPMA) was synthesized by reaction of methacryloyl chloride with 1-aminopropan-2-ol in dichloromethane in the presence of sodium carbonate as previously described.[3,4] 2-methyl-*N*-(6-oxo-6-(2-thioxo-1,3-thiazolidin-3-yl)hexyl)prop-2-enamide (Ma-Acap-TT)[3,4] and the chain transfer agent 2-cyanopropan-2-yl ethyl carbonotrithioate were synthesized as previously described.[5]

The copolymer precursor poly(HPMA-*co*-Ma-Acap-TT) was prepared by reversible addition-fragmentation chain transfer (RAFT) copolymerization.[6,7] HPMA (0.5 g, 3.49 mmol) dissolved in 4.6 ml *tert*-butanol was mixed with a solution of Ma-Acap-TT (350 mg, 1.16 mmol) dissolved in 606 µl dimethyl sulfoxide. 2-Cyanopropan-2-yl ethyl carbonotrithioate (2.39 mg, $1.16x10^{-5}$ mol) and 2,2'-azobis(4-methoxy-2,4-dimethylvaleronitrile) (1.79 mg, $5.82x10^{-6}$ mol) were introduced into the polymerization ampule. The mixture was bubbled with argon for 10 min and the ampule was sealed. Copolymerization was carried out at 40 °C for 16 h. Polymer precursor was isolated by precipitation into ethyl acetate, filtered off, washed with ethyl acetate and diethyl ether, and dried in a vacuum. The terminating trithiocarbonate group was removed as described by Perrier.[4,5] The copolymer precursor poly(HPMA-*co*-Ma-Acap-TT) with molecular weight M_n = 37,900 g/mol, M_w = 39,600 g/mol, dispersity $Đ$ = 1.04, and content of reactive TT groups of 19.4 mol% was obtained.

Determination of molecular weights and polymer composition
The weight-average molecular weights (M_w), number average molecular weights (M_n), and dispersities ($Đ$) of the polymer precursor and conjugates were determined using size exclusion chromatography. The system was configured as previously described.[1,7] The GCPII inhibitor content was determined by quantification of bromine content in polymers using inductively coupled plasma atomic emission spectroscopy (ICP-OES) as previously described.[1]

Synthesis of polymer conjugates
Generally, HPMA copolymer conjugates were prepared by reaction of the copolymer precursor poly(HPMA-*co*-Ma-Acap-TT) containing thiazolidine-2-thione reactive groups (TT) along the polymer chain with a combination of fluorophore (Atto488-amine) and targeting ligand (GCPII inhibitor) according to a previously described procedure.[1]

*Synthesis of fluorescent HPMA polymer without GCPII inhibitor (***pol**, pol*)*

Copolymer precursor poly(HPMA-*co*-Ma-Acap-TT) (65 mg; M_n = 37,900 g/mol, M_w = 39,600 g/mol, $Đ$ = 1.04; 19.4 mol% TT) and Atto488 (3.25 mg, $3.78x10^{-6}$ mol) were dissolved in 0.5 ml dimethyl sulfoxide. Then, DIEA (2.6 µl, $1.5x10^{-5}$ mol) was added. The reaction was carried out for 4 h at room temperature. Then, 60 µl of reaction mixture was removed and 2 µl 1-aminopropan-2-ol (AP) was added to remove residual TT reactive groups, providing **pol**. Copolymer with TT reactive groups [rest of reaction mixture, poly(HPMA-*co*-Ma-Acap-ATTO488-*co*-Ma-Acap-TT)] and copolymer with AP-removed TT groups [poly(HPMA-*co*-Ma-Acap-ATTO488-*co*-Ma-Acap-AP)] were isolated by precipitation into ethyl acetate, filtered off, washed with diethyl ether, and dried in a vacuum. The polymer conjugate was purified on a Sephadex LH-20 chromatography column in methanol. Methanol was evaporated, and the conjugate was dissolved in water and purified on a PD-10 chromatography column, then lyophilized. Yield of the aminoreactive HPMA copolymer was 50 mg (pol). Yield of the quenched polymer was 5 mg (**pol**). The Atto488 content was 4.7 wt% and 17 mol% of TT. M_w and $Đ$ were determined as follows: M_w = 42,100 g/mol, $Đ$ = 1.3.

*Synthesis of fluorescent HPMA polymer with GCPII inhibitor (***pol-inh**, pol-inh*)*
Synthesis was very similar to that of polymers without GCPII inhibitor. In the first step, GCPII inhibitor (compound **1**, 9 mg, $8.27x10^{-6}$ mol) was added to the mixture, and the amount of DIEA was increased correspondingly (7.8 µl, $4.47x10^{-5}$ mol). Yield of the aminoreactive copolymer with GCPII inhibitor was 45 mg (pol-inh). Yield of the polymer quenched with AP was 5 mg (**pol-inh**). The GCPII inhibitor content was 14.1 wt%, Atto488 content was 4.7 wt% and 10 mol% of TT remained on the polymer. The M_w and $Đ$ were determined as M_w = 47,600 g/mol, $Đ$ = 1,3.

Characterization of prepared particles

Fluorescence spectra measurement
Fluorescence of particles (labeled by Atto488 or Alexa Fluor 488) was determined by measuring the difference in fluorescence of 10 nM or 50 nM solutions of particles, analyzed using a TECAN infinite plate reader (M 1000), with excitation at 500 nm and emission at 520 nm.

Electron microscopy
For morphology analysis, MPyV and Qβ particles were visualized by negative staining. Samples (10 µL, 50 µg/mL) were adsorbed on carbon-coated formvar copper grids (Electron Microscopy Sciences). Grids were washed twice in redistilled H_2O and then contrasted on two drops of 2% solution of phosphotungstic acid (pH 7.2). To prepare sample of NDs, carbon-coated copper grids were placed into a UV-ozonizing chamber (UV/Ozone Pro Cleaner Plus, Bioforce Nanosciences) for 15 min. Then, a droplet of poly(ethyleneimine) (2.5 kDa, 0.1 mg/ml) was placed on the grid. After 10 min incubation, it was removed with a piece of tissue. Then, a droplet of aqueous solution of NDs (50 µg/ml) was placed on the grid, and after 3 min incubation, the liquid was removed with a piece of tissue.[8]
The grids were visualized with a JEOL JEM-1011 transmission electron microscope operated at 80 kV.

TEM image analysis
Analysis of particle size distributions was performed with ImageJ software.[9] Because the ND particles are of irregular shape, we used equivalent circular diameter to express their size.[8] To facilitate comparison of the data, we used the same approach for all NPs.
Equivalent circular diameter (d_{eq}) of a particle is defined as the diameter of a circular particle with the same area as the particle of interest (S), as described by the equation

$$d_{eq} = \sqrt{4S/\pi} \qquad \text{(S1)}$$

The data were plotted as the volume-weighted histogram, in which the contribution of each particle in the distribution relates to the volume of that particle (equivalent to mass for samples of uniform density); the relative contribution of a particle is proportional to the cube of its size. Particle volumes (PV) used for the construction of volume-weighted histograms were calculated as if the particles were spheres of diameter equal to the circular equivalent diameter as described by the equation

$$PV = \frac{4}{3}\pi\left(\frac{d_{eq}}{2}\right)^3 \qquad (S2)$$

The particle diameters and the respective standard deviations indicated in the manuscript were obtained by fitting of the volume-weighted histograms with Gaussian function.

Stability test – dynamic light scattering (DLS) measurement

DLS was recorded with a Zetasizer Nano ZS system (Malvern Instruments) at different temperatures with 10-min equilibration. Sample concentrations were 0.25 mg/ml.

SDS-PAGE analysis

For electrophoretic analysis, 2 µg of particles was mixed with 2.5 µl of 100 mM dithiothreitol (DTT), 2.5 µl of 10 M urea, and 2 µl of sample buffer (50 mM Tris, pH 6.8, 25% 2-mercaptoethanol, 5% sodium dodecyl sulfate, 0.005% bromophenol blue) in the total sample volume of 10 µl and incubated for 10 min at 70 °C to disassemble the particles. All samples were separated on SDS-PAGE in MOPS buffer (NuPAGE Novex 4-12% Bis-Tris precast polyacrylamide gels, ThermoFisher Scientific). The running time in SDS-PAGE was 50 min with constant voltage 200 V. The gel was scanned for Alexa Fluor 488 (excitation at 488 nm) fluorescence on a PharosFX Molecular Imager (Bio-Rad). Subsequently, proteins were stained with colloidal Coomassie dye G-250 according to the manufacturer's protocol (GelCode Blue Stain Reagent, ThermoFisher Scientific). The Coomassie-stained SDS-PAGE gel was scanned on a Molecular Imager GS 800 densitometer (Bio-Rad).

Preparation of cell lines with switchable GCPII expression

U251 MG cell lines with switchable GCPII expression were prepared analogously as described by Tykvart *et al.* for HEK cell lines.[10] Briefly, U251 MG cells (supplied by ATCC as U373 MG cells) were stably transfected with pTet-Off® Advanced vector (Clontech) using FuGENE® HD transfection reagent (Roche). Geneticin selection was applied and monoclonal populations were prepared using cloning rings. First, individual clones were tested for the ability to alter expression by addition of doxycycline using transient transfection with GFP. The clone with highest expression difference in ON and OFF state (after addition of doxycycline) was selected for further cotransfection with pTRE-Tight-GCPII and pPUR vector (Clonetech) using similar transfection conditions. Similarly, after puromycin selection and clone preparation using cloning rings, the resulting U251 +/- MG clone with highest/lowest GCPII expression was chosen.

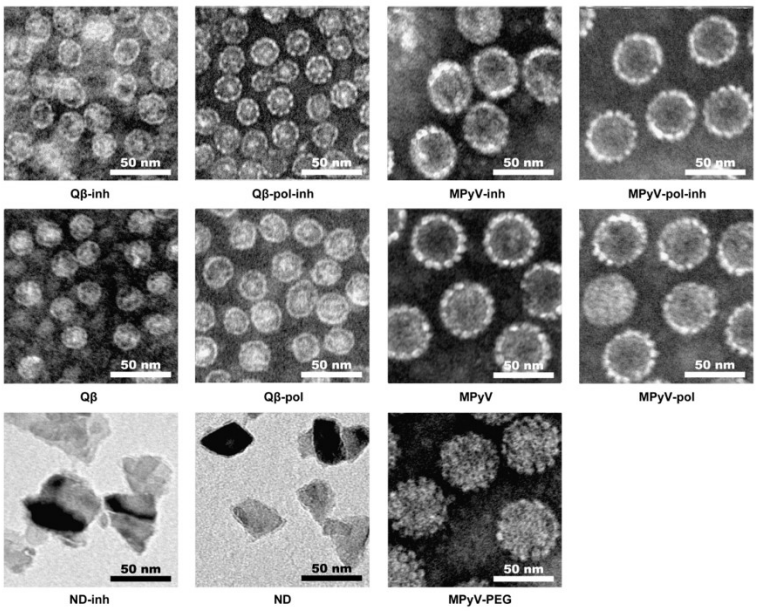

Figure S1. Characterization of all NPs by transmission electron microscopy.

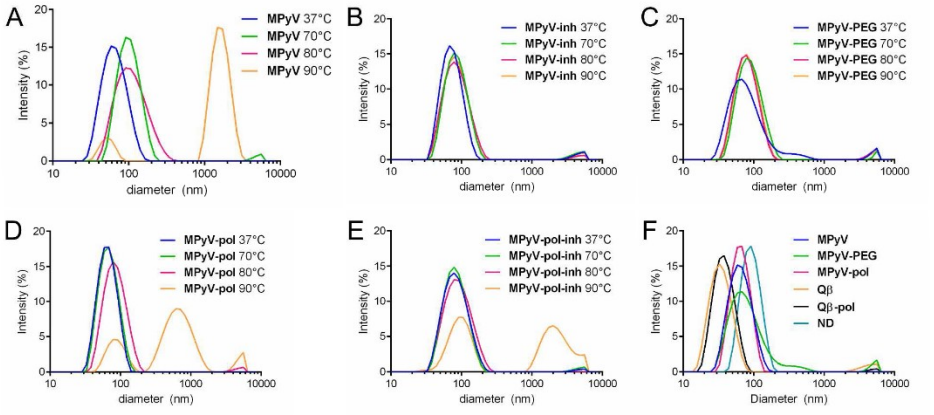

Figure S2. Measurement of the temperature stability of modified NPs in storage buffer (pH 7.4) by dynamic light scattering. Tested temperatures were 37, 70, 80, and 90 °C; the incubation time was 10 min. (A) **MPyV**, (B) **MPyV-inh**, (C) **MPyV-PEG**, (D) **MPyV-pol**, and (E) **MPyV-pol-inh**. (F) Size distribution of all NPs without conjugated inhibitor at 37 °C (negative controls).

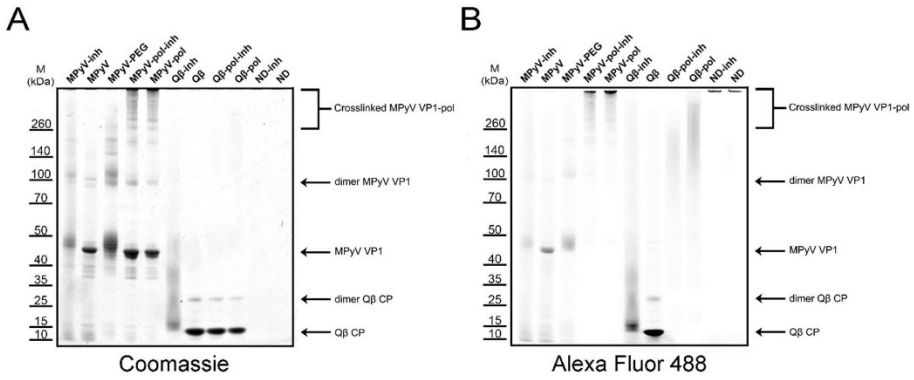

Figure S3. Characterization of all nanoparticles using SDS-PAGE. The gel was (A) stained with Coomassie brilliant blue and (B) scanned for Alexa Fluor 488 fluorescence. The molecular weights are indicated on the left. The particles were disassembled by treatment with dithiothreitol and urea.

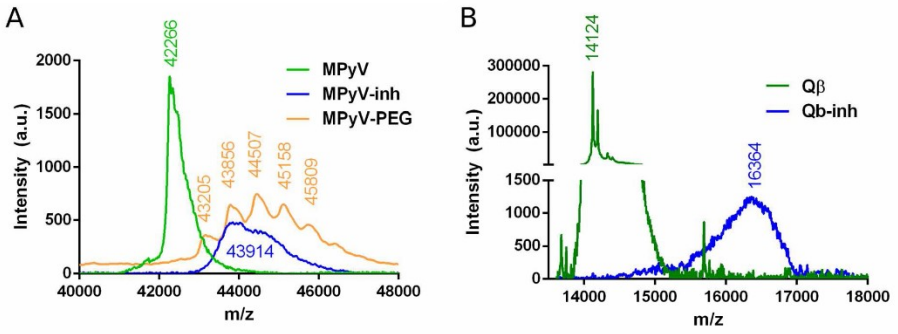

Figure S4. MALDI measurement of disassembled VLPs to subunits. (A) MPyV (MPyV, **MPyV-inh**, **MPyV-PEG**) and (B) Qβ (Qβ, **Qβ-inh**). The marked peaks indicate the corresponding mass.

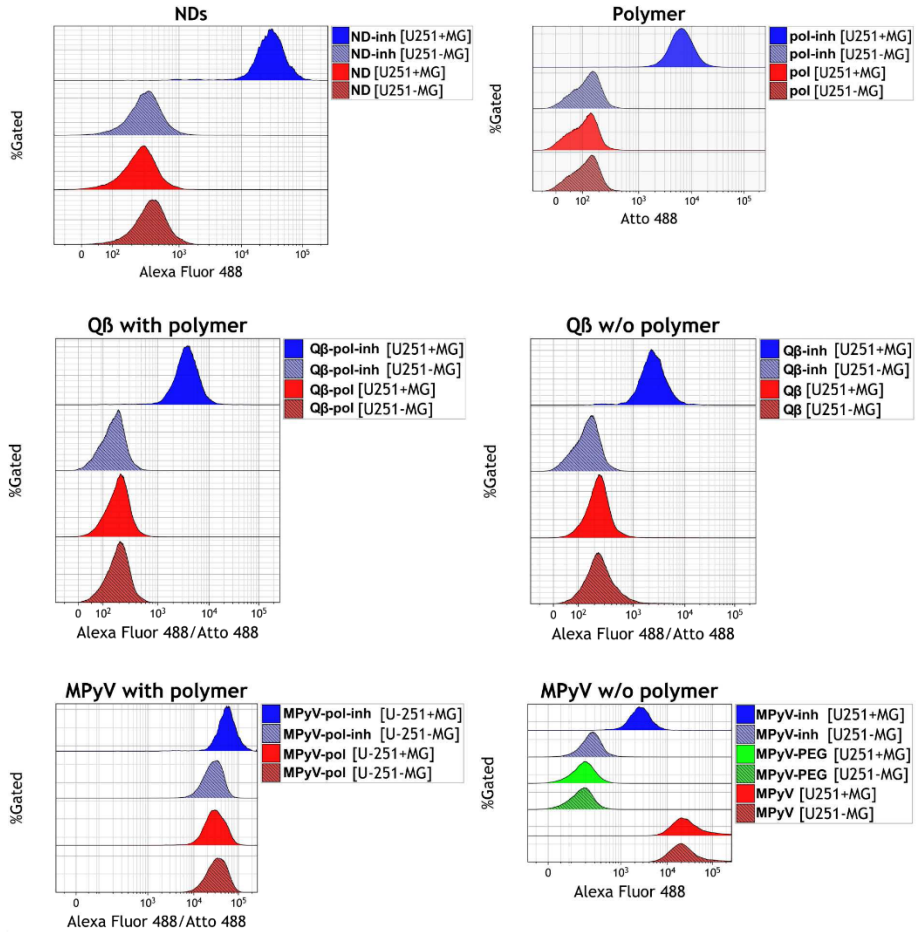

Figure S5. Flow cytometry measurements presented as histogram overlays. Merged data from triplicates are shown for each sample. Cells either with (U-251^{+} MG; solid fills) or without (U-251^{-} MG; hatched fills) GCPII expression were used. The blue histograms denote data for NPs with inhibitor, red for NPs without inhibitor, and green for MPyV VLPs with PEG (additional control). Data were analyzed with Kaluza Analysis Software (v1.5a).

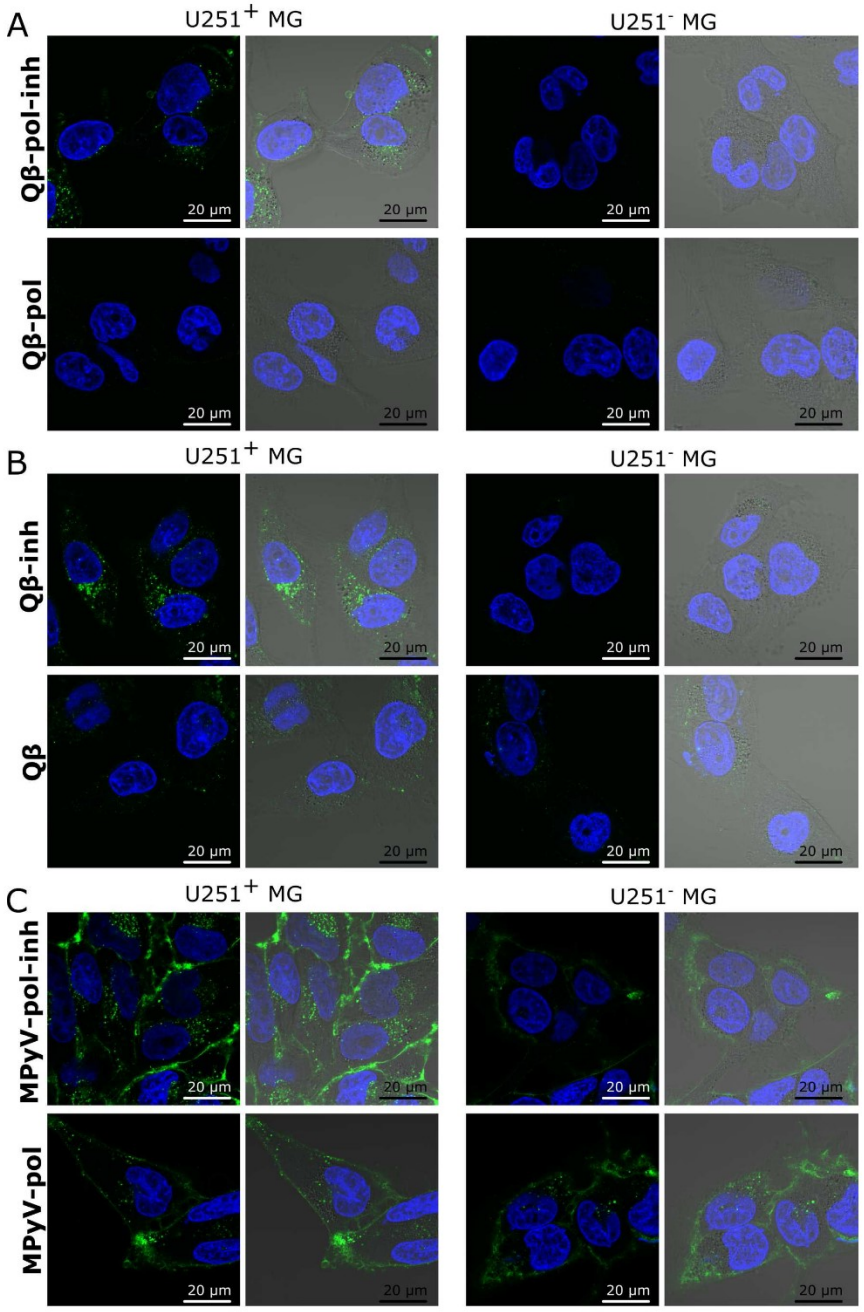
A
U251+ MG
U251- MG
Qβ-pol-inh
Qβ-pol
B
U251+ MG
U251- MG
Qβ-inh
Qβ
C
U251+ MG
U251- MG
MPyV-pol-inh
MPyV-pol
20 μm

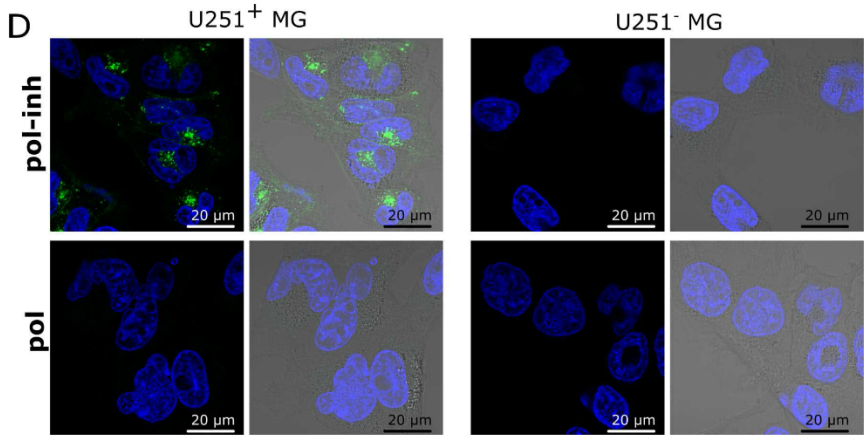

Figure S6. Confocal images of NP uptake by U-251 MG cells. Cells with (U-251^{+} MG) or without (U-251^{-} MG) GCPII expression were incubated with NPs for 1 h. Binding of (A) poly(HPMA)-coated Qβ VLPs, (B) Qβ VLPs, (C) poly(HPMA)-coated MPyV VLPs, and (D) polymer VLPs. Confocal sections of representative cells with corresponding signals in green (NPs conjugated with Alexa Fluor 488 or Atto 488) and blue (nuclei stained with Hoechst) channels are shown. Merge is composed of both channels and bright field image.

References

(1) Šácha, P.; Knedlík, T.; Schimer, J.; Tykvart, J.; Parolek, J.; Navrátil, V.; Dvořáková, P.; Sedlák, F.; Ulbrich, K.; Strohalm, J.; Majer, P.; Šubr, V.; Konvalinka, J. iBodies: Modular Synthetic Antibody Mimetics Based on Hydrophilic Polymers Decorated with Functional Moieties. *Angew. Chem. Int. Ed.* **2016**, *55* (7), 2356–2360.

(2) Tykvart, J.; Schimer, J.; Bařinková, J.; Pachl, P.; Poštová-Slavětínská, L.; Majer, P.; Konvalinka, J.; Šácha, P. Rational Design of Urea-Based Glutamate Carboxypeptidase II (GCPII) Inhibitors as Versatile Tools for Specific Drug Targeting and Delivery. *Bioorg. Med. Chem.* **2014**, *22* (15), 4099–4108.

(3) Ulbrich, K.; Šubr, V.; Strohalm, J.; Plocová, D.; Jelínková, M.; Říhová, B. Polymeric Drugs Based on Conjugates of Synthetic and Natural Macromolecules: I. Synthesis and Physico-Chemical Characterisation. *J. Controlled Release* **2000**, *64* (1), 63–79.

(4) Šubr, V.; Ulbrich, K. Synthesis and Properties of New N-(2-Hydroxypropyl)methacrylamide Copolymers Containing Thiazolidine-2-Thione Reactive Groups. *React. Funct. Polym.* **2006**, *66* (12), 1525–1538.

(5) Ishitake, K.; Satoh, K.; Kamigaito, M.; Okamoto, Y. Stereogradient Polymers Formed by Controlled/Living Radical Polymerization of Bulky Methacrylate Monomers. *Angew. Chem. Int. Ed.* **2009**, *48* (11), 1991–1994.

(6) Chytil, P.; Etrych, T.; Kříž, J.; Subr, V.; Ulbrich, K. N-(2-Hydroxypropyl)methacrylamide-Based Polymer Conjugates with pH-Controlled Activation of Doxorubicin for Cell-Specific or Passive Tumour Targeting. Synthesis by RAFT Polymerisation and Physicochemical Characterisation. *Eur. J. Pharm. Sci. Off. J. Eur. Fed. Pharm. Sci.* **2010**, *41* (3–4), 473–482.

(7) Šubr, V.; Sivák, L.; Koziolová, E.; Braunová, A.; Pechar, M.; Strohalm, J.; Kabešová, M.; Říhová, B.; Ulbrich, K.; Kovář, M. Synthesis of Poly[N-(2-Hydroxypropyl)methacrylamide] Conjugates of Inhibitors of the ABC Transporter That Overcome Multidrug Resistance in Doxorubicin-Resistant P388 Cells in Vitro. *Biomacromolecules* **2014**, *15* (8), 3030–3043.
(8) Rehor, I.; Cigler, P. Precise Estimation of HPHT Nanodiamond Size Distribution Based on Transmission Electron Microscopy Image Analysis. *Diam. Relat. Mater.* **2014**, *46*, 21–24.
(9) Schindelin, J.; Arganda-Carreras, I.; Frise, E.; Kaynig, V.; Longair, M.; Pietzsch, T.; Preibisch, S.; Rueden, C.; Saalfeld, S.; Schmid, B.; Tinevez, J.-Y.; White, D. J.; Hartenstein, V.; Eliceiri, K.; Tomancak, P.; Cardona, A. Fiji: An Open-Source Platform for Biological-Image Analysis. *Nat. Methods* **2012**, *9* (7), 676–682.
(10) Tykvart, J.; Schimer, J.; Jančařík, A.; Bařinková, J.; Navrátil, V.; Starková, J.; Šrámková, K.; Konvalinka, J.; Majer, P.; Šácha, P. Design of Highly Potent Urea-Based, Exosite-Binding Inhibitors Selective for Glutamate Carboxypeptidase II. *J. Med. Chem.* **2015**, *58* (10), 4357–4363.

Appendix F – Publication 6

Ivan Rehor, Karin L. Lee, Kevin Chen, Miroslav Hajek, Jan Havlik, Jana Lokajova, Milan Masat, **Jitka Slegerova**, Sourabh Shukla, Hamed Heidari, Sara Bals, Nicole F. Steinmetz, Petr Cigler: Plasmonic nanodiamonds: targeted core-shell type NPs for cancer cell thermoablation, Advanced Healthcare Materials, *4*, 460, **2015**.

ADVANCED HEALTHCARE MATERIALS
www.advhealthmat.de

Materials Views
www.MaterialsViews.com

Plasmonic Nanodiamonds: Targeted Core–Shell Type Nanoparticles for Cancer Cell Thermoablation

Ivan Rehor, Karin L. Lee, Kevin Chen, Miroslav Hajek, Jan Havlik, Jana Lokajova, Milan Masat, Jitka Slegerova, Sourabh Shukla, Hamed Heidari, Sara Bals, Nicole F. Steinmetz, and Petr Cigler**

Targeted biocompatible nanostructures with controlled plasmonic and morphological parameters are promising materials for cancer treatment based on selective thermal ablation of cells. Here, core–shell plasmonic nanodiamonds consisting of a silica-encapsulated diamond nanocrystal coated in a gold shell are designed and synthesized. The architecture of particles is analyzed and confirmed in detail using electron tomography. The particles are biocompatibilized using a PEG polymer terminated with bioorthogonally reactive alkyne groups. Azide-modified transferrin is attached to these particles, and their high colloidal stability and successful targeting to cancer cells overexpressing the transferrin receptor are demonstrated. The particles are nontoxic to the cells and they are readily internalized upon binding to the transferrin receptor. The high plasmonic cross section of the particles in the near-infrared region is utilized to quantitatively ablate the cancer cells with a short, one-minute irradiation by a pulse 750-nm laser.

1. Introduction

Plasmonic nanostructures (PNs) of various shapes and composition[1,2] have garnered scientific interest in recent years due to their unique optical properties, which allow their use for construction of therapeutic and theranostic nanoparticles, bioprobes, and sensors.[1,3] For a nanosized noble metal particle, the de Broglie wavelength of the valence electrons is of the same order of magnitude as the size of the particle, and quantum size effects may appear. The valence electrons then start to oscillate at a collective oscillation frequency, giving rise to characteristic plasmon resonance bands.[3,4] Because of these properties, PNs gained interest in the fields of biotechnology and biomedicine. Through nanostructure design, their plasmonic absorption wavelength can be finely tuned to fall in the near-infrared tissue imaging window (650–900 nm) where light can penetrate up to a few centimeters into the tissue. The huge absorption and scattering of PNs enables their use as a contrast agent for optical imaging of tissues, e.g., in optical coherence tomography[5,6] or photoacoustic[7] imaging. Furthermore, the absorbed light is transformed into heat, allowing for use of PNs in cancer therapy.[8–10] The heat may be used for thermal ablation of tumors or to control the release of therapeutics, which are usually but not exclusively,[11] attached to the PN surface.[12] Merging diagnostic imaging ability with a therapeutic function in one so-called "theranostic" agent is indeed promising, as evidenced by numerous recent publications addressing the topic.[13,14]

Dr. I. Rehor, Dr. M. Hajek, J. Havlik, Dr. J. Lokajova, Dr. M. Masat, J. Slegerova, Dr. P. Cigler
Institute of Organic Chemistry and Biochemistry, v.v.i
Academy of Sciences of the Czech Republic
Flemingovo nam. 2, 166 10 Prague 6, Czech Republic
E-mail: cigler@uochb.cas.cz

K. L. Lee, K. Chen, Dr. S. Shukla, Dr. N. F. Steinmetz
Department of Biomedical Engineering
Case Western Reserve University
Schools of Medicine and Engineering
10900 Euclid Avenue, Cleveland OH 44106, USA
E-mail: nicole.steinmetz@case.edu

Dr. N. F. Steinmetz
Department of Radiology
Department of Materials Science and Engineering
Department of Macromolecular Science and Engineering
Case Western Reserve University, Schools of Medicine and Engineering
10900 Euclid Avenue, Cleveland, OH 44106, USA

J. Havlik
Faculty of Science
Charles University, Hlavova 2030
128 40 Prague 2, Czech Republic

J. Slegerova
First Faculty of Medicine
Charles University, Katerinska 32
121 08, Prague 2, Czech Republic

Dr. H. Heidari, Dr. S. Bals
EMAT, University of Antwerp
Groenenborgerlaan 171, B-2020 Antwerp, Belgium

DOI: 10.1002/adhm.201400421

Here, we describe preparation of a plasmonic gold nanoshell (GNS) around silica-encapsulated diamond nanocrystals. Nanodiamonds (NDs) are highly biocompatible materials with applications in nanomedicine[15] and bioimaging.[16–19] Previous studies on gold plasmonic structures connected with diamonds were performed primarily on macroscopic substrates.[20–25] They have focused mainly on the photophysics of fluorescent nitrogen-vacancy centers embedded in a diamond crystal lattice. Creation of a well-defined plasmonic system on a single diamond nanoparticle in solution is limited by the colloidal instability of NDs in aqueous buffers.[26] To date, only direct covalent attachment of gold nanoparticles to NDs has been achieved,[27,28] and materials with unordered structural morphology[29,30] have been prepared.

We took advantage of our recently published methodology for silica coating of NDs,[31] which enables the creation of a well-defined plasmonic material based on a ND dielectric core coated with a GNS. We chose the core-shell design because it provides an extremely high plasmonic absorption cross section, as well as the possibility to tune the position of the absorption maximum within the near-infrared region, where light is minimally absorbed and scattered by the tissue. As a first step to demonstrate the utility of this newly constructed biomaterial in nanomedical applications, we show that it can be stabilized and rendered biocompatible by addition of PEG-containing ligands bearing bioorthogonally reactive alkyne groups, followed by decoration with synthetically modified transferrin (Tf). We use these particles to target cancer cells, which overexpress the Tf-receptor, and thermally ablate them by irradiation with a near-infrared pulse laser.

2. Results and Discussion

2.1. Preparation and Characterization of Particles

Creation of GNSs with a diamond core was achieved via multistep encapsulation, as depicted in **Figure 1**A. Commercially available ND particles (Figure 1B) are of irregular shape (circularity ~0.67) with sharp edges and often appear elongated in one dimension (needle–like). Their size distribution is broad, ranging from several nm to more than 50 nm in diameter. Therefore, before the GNS is generated on the ND surface, the particle shape needs to be normalized to spherical, and the size distribution should be narrowed. We achieved this through encapsulation of NDs in a silica shell, approximately 20 nm thick, using a method we described earlier.[31] The formation of the desired architecture was confirmed at each step by transmission electron microscopy (TEM), as shown in Figure 1B-E. After coating with silica (Figure 1C), the particles became more spherical (circularity ~0.87), and their diameter increased to 66 ± 10 nm. These pseudospherical silica-coated NDs (**ND@Sil**) are suitable for encapsulation with a GNS, according to a procedure introduced by Halas and collaborators.[32,33] First, small gold nanoparticles (2–3 nm in diameter) were electrostatically anchored onto the silica particle surface (Figure 1D). These assemblies were exposed to a reductive environment containing gold(III) ions, which served as nucleation centers for GNS growth (Figure 1E). The growth of shells ended after several tens of seconds, yielding a deep blue solution containing GNS-coated NDs (**ND@Au**).

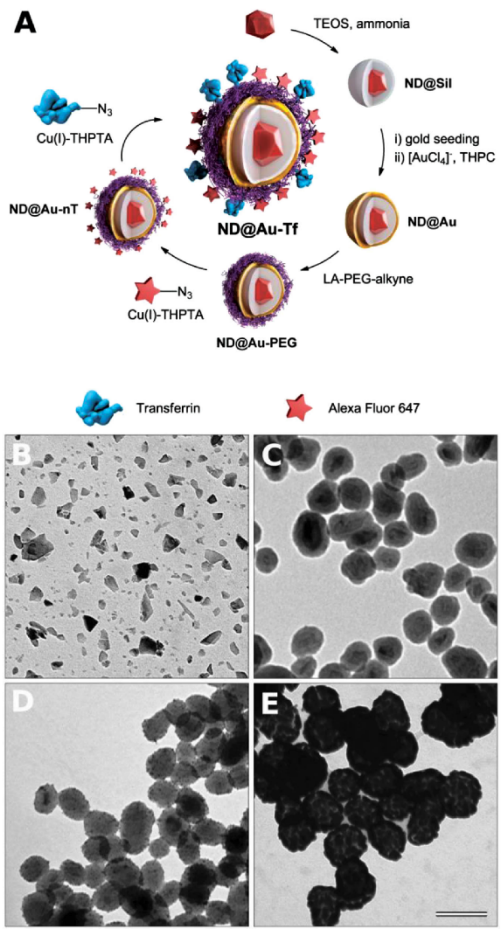

Figure 1. (A) Schematic representation of the preparation of GNSs with a diamond core. First, a silica shell is created on diamond particles, followed by formation of a GNS upon reduction of $[AuCl_4]^-$ promoted by adsorbed gold nanoparticle seeds. The GNS is modified with a lipoic acid-PEG conjugate, which is terminated with an alkyne. Using click chemistry, Alexa Fluor 647 dye and azide-modified transferrin (the targeting protein) are attached in consecutive steps. (B–D) TEM microphotographs of (B) diamond particles, (C) silica-coated diamond particles (**ND@Sil**), (D) silica-coated diamond particles with gold seeds, and (E) GNSs a with diamond core (**ND@Au**). The magnification is the same for all microphotographs, and the scale bar corresponds to 100 nm.

To investigate the structure and thickness of these GNSs in detail, we analyzed individual **ND@Au** particles using HAADF-STEM electron tomography. This technique yields images in which the intensity approximately scales with the square of the atomic number of the elements present in the region

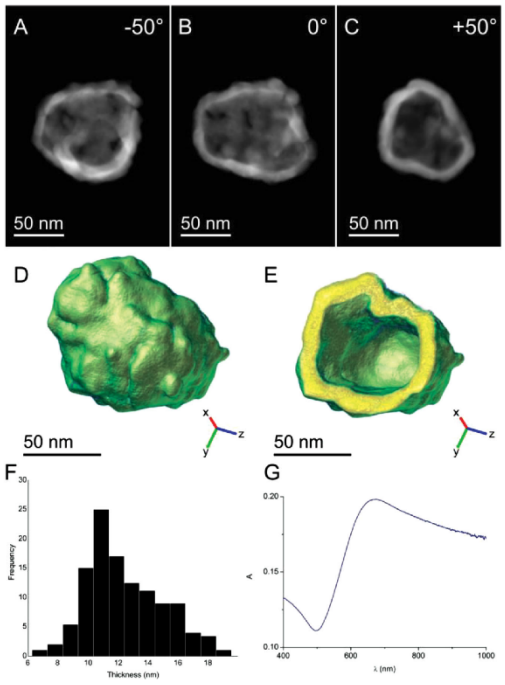

Figure 2. (A–C) 2D HAADF-STEM projections of a ND-silica particle coated with a GNS (**ND@Au**) obtained at different tilt angles. The diamond core and silica coating are not visible due to the limited dynamic range of the image detector. (D) A 3D representation of the reconstructed nanoshell. (E) A slice through the 3D reconstruction of the GNS demonstrating the homogeneity of shell thickness. (F) A histogram indicating the measured thicknesses of the shell based on electron tomography reconstruction. The average shell thickness was 12.6 ± 0.3 nm. (G) Absorption spectrum of **ND@Au** in water at 15 μg/mL concentration (which corresponds to a ND concentration of 0.5 μg/mL).

of interest. Due to the limited dynamic range of the HAADF detector, maintaining similar intensities for Au and silica in the projection images is not feasible because of the large differences in atomic number. We therefore focused on 3-dimensional reconstruction of GNSs. In **Figure 2** A–C, 2-dimensional projections of a GNS imaged at different angles are presented. The 3-dimensional reconstruction resulting from the electron tomography experiment is presented in Figure 2D and E. The shell thickness is mostly homogenous. We evaluated the average shell thickness as 12.6 ± 0.3 nm, and the total internal surface of the GNS was 32 600 nm^2. The intermittent presence of small holes is likely caused by incomplete filling of the spaces between individual seeds with gold.

The formation of the GNS is reflected in absorption spectra by a characteristic broad plasmonic band with an absorption maximum at 675 nm (Figure 2G). The position of the maximum corresponds to values published for silica particles coated with GNSs of similar sizes and thicknesses.[34]

2.2. Introduction of Protective and Bioorthogonally Reactive PEG Coating

The application of GNS-based materials in living systems requires their protection against ionic-strength-induced aggregation/precipitation in buffers and biological liquids, as well as against opsonization. Poly(ethylene oxide) (PEG) is an effective polymeric bio-nanointerface, shielding particles against these factors, rendering them "stealth" to the immune system, and prolonging their circulation in the body.[35] In addition to these attributes, PEG can serve as heterobifunctional linker to connect nanoparticles with attached moieties. For functionalization of **ND@Au**, we utilized mid-size PEG (5 kDa) terminated with lipoic acid at one end and an aliphatic alkyne at the other (**Figure 3**A). Lipoic acid serves as an instant anchoring group, possessing stronger and more stable interaction with gold than terminal aplihatic thiols.[36] Of the available bioconjugation techniques, we chose Cu(I)-catalyzed Huisgen alkyne-azide cycloaddition (click reaction) because of its high orthogonality with other reactive groups in biomolecules and excellent conjugation yields in aqueous solution even at very dilute concentrations.[37]

To analyze the effect of PEG protection on the colloidal stability of particles, we performed comparative stability tests of PEG-modified GNSs (**ND@Au-PEG**) and unmodified **ND@Au**. We exposed the particles to different aqueous solutions with high ionic strength and monitored the hydrodynamic radii over time by dynamic light scattering. While PEG-protected **ND@Au-PEG** exhibited unlimited colloidal stability in PBS, physiological solution (0.15 M NaCl) and cell growth media (RPMI media + serum) (Figure 3B), naked **ND@Au** particles immediately agglomerated and precipitated from the buffers (Figure 3C), with the exception of cell growth media. The particles remained stable in media, most likely due to formation of a protein corona by adsorption of proteins from serum.

2.3. Modification of Particles with Alexa Fluor 647 and Transferrin

For cancer cell targeting experiments, we selected human holotransferrin (Tf), a glycoprotein that is internalized into cells via clathrin-mediated endocytosis upon binding to Tf receptors (TfR). TfR are expressed in negligible numbers on non-dividing cells, but are highly upregulated on rapidly dividing cancer cells, reaching expression levels of up to 10^5 TfR per cell.[38] This makes Tf a suitable targeting ligand to direct nanomaterials, such as **ND@Au**, to cancer cells. This general approach has been successfully demonstrated for various nanoparticles,[39] such as virus-like particles,[40] liposomes[41] and nanodiamonds.[42,43] To ensure protein reactivity for the click bioconjugation strategy, we introduced azide groups to the protein. As previously described,[44] Tf offers a favorable pathway for selective derivatization: a reactive aldehyde can be produced by mild periodate cleavage of 1,2-diols on sialic acid (*N*-acetyl neuraminic acid) moieties present in the Tf glycosylation pattern. We derivatized the obtained aldehydes with aminooxypropylazide, a "clickable" heterobifunctional linker that forms a physiologically stable aldoxime (for structures, see Figure 3A). Compared to ligation via amino or thiol groups, this approach

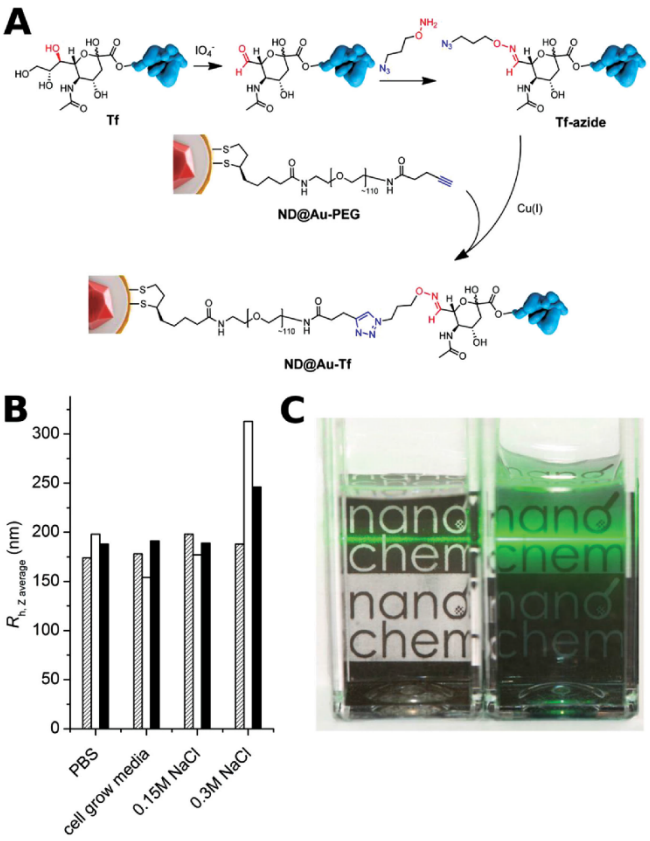

Figure 3. Structure of **ND@Au-PEG** conjugate and its colloidal stability in aqueous solutions with high ionic strength. A) Composition of the particle surface architecture after modification and attachment of Tf. B) Hydrodynamic radii of **ND@Au-PEG** in various solutions after 1 h (hatched), 1 week (white) and 1 month (black), showing no aggregation. C) Photograph of naked (**ND@Au**, left) and PEG-coated (**ND@Au-PEG**, right) particles dispersed in PBS (20 min after mixing; 0.2 mg/mL concentration). The precipitating **ND@Au** particles are already partially sedimented on the bottom of the vial, while the remaining large aggregates unevenly scatter the laser beam. The **ND@Au-PEG** particles form a stable colloidal solution, which evenly and strongly scatters the laser beam.

results in better control over protein attachment points, because one Tf molecule contains only four sialic acids residues at well-defined and sterically accessible positions.[44]

To obtain fluorescent particles, which enable quantification of targeting by flow cytometry and analysis of the particles' subcellular localization by confocal microscopy, we first reacted the alkyne-bearing **ND@Au-PEG** particles with Alexa Fluor 647-azide, yielding fluorescent **ND@Au-nT** conjugate. Although gold plasmonic systems can quench emission from fluorescent dyes,[45] the dye in this case remained fluorescent and was observable with both flow cytometry and confocal microscopy. Linear PEG with a molecular weight of 5000 Da has a Flory dimension of ≈6.0 nm in solution;[46] it is therefore anticipated that the PEG spacer placed between the plasmon surface and fluorophore will effectively shield the quenching effects. The number of Alexa Fluor 647 molecules per particle, however, was difficult to estimate because of the strong interference of particles' plasmonic properties and the extinction and emission fluorescence bands of the dye. As a next step, we attached azide-modified Tf to unreacted alkyne groups of **ND@Au-nT** under similar conditions, providing **ND@Au-Tf**.

2.4. Targeting of Cancer Cells

Target-specificity and cellular uptake of particles was evaluated in TfR-expressing SKBR3 cells (a human breast cancer cell line) using flow cytometry (quantitative) and confocal microscopy (qualitative). Flow cytometry indicated that both types of particles, **ND@Au-nT** and **ND@Au-Tf**, bound to the cells, with the Tf-targeted preparation **ND@Au-Tf** showing enhanced interactions. Our data indicate that 26% of the cell population was targeted by **ND@Au-Tf**, while non-specific uptake was attributed to 18% of the cells, as indicated by **ND@Au-nT**-cell interactions ($p < 0.05$, **Figure 4**). Cell targeting properties were found to be reproducible in other cell lines, such as HeLa cells (not shown).

Competition binding assays using free Tf ligand further confirmed the target-specificity of the **ND@Au-Tf** conjugate. Competition with a molar excess of 5:1 or 20:1 Tf:**ND@Au-Tf** particles resulted in reduced cell uptake, with levels comparable to those observed for non-targeted **ND@Au-nT**. This indicates that the **ND@Au-Tf** particles indeed target the cells, and binding can be attributed to specific interactions between TfR and **ND@Au-Tf** (Supporting Information Figure S2).

Next, we sought to investigate the cellular fates of **ND@Au-Tf** and **ND@Au-nT**, specifically addressing whether the ND formulations would be taken up into cells. Cell membranes and nuclei were stained, and Z-stacked (0.3 micrometer/steps) confocal images were recorded. Data indicate that after a 3-hour incubation period, both **ND@Au-Tf** and **ND@Au-nT** formulations were bound to cell membranes (data not shown). Interestingly, after a 16-hour incubation period, **ND@Au-Tf** appeared intracellularly, whereas **ND@Au-nT** particles co-registered with the cell membrane (**Figure 5**), indicating that although both formulations are able to bind to cellular membranes, only **ND@Au-Tf** are internalized. Because our cell binding studies showed that **ND@Au-Tf** particles specifically bind TfR, **ND@Au-Tf** internalization is

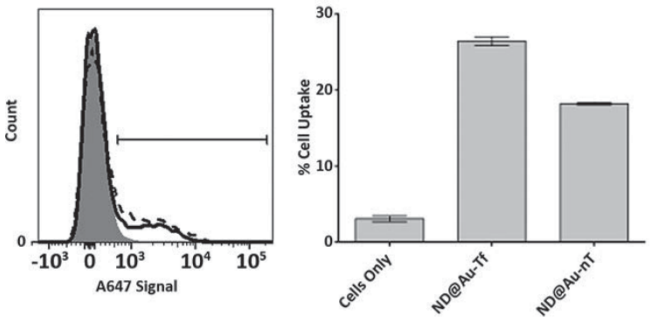

Figure 4. SKBR3 cell interactions with particles determined by flow cytometry. Left histogram: gray, cells only; dashed, **ND@Au-Tf**; solid, **ND@Au-nT**. Right graph: Statistical analysis showing percent cellular uptake (positive cells shown on histogram by gate) for each sample. Error bars indicate standard deviation. Experiments were conducted in triplicate, and 10 000 gated events were analyzed. Student's *t*-test indicates significant differences comparing targeted **ND@Au-Tf** and non-targeted **ND@Au-nT** formulations ($p < 0.05$).

likely mediated by TfR endocytosis. Co-localization studies were carried out, further indicating that non-targeted **ND@Au-nT** are co-localized with the cell membrane with Mander's coefficient M2 = 0.99. In stark contrast, only a fraction of the targeted **ND@Au-Tf** formulation remained bound to the cell membrane (M2 = 0.21), while the remainder translocated inside the cell. Our flow cytometry and confocal imaging results are in agreement, and the data support **ND@Au-Tf** targeting of TfR on cancer cells, leading to receptor-mediated internalization.

2.5. Toxicity Study

The toxicity of the **ND@Au-Tf** particles themselves was investigated in SKBR3 cells, using an XTT cell proliferation assay. After 3- or 24-hour incubation with **ND@Au-Tf** particles, we did not observe significant differences in cell viability compared to non-treated cells, indicating that **ND@Au-Tf** particles are not cytotoxic (Supporting Information Figure S3).

2.6. Laser Ablation

The ability of GNSs to kill cancer cells upon red laser irradiation was demonstrated in vitro. HeLa cells were incubated with **Nd@Au-Tf**, and after successive washing, irradiated with a Ti:Sapphire pulse laser. After a one-minute irradiation, cells were incubated for 24 hours, and their viability was estimated using luciferase assay (**Figure 6**). Exposing HeLa cells to **ND@Au-Tf** did not affect their viability, supporting the non-toxicity of these particles. Laser irradiation of cells also had no influence on their viability. Only cells exposed to both nanoparticles and laser were affected and—after only one minute of irradiation—completely killed. The laser power we used (37 W/cm^2) was of the same order of magnitude as values described in the literature for in vitro experiments.[9,10,47]

3. Conclusion

In summary, we synthesized a novel plasmonic nanomaterial consisting of a diamond core coated with a silica layer and encapsulated with a thin GNS. PEG chains were attached to the surface of GNSs using lipoic acid as an anchor. The other ends of the PEG chains were further functionalized with Alexa Fluor 647 and modified transferrin via click chemistry. Transferrin-labeled ND-based GNSs (**ND@Au-Tf**) target transferrin receptors, which are overexpressed on many cancer cell types. We found that **ND@Au-Tf** bind and are internalized into human SKBR3 breast cancer cells and HeLa cervical cancer cells. Cell viability assays were also conducted using XTT assay; toxic effects were not observed after 3- or 24-hour incubation periods. We also demonstrated the ability of the prepared GNSs to kill cancer cells upon red laser irradiation in vitro. HeLa cells were completely killed after a one-minute irradiation with a pulse 750-nm pulse laser (37 W/cm^2), while no harm was caused to cells by irradiation itself or by the presence of GNSs without irradiation.

This work lays the foundation for the multi-step synthetic route leading to ND core plasmonic nanoparticles and is the first stepping stone toward translational research. Future work will focus on targeted therapeutic studies of plasmonic NDs in vivo. Specifically, studies will set out to gain an understanding on the therapeutic efficacy in the context of biodistribution and overall biocompatibility of the materials. At the same time, studies will assess the photophysical interactions of the fluorescent nitrogen-vacancy (NV) centers in NDs with the gold plasmonic shell.

It is well recognized that cancer nanotechnology holds great promise in modern medicine, and several nanoparticles have advanced into clinical application.[48–50] While the development pipeline with new nanomaterial-based technologies is moving rapidly, the fundamenal understanding of the nanomaterial's in vivo fate; i.e., the biodistribution, clearance or persistence, pharmacokinetics and pharmacodynamics, is often lacking. However, detailed understanding of the biological behaviour, the interplay of tissue-targeting and immune surveillance in the context of imaging sensitivity and therapeutic efficacy, is imperative for rapid clinical viability and success of plasmonic nanostructures.[51] The combined knowledge of the biological properties and diagnostic/therapeutic potential will help identify a suitable nitch application harnessing the unique properties of the proposed material.

4. Experimental Section

Chemicals and Solvents: The NHS ester of lipoic acid was prepared according to a previously published procedure.[52] H_2N-PEG(5000)-alkyne was purchased from Iris Biotech. Alexa Fluor 647-azide was purchased from Invitrogen. Tetrakis(hydroxymethyl)phosphonium chloride (THPC)

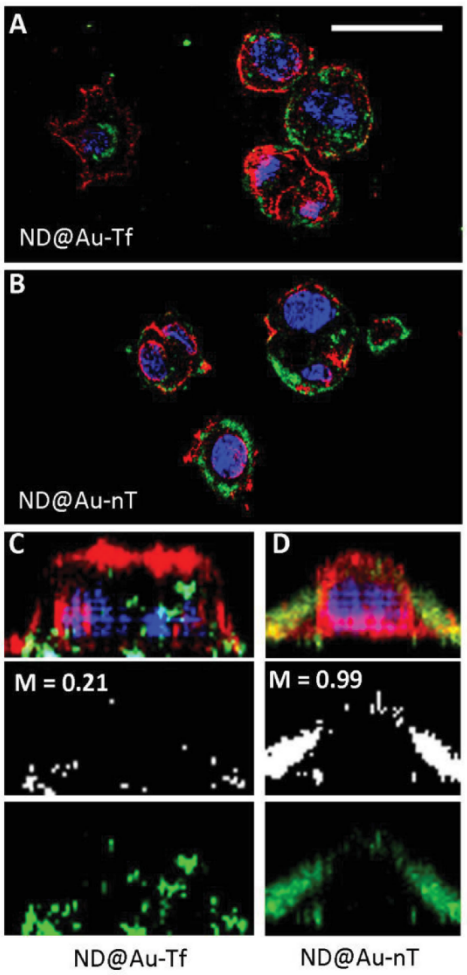

Figure 5. SKBR3 cell interactions with particles observed by confocal microscopy. The particles were incubated with SKBR3 cells for 16 h, fixed, stained, and imaged. **ND@Au-Tf** (A+C) and **ND@Au-nT** (B+D) are pseudo-colored in green (imaged based on the Alexa Fluor 647 label), nuclei are shown in blue (stained with DAPI), and cell membranes are shown in red (stained with WGA-A555); the scale bar is 30 μm. C+D shows 3D reconstruction of single cells: the top panel shows all channels, the middle panel depicts co-localization of the particles and WGA signals (M = Mander's coefficient of co-localization determined using ImageJ software), and the bottom panel shows ND signals.

and tetraethyl orthosilicate (TEOS) were purchased from Sigma-Aldrich. $HAuCl_4$ was purchased from Alfa Aesar.

UV–Vis Spectroscopy: The spectra were recorded with a Specord 210 (Analytik Jena) spectrometer in the 400–1000 nm range at room temperature with an optical path of 1 cm.

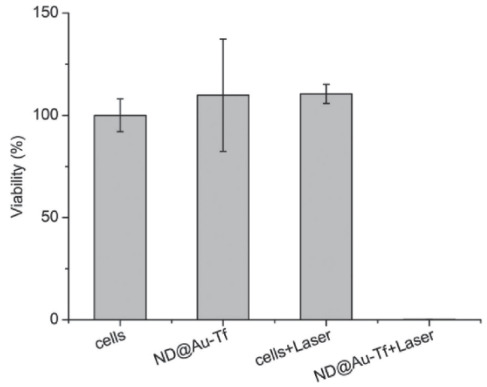

Figure 6. Laser ablation of HeLa cells incubated with **ND@Au-Tf** nanoparticles. Cell viability was estimated by luciferase assay with 24 h delay after 1 min irradiation with 37 W/cm^2 intensity. The viability of cells treated with **ND@Au-Tf** and laser was ≈0.15%.

Dynamic Light Scattering: For stability studies in buffers, DLS was recorded with a Zetasizer Nano ZS system (Malvern Instruments) at 25 °C. The particle concentration was 0.3 mg/mL (10 μg ND/mL).

Electron Microscopy: Bright field TEM experiments were performed with a JEOL JEM-1011 electron microscope operated at 60 kV and equipped with a Veleta side-mounted camera. Carbon coated grids (Pyser) were used in all cases. Nanodiamond samples were prepared according to a previously published procedure.[53] Other samples were prepared as follows: a 3 μL droplet of particle dispersion (0.2 mg/mL) was placed on the grid and gently removed with a piece of tissue after 1 min incubation. Tilt series of 2-dimensional projection images for electron tomography were acquired using a FEI Tecnai G^2 transmission electron microscope operated at 200 kV in scanning transmission electron microscopy (STEM) mode. To prepare the samples, a drop of diluted colloidal solution was placed on a carbon-coated copper grid and left to dry. The high angle annular dark field (HAADF-STEM) image series was acquired using a single tilt tomography holder (Fischione 2020) over the angular range (–64°,+76°) with step increments of 2°. The alignment and 3D reconstruction were carried out with FEI Inspect3D software. Quantification of the 3D data was performed using MATLAB codes.

Synthesis of LA-PEG-alkyne: Synthesis was performed according to published procedures,[36,54] with some modifications. Briefly, H_2N-PEG(5000)-alkyne (50 mg, 10 μmol) was dissolved in DCM (1 mL) and mixed with LA-NHS (50 mg, 165 μmol). The reaction mixture was stirred overnight, then washed 3 times with 10 mL hot water. The combined aqueous fractions were purified using a Millipore Ultracel 3K separation tube (washed 3 times with 20 mL water). TLC: MeOH:triethylamine 100:5 (R_f = 0.5), visualized with $Co(NCS)_x$ and $KMnO_4$ (no reaction with ninhydrin). H_2N-PEG(5000)-alkyne R_f < 0.3, visualized with ninhydrin and $Co(NCS)_x$ (no reaction with $KMnO_4$). ^{1}H NMR (400 MHz, $CDCl_3$, δ): 1.6 (m, 2H), 1.7–1.9 (m, 3H), 2.0 (m, 1H), 2.1 (t, 1H, J = 3.6 Hz), 2.2–2.4 (m, 4H), 2.5 (t, 2H, J = 7.2 Hz), 2.6 (m, 3H), 3.2–3.3 (m, 2H), 3.5–3.9 (m, ~240H), 3.9 (t, 1H, J = 5.2).

4.1. Transferrin-Azide (Tf-Azide)

Preparation: (see Figure 3A) We used a procedure similar to that previously described for preparation of transferrin-alkyne.[44] $NaIO_4$ solution was slowly added to a cooled solution of human holo-transferrin (30 mg, 390 nmol; 2 mg/mL) in acetate buffer (0.1 M, pH 5.5) to a final $NaIO_4$ concentration of 1 mM. The mixture was incubated

on ice in the dark for 30 min. The solution containing Tf-aldehyde was concentrated six times in an ultrafiltration cell (from 70 mL to 5 mL). HEPES buffer (0.1 M, pH 7.2) was used to refill the volume. Tf-aldehyde was incubated with 3-aminooxypropyl-1-azide (16.2 mg, 140 μmol) in HEPES buffer with dimethyl sulfoxide (DMSO, 20%, total volume of 17 mL) for 5 h at room temperature with gentle mixing. Removal of excess 3-aminooxypropyl-1-azide was performed by ultrafiltration (70 mL to 5 mL, repeated six times) in HEPES buffer (0.1 M, pH 8). The solution was freeze-dried to obtain **Tf-azide**.

Characterization: The presence of a reactive azide group in **Tf-azide** was tested by reaction with fluorescein-alkyne. All solutions were aqueous except the fluorescein-alkyne stock, which was prepared in DMSO. The solutions were mixed to achieve the following final concentrations: 0.02 mM**Tf-azide**, 0.075 mM fluorescein-alkyne, 0.17 mM $CuSO_4{\cdot}5H_2O$, 0.33 mM tris(3-hydroxypropyltriazolylmethyl) amine (THPTA), and 5 mM sodium ascorbate. The solutions of $CuSO_4{\cdot}5H_2O$ and THPTA were premixed (in a 1:2 molar ratio) before adding to the reaction mixture. The reaction mixture was well-sealed after adding sodium ascorbate, mixed, and reacted for 2 h with no stirring. The reaction product (**Tf-Fl**) was analyzed by SDS-PAGE (for details, see ESI). All samples (**Tf**, **Tf-azide**, and **Tf-Fl**) were of the same molecular weight, and only **Tf-Fl** can be seen under UV-lamp (Supporting Information Figure S1).

4.2. Nanoshell Preparation

Silica Encapsulation: NDs were solubilized in a manner similar to that described in commonly used procedures.[16,55] Briefly, NDs were treated with a mixture of HNO_3 and H_2SO_4 (85 °C, 3 days), washed with 2 M NaOH and 2 M HCl, washed five times with water, and freeze-dried. Prior to use, the particles were dissolved in water (2 mg/mL) and sonicated with a probe (Cole-Parmer, 750 W) for 30 min. The resulting transparent colloid was filtered using a 0.2 μm PVDF microfilter to provide a colloidal solution of ND particles. A modified version[31] of previously described general procedure[56] was used to coat NDs with silica shells. Polyvinylpyrrolidone (96 mg, 9.6 μmol) was dissolved in water (204 mL) and sonicated for 10 min in an ultrasonic bath. ND colloid (6 mL, 2 mg/mL) was added, and the mixture was stirred for 24 h. The colloid was then concentrated via centrifugation in two steps. In the first step (40 000 rcf, 1 h), the volume was reduced to approximately 12 mL. The second centrifugation step (30 000 rcf, 30 min) was performed in microvials and reduced the solvent volume to approximately 0.4 mL. Sedimented NDs were resuspended in ethanol (12 mL) in a round bottom flask and sonicated in an ultrasonic bath for 2–4 min. TEOS (112 mg, 539 μmol) was added. After 2 min of vigorous stirring, ammonia solution (25%, 500 μL) was added, and the reaction mixture was stirred for 14 h, affording silica-coated particles **ND@Sil**. The product was purified by centrifugation (14 000 rcf, 5 min) with ethanol (12 mL, 4×) and MeCN (12 mL, 2×) and was dissolved in 6 mL MeCN. **ND@Sil** particles were stored in the freezer (–18 °C) as a stable colloid for several months without changes in particle characteristics (confirmed with TEM and DLS) or reactivity.

GNS Formation: GNSs were prepared according to modified published procedures.[32–34] First, seeding gold colloid was prepared. Water (45 mL) was mixed with NaOH (5 mL, 0.1 M). Tetrakis(hydroxymethyl) phosphonium chloride (THPC, 67.2 μmol in 1 mL water) was added. After exactly 5 min, $HAuCl_4$ solution (2 mL of a 1% w/w solution in water, 59 μmol) was added in one portion under vigorous stirring. The mixture was stirred for 10 min, and the resulting gold colloid was aged at 4 °C for 2 weeks without purification. **ND@Sil** particles (1 mL MeCN dispersion, 2 mg ND content, 8 mg total **ND@Sil** weight) were mixed with 2-week aged gold colloid (30 mL). The pH of the mixture was adjusted to 3. The mixture was gently stirred for 20 min and then kept at 4 °C for 16 h. **ND@Sil** particles coated with gold seeds were isolated by centrifugation (2500 rcf, 1 h) and washed twice with water (30 mL, isolated at 2500 rcf, 1 h). The volume of the dispersion was adjusted to 5 mL. K_2CO_3 (200 mg, 1.44 mmol) was dissolved in 800 mL water, and $HAuCl_4$ solution (12 mL of a 1% w/w solution in water, 3.5 μmol) was added. The solution was stirred for 24 h in the dark. Then, the pH of the solution was adjusted to 9.0. Gold-seeded **ND@Sil** dispersion (1.25 mL; 0.5 mg ND content) was added to 200 mL solution. A stream of CO was bubbled through the solution for 2 min under vigorous stirring. The color changed from transparent to red, purple, and then dark blue. Gold encapsulated **ND@Sil** (**ND@Au**) were separated by centrifugation at 20 rcf overnight and concentrated to 2.5 mL. The total mass of **ND@Au** particles obtained in one run was on average 15 mg, i.e., 30-fold the mass of ND and 7.5-fold the mass of **ND@Sil**.

PEGylation of **ND@Au**: LA-PEG-alkyne (10.3 mg, 2 μmol) was added to **ND@Au** dispersion (15 mg; corresponds to 0.5 mg ND) in 2.5 mL water. The mixture was sonicated in an ultrasonic bath for 20 min, then stirred overnight and sonicated for another 20 min. PEG-coated **ND@Au** particles were separated by centrifugation (5×, 500 rcf, 20 min), yielding **ND@Au-PEG**.

Modification with transferrin and Alexa Fluor 647: A solution of Cu-catalyst was prepared in a separate vial by mixing $CuSO_4{\cdot}5H_2O$ (20 μL of a 25 mM solution) and THPTA ligand (20 μL of a 50 mM solution).The click reactions were performed similarly to those described in the literature[57] by mixing reactants in a 0.6 mL vial. **ND@Au-PEG** solution (1.5 mg particles in 125 μL) was mixed with a DMSO solution of Alexa Fluor 647-azide (1.7 μL of a 5.88 mM solution). Other components were added in the following order and quantities: aminoguanidine hydrochloride (12 μL of a 100 mM solution) and Cu-catalyst solution (3.2 μL) (see above). Water was added to adjust the total reaction volume to 200 μL. Sodium ascorbate (12 μL of a 100 mM solution) was added. The vials were well-sealed and kept for 2 h without stirring or shaking. Modified nanoparticles were isolated in near-quantitative yield by centrifugation (500 rcf, 20 min) and washed with water (2×, 1 mL) and PBS (1×, 1 mL) to yield gold-coated NDs tagged with Alexa Fluor 647 (**ND@Au-nT**). **ND@Au-nT** was further modified with Tf-azide in a similar manner. Solid Tf-azide (0.2 mg) was added to nanoparticles, and other components were added in the same quantities and order as in the previous reaction step. After centrifugal separation, **ND@Au-Tf** was obtained.

Stability Experiments: A colloidal aqueous solution of **ND@Au-PEG** (1.5 mg/mL, 100 μL) was added to buffer (900 μL). The following buffers were used: PBS (pH = 7.5), 0.15 M NaCl, 0.3 M NaCl, and cell growth medium (RPMI-1640 + serum). The samples were stored at 25 °C, and the aggregation state was examined with DLS 2 h, 1 day, and 1 month after mixing. Ten minutes before each measurement, samples were sonicated in a bath for 20 s.

4.3. Cell Studies

Flow Cytometry: SKBR3 cells were cultured in McCoy's 5A media supplemented with 10% (v/v) fetal bovine serum (FBS), 1% (v/v) penicillin-streptomycin, and 1% (v/v) L-glutamine at 37 °C and 5% CO_2 (all reagents were obtained from Invitrogen). Cells (100 000 cells/500 μL media/well) were added to untreated 24-well plates and incubated overnight. The following day, triplicates of i) culture medium alone (negative control), ii) gold-coated NDs tagged with Alexa Fluor 647 (**ND@Au-nT**), and iii) gold-coated NDs tagged with Alexa Fluor 647 and transferrin (**ND@Au-Tf**) were added. Particle concentrations were approximately 1×10^{12} particles/mL (1.2 mg particles per 1 mL, 300 μL final volume; 3×10^6 particles/cell) in culture medium. Particles were incubated with cells for 3 h. (Competition binding assays were also carried out: **ND@Au-Tf** were incubated with free Tf added to the medium in a molar excess of 5:1 or 20:1, see Supporting Information). Following incubation, cells were washed three times with 0.09% (w/v) saline to remove non-bound particles remaining in solution. Cells were removed using 200 μL enzyme-free Hank's based cell dissociation buffer (Gibco), added to untreated 96-well v-bottom plates, and centrifuged at 500 g for 4 min. The supernatant was removed. Cells were then washed in FACS buffer (0.1 mL of 0.5 M EDTA, 0.5 mL FBS, and 1.25 mL of 1 M HEPES, pH 7.0, in 50 mL Ca^{2+}- and Mg^{2+}-free PBS). Washing was repeated twice.

Cells were fixed in 2% (v/v) paraformaldehyde in FACS buffer at room temperature for 10 min and washed twice. Samples were analyzed using a BD LSR II flow cytometer, with a total of 10,000 gated events collected per sample. FlowJo 10.0.00003 software was used for data analysis.

Confocal Microscopy: SKBR3 cells (25 000 cells/500 µL media/well) were added to coverslips, which were placed in untreated 24-well plates and incubated overnight. The following day, duplicates of i) no particles, ii) **ND@Au-nT**, and iii) **ND@Au-Tf** were added at concentrations of approximately 1×10^{12} particles/mL (1.2 mg particles per 1 mL, 300 µL final volume, 1.2×10^{7} particles/cell) and incubated with the cells for 16 h. Following incubation, cells were washed three times with 0.09% (w/v) saline to remove excess particles. Samples were fixed in 5% (v/v) paraformaldehyde and 0.3% (v/v) gluteraldehyde in Dulbecco's PBS (Fisher) for 10 min at room temperature. Cells were blocked in 5% (v/v) goat serum (Invitrogen) for 90 min at room temperature. Cell membranes were stained using 1 µg/mL wheat germ agglutinin-A555 (Invitrogen) and 1% (v/v) goat serum in Dulbecco's PBS for 45 min at room temperature. Cell nuclei were stained using 4'6'-diamidino-2-phenylindole (DAPI) (MP Biomedicals) diluted 1:9,500 in Dulbecco's PBS for 15 min at room temperature. In between each step, cells were washed three times with Dulbecco's PBS. Slides were mounted using Permount mounting media (Fisher). Confocal analysis was performed using the Olympus FV1000 laser scanning confocal microscope and a 40x objective. Images were analyzed using ImageJ 1.43u software.

XTT Cell Proliferation Assay: SKBR3 cells (25,000 cells, 200 µL media per well) were added to 96-well plates and incubated at 37 °C under 5% CO_2 overnight. The following day, **ND@Au-Tf** particles were added at a concentration of approximately 1×10^{12} particles/mL (1.2 mg particles per 1 mL, 75 µL final volume, 3×10^{6} particles/cell); control cells with no added particles were also set up. Following a 3 or 24 h incubation, wells were washed three times with 0.09% (w/v) saline to remove unbound NDs. Then, 200 µL fresh media was added, and cells were returned to incubate for an additional 24 h. An XTT cell proliferation assay (ATCC) was used to assess cellular viability; the protocol was performed according to the manufacturer's instructions. A Tecan Infinite 200 plate reader was used to measure the absorbance, and percent viability was determined by normalizing to the cell-only control.

Laser Ablation Experiments: Human cervical adenocarcinoma (HeLa) cells (ATCC® CCL-2™) were cultured in RPMI 1640, Dutch modification medium supplemented with 10% (v/v) heat-inactivated fetal bovine serum (FBS), antibiotics (200 µg/mL streptomycin and 100 U/mL penicillin G) and 2 mM glutamine (all purchased from Sigma-Aldrich) at 37 °C in a humidified atmosphere containing 5% CO_2. Cells were subcultured as needed (2–3 times a week in a subcultivation ratio of 1:5 to 1:8) and harvested from flasks using 0.25% (w/v) trypsin-EDTA. HeLa cells were seeded into a white wall clear bottom 384-well plate in 30 µL at a density of 3000 cells/well. Then, cells were grown for 48 h under standard conditions (37 °C and 5% CO_2) before adding **ND@Au-Tf** nanoparticles at a final amount of approximately 2×10^{11} (240 µg of particles per 1 mL) in tetraplicates. After 24 h of treatment with or without nanoparticles, the medium was removed, and the cells were thoroughly washed with fresh medium (three times). Then, the medium in each well was replaced with PBS, and selected wells were illuminated immediately (Ti:Sapphire laser – 75 MHz, 750 nm, pumped at 532 nm by ND:YAG, laser power of 2.1 W, spot diameter of 2.7 mm, irradiation time of 60 sec). After irradiation, PBS was replaced with a fresh complete growth medium (30 µL), and the plate was incubated for an additional 24 h before viability measurement. Cell viability was determined using the CellTiter-Glo Luminescent Cell Viability Assay (Promega, Madison, WI, USA), which is based on quantification of the ATP present in cell lysates, according to the manufacturer's protocol. Briefly, the 384-well plate and its contents were equilibrated at room temperature for 30 min. CellTiter-Glo reagent was prepared by reconstituting the lyophilized enzyme/substrate mixture with CellTiter-Glo buffer equilibrated to room temperature. After an equal volume of CellTiter-Glo reagent was added to the wells (30 µL), the plate was shaken for 2 min on an orbital shaker (500 RPM) to induce cell lysis. Luminescence was recorded after an additional 10 min incubation in the dark using the multimode microplate reader Tecan Infinite M1000 (Tecan Austria GmbH, Grödig, Austria). Blank wells (containing medium without cells) were measured for luminescence and deducted from the values obtained from experimental wells (background luminescence). The viability values of treated cells were expressed as percentages of the values obtained for the corresponding control cells. Values (of the luminescent signal) represent the mean ± S.D. of four replicates obtained from two independent experiments.

Supporting Information

Supporting Information is available from the Wiley Online Library or from the author.

Acknowledgements

I. Rehor and K. L. Lee contributed equally to this work. This work was supported by GACR project P108/12/0640, MSMT CR grant no. LH11027, the National Science Foundation, CMMI NM 333651 (to NFS), a NCI R25 CA148052 Cancer Pharmacology training grant (KLL), and NPU I project LO 1302 from Ministry of Education (MH). Part of this work was performed within OPPK project CZ.2.16/3.1.00/24016. S.B. acknowledges financial support from the European Research Council (ERC Starting Grant #335078-COLOURATOMS).

Received: July 19, 2014
Revised: September 3, 2014
Published online: October 21, 2014

[1] N. G. Khlebtsov, L. A. Dykman, *J. Quant. Spectrosc. Radiat. Transf.* **2010**, *111*, 1.
[2] M. R. Jones, K. D. Osberg, R. J. Macfarlane, M. R. Langille, C. A. Mirkin, *Chem. Rev.* **2011**, *111*, 3736.
[3] M. C. Daniel, D. Astruc, *Chem. Rev.* **2004**, *104*, 293.
[4] A.-I. Henry, J. M. Bingham, E. Ringe, L. D. Marks, G. C. Schatz, R. P. Van Duyne, *J. Phys. Chem. C* **2011**, *115*, 9291.
[5] A. Agrawal, S. Huang, A. Wei Haw Lin, J. K. Barton, R. A. Drezek, T. J. Pfefer, M.-H. Lee, *J. Biomed. Opt.* **2006**, *11*, 041121.
[6] J. C. Y. Kah, T. H. Chow, B. K. Ng, S. G. Razul, M. Olivo, C. J. R. Sheppard, *Appl. Opt.* **2009**, *48*, D96.
[7] Y.-S. Chen, W. Frey, S. Kim, P. Kruizinga, K. Homan, S. Emelianov, *Nano Lett.* **2011**, *11*, 348.
[8] J. M. Stern, J. Stanfield, W. Kabbani, J.-T. Hsieh, J. A. Cadeddu, *J. Urol.* **2008**, *179*, 748.
[9] W. Lu, C. Xiong, G. Zhang, Q. Huang, R. Zhang, J. Z. Zhang, C. Li, *Clin. Cancer Res.* **2009**, *15*, 876.
[10] X. Huang, I. H. El-Sayed, W. Qian, M. A. El-Sayed, *J. Am. Chem. Soc.* **2010**, *128*, 2115.
[11] G. Wu, A. Mikhailovsky, H. A. Khant, C. Fu, W. Chiu, J. A. Zasadzinski, *J. Am. Chem. Soc.* **2008**, *130*, 8175.
[12] R. Bardhan, S. Mukherjee, N. A. Mirin, S. D. Levit, P. Nordlander, N. J. Halas, *J. Phys. Chem. C* **2010**, *114*, 7378.
[13] R. Bardhan, S. Lal, A. Joshi, N. J. Halas, *Acc. Chem. Res.* **2011**, *44*, 936.
[14] A. M. Gobin, M. H. Lee, N. J. Halas, W. D. James, R. A. Drezek, J. L. West, *Nano Lett.* **2007**, *7*, 1929.
[15] E. K. Chow, X.-Q. Zhang, M. Chen, R. Lam, E. Robinson, H. Huang, D. Schaffer, E. Osawa, A. Goga, D. Ho, *Sci Transl Med* **2011**, *3*, 73ra21.
[16] V. Vaijayanthimala, P.-Y. Cheng, S.-H. Yeh, K.-K. Liu, C.-H. Hsiao, J.-I. Chao, H.-C. Chang, *Biomaterials* **2012**, *33*, 7794.

[17] Y. Y. Hui, C. L. Cheng, H. C. Chang, *J. Phys. Appl. Phys.* **2010**, *43*, 374021.
[18] J. Slegerova, M. Hajek, I. Rehor, F. Sedlak, J. Stursa, M. Hruby, P. Cigler, *Nanoscale* **2014**, DOI: 10.1039/C4NR02776K.
[19] J. Slegerova, I. Rehor, J. Havlik, H. Raabova, E. Muchova, P. Cigler, in *Intracellular Delivery II*, (Eds: A. Prokop, Y. Iwasaki, A. Harada), Dordrecht: Springer, Netherlands **2014**, 363.
[20] T.-S. Lim, C.-C. Fu, K.-C. Lee, H.-Y. Lee, K. Chen, W.-F. Cheng, W. W. Pai, H.-C. Chang, W. Fann, *Phys. Chem. Chem. Phys.* **2009**, *11*, 1508.
[21] S. Schietinger, M. Barth, T. Aichele, O. Benson, *Nano Lett.* **2009**, *9*, 1694.
[22] Y. Y. Hui, Y.-C. Lu, L.-J. Su, C.-Y. Fang, J.-H. Hsu, H.-C. Chang, *Appl. Phys. Lett.* **2013**, *102*, 013102.
[23] M. Barth, S. Schietinger, T. Schröder, T. Aichele, O. Benson, *J. Lumin.* **2010**, *130*, 1628.
[24] G. Chen, Y. Liu, M. Song, B. Wu, E. Wu, H. Zeng, *IEEE J. Sel. Top. Quantum Electron.* **2013**, *19*, 4602404.
[25] Y. Chi, G. Chen, F. Jelezko, E. Wu, H. Zeng, *IEEE Photonics Technol. Lett.* **2011**, *23*, 374.
[26] I. Rehor, H. Mackova, S. K. Filippov, J. Kucka, V. Proks, J. Slegerova, S. Turner, G. Van Tendeloo, M. Ledvina, M. Hruby, P. Cigler, *ChemPlusChem* **2014**, *79*, 21.
[27] B. Zhang, C.-Y. Fang, C.-C. Chang, R. Peterson, S. Maswadi, R. D. Glickman, H.-C. Chang, J. Y. Ye, *Biomed. Opt. Express* **2012**, *3*, 1662.
[28] H. Ismaili, M. S. Workentin, *Chem. Commun.* **2011**, *47*, 7788.
[29] L.-C. Cheng, H. M. Chen, T.-C. Lai, Y.-C. Chan, R.-S. Liu, J. C. Sung, M. Hsiao, C.-H. Chen, L.-J. Her, D. P. Tsai, *Nanoscale* **2008**, *5*, 3931.
[30] Y. L. Liu, K. W. Sun, *Appl. Phys. Lett.* **2011**, *98*, 153702.
[31] I. Rehor, J. Slegerova, J. Kucka, V. Proks, V. Petrakova, M.-P. Adam, F. Treussart, S. Turner, S. Bals, P. Sacha, M. Ledvina, A. M. Wen, N. F. Steinmetz, P. Cigler, *Small* **2014**, *10*, 1106.
[32] B. E. Brinson, J. B. Lassiter, C. S. Levin, R. Bardhan, N. Mirin, N. J. Halas, *Langmuir* **2008**, *24*, 14166.
[33] S. Oldenburg, R. Averitt, S. Westcott, N. Halas, *Chem. Phys. Lett.* **1998**, *288*, 243.
[34] M. R. Rasch, K. V. Sokolov, B. A. Korgel, *Langmuir* **2009**, *25*, 11777.
[35] A. Prokop, J. M. Davidson, *J. Pharm. Sci.* **2008**, *97*, 3518.
[36] B. C. Mei, K. Susumu, I. L. Medintz, J. B. Delehanty, T. J. Mountziaris, H. Mattoussi, *J. Mater. Chem.* **2008**, *18*, 4949.
[37] S. I. Presolski, V. P. Hong, M. G. Finn, *Curr. Protoc. Chem. Biol.* **2011**, *3*, 153.
[38] T. R. Daniels, T. Delgado, G. Helguera, M. L. Penichet, *Clin. Immunol.* **2006**, *121*, 159.
[39] T. R. Daniels, E. Bernabeu, J. A. Rodríguez, S. Patel, M. Kozman, D. A. Chiappetta, E. Holler, J. Y. Ljubimova, G. Helguera, M. L. Penichet, *Biochim. Biophys. Acta BBA – Gen. Subj.* **2012**, *1820*, 291.
[40] R. K. Huang, N. F. Steinmetz, C.-Y. Fu, M. Manchester, J. E. Johnson, *Nanomedicine* **2006**, *6*, 55.
[41] H. Iinuma, K. Maruyama, K. Okinaga, K. Sasaki, T. Sekine, O. Ishida, N. Ogiwara, K. Johkura, Y. Yonemura, *Int. J. Cancer* **2002**, *99*, 130.
[42] M.-F. Weng, B.-J. Chang, S.-Y. Chiang, N.-S. Wang, H. Niu, *Diam. Relat. Mater.* **2012**, *22*, 96.
[43] B.-M. Chang, H.-H. Lin, L.-J. Su, W.-D. Lin, R.-J. Lin, Y.-K. Tzeng, R. T. Lee, Y. C. Lee, A. L. Yu, H.-C. Chang, *Adv. Funct. Mater.* **2013**, *23*, 5737.
[44] D. Banerjee, A. P. Liu, N. R. Voss, S. L. Schmid, M. G. Finn, *ChemBioChem* **2010**, *11*, 1273.
[45] K. A. Kang, J. Wang, J. B. Jasinski, S. Achilefu, *J. Nanobiotechnology* **2011**, *9*, 16.
[46] P. G. de Gennes, *Adv. Colloid Interface Sci.* **1987**, *27*, 189.
[47] R. J. Bernardi, A. R. Lowery, P. A. Thompson, S. M. Blaney, J. L. West, *J. Neurooncol.* **2008**, *86*, 165.
[48] O. C. Farokhzad, R. Langer, *ACS Nano* **2009**, *3*, 16.
[49] M. Ferrari, *Nat. Rev. Cancer* **2005**, *5*, 161.
[50] E. K.-H. Chow, D. Ho, *Sci. Transl. Med.* **2013**, *5*, 216rv4.
[51] J. A. Webb, R. Bardhan, *Nanoscale* **2014**, *6*, 2502.
[52] M. Howarth, W. Liu, S. Puthenveetil, Y. Zheng, L. F. Marshall, M. M. Schmidt, K. D. Wittrup, M. G. Bawendi, A. Y. Ting, *Nat. Methods* **2008**, *5*, 397.
[53] I. Rehor, P. Cigler, *Diam. Relat. Mater.* **2014**, *46*, 21.
[54] K. Susumu, B. C. Mei, H. Mattoussi, *Nat. Protoc.* **2009**, *4*, 424.
[55] N. Mohan, C.-S. Chen, H.-H. Hsieh, Y.-C. Wu, H.-C. Chang, *Nano Lett.* **2010**, *10*, 3692.
[56] C. Graf, D. L. J. Vossen, A. Imhof, A. van Blaaderen, *Langmuir* **2003**, *19*, 6693.
[57] V. Hong, S. I. Presolski, C. Ma, M. G. Finn, *Angew. Chem. Int. Ed.* **2009**, *48*, 9879.

ADVANCED HEALTHCARE MATERIALS

Supporting Information

for *Adv. Healthcare Mater.*, DOI: 10.1002/adhm.201400421

Plasmonic Nanodiamonds: Targeted Core–Shell Type Nanoparticles for Cancer Cell Thermoablation

Ivan Rehor, Karin L. Lee, Kevin Chen, Miroslav Hajek, Jan Havlik, Jana Lokajova, Milan Masat, Jitka Slegerova, Sourabh Shukla, Hamed Heidari, Sara Bals, Nicole F. Steinmetz, and Petr Cigler**

Supporting Information

Plasmonic Nanodiamonds – Targeted Core-shell Type Nanoparticles for Cancer Cell Thermoablation

Ivan Rehor, Karin L. Lee, Kevin Chen, Miroslav Hajek, Jan Havlik, Jana Lokajova, Milan Masat, Jitka Slegerova, Sourabh Shukla, Hamed Heidari, Sara Bals, Nicole F. Steinmetz, Petr Cigler**

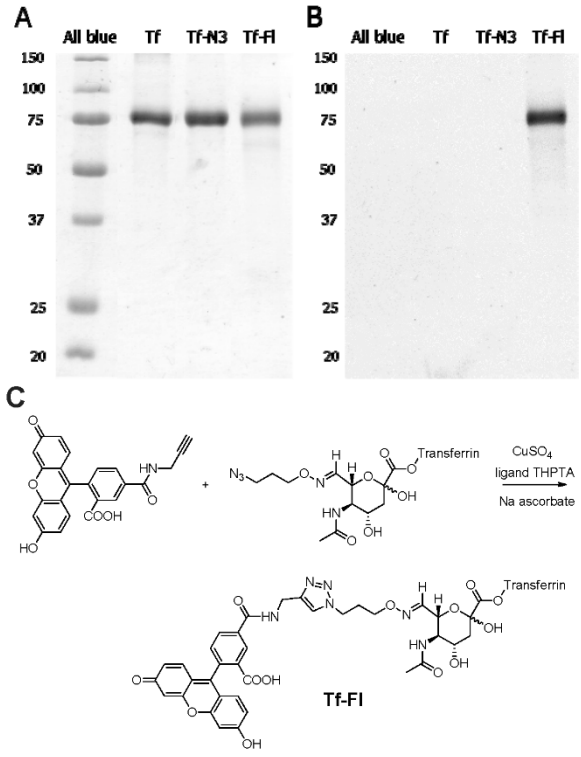

Figure S1. SDS-PAGE of Tf-Fl. (A) 14% SDS-PAGE gel stained with Coomassie Brilliant Blue. From left to right, the lanes contain 4 µL each of Precision Plus Protein All blue standards, **Tf**, **Tf-azide** (Tf-N3), and **Tf-Fl**. (B) Photograph of the gel under UV lamp (before staining). (C) Reaction scheme of **Tf-azide** with fluorescein-alkyne, yielding **Tf-Fl**.

Details of SDS-PAGE analysis: Aliquots (25 µl) of twice-diluted samples (Tf, Tf-azide, and Tf-Fl; 0.01 mM) were mixed with 5 µL sample buffer and boiled for 5 min. We loaded 4 µL portions of the mixtures to the gel.

Resolving gel (14%): 313 mM Tris-HCl, pH 8.8; 13.3% acrylamide; 0.37% N,N′-methylene-bisacrylamide; 0.1% sodium dodecylsulfate (SDS); 0.001% tetramethylethylendiamine; 0.1% ammonium persulfate
Stacking gel (6.6%): 250 mM Tris-HCl, pH 6.8; 6.42% acrylamide, 0.18% N,N′-methylene-bisacrylamide; 0.1% SDS; 0.005% tetramethylethylendiamine; 0.1% ammonium persulfate
Sample buffer: 50 mM Tris-HCl, pH 6.8; 30% glycerol; 10% SDS; 6% 2-mercaptoethanol; 0.012% bromphenol blue
Running buffer: 125 mM Tris-HCl, 1.25M glycine, 0.5% SDS, pH 8.8
Coomassie staining: 0.5% Coomassie Brilliant Blue; 50% methanol; 10% acetic acid
Destaining solution: 10% acetic acid
The gel was stained for 10 min with Coomassie Brilliant Blue and destained overnight. SDS-PAGE was run at 140 V. Figures were processed in Inkscape and the GNU Image Manipulation Program.

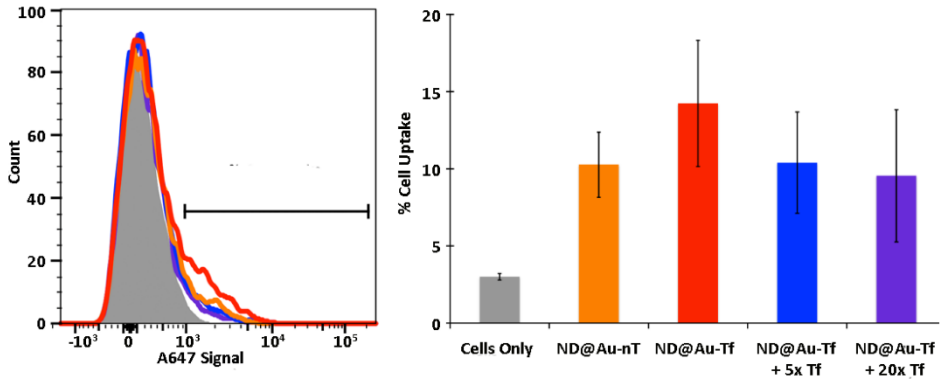

Figure S2. Nanodiamond-SKBR3 cell interactions determined by flow cytometry – competition binding assay. Left: Histograms: gray, cells only; red, **ND@Au-Tf**; orange, **ND@Au-nT**; blue, competition with 5-fold molar excess of free Tf; purple, competition with 20-fold molar excess of free Tf. Right: Statistical analysis showing percent cellular uptake (positive cells shown on histogram by gate) for each sample. Error bars indicate mean ± standard deviation. Experiments were conducted in triplicate, and 10,000 gated events were analyzed.

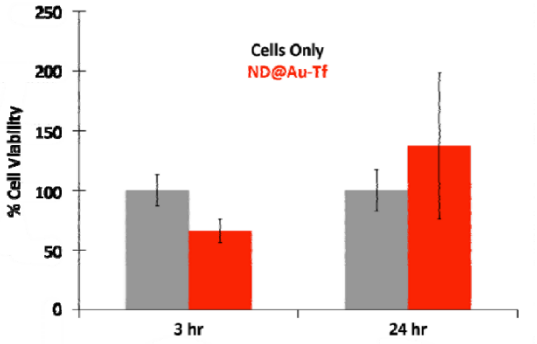

Figure S3. Viability of SKBR3 cells after exposure to ND@Au-Tf. **ND@Au-Tf** (red) were incubated with SKBR3 cells for 3 or 24 h. Cell viability (%) was evaluated using an XTT assay and compared to a cell-only control (gray). Toxicity is not indicated. Although reduced cell viability was indicated for cells exposed to **ND@Au-Tf** for a 3-h time frame, the toxic effects were not statistically significant, nor were toxic effects observed at longer exposure times (24 h).

Appendix G – Publication 7

Torsten Rendler, **Jitka Neburkova**, Ondrej Zemek, Jan Kotek, Andrea Zappe, Zhiqin Chu, Petr Cigler, Joerg Wrachtrup: Optical imaging of localized chemical events using programmable diamond quantum nanosensors, Nature Communications *8*, 14701, **2017**.

nature COMMUNICATIONS

ARTICLE

Received 19 Jul 2016 | Accepted 23 Jan 2017 | Published 20 Mar 2017

DOI: 10.1038/ncomms14701 OPEN

Optical imaging of localized chemical events using programmable diamond quantum nanosensors

Torsten Rendler[1,*], Jitka Neburkova[2,3,*], Ondrej Zemek[4], Jan Kotek[4], Andrea Zappe[1], Zhiqin Chu[1], Petr Cigler[2] & Jörg Wrachtrup[1]

Development of multifunctional nanoscale sensors working under physiological conditions enables monitoring of intracellular processes that are important for various biological and medical applications. By attaching paramagnetic gadolinium complexes to nanodiamonds (NDs) with nitrogen-vacancy (NV) centres through surface engineering, we developed a hybrid nanoscale sensor that can be adjusted to directly monitor physiological species through a proposed sensing scheme based on NV spin relaxometry. We adopt a single-step method to measure spin relaxation rates enabling time-dependent measurements on changes in pH or redox potential at a submicrometre-length scale in a microfluidic channel that mimics cellular environments. Our experimental data are reproduced by numerical simulations of the NV spin interaction with gadolinium complexes covering the NDs. Considering the versatile engineering options provided by polymer chemistry, the underlying mechanism can be expanded to detect a variety of physiologically relevant species and variables.

[1] 3. Physikalisches Institut, Universität Stuttgart, Pfaffenwaldring 57, 70569 Stuttgart, Germany. [2] Institute of Organic Chemistry and Biochemistry of the CAS, Flemingovo nam. 2, 166 10 Prague 6, Czech Republic. [3] First Faculty of Medicine, Charles University, Katerinska 32, 121 08 Prague 2, Czech Republic. [4] Faculty of Science, Department of Inorganic Chemistry, Charles University, Hlavova 2030, 128 43, Prague 2, Czech Republic. * These authors contributed equally to this work. Correspondence and requests for materials should be addressed to Z.Q.C. (email: z.chu@physik.uni-stuttgart.de) or to P.C. (email: cigler@uochb.cas.cz).

Physiological processes inside a living cell are accompanied by transient changes in variables including concentrations of ions[1], reactive oxygen species[2], enzymes[3], nucleic acids[4], pH[5] and redox potential[6]. Although a vast range of sensing principles for these variables based on selective molecular and nanoparticle probes have been developed[7–9], the field is still limited by the chemical and optical stabilities of probes, probe toxicity and perturbation of the biological environment, and, above all, probe sensitivity and spatiotemporal resolution. Therefore, reliable intracellular sensors designed for non-invasive quantitative monitoring of physiologically relevant species with near-atomic resolution are urgently needed to elucidate critical underlying mechanisms in cell biology and physiology, which in turn may lead to new possibilities for diagnostics and therapeutics at the subcellular level.

Nanodiamonds (NDs; nanometre-sized diamond particles) with nitrogen-vacancy (NV) defect centres exhibit excellent biocompatibility[10–12], long-term stability[13,14] and unique quantum sensing capability by optical means[15–17]. These NDs hold great promise for a range of biomedical applications, including serving as nanomedicine platforms for delivery of drugs[18], genes and proteins[19,20], use as fluorescent/photoacoustic imaging agents[13,21,22] and applications in multifunctional intracellular sensing[23–25]. The fluorescence of these atomic-scale NV centres in NDs depends on their electronic spin states, which show a long coherence time even under ambient conditions, enabling direct nanoscale sensing for magnetic/electric field[15,26], temperature[24,27,28] and mechanical force/pressure[29,30]. In fact, the facile optical readout of NV centres in NDs facilitates quantum sensing in living cells[23,24]. However, direct measurement of chemical reactions and processes through quantum detection of NDs remains challenging, especially under physiological conditions. The main challenges lie in developing selective detection principles enabling direct quantum sensing of chemical transformations via spin-dependent fluorescence of NV centres, the related chemical architectures on the ND surface that host the primary sensing system and robust quantum-sensing schemes applied to NV centres in NDs, especially when they are introduced to complicated environments such as the interior of living cells.

A critical step towards developing NDs with biomedical applications is customizing the diamond surface chemistry for required functionalization, while maintaining excellent colloidal stability under physiological conditions[31]. NDs engineered with our recently developed polymer-coating approach[32,33] exhibit long-term colloidal stability, reduced nonspecific binding and the capability for convenient chemical modification. In the current study, we connected macrocyclic complexes of Gd^{3+} ions with a biocompatible copolymer shell on NDs via selectively cleavable linkers. In this sense, the attachment of Gd^{3+} complexes to the polymer is strictly programmed, paving the way for their subsequent detachment in response to changes in a sole parameter. By quantifying the change in NV spin relaxation time due to the Gd^{3+} complexes (spin noise), we show that this platform can be chemically programmed to sense fundamental physiological quantities. We designed and demonstrated time dependent pH and redox potential detection in a microfluidic device with sub-micrometre spatial resolution and minute temporal resolution. In particular, the excellent agreement between our experimental data and theoretical modelling suggests that this scheme can serve as a multifunctional platform for sensing of various chemical and biochemical transformations under physiological conditions with high selectivity (enabled by available libraries of selective cleavage reactions) and unprecedented sensitivity and resolution (yielded by the quantum detection approach).

Results

Design of ND-polymer-Gd multifunctional nanosensors. To enable direct selective quantum detection of chemical processes by means of NV centres, we designed a general nanosensing platform that combines NV centres in NDs and surface polymer coating bearing spin labels. Specifically, complexes of Gd^{3+} ions with electronic spin $S=7/2$ were chemically attached via selectively cleavable linkers to poly[(2-hydroxypropyl)methacrylamide]-based (HPMA) co-polymer chains. Coating of NDs with an HPMA co-polymer shell improves the colloidal stability of the particles, reduces nonspecific interactions with proteins under physiological conditions, maintains the optical properties of NDs and enables further chemical modification[32,33]. The vicinity of Gd^{3+} complexes (spin labels) acting as stochastically fluctuating magnetic fields can be sensed by NV relaxometry[34–37], providing us a novel route to monitor local

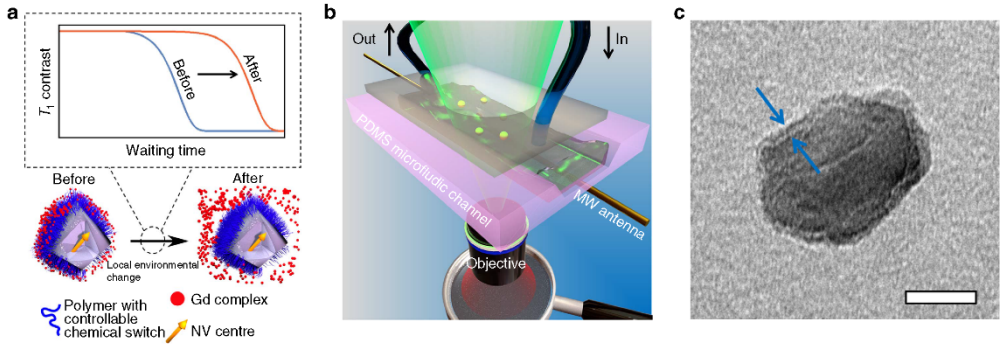

Figure 1 | Basic principle of a ND-based multifunctional sensor. (**a**) Cartoon showing the sensing mechanism of a ND-polymer-Gd hybrid nanosensor in response to a local environmental change. The Gd^{3+} complexes (spin labels attached to the polymer shell on the ND surface) are released after activation of a chemical switch due to a local change, which can be monitored by the change in T_1 relaxation time of NV centres. (**b**) Cartoon showing the experimental setup: polydimethylsiloxane (PDMS) microfluidic channel (pink), pipe system enabling real-time measurement (blue), microwave antenna (gold), optical excitation for NV (green) and fluorescence detection (red). (**c**) Representative TEM image of a polymer-coated ND (ND-HPMA); arrows indicate the polymer shell. Scale bar, 20 nm.

changes. As illustrated in Fig. 1a, the T_1 relaxation time of NV centres in NDs can be quantitatively modulated by the surrounding Gd^{3+} complexes: the more Gd^{3+} complexes loading inside the surface polymer shell, the shorter the T_1 relaxation time. Detachment of Gd^{3+} complexes from the ND particle strongly influences T_1 and can proceed only upon selective cleavage of the linker connecting the complex with the polymer. Importantly, we utilized complexes of Gd^{3+} ions with macrocyclic ligands bearing one phosphonate/phosphinate and three acetate groups, which were originally designed as magnetic resonance imaging (MRI) contrast agents[38]. Thanks to their kinetic inertness and thermodynamic stability, these complexes do not release toxic Gd^{3+} ions under physiological conditions and therefore exhibit excellent biocompatibility and negligible toxicity[39,40]. We developed a convenient synthetic pathway to their modification with cleavable linkers terminated with azido group for attachment to polymers via click chemistry (see Supplementary Methods). To demonstrate the potential applications of the developed nanosensor in cell biology and analytical chemistry, we performed experiments in a home-built microfluidic device made of polydimethylsiloxane (Fig. 1b). The NDs used are in average ~33 nm in diameter with a fairly narrow size distribution[41] (Supplementary Fig. 1) and coated with a HPMA shell a few nanometre thick, as indicated by transmission electron microscopy (TEM) image (Fig. 1c). These NDs contain few NV centres (<10 per particle on average, Supplementary Fig. 2).

Chemical engineering and characterization of the ND surface. To test the utility of our ND-polymer-Gd hybrid nanosensors, we developed two kinds of chemical linkers to sense pH and redox potential, and corresponding nanosensors are denoted as ND@pH and ND@redox particles, respectively (Fig. 2a). ND@pH particles contain an aliphatic hydrazone linker, for which the rate of hydrolytic cleavage is greatly accelerated at lower pIIs in the physiologically relevant range[42] (pH 4–8; Fig. 2b). ND@redox particles contain a disulfide linker that can be cleaved into two thiol fragments in reducing environments (in this case, by the presence of glutathione, GSH) (Fig. 2c). As a control, we also synthesized a system with non-cleavable bonds (denoted ND-HPMA-Gd; Fig. 2a). The HPMA polymer is electroneutral but the macrocyclic Gd^{3-} complexes are negatively charged, introducing an overall negative charge to the polymer shell. The electrostatic repulsion between complexes facilitates the departure of the cleaved complexes from the shell.

Based on the NV relaxometry-sensing scheme, the T_1 relaxation time of an NV centre is determined by the number of spins within the effective NV-sensing radius[35]. Therefore, the critical parameter is the actual concentration of Gd^{3+} in the ND nanoenvironment as the relaxation time scales with the Gd^{3+} concentration in the shell (see Supplementary Equations (2, 7, 12)). Either swelling or collapse of the polymer shell would affect this quantity and therefore influence the measured T_1 relaxation time, even if the Gd^{3+} complexes are not released. As polymers can reversibly respond to pH and ionic strength by changes in their hydrodynamic diameters and also by nonspecific adsorption of ions resulting in changes in zeta potential, we studied the influence of these parameters on the behaviour of our nanosensors. First, we measured the size distribution of ND-HPMA-Gd particles (with non-cleavable bonds) in various pH buffers by dynamic light scattering. As shown in Fig. 2d, the hydrodynamic radii of ND-HPMA-Gd in the whole range of buffers were fairly uniform, indicating that the shell thickness of our nanosensor does not change in response to various buffer conditions. In two selected buffers (pH 2.0 and 7.4), we measured

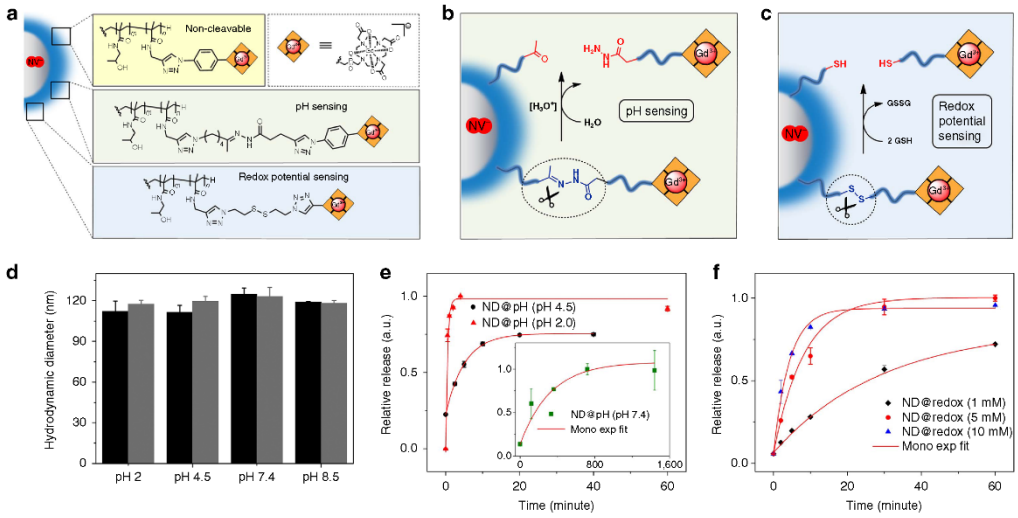

Figure 2 | Design and characterization of ND-polymer-Gd hybrid nanoscale sensors. (**a**) Chemical structure of the polymer interface with Gd^{3+} complexes attached via a non-cleavable and two types of cleavable linkers. The specific release mechanisms for (**b**) pH-dependent hydrolytically cleavable and (**c**) reductively cleavable linkers are shown in detail. (**d**) Hydrodynamic diameters of poly(HPMA)-coated NDs (ND-HPMA, black) and poly(HPMA)-coated NDs modified with non-cleavable Gd^{3+} complexes (ND-HPMA-Gd, grey) determined by dynamic light scattering in different buffers used for Gd-release measurements. (**e**) Release kinetics of Gd^{3+} complexes in ND@pH particles in pH 2.0, 4.5 and 7.4 buffers analysed by ICP MS. The red line is the corresponding mono-exponential fitting. (**f**) Release kinetics of Gd^{3+} complexes in ND@redox particles in the presence of 1, 5 and 10 mM GSH in pH 8.5 buffer analysed by ICP MS. The red line is the corresponding mono-exponential fitting. The error bars in **d–f** represent s.d. from at least three independent measurements.

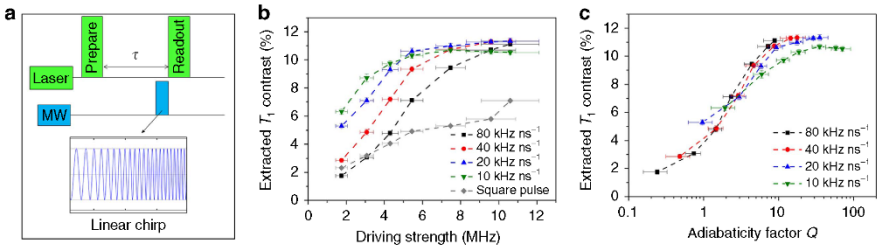

Figure 3 | Robust relaxation measurement with linear chirp pulse. (**a**) Schematic cartoon showing the used optical and microwave pulse sequence for T_1 relaxation measurement. (**b**) Comparison of experimentally extracted contrast of T_1 relaxation measurement with chirp pulse and square pulse for control sample ND-HPMA. The contrast is defined as the normalized initial difference between the sensing sequence with and without the inversion pulse. (**c**) Dependence of extracted T_1 contrast on the extracted minimum adiabaticity factor Q, where Q is defined as the effective driving amplitude over its angular velocity in the rotating frame. The vertical error bars in **b**,**c** represent the s.d. from 20 independent measurements with $\tau \ll T_1$, whereas the horizontal error bars represent the s.e. (95% confidence intervals) from Lorentzian fits (for Fourier transformed Rabi oscillation).

hydrodynamic radii, zeta potentials and T_1 for ND-HPMA-Gd at increasing ionic strengths (up to $\sim$0.25 M, achieved by addition of NaCl and precisely quantified according to the conductivity of the solution). We observed that both pH and ionic strength exert only a marginal influence on hydrodynamic radii (Supplementary Fig. 3a). Although the zeta potentials increased with increasing ionic strength, most likely because of preferential adsorption of sodium ions (Supplementary Fig. 3b), this effect had no influence on T_1 (Supplementary Fig. 3c). This observation confirms the insensitivity of the polymer surface architecture to various environments, which is essential for the construction of stable and robust nanosensors for bio-applications.

To verify whether our nanosensors could release Gd^{3+} complexes on demand, we incubated them in different environments, removed them from solution by centrifugation and analysed the amount of Gd^{3+} complexes in the supernatant with inductively coupled plasma mass spectrometry (ICP MS) as a function of incubation time. This method allowed us to study the temporal evolution of Gd^{3+} complexes release from our nanosensors. As shown in Fig. 2e, the ND@pH particles showed pH-dependent release, whereas the ND-HPMA-Gd (with non-cleavable bonds) particles (Supplementary Fig. 4) were stable under all conditions examined within the current chosen measurement time window ($\sim$ 1 h). Furthermore, the slope of the release profile measured at pH 2.0 was two orders of magnitude higher than that for pH 7.4, indicating a much faster cleaving rate of Gd^{3+} complexes from the polymer at low pH values. The very slow change (as shown in insert of Fig. 2e) at pH 7.4 indicates that the sensor can continuously operate for several hours before measurements at lower pH values.

Similarly, the ND@redox particles showed an obvious GSH concentration-dependent release: the higher the applied concentration of GSH, the steeper the release slope (Fig. 2f), whereas the ND-HPMA-Gd control sample (with non-cleavable bonds) were stable in the presence of GSH (Supplementary Fig. 5). All the measured release kinetics for ND@pH and ND@redox particles fit well with standard first-order reaction kinetics

$$C = C_0 e^{-kt} \quad (1)$$

where C_0 is the initial concentration of the reactant and k is the first order rate constant, indicating that the release rate is solely dependent on one specific reactant in solution.

Robust NV spin relaxometry utilizing a linear chirp pulse. Our experiments are based on probing the spin relaxation time T_1 of the NV centre. T_1 is measured by first initializing the NV spin into $m_s = 0$ by an optical pulse. After a waiting time τ, the spin state is readout by an optical excitation pulse generating fluorescence, which is proportional to the population probability of $m_s = 0$. Measuring this fluorescence as a function of the waiting time τ thus determines T_1. However, special care needs to be taken when performing relaxometric measurements on NV centres, as, for example, charge-state fluctuations can mask the T_1 decay in this approach[43]. To derive pristine T_1 curves, one needs to apply an additional microwave pulse in resonance with for example the $m_S = 0$ to $m_S = +1$ spin transition in a second measurement to invert the population of spin state sublevels and subtract the result of both (see Supplementary Discussion). As the spin state has to be manipulated, knowledge about the spin resonance frequency is required. In addition, the excitation power and pulse duration of the used microwave pulse has to be set correctly for a precise state adjustment. Later parameters for their part differ when the orientation of the NV axis to the local microwave field is changed. Therefore, it is highly desirable to use pulse schemas that intrinsically compensate for such variations. In the current study, we optimized the T_1 readout by introducing an adiabatic passage (see Supplementary Discussion) in form of a linear chirp pulse (Fig. 3a), which is robust against detuning and microwave driving power[44]. To compare the performance of different schemes used in T_1 measurement, we extracted the spin contrast from experimental measurement as a function of driving strength (estimated by Rabi oscillations driven on the optically detected magnetic resonance (ODMR) transitions, see Supplementary Fig. 10a) for the control sample ND-HPMA (without Gd^{3+} complexes) (Fig. 3b). The obtained spin contrast decreased as the driving strength reduced for both measurement schemes, but the chirp pulse always resulted in a higher contrast than that obtained with square pulse. We also plotted the extracted spin contrast as a function of expectable minimal adiabaticity factor Q (a measure of the adiabaticity of the used pulse scheme[45]) when using linear chirp pulse at different chirp rate (Fig. 3c). For the data shown in this work using linear chirp pulse, we experimentally obtained a contrast ranging from 4 to 10%, corresponding to a factor Q in the range of around 1.5 up to 10. Indeed, in terms of sensitivity, the chirp pulse resulted in a twofold sensitivity enhancement with different chirp rate when the microwave power is large enough (Supplementary Fig. 6).

Microfluidic measurement of nanosensors. Because of the excellent colloidal stability of our nanosensor under physiological conditions, we performed our T_1 measurements on diffusing NDs (Fig. 4a). We first investigated two kinds of control sample,

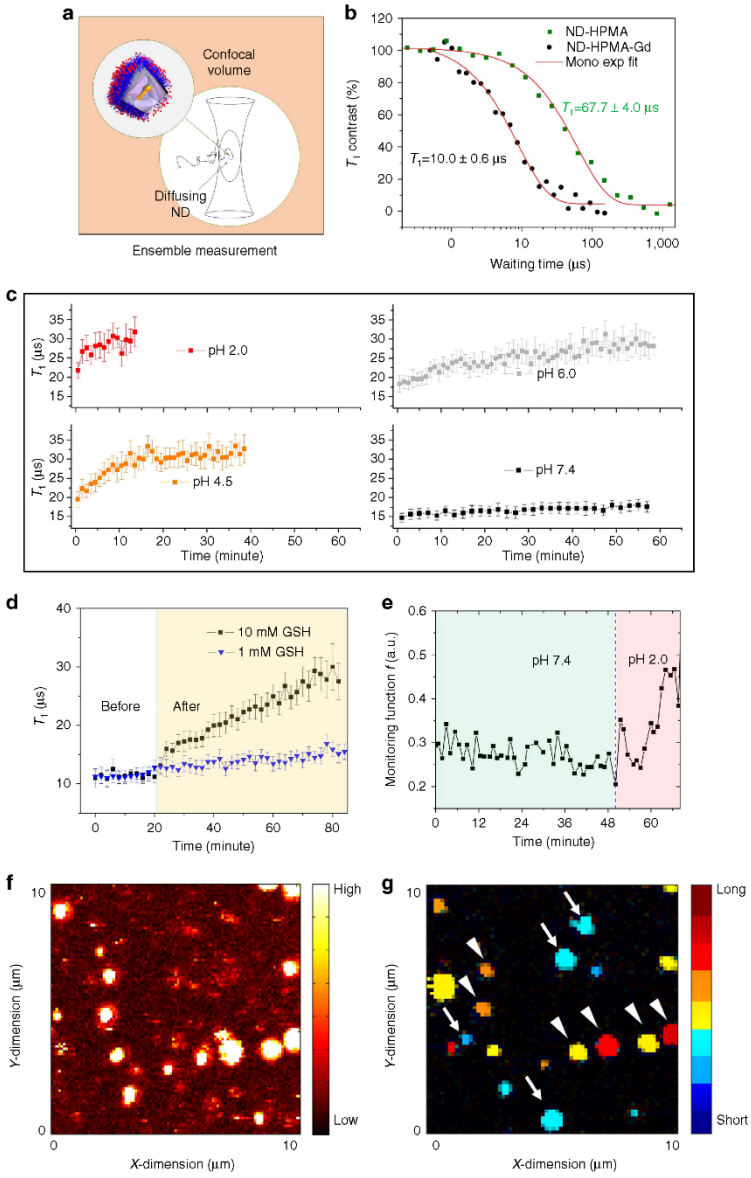

Figure 4 | *In situ* measurements in a microfluidic channel. (**a**) Schematic cartoon showing the ensemble measurements on the averaged T_1 of ND particles diffusing through the confocal volume. (**b**) Typical T_1 ensemble measurement of ND-HPMA and ND-HPMA-Gd (with non-cleavable bond) particles in pH 7.4 buffer. (**c**) Time-dependent ensemble measurement for T_1 of the ND@pH particles when incubated with pH 2.0, 4.5, 6.0 and 7.4 buffers. (**d**) Time-dependent ensemble measurement for T_1 of the ND@redox particles in buffer solution before and after addition of 1 mM (blue) and 10 mM (black) GSH. (**e**) Time-dependent fixed-τ measurement for chosen ND@pH particles when incubated at pH 7.4 followed by a change to pH 2.0 buffer (details are given in Methods). (**f**) Confocal image for the chosen view of ND@pH particles on cover glass in pH 2.0 buffer; the bar indicates the measured fluorescence intensity. (**g**) Reconstructed T_1 contrast image of the same view as in **f** after rinsing with pH 7.4 buffer and adding again freshly prepared ND@pH particles (loaded with Gd^{3-} complexes) in pH 7.4 buffer. White triangles point to old ND@pH particles (Gd^{3+} complexes released), while white arrows point to those newly emerging ones (loaded with Gd^{3+} complexes), the colour bar indicates the extracted T_1 value ranging from short (blue) to long (red). The error bars in **c** and **d** represent the s.e. (95% confidence intervals) from mono exponential decay fits.

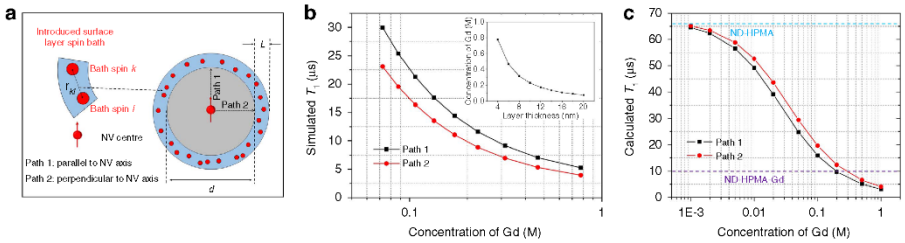

Figure 5 | Simulation for the influence of Gd^{3+} complexes on relaxometry. (**a**) The ND is modeled as a sphere with diameter *d* coated with polymer with thickness *L*. The Gd^{3+} complexes embedded in the polymer layer acts as a randomly fluctuating spin bath. The NV centre is positioned along two orientations (Path 1 and 2). (**b**) The influence of varying HPMA layer thickness (varying concentration of Gd^{3+} complexes) on simulated T_1 value when the number of Gd^{3+} complexes is fixed. The inset shows the concentration of Gd^{3+} complexes versus the layer thickness of the shell (here, $d = 33$ nm and the number of Gd^{3+} complexes was fixed at ~8,000). (**c**) The influence of varying concentrations of Gd^{3+} complexes on calculated T_1 value when the thickness of the polymer layer is fixed ($d = 33$ nm and $L = 10$ nm). The purple dashed line (ND-HPMA-Gd) and blue dashed line (ND-HPMA) denote the lower and upper limit for the measured T_1 value in current study, respectively.

namely ND-HPMA (without Gd^{3+} complexes) and ND-HPMA-Gd (non-cleavable). As shown in Fig. 4b, the ND-HPMA particles had an average measured T_1 value of 67.7 ± 4.0 μs, whereas the ND-HPMA-Gd particle showed a significantly lower value of 10.0 ± 0.6 μs in pH 7.4 buffer. In fact, we also checked the stability of these control samples in all the buffer conditions used in current study (see Supplementary Figs 4 and 5).

We then used the ND@pH particles (pH cleavable) to perform time-dependent T_1 measurement in various conditions including pH 2.0, 4.5, 6.0 and 7.4 (Fig. 4c). At physiological pH environment (pH 7.4), we observed only a slight change for the measured T_1 over a period of 1 h, whereas the T_1 changed dramatically at acidic condition. The measured T_1 curve as a function of the incubation period showed the following behaviour (Fig. 4c): the lower the pH value the steeper the changes in T_1, being consistent with our previous ICP MS measurements (Fig. 2e). Taking a moderate pH (pH 4.5) as an example, the release kinetics of Gd^{3+} complexes (after converting T_1 to a Gd^{3+} concentrations using Supplementary Equations, also see Fig. 5) from ND@pH particles ($\tau_{rel} = 315.7 \pm 42.8$ s) agree excellently with ICP MS measurements ($\tau_{rel} = 306.4 \pm 9.9$ s) (Supplementary Fig. 7). Using set of Britton–Robinson buffers (with equal composition and ionic strength), we also investigated the sensitivity of our sensor in the physiologically relevant pH range (3.7–6.9) for a short measurement time frame (12 min). We estimated the T_1 change rate for each measured pH and found a monotonous dependence on pH (Supplementary Fig. 8) allowing for accuracy of a pH difference at least ~0.7.

Furthermore, we also investigated the change in T_1 of ND@redox nanosensor (cleavable at reduction conditions) in the presence of GSH, an important antioxidant found in most of the animal cells[46]. As shown in Fig. 4d, we observed a mild increase in the T_1 change rate after adding 1 mM GSH and a significant change for 10 mM GSH, while the measured T_1 value was constant before GSH addition.

We can reduce the used measurement schema into fast fixed-τ measurement by directly counting the ratio (monitoring function *f*) of fluorescence signal at two fixed time points[43]. A large monitoring function *f* value indicates a longer relaxation time. As shown in Fig. 4e, the monitoring function *f* kept almost the same in pH 7.4 buffer, but starts to increase once the pH 2.0 buffer is introduced, indicating the increase of T_1 time due to Gd^{3+} complexes release (being consistent with data in Figs 2e and 4c). With the fast measurement scheme, we can perform T_1 contrast imaging on several different NDs in a confocal scanning approach. To demonstrate this, we first incubated ND@pH particles in pH 2.0 buffer as shown in Fig. 4f, followed by rinsing with pH 7.4 buffer and adding again freshly prepared ND@pH particles in pH 7.4 buffer. Next, we performed fixed-τ measurement for each pixel within the chosen field of view and reconstructed a T_1 contrast image shown in Fig. 4g. ND@pH particles that were not subject to low pH (white arrows in Fig. 4g) showed short T_1 times, whereas particles that were subject to pH 2.0 (white triangles in Fig. 4g) showed long T_1 times, as most of their loaded Gd^{3+} complexes had been released during pH 2.0 treatment. This is consistent with the statistical view of T_1 observations for the sample ND@pH, indicating significant different T_1 in two different pH buffers (pH 2.0 and pH 7.4; Supplementary Fig. 9).

Modelling the NV relaxometry modulated by Gd^{3+} complexes. To fully understand the observed effects, we started with the model description[47] and revised it to describe the function of our nanosensors (see Supplementary Methods). As shown in Fig. 5a, we modelled a single ND particle as a sphere and considered the introduced Gd^{3+} complexes as randomly fluctuating spin bath inside the polymer shell at the beginning. As the actual position of our NV centre in the crystal is not known, we considered various positions of the NV centre between the centre and the edge of the sphere. By this we derive an average value of the simulated T_1. From measurements using ICP atomic emission spectroscopy (AES), we obtained the average content of Gd^{3+} complexes in ND particles ~3.2%. Therefore, we can estimate the approximate number of Gd^{3+} complexes is around 8,000 per particle if we assume an average diameter of NDs as 33 nm, equivalent to the average value obtained from our TEM measurements (Supplementary Fig. 1). To estimate the shell thickness of the HPMA for the given sample in the used buffer solutions, we fixed the number of Gd^{3+} complexes inside the polymer shell and varied its thickness to investigate the corresponding T_1 change. In this way, we derive the T_1 value as a function of shell thickness as shown in Fig. 5b. The measured T_1 of ND-HPMA-Gd is ~10 μs (Fig. 4b) pointing to ~0.2 M Gd^{3+} concentration in our simulation (Fig. 5b) with a ~10 nm shell (insert in Fig. 5b). This shell thickness is similar with our TEM observation in Fig. 1c and Supplementary Fig. 1, and we used it in all further analysis steps. One could also account for paramagnetic centres lying on the surface of NDs[47], but as we know the relaxation rate for the situation when the Gd^{3+} is absent, we can use the already gained T_1 time from the control sample ND-HPMA as a basis

offset. The measured T_1 value was 67.7 μs (Fig. 4b) for the control sample ND-HPMA in buffer solutions. We interpreted this as the intrinsic relaxation rate

$$R^{\mathrm{int}} = \frac{1}{T_1^{\mathrm{int}}} \quad (2)$$

where $T_1^{\mathrm{int}} = 67.7\mu s$ of the nanosensors in solution and calculated the expected relaxation T_1 time (Fig. 5c) using

$$T_1^{\mathrm{Calculated}} = \left(R^{\mathrm{int}} + R^{\mathrm{Gd}}\right)^{-1} \quad (3)$$

where R^{int} is the intrinsic relaxation rate and R^{Gd} is the simulated relaxation rate induced by Gd^{3+} complexes. From this, we can deduct that we are able to detect Gd^{3+} complexes with concentration ranging from 0.2 M (~8,000 Gd^{3+} complexes per particle) down to 0.001 M (~40 Gd^{3+} complexes per particle), corresponding to the measured highest (purple dashed line in Fig. 5c) and lowest (blue dashed line in Fig. 5c) Gd content, respectively.

Discussion

Our hybrid nanosensor achieves signal transduction, recording and amplification simultaneously. Subtle changes in physiological systems (weak signals) can be recorded by counting the variance of Gd^{3+} complexes (strong interaction with NV centres) inside the polymer shell due to a programmed chemical reaction. The well-fitted first-order reaction equation for measured release kinetics (Fig. 2e,f and Supplementary Fig. 7) indicates that our nanosensor responds to changes in a single, pre-defined chemical parameter. Importantly, the thickness of the polymer shell was insensitive to pH and ionic strength (Fig. 2d and Supplementary Fig. 3a). We observed neither swelling nor collapse of the polymer shell in any of the conditions used. Consistently, we observed no influence of these factors on T_1 (Supplementary Fig. 3c), which is critical for reliable and robust function of the nanosensors in biological environments.

The excellent agreement between the experimental results (Fig. 4b) and theoretical modelling (Fig. 5c) indicates the underlying mechanism: the change in T_1 relaxation time is caused by release of Gd^{3+} complexes from the polymer shell. Precise agreement of ICP MS with T_1 kinetic measurements (Supplementary Fig. 7) suggests the high accuracy and sensitivity of the current detection method. In principle, we can monitor gradual release down to several tens of molecules of Gd^{3+} complexes (Fig. 5c) at a single-particle level (Fig. 4e–g), which allows us to monitor a localized chemical process occurring on an extremely small scale (~10^{-22}–10^{-20} mol). Although the achieved accuracy (~0.7 pH unit) is lower compared with the current, most sensitive measurement techniques[48] (~0.1 pH unit for intracellular measurement), our system operates in quite a broad pH range. In contrast, for some optical pH sensors, which exhibit a sigmoidal response towards changes in pH, their narrow dynamic range represent often a limitation[49]. Considering practical measurements in cells, the accuracy of our sensor is sufficient, as pH differences between extracellular space, cytosol and some organelles are much higher than 0.7. For example, the cytosol pH is ~7.4, whereas endo/lysosomal compartments show pH ~4.5 (ref. 50). Similarly, the intracellular GSH concentrations usually range from 0.5 to 10 mM, whereas extracellular values are almost three orders of magnitude lower[51]. These differences are in a range well measurable by our nanosensor.

Many of the currently used nanosensors are based on mechanisms, which are either irreversible (based on formation or cleavage of covalent bonds) or practically irreversible, because the formed non-covalent sensing assembly is extremely stable (for instance, nucleic acid hybridization, antibody and aptamer affinity probes, fluorescence resonance energy transfer sensors utilizing cleavage reactions[52]). Irreversibility is typical also for current approaches to detect GSH[53,54]. The chemical nature of our sensing mechanism also renders our scheme irreversible, which limits the possible durations of measurements, especially for higher cleavage rates. To enlarge the measurement window to basically unlimited time, we are currently developing a reversibly responding polymer coating on NDs, which operates without a need of irreversible cleavage events.

For a typical T_1 measurement with an additional control sequence using a square pulse, one needs to find the resonance frequency and the length of used pulse to effectively invert the spin population. This is especially important for NDs, because their NV centres are typically arbitrary oriented and with a strain-induced variation in resonance frequency[23]. In comparison, the used linear chirp pulse scheme simplifies T_1 measurements into a single step: direct T_1 measurement by applying chirp pulse acting as 'inversion pulse' without any preliminary measurements for identifying the resonance frequency and pulse length. In addition, the chirp pulse scheme results in enhanced sensitivity compared to that with a square pulse (Fig. 3 and Supplementary Fig. 6). This is also consistent with our simulation of NV spin state evolution excited by different pulse scheme: the square pulse is sensitive to the changes in microwave excitation while the linear chirp pulse is much more robust, especially in the presence of inhomogeneous ODMR line broadening (see Supplementary discussion and Supplementary Fig. 10). Thus, the chirp pulse scheme enables robust T_1 measurement on different NDs simultaneously (ensemble measurement).

In conclusion, our hybrid nanosensor, owing to its versatility, can serve as a general platform with potential applications ranging from catalytic chemistry to cell biology and physiology, especially for label-free three-dimensional imaging of physiological variables by optical means. Development of molecular-sized NDs with NV centres[55,56] can further increase the sensitivity of the current method due to improved spin sensitivity of NV centres.

Methods

Experimental setup. In the current study, we adapted a confocal microscopy apparatus. The laser (CNI, CW DPSS Laser 532 nm) was directed through acousto-optic modulator (AOM) and focused onto the focal plane of a ×60 water-immersion objective (Olympus) for the ensemble measurements and a ×60 oil objective (Olympus) when measuring individual NDs. The fluorescence of NV centre was filtered (long pass, cutoff at 647 nm) and collected by two avalanche photo diode (Perkin-Elmer) in Hanbury-Brown and Twist configuration. Resonant microwave manipulation of the NV centre was achieved using a spanned copper wire inside a home-built microfluidic channel made of transparent poly-dimethylsiloxane (Sylgard 184 silicone elastomer kit, Dow Corning) in the vicinity of the optical focus. Two small plastic tubes are used to exchange the solution in the microfluidic channel.

Preparation of ND-polymer-Gd nanosensors. Detailed descriptions for preparation of fluorescent NDs with NV centres[57], their coating with HPMA polymer and synthesis of Gd^{3+} complexes can be found in the Supplementary Information. Briefly, alkyne-modified HPMA-coated NDs were decorated with azide-modified Gd^{3+} complexes using Cu(I)-catalysed azide-alkyne cycloaddition (CuACC). HPMA-coated NDs (10 mg in a final reaction volume of 12.8 ml of 50 mM HEPES buffer, pH 7.4) were mixed with either non-cleavable Gd^{3+} complexes or Gd^{3+} complexes with hydrazone or disulfide linker (in final concentrations of 0.96, 1.92 and 2.4 mM, respectively), pre-mixed 0.32 mM $CuSO_4$ and 0.64 mM tris(3-hydroxypropyltriazolylmethyl)amine ligand, and a freshly prepared solution of sodium ascorbate (5 mM). The reaction mixture was well sealed, left for 1 h with no stirring and washed by centrifugation with water (Gd^{3+} conjugates with non-cleavable linker, ND-HPMA-Gd and disulfide linker, ND@redox) or methanol (Gd^{3+} conjugate with hydrazone linker, ND@pH). The resulting nanosensors were stored in water (ND-HPMA-Gd and ND@redox) or in dry methanol (ND@pH) at 4 °C.

Characterization of ND-polymer-Gd nanosensors. The morphology and size of the particles were characterized with TEM (JEOL JEM-1011)[58]. The stability and

surface charge of HPMA-coated NDs with Gd^{3+} complexes were tested by dispersing them in buffer solutions (50 mM citric acid buffer pH 2.0, 50 mM acetate buffer pH 4.5, 50 mM HEPES buffer pH 7.4, 50 mM TRIS buffer pH 8.5 and 1.5 M PBS buffer pH 7.4) for further experiments. Dynamic light scattering and zeta potential were recorded with a Zetasizer Nano ZS system (Malvern Instruments) at 37 °C at a concentration of 0.1 mg ml^{-1}.

To quantitatively measure the amount of Gd^{3+} complexes released from the nanosensors, the particles were mixed with buffer and incubated for a certain time. Then, cleavage conditions were stopped, the particles were centrifuged and the released Gd^{3+} complexes in supernatant were measured with an ICP MS 7700 (Agilent Technologies) instrument in duplicates. The non-cleavable ND-HPMA-Gd^{3+} conjugate was used as a control and processed under the same conditions. The relative release at a given time was calculated as a ratio of the amount released to the maximum release amount. A detailed description of these release experiments can be found in the Supplementary Information. The total amount of Gd^{3+} conjugated to HPMA-coated NDs was measured as ~3.2% (weight percentage to NDs) using ICP AES (Spectro Arcos SOP).

Relaxation measurement with linear chirp pulse. For full T_1 relaxometry measurement, laser light modulation was achieved by passing continuous wave laser through an acousto-optical modulator for polarization and readout of NV centres. We first applied a laser pulse for polarizing NV centres into $m_s = 0$ (initialization) and then wait for the time τ, followed by another laser pulse to detect NV fluorescence revealing the spin state (readout). Afterwards, we applied a similar sequence that differs from the first one, by adding a microwave pulse before the readout. The microwave pulse (linear chirp) is generated by mixing the output of one microwave source (SMIQ 03B, Rhode & Schwarz) with an arbitrary waveform generator (AWG2041, Tectronixs) and amplified by a microwave amplifier (ZHL-16W-43 + , mini circuits). The linear chirp microwave pulse starts from 2.845 GHz and is swept over 100 MHz (covering most of the detuning range in NDs) at certain speed. The chirp speed was kept as 10–100 kHz ns^{-1}. The obtained difference in fluorescence $\Delta F(\tau)$ is proportional to the residual spin polarization after time τ of only those NV centres excited by microwave pulse. We thus further normalized the obtained $\Delta F(\tau)$ (named T_1 contrast)[43], fitted it with a single exponential function:

$$\Delta F(\tau) = A e^{-\tau/T_1} \quad (4)$$

to get an average decay constant T_1 value. For comparison of a chirp pulse with a square pulse for effective spin state inversion during T_1 measurement, 10 µl poly(HPMA)-coated NDs (4 mg ml^{-1} in water) were dropped in the vicinity of the copper wire on top of cover glass and air dried. The analysed detection volume contains more than several hundreds of NV centres, estimated on the detected photon flux in this experiment in comparison with that detected from a single NV centre measured with the same setup. The focal point of the laser was tuned to any position of the dense packed NDs nearby the copper wire for ensemble measurements (all the NDs inside the focus volume). At different microwave power, we performed T_1 measurement through both square pulse and chirp pulse with different sweeping speed. The adiabaticity factor Q is defined as the effective Larmor precession around the effective magnetic field in the rotating frame over the angular change of the field[45]. The driving strength is defined as the effective Rabi frequency of an ensemble of NV centres driven by an external microwave. To quantify the performance of individual scheme in an experiment, the sensitivity enhancement factor is calculated as ratio of power noise equivalents δT_1 of the different pulse scheme:

$$\mathrm{EF} = \frac{\delta T_1^{\mathrm{chirp}}}{\delta T_1^{\mathrm{square}}} = \frac{c_{\mathrm{chirp}}}{c_{\mathrm{square}}} \cdot \sqrt{\frac{t_{\mathrm{square}}}{t_{\mathrm{chirp}}}} \quad (5)$$

where c is the contrast and t is the cycle time of the measurement.

NV relaxometry measurements in a microfluidic channel. For all time-dependent T_1 measurements (Fig. 4 and Supplementary Fig. 9), the freshly prepared nanosensor particles were dispersed in the respective buffer at a concentration of approximately 100 µg ml^{-1} and were injected into a microfluidic channel through the conjugated tube. In case of the ensemble measurement we used a PDMS chamber that can be opened and covered from top. The focal point of the laser was placed to any position inside the channel for ensemble measurements (all the free diffusing particles). For fixed τ measurement, we only collected the fluorescence signal (F) at two fixed time points ($\tau_1 = 0.001$ µs and $\tau_2 = 20$ µs) on the obtained full T_1 curve of chosen ND spot and compare the change of T_1 by monitoring function:

$$f = F(\tau_2)/F(\tau_1) \quad (6)$$

Data availability. Data supporting the findings of this study are available within the article and its Supplementary Information files and from the corresponding authors upon reasonable request.

References

1. Orrenius, S., Zhivotovsky, B. & Nicotera, P. Regulation of cell death: the calcium-apoptosis link. *Nat. Rev. Mol. Cell Biol.* **4,** 552–565 (2003).
2. Winterbourn, C. C. Reconciling the chemistry and biology of reactive oxygen species. *Nat. Chem. Biol.* **4,** 278–286 (2008).
3. Wu, J. & Kaufman, R. J. From acute ER stress to physiological roles of the unfolded protein response. *Cell Death Differ.* **13,** 374–384 (2006).
4. He, L. & Hannon, G. J. MicroRNAs: small RNAs with a big role in gene regulation. *Nat. Rev. Genet.* **5,** 522–531 (2004).
5. Casey, J. R., Grinstein, S. & Orlowski, J. Sensors and regulators of intracellular pH. *Nat. Rev. Mol. Cell Biol.* **11,** 50–61 (2010).
6. Schafer, F. Q. & Buettner, G. R. Redox environment of the cell as viewed through the redox state of the glutathione disulfide/glutathione couple. *Free Radic. Biol. Med.* **30,** 1191–1212 (2001).
7. Domaille, D. W., Que, E. L. & Chang, C. J. Synthetic fluorescent sensors for studying the cell biology of metals. *Nat. Chem. Biol.* **4,** 168–175 (2008).
8. Howes, P. D., Chandrawati, R. & Stevens, M. M. Bionanotechnology. Colloidal nanoparticles as advanced biological sensors. *Science* **346,** 1247390 (2014).
9. Zhang, J., Campbell, R. E., Ting, A. Y. & Tsien, R. Y. Creating new fluorescent probes for cell biology. *Nat. Rev. Mol. Cell Biol.* **3,** 906–918 (2002).
10. Schrand, A. M. *et al.* Are diamond nanoparticles cytotoxic? *J. Phys. Chem. B* **111,** 2–7 (2007).
11. Mochalin, V. N., Shenderova, O., Ho, D. & Gogotsi, Y. The properties and applications of nanodiamonds. *Nat. Nanotechnol.* **7,** 11–23 (2012).
12. Zhu, Y. *et al.* The biocompatibility of nanodiamonds and their application in drug delivery systems. *Theranostics* **2,** 302–312 (2012).
13. Fang, C. Y. *et al.* The exocytosis of fluorescent nanodiamond and its use as a long-term cell tracker. *Small* **7,** 3363–3370 (2011).
14. Mohan, N., Chen, C. S., Hsieh, H. H., Wu, Y. C. & Chang, H. C. *In vivo* imaging and toxicity assessments of fluorescent nanodiamonds in *Caenorhabditis elegans*. *Nano Lett.* **10,** 3692–3699 (2010).
15. Balasubramanian, G. *et al.* Nanoscale imaging magnetometry with diamond spins under ambient conditions. *Nature* **455,** 648–651 (2008).
16. Maze, J. R. *et al.* Nanoscale magnetic sensing with an individual electronic spin in diamond. *Nature* **455,** 644–647 (2008).
17. Gruber, A. *et al.* Scanning confocal optical microscopy and magnetic resonance on single defect centers. *Science* **276,** 2012–2014 (1997).
18. Chow, E. K. *et al.* Nanodiamond therapeutic delivery agents mediate enhanced chemoresistant tumor treatment. *Sci. Transl. Med.* **3,** 73ra21 (2011).
19. Kuo, Y., Hsu, T. Y., Wu, Y. C. & Chang, H. C. Fluorescent nanodiamond as a probe for the intercellular transport of proteins *in vivo*. *Biomaterials* **34,** 8352–8360 (2013).
20. Chu, Z. *et al.* Rapid endosomal escape of prickly nanodiamonds: implications for gene delivery. *Sci. Rep.* **5,** 11661 (2015).
21. Zhang, T. *et al.* Photoacoustic contrast imaging of biological tissues with nanodiamonds fabricated for high near-infrared absorbance. *J. Biomed. Opt.* **18,** 26018 (2013).
22. Chu, Z. *et al.* Unambiguous observation of shape effects on cellular fate of nanoparticles. *Sci. Rep.* **4,** 4495 (2014).
23. McGuinness, L. P. *et al.* Quantum measurement and orientation tracking of fluorescent nanodiamonds inside living cells. *Nat. Nanotechnol.* **6,** 358–363 (2011).
24. Kucsko, G. *et al.* Nanometre-scale thermometry in a living cell. *Nature* **500,** 54–58 (2013).
25. Petrakova, V. *et al.* Imaging of transfection and intracellular release of intact, non-labeled DNA using fluorescent nanodiamonds. *Nanoscale* **8,** 12002–12012 (2016).
26. Dolde, F. *et al.* Electric-field sensing using single diamond spins. *Nat. Phys.* **7,** 459–463 (2011).
27. Neumann, P. *et al.* High-precision nanoscale temperature sensing using single defects in diamond. *Nano Lett.* **13,** 2738–2742 (2013).
28. Toyli, D. M., Charles, F., Christle, D. J., Dobrovitski, V. V. & Awschalom, D. D. Fluorescence thermometry enhanced by the quantum coherence of single spins in diamond. *Proc. Natl Acad. Sci. USA* **110,** 8417–8421 (2013).
29. Doherty, M. W. *et al.* Electronic properties and metrology applications of the diamond NV − center under pressure. *Phys. Rev. Lett.* **112,** 047601 (2014).
30. Momenzadeh, S. A. *et al.* Thin circular diamond membrane with embedded nitrogen-vacancy centers for hybrid spin-mechanical quantum systems. *Phys. Rev. Applied* **6,** 024026 (2016).
31. Neburkova, J., Vavra, J. & Cigler, P. Coating nanodiamonds with biocompatible shells for applications in biology and medicine. *Curr. Opin. Solid State Mater. Sci.* **21,** 43–53 (2017).
32. Slegerova, J. *et al.* Designing the nanobiointerface of fluorescent nanodiamonds: highly selective targeting of glioma cancer cells. *Nanoscale* **7,** 415–420 (2015).
33. Rehor, I. *et al.* Fluorescent nanodiamonds with bioorthogonally reactive protein-resistant polymeric coatings. *ChemPlusChem* **79,** 21–24 (2014).
34. Ermakova, A. *et al.* Detection of a few metallo-protein molecules using color centers in nanodiamonds. *Nano Lett.* **13,** 3305–3309 (2013).

35. Steinert, S. *et al.* Magnetic spin imaging under ambient conditions with sub-cellular resolution. *Nat. Commun.* **4,** 1607 (2013).
36. Kaufmann, S. *et al.* Detection of atomic spin labels in a lipid bilayer using a single-spin nanodiamond probe. *Proc. Natl Acad. Sci. USA* **110,** 10894–10898 (2013).
37. Sushkov, A. O. *et al.* All-optical sensing of a single-molecule electron spin. *Nano Lett.* **14,** 6443–6448 (2014).
38. Rudovský, J. *et al.* Lanthanide(III) complexes of a mono(methylphosphonate) analogue of H_4dota: the influence of protonation of the phosphonate moiety on the TSAP/SAP isomer ratio and the water exchange rate. *Chemistry* **11,** 2373–2384 (2005).
39. Försterová, M. *et al.* Thermodynamic study of lanthanide(III) complexes with bifunctional monophosphinic acid analogues of H_4dota and comparative kinetic study of yttrium (III) complexes. *Dalton Trans.* 535–549 (2007).
40. Kotková, Z. *et al.* Cyclodextrin-based bimodal fluorescence/MRI contrast agents: an efficient approach to cellular imaging. *Chemistry* **16,** 10094–10102 (2010).
41. Havlik, J. *et al.* Benchtop fluorination of fluorescent nanodiamonds on a preparative scale: toward unusually hydrophilic bright particles. *Adv. Funct. Mater.* **26,** 4134–4142 (2016).
42. Hrubý, M., Koňák, Č. & Ulbrich, K. Polymeric micellar pH-sensitive drug delivery system for doxorubicin. *J. Control Release* **103,** 137–148 (2005).
43. Häberle, T., Schmid-Lorch, D., Reinhard, F. & Wrachtrup, J. Nanoscale nuclear magnetic imaging with chemical contrast. *Nat. Nanotechnol.* **10,** 125–128 (2015).
44. Niemeyer, I. *et al.* Broadband excitation by chirped pulses: application to single electron spins in diamond. *New J. Phys.* **15,** 033027 (2013).
45. Garwood, M. & DelaBarre, L. The return of the frequency sweep: designing adiabatic pulses for contemporary NMR. *J. Magn. Reson.* **153,** 155–177 (2001).
46. Wu, G., Fang, Y.-Z., Yang, S., Lupton, J. R. & Turner, N. D. Glutathione metabolism and its implications for health. *J. Nutr.* **134,** 489–492 (2004).
47. Tetienne, J.-P. *et al.* Spin relaxometry of single nitrogen-vacancy defects in diamond nanocrystals for magnetic noise sensing. *Phys. Rev. B* **87,** 235436 (2013).
48. Ray, A., Yoon, H. K., Lee, Y. E. K., Kopelman, R. & Wang, X. Sonophoric nanoprobe aided pH measurement *in vivo* using photoacoustic spectroscopy. *Analyst* **138,** 3126–3130 (2013).
49. Wencel, D., Abel, T. & McDonagh, C. Optical chemical pH sensors. *Anal. Chem.* **86,** 15–29 (2013).
50. Grant, B. D. & Donaldson, J. G. Pathways and mechanisms of endocytic recycling. *Nat. Rev. Mol. Cell Biol.* **10,** 597–608 (2009).
51. Lushchak, V. I. Glutathione homeostasis and functions: potential targets for medical interventions. *J. Amino Acids* **2012,** 736837 (2012).
52. Howes, P. D., Chandrawati, R. & Stevens, M. M. Colloidal nanoparticles as advanced biological sensors. *Science* **346,** 1247390 (2014).
53. Jung, H. S., Chen, X., Kim, J. S. & Yoon, J. Recent progress in luminescent and colorimetric chemosensors for detection of thiols. *Chem. Soc. Rev.* **42,** 6019–6031 (2013).
54. Wang, K., Peng, H. & Wang, B. Recent advances in thiol and sulfide reactive probes. *J. Cell Biochem.* **115,** 1007–1022 (2014).
55. Vlasov, I. I. *et al.* Molecular-sized fluorescent nanodiamonds. *Nat. Nanotechnol.* **9,** 54–58 (2014).
56. Boudou, J.-P. *et al.* Fluorescent nanodiamonds derived from HPHT with a size of less than 10nm. *Diam. Relat. Mater.* **37,** 80–86 (2013).
57. Stursa, J. *et al.* Mass production of fluorescent nanodiamonds with a narrow emission intensity distribution. *Carbon* **96,** 812–818 (2016).
58. Rehor, I. & Cigler, P. Precise estimation of HPHT nanodiamond size distribution based on transmission electron microscopy image analysis. *Diam. Relat. Mater.* **46,** 21–24 (2014).

Acknowledgements

The authors thank Philipp Neumann, Thomas Häberle and Florestan Ziem for fruitful discussions, Matthias Widmann for his assistance with drawing illustration cartoons in Fig. 1, Tomas Matousek for ICP MS measurements, and David Chvatil and Jan Stursa (Nuclear Physics Institute AS CR, Czech Republic) for irradiation of nanodiamonds, which was supported by grant project RVO61389005. P.C. and J.N. acknowledges the support from the Grant Agency of the Czech Republic (Project Number 16-16336S). J.K. and O.Z. acknowledge the support from the Grant Agency of the Czech Republic (Project Number 16-03156S). J.W. acknowledges funding by the DFG via SPP 1601 and FOR 1493, the Volkswagenstiftung and the EU via the IP DIADEMS.

Author contributions

Z.Q.C., P.C. and J.W. conceived the idea. T.R. designed and carried out all the optical measurements. J.N., O.Z. and J.K. performed all materials synthesis and characterization. A.Z. prepared all the buffer solution involved in optical measurements and participated in the optimization for optical measurements. T.R. carried out the theoretical calculations. T.R., Z.Q.C. and P.C. analysed the data. J.W. supervised the project. Z.Q.C., P.C. and J.W. wrote the manuscript with the comments from all co-authors. All authors discussed the results and commented on the manuscript.

Additional information

Supplementary Information accompanies this paper at http://www.nature.com/naturecommunications

Competing financial interests: The authors declare no competing financial interests.

Reprints and permission information is available online at http://npg.nature.com/reprintsandpermissions/

How to cite this article: Rendler, T. *et al.* Optical imaging of localized chemical events using programmable diamond quantum nanosensors. *Nat. Commun.* **8,** 14701 doi: 10.1038/ncomms14701 (2017).

Publisher's note: Springer Nature remains neutral with regard to jurisdictional claims in published maps and institutional affiliations.

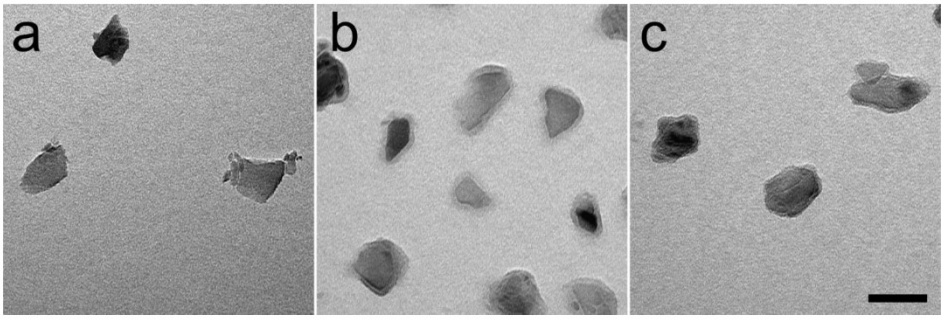

Supplementary Figure 1. Typical TEM image of various ND particles. **(a)** non-coated oxidized NDs. **(b)** Polymer coated ND-HPMA. **(c)** ND@redox. The scale bar represents 50 nm.

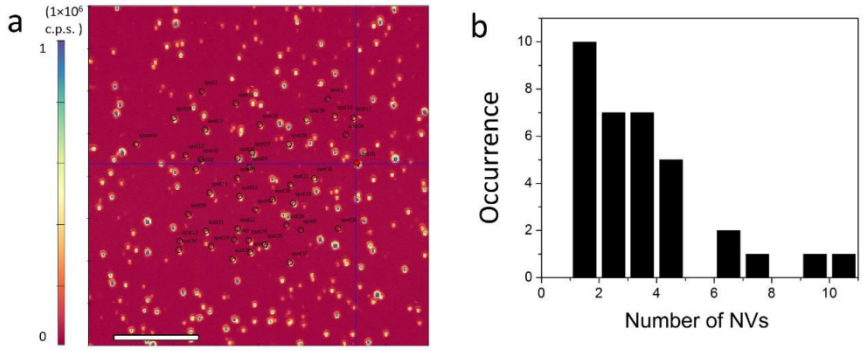

Supplementary Figure 2. Number of NV centers per particle. The number was calculated through analysis of 40 randomly chosen ND particles. **(a)** Typical confocal image of ND-HPMA particles dispersed on top of coverglass. The scale bar represents 10 μm. **(b)** The distribution of the number of NV centers in selected (marked with black circle) spots in **(a)**; the number of NV centers in an individual particle was determined from the autocorrelation function $g^{(2)}(\tau)$.

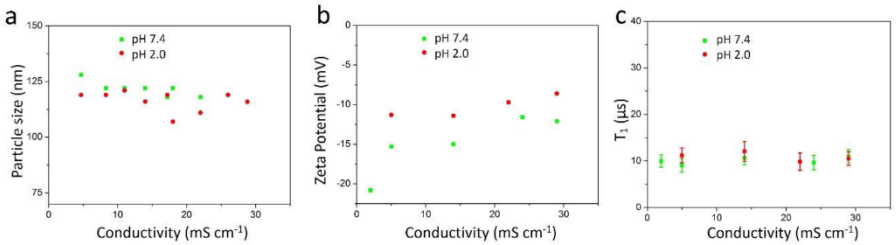

Supplementary Figure 3. The influence of ionic strength on the behavior of ND-HPMA-Gd. **(a)** Hydrodynamic radii, **(b)** zeta potentials, and **(c)** T_1 ensemble measurement of ND-HPMA-Gd in pH 7.4 and pH 2.0 buffers. The ionic strength is expressed as conductivity.

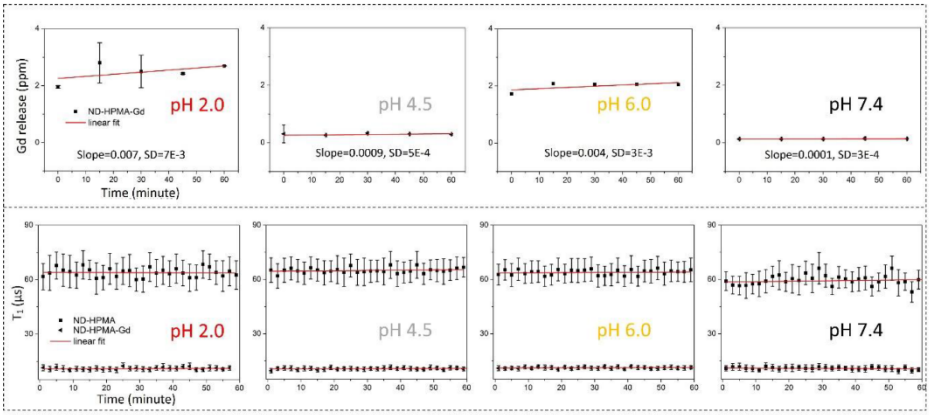

Supplementary Figure 4. Behavior of the control sample in different pH buffers. Release kinetics of Gd^{3+}-complex from ND-HPMA-Gd (non-cleavable) checked by ICP MS (upper panel) in different buffers (pH 2.0, 4.5, 6.0, and 7.4). Time-dependent ensemble measurement for T_1 (lower panel) of ND-HPMA and ND-HPMA-Gd (non-cleavable) in different buffers (pH 2.0, 4.5, 6.0, and 7.4). The slope of all linear fit is approaching zero, indicating negligible change of Gd^{3+} -complex within the measurement time period.

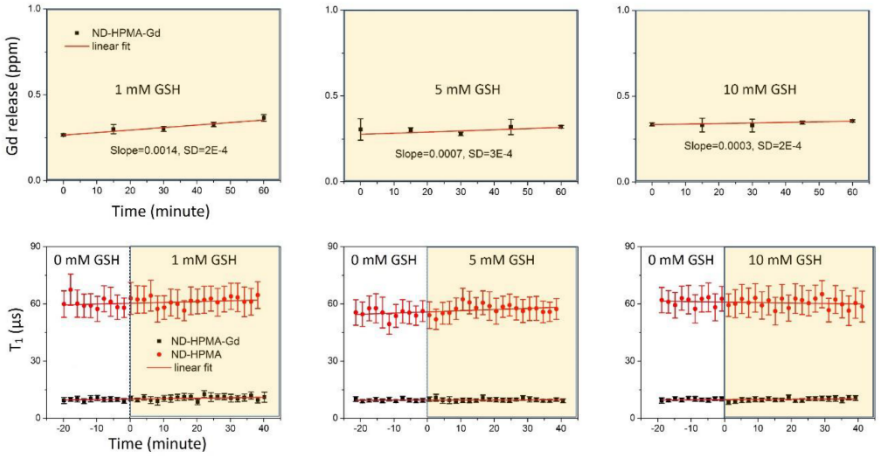

Supplementary Figure 5. The behavior of the control sample in buffers containing GSH. Release kinetics of Gd^{3+}-complex from ND-HPMA-Gd (non-cleavable) checked by ICP MS (upper panel) in different GSH buffers (1 mM, 5 mM and 10 mM GSH). Time-dependent ensemble measurement for T_1 (lower panel) of ND-HPMA and ND-HPMA-Gd (non-cleavable) in different GSH buffers (1 mM, 5 mM and 10 mM). The slope of all linear fit is approaching zero, indicating negligible change of Gd^{3+} complex within the measurement time period.

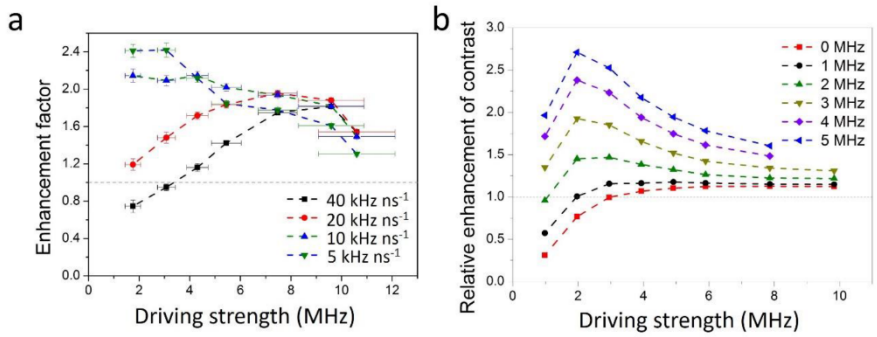

Supplementary Figure 6. Relative enhancement for chirp pulse versus a square pulse. **(a)** Comparison of experimentally obtained enhancement in sensitivity between T_1 relaxation measurement with linear chirp pulse over square pulse; the enhancement factor is calculated as the ratio of sensitivity obtained with linear chirp pulse to that with square pulse. The vertical error bars represent the standard deviations from 20 independent measurements with $\tau \ll T_1$, while the horizontal error bars represent the standard errors (95% confidence intervals) from Lorentzian fits (for Fourier transformed Rabi oscillation). **(b)** Simulation of relative enhancement of the probability to depopulate the NV $m_s = 0$ sublevel after applying linear chirp pulse over square pulse with different microwave driving strength.

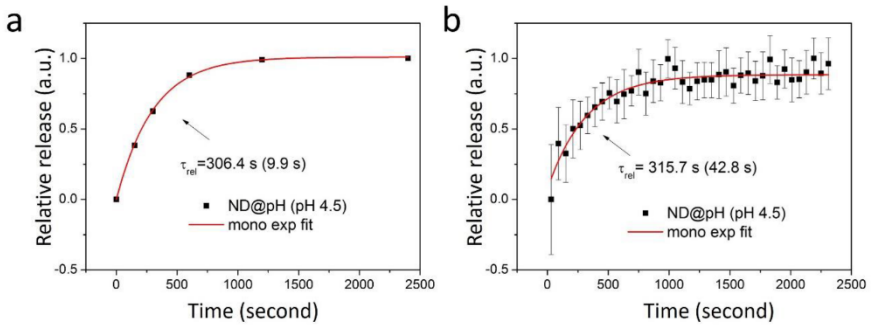

Supplementary Figure 7. Release kinetics of Gd^{3+} complexes. The results were obtained by **(a)** ICP MS and **(b)** ensemble T_1 measurement (ND@pH particles in pH 4.5 buffer). The standard deviations are stated in parentheses.

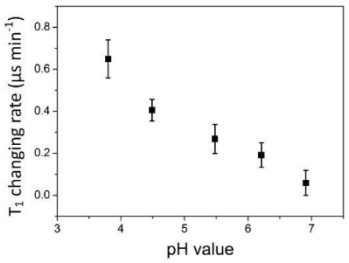

Supplementary Figure 8. Dependence of the fitted T_1 changing rate of ND@pH nanosensor on pH. Six T_1 measurement points (120 seconds per point) were linearly fitted to extract the actual T_1 change rate corresponding to a particular pH. Britton-Robinson buffers with same composition were used. Their conductivity was normalized using KCl to ensure environment with equal ionic strength for all measurements.

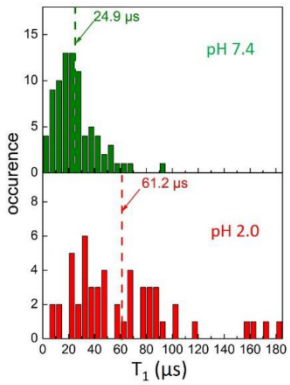

Supplementary Figure 9. Statistical view of ND@pH nanosensors in pH 7.4 and pH 2.0 buffers. After injecting the sample into a microfluidic chamber, the individual relaxation times for different adsorbed ND@pH nanosensors had been measured at pH 7.4 (green) and after changing to pH 2.0 (red).

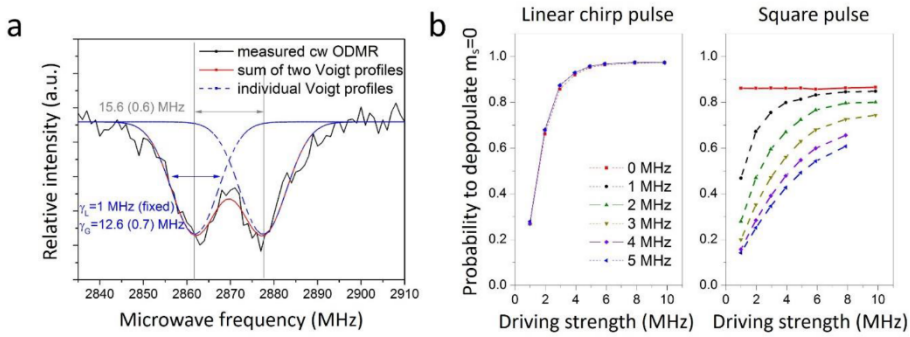

Supplementary Figure 10. Simulated NV spin flip probability induced by different pulse scheme. **(a)** A typical measured ODMR line for a randomly picked cluster of the ND-HPMA particles (black) excited with 45μW laser and weak microwave. The ODMR spectrum had been fitted by two Voigt profiles with a fixed Lorenzian linewidth of 1 MHz and a variable Gaussian linewidth (see below for used parameters). Both transitions in the measured ODMR line are quite broad and separated by around 16 MHz. **(b)** Simulated NV spin flip probability excited with a linear chirp pulse and square pulse plotted as a function of microwave driving strengths. The probability was calculated for an ensemble by averaging over all polar angle and assuming an inhomogeneous broadening of both ESR transitions with a variable value (color coded from 0 MHz (red) to 5MHz (blue)). Both transitions of ODMR line are set to split in average ~16 MHz to mimic the experimental situation in (**a**). The parameters of the chirp pulse had been set to typical values used under real experimental conditions (50 MHz sweep bandwidth with a 20 kHz ns^{-1} sweep speed).

Supplementary Methods

Chemical synthesis of Gd^{3+} complexes and diamond nanosensors

Chemicals and methods

3-Bromo-1-(trimethylsilyl)-1-propyne (**1**)[1], *t*Bu_3DO3A·HBr (**4**·HBr)[2], 1,6-bis(azido)-3,4-dithiahexane (**6**)[3], 10-({hydroxy[4-aminobenzyl]phosphoryl}methyl)-1,4,7,10-tetraazacyclododecane-1,4,7-triacetic acid (**7**)[4] and pent-4-ynehydrazide (**8**) (*via* methyl pent-4-ynoate[5]) were prepared according to published procedures. 6-Azido-hexan-2-one (**9**) was prepared analogously as published for related compounds[6]. Paraformaldehyde was filtered from aged aqueous formaldehyde solutions (Lachema) and dried in a desiccator over concentrated H_2SO_4. Other chemicals from commercial sources were used as received. Acetonitrile and dichloromethane were dried by distilling over P_4O_{10}.

NMR spectra were recorded on VNMRS300, Varian^{UNITY} INOVA 400 or Bruker Avance III 600 spectrometers. NMR chemical shifts are given in ppm, and coupling constants are reported in Hz. For ^{1}H and ^{13}C NMR measurements in D_2O, *t*BuOH was used as internal standard (δ_H = 1.25, δ_C = 30.29). For measurements in $CDCl_3$, TMS was used as internal standard (δ_H = 0.00, δ_C = 0.00). For ^{31}P NMR measurements, 85% aqueous H_3PO_4 was used as external reference (δ_P = 0.00). The abbreviations s (singlet), d (dublet), t (triplet), m (multiplet) and br (broad) are used to express signal multiplicities.

Mass spectra were measured on a Bruker Esquire 3000 mass spectrometer with electrospray ionization with ion-trap detection in both positive and negative modes. Mass signals are provided with their relative abundance to the strongest one. For Gd^{3+} complexes, only the one containing the most abundant isotope is stated. HR MS spectra were recorded on an LTQ Velos Pro or Orbitrap ELITE mass spectrometer by Thermo.

HPLC measurements were performed on a ReproSil Gold C8 5 μm 150×4.6 mm column with a flow rate of 1 ml·min^{-1} using UV-absorption detection at 210 nm and 256 nm. The following methods with linear v/v gradients of water/acetonitrile were used: method **A**: 5% ACN to 90% ACN with 10 ppm v/v trifluoroacetic acid (TFA) in 5 min, then 90% ACN with 10 ppm v/v TFA for 5 min; method **B**: 0% ACN to 10% ACN with 5 ppm v/v TFA in 10 min, then 10% ACN to 25% ACN with 5 ppm v/v

TFA in 10 min, then 25% ACN to 95% ACN with 5 ppm v/v TFA in 10 min, then 95% ACN to 99% ACN with 1 ppm v/v TFA in 5 min; method **C**: 0% ACN to 10% in 10 min, then 10% ACN to 25% ACN in 10 min, then 25% ACN to 95% in 10 min, then 95% ACN to 99% ACN in 5 min.

Thin-layer chromatography (TLC) was performed on TLC aluminium sheets silica gel 60 F254 (Merck). UV light or dipping in 2% $KMnO_4$/10% Na_2CO_3 or 5% aqueous $CuSO_4$ were used for detection.

Elemental analyses were performed at the Institute of Macromolecular Chemistry (Academy of Sciences of the Czech Republic, Prague).

Synthesis of redox sensitive complex $[Gd(L^1)]^-$–SS–N_3

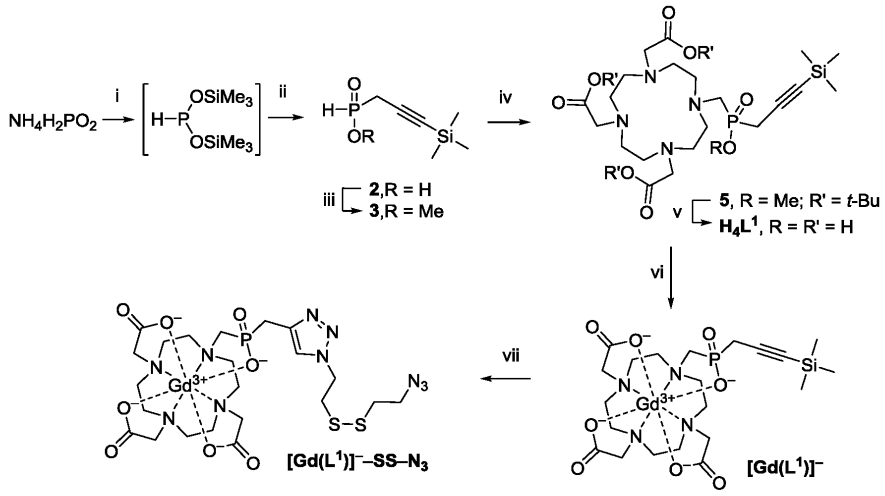

Reaction conditions and yields: i) Hexamethyldisilazane, under Ar, 105 °C, 12 h ii) 3-Bromo-1-(trimethylsilyl)-1-propyne (**1**)/CH_2Cl_2, under Ar, -10 °C to rt, 24 h, 54 % iii) methyl chloroformate, pyridine/CH_2Cl_2, reflux, 15 min, 97 % iv) *t*Bu_3DO3A·HBr (**4**·HBr), $(CH_2O)_n$/MeCN (dry), 65 °C, 3 days, ~90 % v) 1. 85% aq. HCOOH, 65 °C, 4 days, 2. 1,5% aq. HCl, rt, overnight, 78% vi) $GdCl_3 \cdot 5H_2O$/aq. NH_4OH, pH 4,8, rt, overnight, ~60 % vii) 1,6-bis(azido)-3,4-dithiahexane (**6**), $CuSO_4$, NaF, Sodium Ascorbate/ THF:*i*PrOH:H_2O (1:1:2), rt, 12 h, ~50%

3-(Trimethylsilyl)prop-2-ynylphosphinic acid (2)

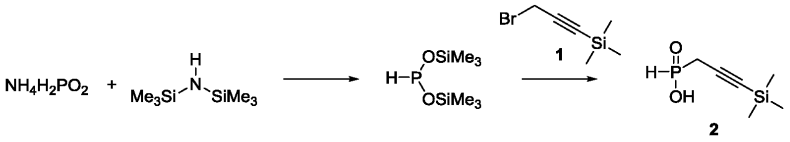

$NH_4H_2PO_2$ (5.0 g; 60 mmol) was securated in a 50 ml three-neck flask equipped with an argon inlet, a reflux condenser with vacuum trap and a septum. Hexamethyldisilazane (15 ml; 72 mmol) was added and the reaction mixture was stirred at 105 °C for 12 h under gentle flow of argon. In the course of the reaction, $NH_4H_2PO_2$ dissolved and ammonia evolved. The reaction mixture was then cooled to –10 °C and diluted with anhydrous dichloromethane (30 ml). Under an argon atmosphere, alkylation agent **1** (3.1 g; 16.2 mmol) was slowly added *via* syringe and the mixture was left to warm to RT under stirring. After 24 h, the reaction was terminated by addition of anhydrous EtOH (10 ml) and the reaction mixture was evaporated to dryness. The reaction mixture was co-evaporated two times with anhydrous EtOH (15 ml) and the remaining matter was dissolved in $CHCl_3$ (20 ml) and quickly washed with 3% HCl (2×20 ml). The combined aqueous phases were extracted with $CHCl_3$ (20 ml). The organic phases were combined, dried with Na_2SO_4 and volatiles were removed with rotary evaporator at 50 °C to yield (**2**) (1.54 g; 54 %) as a colorless oil.

The product contained ca 3% (by ^{31}P NMR) of bis(3-(trimethylsilyl)prop-2-ynyl)phosphinic acid, which does not react in the next step, and therefore, the crude **2** can be used without further purification. For analytic purposes, the compound **2** was purified by flash column chromatography on silica (EtOAc:MeOH = 5:4 v/v).

TLC: (EtOAc:MeOH = 5:4 v/v), R_f = 0.50, $KMnO_4$; ^1H NMR (299.94 MHz, $CDCl_3$): δ 0.17 (s, 9H, CH_3); 2.83 (dd, $^2J_{HP}$ = 20.1, $^3J_{HH}$ = 1.8, 2H, CH_2); 7.11 (d, $^1J_{HP}$ = 584, 1H, P–*H*); 10.9 (bs, O*H*); ^{13}C NMR (75.43 MHz, $CDCl_3$): δ –0,1 (s, CH_3); 24.6 (d, $^1J_{CP}$ = 84.5, CH_2); 86.8 (d, $^3J_{CP}$ = 7.5, C–*C*–Si); 99.4 (d, $^2J_{CP}$ = 8.7, P–C–*C*); ^{31}P NMR (121.42 MHz, $CDCl_3$): δ 27.8 (dt, $^1J_{HP}$ = 584, $^2J_{HP}$ = 20.0).

Methyl 3-(trimethylsilyl)prop-2-ynylphosphinate (3)

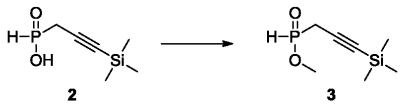

2 **3**

Phosphinic acid **2** (1.64 g; 9.31 mmol) was dried in a 100 ml flask by triple co-evaporation with anhydrous EtOH (5 ml). After evaporation, phosphinic acid was dissolved in anhydrous CH_2Cl_2 (19 ml), and methyl chloroformate (0.88 g; 9.31 mmol) was added. Anhydrous pyridine (0.74 g; 9.31 mmol) was added dropwise with stirring. After evolution of CO_2, the flask was equipped with a reflux condenser and the mixture was heated to reflux for 15 min. The reaction mixture was then cooled to RT and washed with 3% aqueous HCl (3×20 ml) and brine (20 ml). Combined aqueous phases were extracted with CH_2Cl_2 (2×20 ml) and organic phases were dried with Na_2SO_4, and solvent was removed with a rotary evaporator at 50 °C to yield methylester **3** (1.72 g; 97%) as a colorless liquid.

^{1}H NMR (299.94 MHz, $CDCl_3$): δ 0.12 (s, 9H, SiCH_3); 2.81 (d, $^2J_{HP}$ = 18.9, 2H, CH_2); 3.81 (d, $^3J_{HP}$ = 12.0, 3H, OCH_3); 7.16 (d, $^1J_{HP}$ = 585, 1H, P–*H*); ^{13}C NMR (75.43 MHz, $CDCl_3$): δ 0.3 (s, Si*C*H$_3$), 21.9 (d, $^1J_{CP}$ = 91.3, *C*H$_2$); 53.1 (d, $^2J_{CP}$ = 7.2, P–C–*C*); 89.9 (d, $^3J_{CP}$ = 8.5, C–*C*–Si); 93.4 (d, $^2J_{CP}$ = 10.9, O*C*H$_3$); ^{31}P NMR (121.42 MHz, $CDCl_3$): δ 31.5 (bd, $^1J_{HP}$ = 571.3).

Methyl ({4,7,10-tris[(*tert*-butyloxykarbonyl)methyl]-1,4,7,10-tetraazacyclododecane-1-yl}methyl)-3-(trimethylsilyl)prop-2-ynylphosphinate (5)

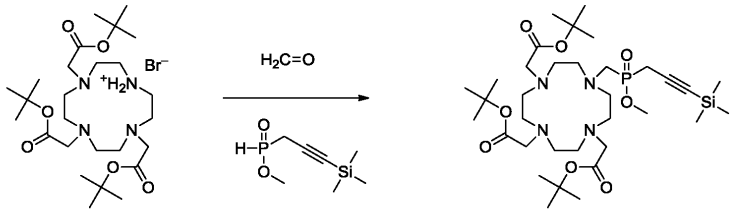

4 **3** **5**

*t*Bu$_3$DO3A·HBr (**4**·HBr, 1.000 g; 1.679 mmol) was placed into a 25 ml flask, and methyl ester **3** (336 mg; 1.763 mmol) and paraformaldehyde (53 mg; 1.763 mmol) were added under stirring. Anhydrous acetonitrile (10 ml) was then added, the flask was tightly closed, and the mixture was heated in an oil bath at 65 °C. The progress of the reaction was monitored with ^{31}P NMR spectra in 12-h intervals. A decrease in signal intensity of the starting compound **3** at 30 ppm (bd, $^{1}J_{HP}$ = 571 Hz) and increase in the product **5** signal at 43 ppm (s) was observed. In addition, approximately 3% of acid **2** was detected. Over time, the reaction mixture turned from a white suspension into pale brown clear solution. After 3 days, more than 95% of ester **3** had reacted, and solvent was removed with a rotary evaporator. The obtained oil was dissolved in minimal amount of hot MeOH, the solution was cooled, and the product was precipitated by addition of diethylether. The product **5** was collected by filtration (S3 frit), washed with diethylether (5 ml) and air-dried, affording 1.095 g (~90%) of off-white powder.

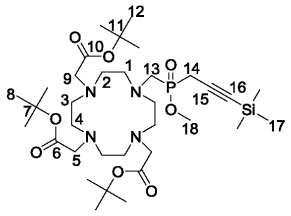

TLC: (EtOAc:EtOH:25% aq. NH_4OH = 60:33:7 v/v/v), R_f = 0.70, $KMnO_4$; ^{1}H NMR (299.94 MHz, $CDCl_3$): δ 0.07 (s, 9H, H-17); 1.40 (bs, 27H, H-8, H-12); 2.62 (d, $^{2}J_{HP}$ = 18.3, 2H, H-13); 2.60–3.60 (m, 24H, H-1-5, H-9, H-14); 3.75 (d, $^{3}J_{PH}$ = 10.8, 3H, H-18); ^{13}C NMR (75.43 MHz, $CDCl_3$): δ 0.1 (s, C-17); 23.2 (d, $^{1}J_{CP}$ = 84.8, C-14); 29.4 (s ,C-12); 30.6 (s, C-8); 51.2 (s, C-2); 51.8 (s, C-1,3); 52.2 (d, $^{2}J_{CP}$ = 97.8, C-13); 53.8 (s, C-4); 54.9 (s, C-9); 56.3 (s, C-5); 58.3 (d, $^{2}J_{CP}$ = 7.2, C-18); 84.6 (s, C-7); 86.1 (s, C-11); 92.1 (d, $^{3}J_{CP}$ = 8.9, C-16); 98.3 (d, $^{2}J_{CP}$ = 12.1, C-15); 170.2 (s, C-6); 174.2 (s, C-10); ^{31}P NMR (121.42 MHz, CD_3OD): δ 44.3 (bs); MS(+): 717.7 ($[M+H]^+$).

10-({Hydroxy[3-(trimethylsilyl)prop-2-ynyl]phosphoryl}methyl)-1,4,7,10-tetraazacyclododecane-1,4,7-triacetic acid (H_4L^1)

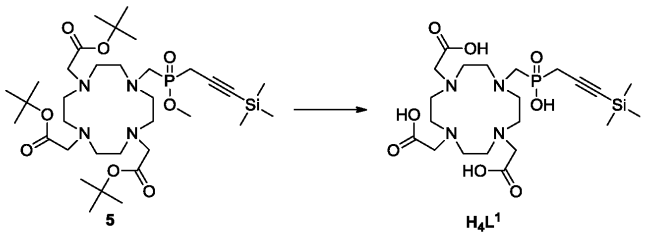

Compound **5** (1.000 g; 1.395 mmol) was dissolved in 85% formic acid (10 ml) in a 25-ml flask equipped with a magnetic stirring bar. The flask was closed, and the reaction mixture was heated in an oil bath at 65 °C for 4 days. Solvent was removed *in vacuo*, and the resulting oil was co-evaporated with water (3×5 ml) to remove the remaining formic acid. The obtained pale brown oil was dissolved in 1.5% aqueous HCl (10 ml) and stirred at RT overnight. Solvent was removed with a rotary evaporator. The resulting oil was dissolved in minimal amount of hot MeOH, the solution was cooled, and the product was precipitated by addition of diethylether. The product was collected by filtration on S3 frit, washed with diethylether (5 ml), dried in a vacuum and left to equilibrate at ambient conditions for three weeks. Product **H_4L^1** (0.694 g; 78%) was obtained as dihydrochloride sesquihydrate in form of an off-white powder.

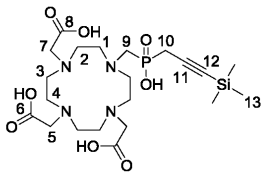

TLC: (EtOH:10% aq. AcOH = 8:2 v/v), R_f = 0.40; (EtOAc:EtOH:25% aq. NH_4OH = 60:33:7 v/v), R_f = 0.10, $CuSO_4$ or $KMnO_4$; ^{1}H NMR (299.94 MHz, D_2O): δ 0.07 (s, 9H, H-13), 2.64 (t, $^2J_{PH}$ = 18.6; 2H, H-10) 2.75–3.95 (bm, 24H; H-1-5, H-7, H-9); ^{13}C NMR (75.43 MHz, D_2O): δ 1.5 (s, C-13); 26.5 (d, $^1J_{CP}$ = 91.7; C-10); 50.5 (s, C-2); 51.6 (s, C-1,3); 51.8 (d, $^2J_{CP}$ = 98.3; C-9); 53.4 (s, C-4); 54.3 (s, C-7); 55.7 (s, C-5); 91.3 (d, $^3J_{CP}$ = 7.2, C-12); 102.8 (d, $^2J_{CP}$ = 10.5; C-11); 172.2 (s, C-6); 177.1 (s, C-8); ^{31}P

NMR (121.42 MHz, D_2O): δ 21.0–26.5 (br s); EA: calc. for $\mathbf{H_4L^1}\cdot 2HCl\cdot 1.5H_2O$, $C_{21}H_{44}Cl_2N_4O_{9.5}PSi$, M = 634.56: C 39.76; H 6.99; N 8.83; Cl 11.18; found: C 40.03; H 7.02; N 8.64; Cl 11.23; MS(+): 535.1 (51$[M+H]^+$); 557.1 (100$[M+Na]^+$); 573.1 (50$[M+K]^+$); MS(–): 532.9 (100$[M–H]^-$); 570.9 (21$[M+K–H]^+$).

$(NH_4)[Gd(L^1)]$ complex

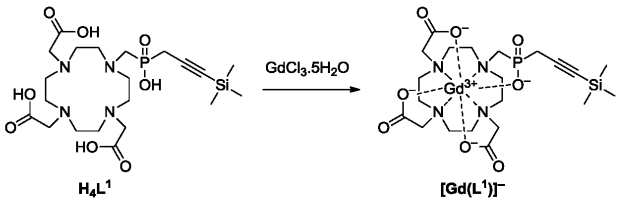

$GdCl_3\cdot 5H_2O$ (158 mg, 0.60 mmol) was added to a solution of $\mathbf{H_4L^1}$ (350 mg, 0.55 mmol) in water (10 ml) with stirring. The pH of the solution was adjusted to 4.8 with 5% aqueous NH_3 and the mixture was left at RT overnight. Solvent was then evaporated *in vacuo*, and the product was purified by reversed-phase chromatography (40 g YMC DispoPackAT 25-ODS cartridge) with a water–acetonitrile gradient and 10 ppm trifluoroacetic acid modifier. Fractions containing the product were collected and lyophilized to obtain $(NH_4)[Gd(\mathbf{L^1})]$ (253 mg, ~60% yield) as a white powder.

MS(+): 712.1 (66$[[Gd(\mathbf{L^1})]+H+Na]^+$); 734.1 (100$[[Gd(\mathbf{L^1})]+2Na]^+$); 750.0 (97$[[Gd(\mathbf{L^1})]+Na+K]^+$); MS(–): 615.9 (15$[[Gd(\mathbf{L^1})]–TMS]^-$); 688.0 (100$[Gd(\mathbf{L^1})]^-$); HPLC: Program **A**: Retention time = 5.97 min.

Na[Gd(L^1)]–SS–N_3 complex

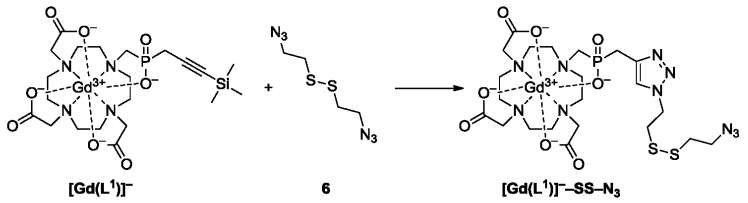

(NH_4)[Gd($\mathbf{L}^1$)] (250 mg, 0.36 mmol) was dissolved in a mixture of water (10 ml), *i*PrOH (5 ml) and THF (5 ml) in a 50-ml flask. Then 1,6-bis(azido)-3,4-dithiahexane (456 mg, 2.23 mmol), 1 M aqueous NaF (450 µl) and 1 M aqueous $CuSO_4$ (90 µl) were added, and the flask was sealed with a septum. Using a needle, a gentle stream of argon was passed through the reaction mixture for 3 min with sonication. Then, 1 M aqueous sodium ascorbate (225 µl) was added, and the reaction mixture was stirred for 12 h at RT under an argon atmosphere. The solvent was removed with a rotary evaporator, and the product was purified by reversed-phase chromatography (40 g YMC DispoPackAT 25-ODS cartridge) with a water–acetonitrile gradient and 10 ppm trifluoroacetic acid modifier. Fractions containing the product were collected and lyophilized to obtain Na[Gd($\mathbf{L}^1$)]–SS–N_3 (153 mg, approx. 50% yield) as a yellowish sticky solid.

MS(+): 822.2 ([[Gd($\mathbf{L}^1$)]–SS–N_3+2H]$^+$); MS(–): 819.1 ([[Gd($\mathbf{L}^1$)]–SS–N_3]$^-$); HRMS (ESI): calcd. for: $C_{33}H_{37}O_8N_{10}GdPS_2$ ([[Gd($\mathbf{L}^1$)]–SS–N_3+2H]$^+$): 822.12104; found: 822.12158; calcd. for: $C_{33}H_{36}O_{10}N_{10}GdNaPS_2$ ([[Gd($\mathbf{L}^1$)]–SS–N_3+H+Na]$^+$): 844.10298; found: 844.10355; HPLC: Program **B**: Retention time = 18.6 min.

Synthesis of pH sensitive complex $[Gd(L^2)]^-$–NHN–N_3

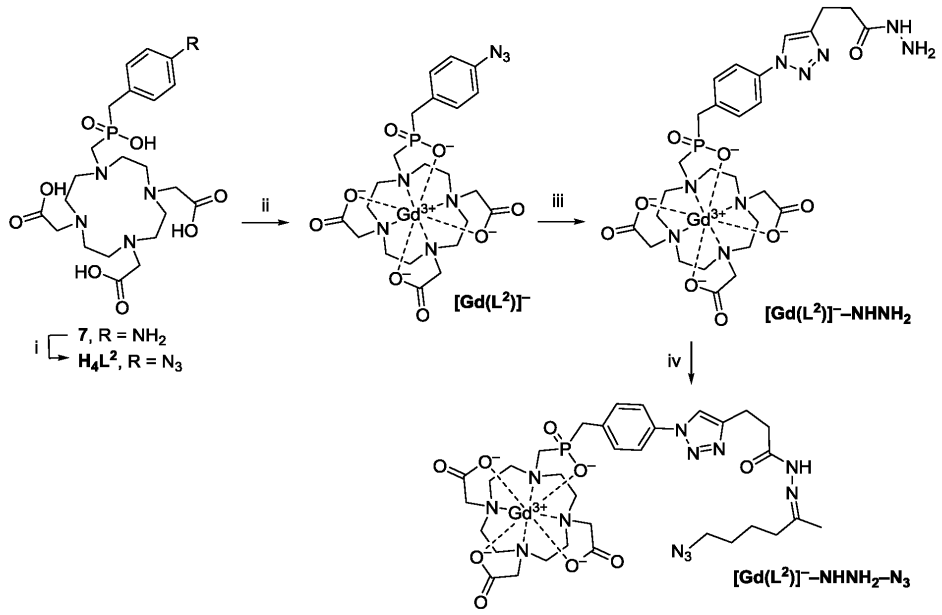

Reaction conditions and yields: i) 1. $NaNO_2$/aq. HCl 0 °C, 25 min; 2. NaN_3/aq. HCl 0 °C, 25 min, 70 % ii) $GdCl_3 \cdot 5H_2O$/aq. NH_4OH, pH 9, rt, overnight, ~70 % iii) pent-4-ynehydrazide (**8**), $CuSO_4$, Sodium Ascorbate/ THF:H_2O (1:1), rt, overnight, ~60 % iv) 6-azido-hexan-2-one (9), AcOH, $MgSO_4$/MeOH (dry), reflux, 3 days, ~30 %

10-({Hydroxy[4-azidobenzyl]phosphoryl}methyl)-1,4,7,10-tetraazacyclododecane-1,4,7-triacetic acid (H_4L^2)

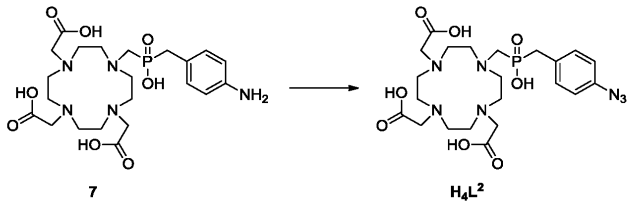

A solution of 10-({hydroxy[4-aminobenzyl]phosphoryl}methyl)-1,4,7,10-tetraazacyclododecane-1,4,7-triacetic acid tetrahydrochloride (**7**·4HCl, 653 mg; 0.97 mmol) in a mixture of deionized water (5 ml) and 6 M HCl (1 ml) in a 25-ml flask was cooled to 0 °C. Then, $NaNO_2$ (95 mg; 1.38 mmol) was slowly added, and the reaction mixture was stirred at 0 °C for 25 min. NaN_3 (104 mg; 1.60 mmol) was then slowly added, and the reaction mixture was stirred at 0 °C for another 25 min. The reaction

mixture was placed in a rotary evaporator and twice co-evaporated with water (3 ml) to remove excess HCl. The product was purified by reversed-phase chromatography (40 g YMC DispoPackAT 25-ODS cartridge) with a water–acetonitrile gradient and 10 ppm trifluoroacetic acid modifier. Fractions containing the product were collected, lyophilized and left for three weeks to equilibrate in ambient air in the dark to obtain (**H_4L^2**) (495 mg; 70% yield) as white powder, which turns brown when exposed to light.

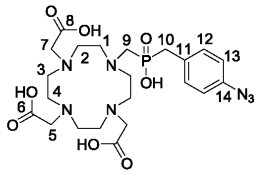

TLC: (EtOH:25% aq. NH_4OH = 8:2 v/v), R_f = 0.25, UV, $KMnO_4$ or $CuSO_4$; ^{1}H NMR (299.94 MHz, DMSO-d_6): δ 2.97–3.60 (bm, 24H; H-1-4, H-9, H-10); 3.64 (bm, 2H, H-5); 4.08 (bm, 4H, H-7); 7.03 (d, $^3J_{HH}$ = 7.9; 2H, H-13); 7.29 (d, J = 7.9 Hz, 2H, H-13); ^{13}C NMR (75.43 MHz, DMSO-d_6): δ 36.5 (d, $^1J_{CP}$ = 85.6; C-10); 49.9 (s, C-2); 50.8 (s, C-4); 51.3 (s, C-1); 50.6 (d, $^2J_{CP}$ = 105.1; C-9); 51.8 (s, C-3); 54.1 (s, C-5); 54.8 (s, C-7); 119.8 (d, $^4J_{CP}$ = 1.6; C-13); 130.2 (d, $^2J_{CP}$ = 10.0; C-11); 132.5 (d, $^3J_{CP}$ = 4.8; C-12); 138.3 (s, C-14); 170.1 (s, C-8); 172.6 (s, C-6); ^{31}P NMR (121.42 MHz, DMSO-d_6): δ 38.1 (s); EA: calc. for **H_4L^2**·3.4HCl·3H_2O, $C_{22}H_{43.4}Cl_{3.4}N_7O_{11}P$, M = 733.53: C 36.02; H 5.96; N 13.37, Cl 16.43; found: C 36.06; H 5.74; N 12.87, Cl 16.49; MS(+): 555.9 (100$[M+H]^+$); 577.9 (20$[M+Na]^+$); 593.9 (16$[M+K]^+$); MS(–): 553.7 ($[M–H]^-$); HPLC: Program **A**: Retention time = 5.79 min.

(NH_4)[Gd(L^2)] complex

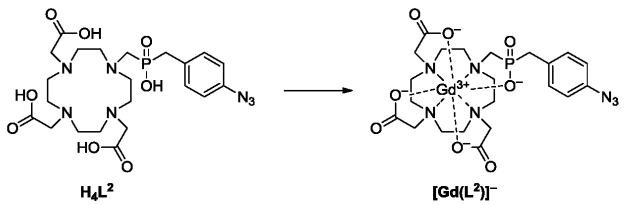

$GdCl_3 \cdot 5H_2O$ (126 mg, 0.49 mmol) was added to a solution of $\mathbf{H_4L^2}$ (300 mg, 0.41 mmol) in water (6 ml) with stirring. The pH of the solution was adjusted to 9.0 with 3% aqueous NH_4OH, and the mixture was left at RT overnight. The solvent was removed with a rotary evaporator, and the resulting solid was purified by flash chromatography (Buchi Sepacore® Silica 25 g cartridge) with an EtOH:25% aqueous NH_4OH (10:1 v/v) mobile phase. Fractions containing the product were collected and dried on a rotary evaporator. The product $(NH_4)[Gd(\mathbf{L^2})]$ (227 mg, ~70% yield) was obtained after lyophilization from water (10 ml) as a pale powder that turns dark when exposed to light.

TLC: (EtOH:25% aq. NH_4OH = 5:1 v/v), R_f = 0.65, UV, $KMnO_4$; MS(–):707.4 $(Gd(\mathbf{L^2})]^-$); HPLC: Program **A**: Retention time = 5.69 min.

$(NH_4)[Gd(L^2)]^-$–$NHNH_2$ complex

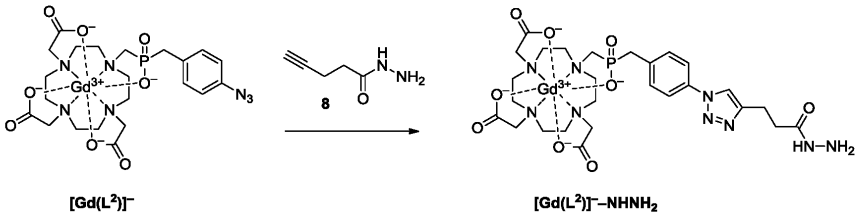

$(NH_4)[Gd(\mathbf{L^2})]$ (203 mg; 0.28 mmol) and pent-4-ynehydrazide **8** (62 mg, 0.55 mmol) were dissolved in a mixture of water (1.5 ml) and THF (1.5 ml) in a 4-ml vial equipped with a septum and magnetic stirring bar. Then, 1 M aqueous $CuSO_4$ (32 µl) was added, and the mixture was bubbled under a brisk stream of argon for 3 min. Subsequently 1 M aqueous sodium ascorbate (100 µl) was added, and the solution was stirred at RT overnight in the dark. The solvent was removed with a rotary evaporator, and the resulting solid was purified with reversed-phase chromatography (40 g YMC DispoPackAT 25-ODS cartridge) with a water–acetonitrile gradient and 10 ppm trifluoroacetic acid modifier. Fractions containing the product were collected and lyophilized to obtain $(NH_4)[Gd(\mathbf{L^2})]$–$NHNH_2$ (154 mg, ~60% yield).

MS(+): 821.5 (33[[Gd(**L**^{2})]–NHNH$_2$+2H]$^+$); 844.6 (66[[Gd(**L**^{2})]–NHNH$_2$+H+Na]$^+$); 866.6 (100[[Gd(**L**^{2})]–NHNH$_2$+H+K]$^+$); MS(–): 820.5 ([[Gd(**L**^{2})]–NHNH$_2$–H]$^-$); HPLC: Program **B**: Retention time = 10.5 min.

(NH$_4$)[Gd(L^2)]–NHN–N$_3$ complex

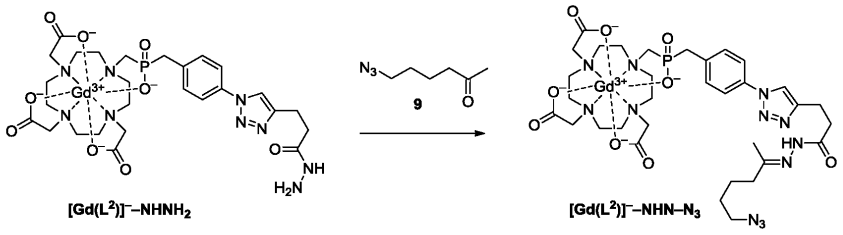

(NH$_4$)[Gd(**L**^{2})]–NHNH$_2$ (100 mg; 0.12 mmol) and 6-azido-hexan-2-one **9** (137 mg; 0.97 mmol) were dissolved in anhydrous MeOH (8 ml) in a 25-ml flask equipped with a reflux condenser with a chlorcalcium tube. Glacial acetic acid (22 mg; 0.37 mmol) and anhydrous MgSO$_4$ (1.00 g; 8.33 mmol) were added, and the reaction mixture was heated to reflux under chlorcalcium tube for 3 days. The solvent was removed with a rotary evaporator, and the resulting solid was purified with reversed-phase chromatography (40 g YMC DispoPackAT 25-ODS cartridge) with a water–acetonitrile gradient. Fractions containing the product were combined and lyophilized to obtain **(NH$_4$)[Gd(L^2)]–NHN–N$_3$** (33 mg, ~30% yield).

MS(–): 944.3 ([M–H]$^-$); HRMS (ESI): calcd. for: C$_{33}$H$_{47}$O$_9$N$_{12}$GdP ([[Gd(**L**^{2})]–NHN–N$_3$]$^-$): 944.25731; found: 944.25711; HPLC: Program **C**: Retention time = 18.9 min.

Preparation of ND-HPMA-Gd conjugates

Nanodiamonds (NDs) (MSY 0–0.05, Microdiamant, Switzerland) were oxidized by air in a furnace at 510 °C for 4 h; treated with a mixture of HF and HNO$_3$ (2:1) at 160 °C for 2 days; and washed with water, 1 M NaOH, 1 M HCl and water. Purified ND powder was irradiated in an external target holder for 21 hours with a 16.6 MeV electron beam (1.25 × 10^{19} particles cm^{-2}) from an MT-25 microtron.

The irradiated material was annealed at 900 °C for 1 h and subsequently oxidized for 4 h at 510 °C. The resulting powder was again treated with a mixture of acids and washed with NaOH, HCl and water, providing a colloidal solution of ND-COOH.

Poly(vinylpyrrolidone) (MW = 10,000, 136 mg) was dissolved in water (120 ml) and sonicated for 10 min in an ultrasonic bath. ND-COOH colloid (24 ml, 2 mg ml^{-1}, filtered using a 0.4 μm GMF filter) was added, and the mixture was stirred for 24 h. The colloid was then concentrated by centrifugation. NDs (in approximately 3 ml solvent) were resuspended in ethanol (48 ml). Tetraethyl orthosilicate (360 μl) and 3-(trimethoxysilyl)propylmethacrylate (120 μl) were added, and the mixture was sonicated for 20 s in an ultrasonic bath. Ammonia (25%, 2 ml) then was added. The reaction mixture was stirred for 14 h. The product was purified by centrifugation, washed with methanol and transferred to 0.3 ml of DMSO using a rotary evaporator. (2-Hydroxypropyl)methacrylamide (HPMA) (735 mg), N-propargyl acrylamide (315 mg) and 2,2-azobis(2-methylpropionitrile) (AIBN, 300 mg) were dissolved in DMSO (3 ml). The mixture was filtered using a 0.4 μm glass microfiber microfilter. Methacrylate-terminated NDs (48 mg) dispersed in 0.3 ml DMSO were added. The reaction proceeded for 3 days under argon at 55 °C. The particles were purified by centrifugation with methanol. Alkyne-modified HPMA-coated NDs were decorated with azide-modified Gd^{3+} complexes using Cu(I)-catalyzed azide-alkyne cycloaddition (CuACC). HPMA-coated NDs (10 mg in a final reaction volume of 12.8 ml 50 mM HEPES buffer, pH 7.4) were mixed with non-cleavable Gd^{3+} complex (**$NH_4[Gd(L^2)]$**), cleavable Gd complex with hydrazone (**$NH_4[Gd(L^2)]$–NHN–N_3**) or a disulfide linker (**$Na[Gd(L^1)]$–SS–N_3**) in final concentrations of 0.96, 1.92 and 2.4 mM, respectively, pre-mixed 0.32 mM $CuSO_4$ and 0.64 mM tris(3-hydroxypropyltriazolylmethyl)amine (THPTA) ligand and a freshly prepared solution of sodium ascorbate (5 mM). The reaction mixture was well-sealed, left for 1 h with no stirring and washed by centrifugation with water (Gd^{3+} conjugates with non-cleavable, ND-HPMA-Gd, and disulfide, ND@redox, linkers) or methanol (Gd^{3+} conjugates with hydrazone linker, ND@pH). The resulting nanosensors were stored in water (ND-HPMA-Gd and ND@redox) or in dry methanol (ND@pH) at 4 °C.

Characterization of ND-polymer-Gd nanosensors

The stability and surface charge of HPMA-coated NDs with Gd^{3+} complexes were tested in solutions later used for further experiments: 50 mM citric acid (pH 2.0), 50 mM acetate buffer (pH 4.5), 50 mM HEPES buffer (pH 7.4), 50 mM TRIS buffer (pH 8.5) and 10× concentrated PBS. Dynamic light scattering (DLS) and zeta potential were recorded with a Zetasizer Nano ZS system (Malvern Instruments) at 37 °C. Sample concentrations were 0.1 mg ml^{-1}.

To prepare the samples for transmission electron microscopy (TEM), carbon-coated copper grids were placed into a UV-ozonizing chamber (UV/Ozone Pro Cleaner Plus, Bioforce Nanosciences) for 15 min. Then, a droplet of jetPEI (Polyplus tranfection, cat no. 101-10) was placed on the grid. After 10 min incubation, it was removed with a piece of tissue. Then, a droplet of aqueous solution of NDs (0.05 mg ml^{-1}) was placed on the grid, and after 3 min incubation, liquid was removed with a piece of tissue. TEM pictures were captured using a JEOL JEM-1011 electron microscope operated at 80 kV.

Total amounts of Gd^{3+} complexes conjugated to HPMA-coated NDs were estimated using inductively coupled plasma atomic emission spectroscopy (ICP AES). The analysis was performed using a Spectro Arcos SOP ICP AES spectrometer, power 1450 W, sample flow 2 ml min^{-1}.

Kinetics of release of Gd^{3+} complex from the conjugate

ND@pH: A 5-µl aliquot of NDs colloid (20 mg ml^{-1} in water) was diluted with 95 µl buffer (either 50 mM citrate, pH 2.0; 50 mM acetate, pH 4.5 or 50 mM HEPES, pH 7.4). The mixture was incubated for a certain time (30 s, 1, 2, 4 and 60 min for pH 2.0; 2.5, 5, 10, 20, 40 min and 8 h for pH 4.5; and 2, 6, 12 and 24 hours for pH 7.4) at 37 °C. The cleavage reaction was then stopped by addition of HEPES buffer (300 mM, pH 8.0) to the mixture (100 µl for pH 2.0, 20 µl for pH 4.5). NDs were centrifuged (10 min 55,000 rcf, 4 °C), and the supernatant was removed and diluted with 2% HNO_3 for ICP MS measurements. A control representing time 0 s was set up with the opposite order of mixing: first, the NDs colloid was diluted in HEPES buffer, then cleavage buffer (acidic conditions) was added. The non-cleavable ND-HPMA-Gd conjugate was used as a control at the 0, 15, 30, 45 and

60 minutes and processed under the same conditions. All samples were prepared in duplicate. Concentrations of Gd^{3+} complexes in solutions were analyzed in duplicate (performed with two independent samples, where each was measured twice (4 results)) using an ICP MS 7700 (Agilent Technologies) instrument.

ND@redox: A 5-µl aliquot of NDs colloid (20 mg ml^{-1} in water) was diluted with 95 µl buffer (50 mM HEPES buffer, pH 7.4, or 50 mM TRIS, pH 8.5). A solution of glutathione (final concentrations of 1, 5 and 10 mM) was added. The mixture was incubated for a certain time (2, 5, 10, 30 and 60 min) at 37 °C under inert conditions. The cleavage reaction was then stopped by addition of 6-maleimidohexanoic acid (diluted in 10% DMSO in 0.5 M phosphate buffer, pH 7.0, final concentration 100 mM). NDs were centrifuged (10 min 55,000 rcf, 4 °C), and the supernatant was removed and diluted with 2% HNO_3 for ICP MS measurements. A control representing time 0 s was set up with the opposite order of mixing: 6-maleimidohexanoic acid was first added to NDs colloid diluted in buffer and then glutathione was added. The non-cleavable ND-HPMA-Gd conjugate was used as a control at the 0, 15, 30, 45 and 60 minutes and processed under the same conditions. All samples were prepared in duplicate. Concentrations of Gd^{3+} complexes in solutions were analyzed in duplicate (performed with two independent samples, where each was measured twice (4 results)) using an ICP MS 7700 (Agilent Technologies) instrument.

Preparation of Britton-Robinson buffers (measurements in Supplementary Figure 8)

Britton-Robinson buffers (with equal composition and ionic strength) were prepared according to the established procedure: 0.5 M Britton-Robinson buffer at pH 3.29 was prepared (by mixing 0.0667 g of NaOH, 0.0664 ml CH_3COOH, 0.114 ml H_3PO_4, 0.103 g H_3BO_3 and 1.729 g KCl). For T_1 measurements, stock buffer was diluted to 50 mM concentration and pH was adjusted to required pH (3.8, 4.5, 5.5, 6.2 and 6.9) by NaOH. The conductivity of all solutions was adjusted to the same value (6.40 mS) by addition of KCl.

Theoretical model of NV relaxometry influenced by the release of Gd^{3+} complex

The total NV relaxation rate is:

$$\Gamma_{total} = \Gamma_{int} + \Gamma_{external} \quad (1)$$

The intrinsic decay rate Γ_{int} is attributed to spin noise (impurities) in the diamond lattice like Orbach or Raman process[7]. The external part $\Gamma_{external}$ is attributed to the randomly distributed Gd^{3+} complex locating in the polymer shell surrounding ND, and can be written as[8]:

$$\Gamma_{extrernal} = 3g_{NV}\mu_B \sum_i \frac{g_i\mu_i}{\hbar^2} < B_i^2 > \frac{\tau_{c_i}}{1+\omega_0^2{\tau_{c_i}}^2} \quad (2)$$

Where g_i is the g-factor, μ_i the magneton and τ_{c_i} is the typical correlation time of the spin species with index i.

As in equation (1) the decay rates just sum up, we can also combine several decay channels that are kept constant over time. We therefore consider the sample ND-HPMA (without Gd^{3+} complex) has an intrinsic relaxation time, and add another decay channel induced by Gd^{3+} for other samples (with Gd^{3+} complex).

Starting with a spin S_j placed at the distance r_j to the NV to derive an expression for $< B_i^2 >$, the spin creates a time fluctuating magnetic field B_j at the position of the NV:

$$\mathbf{B_j} = \frac{\mu_0}{4\pi} g_j \mu_j \cdot \frac{1}{r_j^3}\left(\mathbf{S_j} - \frac{3(\mathbf{S_j}\cdot\mathbf{r_j})\cdot\mathbf{r_j}}{r_j^2}\right) \quad (3)$$

Weak magnetic field components along the NV quantization axis (z) only lead to a detuning off the NV resonance, but don't introduce a change in the spin level populations, as the x and y components will do. Therefore we can neglect the z-component of the B field:

$$B_{\perp,j}^{\ 2} = < B_{x,j}^2 > + < B_{y,j}^2 > \quad (4)$$

We assume the spin to be in a purely mixed state. Its density matrix ρ can be written as:

$$\rho = \frac{1}{2S+1} E_{2S+1} \quad (5)$$

Than $B_{\perp,j}^{\ 2}$ can be expressed as:

$$B_{\perp,j}^{\ 2} = Tr\left(\rho B_{x,j}^2\right) + Tr\left(\rho B_{y,j}^2\right) = \left(\frac{\mu_0}{4\pi} g_e \mu_B\right)^2 \cdot C_s \cdot \frac{2+3\sin^2(\alpha_j)}{r_j^6} \quad (6a)$$

with:

$$C_s = \frac{1}{2S+1}\sum_{m=-S}^{S} m^2 = \frac{S(S+1)}{3} \quad (6b)$$

In the following we consider spins randomly distributed in a layer with thickness δd and the volume density of σ_i on the surface of a spherical diamond with diameter d_o. The total magnetic field experienced by the NV center for all spin species can then be summarized in spherical coordinates:

$$< B_i^2 >= \sum_j B_{\perp,j}^2 = \left(\frac{\mu_0}{4\pi} g_i \mu_i\right)^2 \cdot C_s \cdot \sigma_i \int_{\frac{d_o}{2}}^{\frac{d_0}{2}+\delta d} dr' \int_0^{2\pi} d\phi \int_0^{\pi} d\theta \sin\theta \frac{2+3\sin^2(\alpha(\theta,\phi))}{r(r\prime,\delta r,\theta,\phi)^4} \quad (7a)$$

With:

$$\sin^2\alpha = \sin^2\theta \quad (7b)$$

And

$$r = \sqrt{r'^2 - \delta r^2 \sin^2\theta} + \delta r\cos\theta \quad (7c)$$

When moving δr from the center of a spherical shaped nanodiamond along the NV spin quantization axis (parallel to the NV axis).

If the NV is moved on a path perpendicular to its quantization axis, then $\sin^2\alpha$ and r have the following expression[8]:

$$\sin^2\alpha = \cos^2\theta + \sin^2\theta\sin^2\phi \quad (7d)$$

And

$$r = \sqrt{r'^2 - \delta r^2 \sin^2\theta} + \delta r\cos\theta \quad (7e)$$

The total fluctuation rate of the Gd^{3+} complex is $R = 1/\tau_c = R_{dip} + R_{vib}$where R_{dip} is due to the inter bath dipolar coupling while R_{vib} is caused by intrinsic vibrational spin relaxation of the Gd^{3+}

complex in solution. In current study, we adapted the typical value of $R_{vib} = 50\ GHz$ for Gd^{3+} complex[9].

In the following, we calculate the R_{dip}:

The spin-spin interaction of two spins k and l can be describe by the following Hamiltonian:

$$\mathbf{H_{kl}} = \frac{\mu_0}{4\pi} g_k \mu_k \cdot g_l \mu_l \frac{1}{r_{kl}^3}\left(\mathbf{S_k S_l} - \frac{3(\mathbf{S_k}\cdot\mathbf{r_{kl}})\cdot(\mathbf{S_l}\cdot\mathbf{r_{kl}})}{r_{kl}^2}\right) \quad (8)$$

And is connected to the interaction rate $R_{dip} = 1/\tau_c^{dip}$ with:

$$\hbar R_{dip} = \sqrt{\sum_{k\neq l} < H_{kl}^2 >} \quad (9)$$

By using (8) one finds[8]:

$$< H_{kl}^2 >= \left(\frac{\mu_0}{4\pi} g_k \mu_k \cdot g_l \mu_l\right)^2 \cdot 6C_s^2 \cdot \frac{1}{r_{kl}^6} \quad (10)$$

Spins in a thick layer:

For a layer with height of δd consisting of spins with the density σ we use the following approximation:

$$\sum_{k\neq l} \frac{1}{r_{kl}^6} \approx \sigma \int_0^{2\pi} d\phi \int_{d_{min}}^{\delta d - d_{min}} dz \int_{r_{min}}^{\infty} dr\ \frac{r}{(r^2+z^2)^3} = 2\pi\sigma \int_{d_{min}}^{\delta d - d_{min}} dz \int_{r_{min}}^{\infty} dr\ \frac{r}{(r^2+z^2)^3}$$

(11a)

Where $d_{\min}$ and r_{min} accounts for the minimal distance between neighbor spins since the spins later can't be infinitesimally dense packed. Now assuming homogeneous distributed spins each caged in a sphere with radius of r_s, we make the following approach for a thick layer: $d_{min} \approx r_{min} \approx \frac{1}{\sqrt{2}} \cdot r_s$ and $\delta d \gg r_s$.

Spins in the center of the layer will have more neighbors to interact then spins directly at the surface. As an approximation we modify Equation (11a) by average over all possible positions:

$$\sum_{k\neq l}\frac{1}{r_{kl}^6} \approx \frac{\sigma}{\delta d-2d_{min}} \int_0^{\delta d-2d_{min}} dh \int_{-h}^{\delta d-2d_{min}-h} dz \int_0^{2\pi} d\phi \int_{r_{min}}^{\infty} dr \frac{r}{(r^2+z^2)^3} \quad (11b)$$

$$\sum_{k\neq l}\frac{1}{r_{kl}^6} \approx 2\pi\sigma \cdot \frac{\pi}{2\sqrt{2}r_s^3} \approx 7 \cdot \frac{\sigma}{r_s^3} \quad (11c)$$

And the average spin-spin interaction rate of a spin bath in a thick layer can be approximated by:

$$R_{dip}^{layer} \approx 0.5157 \cdot \mu_0 \cdot \frac{g^2 \cdot \mu^2}{\hbar} \cdot C_s \cdot \sqrt{\frac{\sigma}{r_s^3}} \quad (12)$$

Supplementary Discussion

NV spin population readout in NDs

The charge state of the NV centers can be influenced by various quantities, such as the local environments, surface treatment of the diamond, excitation wavelength of laser and etc.[10,11,12,13]. In particular, the charge state of NV centers in NDs is highly depending on the surface passivation due to their high surface to volume ratio[12]. In addition, their charge state can adjust over time without illumination, and also differs under laser illumination. As a consequence, the NV centers can change their charge state on the time scale of several μs to ms, depending on the used laser power and wavelength[13], which can be directly observed as an increase or decrease of the NV fluorescence after turning on the laser[10]. A typical single T_1 measurement containing no additional control sequence will contain that information, diminishing the measured spin contrast significantly. If one now applies a second measurement (control), i.e., by an additional microwave pulse (e.g., square or linear chirp pulse) before read out, the NV sublevel population is inverted and the spin contrast can be calculated. In other words, one can extract the pristine spin contrast by subtracting the normalized T_1 measurement from the control[14].

Simulation of NV spin sublevel flip induced by microwave excitation

We simulated the evolution of the spin-state using the NV spin Hamiltonian[15,16] by applying a linear polarized microwave excitation along the x-direction of the NV reference frame, while its z-

direction is along the NV rotational symmetry axis. We introduced the desired broadening as a Zeeman-like term, which would be introduced by a magnetic field aligned along the NV quantization axis. Both transitions are split by the "Zeeman-like term" around 16 MHz (see Supplementary Fig. 10). In this scenario we only have to consider the angular dependence of the microwave excitation field versus the NV quantitation axis. To simplify the simulated model, we also intentionally discard the Zero field parameter E that is accounting for strain in the NDs crystal. After averaging over all possible angular orientations of the microwave driving field, we extract the average probability to flip NV sublevel.

Inhomogeneous ODMR linewidth broadening in NDs

From Hahn-echo measurements on a well dispersed NDs sample we estimated an average T_2 time around ~1μs (data not shown) for single to few NVs in an individual diamond nanocrystal. This is a typical value for NDs[17,18,19]. The corresponding natural line width of one ODMR line would be around several hundreds of kHz, and therefore cannot be the origin of the observed line-broadening (Supplementary Fig. 10a). Another possible broadening by laser excitation could be ruled out by checking its laser power dependent behaviors (data not shown). Therefore, we attribute the observed inhomogeneous ODMR line broadening to the variations of strain among different diamond nanocrystals[20,21]. In addition, a weak residual static magnetic field, e.g., the earth magnetic field, may also partially account for such splitting and broadening.

Supplementary References

1. Schaefer, M., Hanik, N. & Kilbinger, A. F. M. ROMP Copolymers for Orthogonal Click Functionalizations. *Macromolecules* **45**, 6807–6818 (2012).

2. Moore, D. A. Selective Trialkylation of Cyclen with tert-Butyl Bromoacetate. *Org. Synth.* 10–14 (2008).

3. Wang, Y. *et al.* Reduction-Degradable Linear Cationic Polymers as Gene Carriers Prepared by Cu(I)-Catalyzed Azide−Alkyne Cycloaddition. *Biomacromolecules* **12**, 66–74 (2011).

4. Rudovský, J. *et al.* Synthesis of a bifunctional monophosphinic acid DOTA analogue ligand and its lanthanide(III) complexes. A gadolinium(III) complex endowed with an optimal water exchange rate for MRI applications. *Org. Biomol. Chem.* **3**, 112–117 (2005).

5. Gilchrist, T. L., Wasson, R. C., King, F. D. & Wootton, G. Intramolecular cycloaddition of azoalkenes derived from terminal alkenoic and alkynoic acids. *J. Chem. Soc. Perkin Trans. 1*, 2511–2516 (1987).

6. Yau, H. M., Croft, A. K. & Harper, J. B. Investigating the origin of entropy-derived rate accelerations in ionic liquids. *Faraday Discuss.* **154**, 365–371 (2011).

7. Jarmola, A., Acosta, V. M., Jensen, K., Chemerisov, S. & Budker, D. Temperature- and magnetic-field-dependent longitudinal spin relaxation in nitrogen-vacancy ensembles in diamond. *Phys. Rev. Lett.* **108**, 197601 (2012).

8. Tetienne, J. P. et al. Spin relaxometry of single nitrogen-vacancy defects in diamond nanocrystals for magnetic noise sensing. *Phys. Rev. B* **87**, 235436 (2013).

9. Caravan P., Ellison J. J., McMurry T. J. & Lauffer R. B. Gadolinium(III) Chelates as MRI Contrast Agents: Structure, Dynamics, and Applications. *Chem. Rev.* **99**, 2293 – 2352 (1999).

10. Gaebel T, et al. Photochromism in single nitrogen-vacancy defect in diamond. *Appl. Phys. B* **82**, 243-246 (2006).

11. Hauf M, et al. Chemical control of the charge state of nitrogen-vacancy centers in diamond. *Phys. Rev. B* **83**, 081304 (2011).

12. Petráková V, et al. Luminescence of nanodiamond driven by atomic functionalization: towards novel detection principles. *Adv. Funct. Mater.* **22**, 812-819 (2012).

13. Aslam N, Waldherr G, Neumann P, Jelezko F, Wrachtrup J. Photo-induced ionization dynamics of the nitrogen vacancy defect in diamond investigated by single-shot charge state detection. *New J. Phys.* **15**, 013064 (2013).

14. Häberle T, Schmid-Lorch D, Reinhard F, Wrachtrup J. Nanoscale nuclear magnetic imaging with chemical contrast. *Nat. Nanotechnol.* **10**, 125-128 (2015).

15. Michl J, et al. Perfect alignment and preferential orientation of nitrogen-vacancy centers during chemical vapor deposition diamond growth on (111) surfaces. *Appl. Phys. Lett.* **104**, 102407 (2014).

16. Alegre TPM, Santori C, Medeiros-Ribeiro G, Beausoleil RG. Polarization-selective excitation of nitrogen vacancy centers in diamond. *Phys. Rev. B* **76**, 165205 (2007).

17. Tisler J, et al. Fluorescence and spin properties of defects in single digit nanodiamonds. *ACS Nano* **3**, 1959-1965 (2009).

18. Laraoui A, Hodges JS, Meriles CA. Nitrogen-vacancy-assisted magnetometry of paramagnetic centers in an individual diamond nanocrystal. *Nano Lett.* **12**, 3477-3482 (2012).

19. Trusheim ME, et al. Scalable fabrication of high purity diamond nanocrystals with long-spin-coherence nitrogen vacancy centers. *Nano Lett.* **14**, 32-36 (2013).

20. Bradac C, et al. Observation and control of blinking nitrogen-vacancy centres in discrete nanodiamonds. *Nat. Nanotechnol.* **5**, 345-349 (2010).

21. McGuinness L, et al. Quantum measurement and orientation tracking of fluorescent nanodiamonds inside living cells. *Nat. Nanotechnol.* **6**, 358-363 (2011).